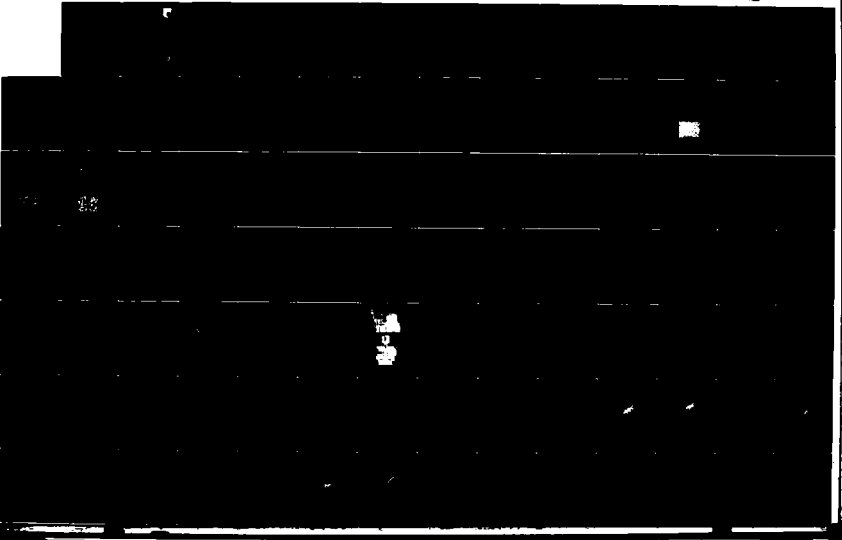
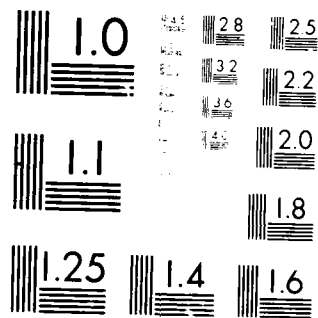


AD-A199 842 GROWTH OF SMALL CRACKS IN AEROENGINE DISC MATERIALS(U) 1/3  
SOUTHWEST RESEARCH INST SAN ANTONIO TX  
S J HUDAK ET AL JUN 88 AFML-TR-88-4090  
UNCLASSIFIED F33615-85-C-5051 F/G 11/6.1 NL





MICROCOPY RESOLUTION TEST CHART  
 NATIONAL BUREAU OF STANDARDS-1963-A

AD-A199 842

AFWAL-TR-88-4090

THE FILE



GROWTH OF SMALL CRACKS IN AEROENGINE DISC MATERIALS

S. J. Hudak, Jr.  
D. L. Davidson  
K. S. Chan

Southwest Research Institute  
P. O. Drawer 28510  
6220 Culebra Road  
San Antonio, TX 78264

A. C. Howland  
M. J. Walsch  
Rolls-Royce plc  
P. O. Box 31  
Derby, England

June 1988

Final Report for Period August 1985 - January 1988

Approved for public release; distribution is unlimited

DTIC  
ELECTE  
OCT 05 1988  
S D

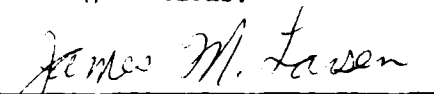
MATERIALS LABORATORY  
AIR FORCE WRIGHT AERONAUTICAL LABORATORIES  
AIR FORCE SYSTEMS COMMAND  
WRIGHT-PATTERSON AIR FORCE BASE, OHIO 45433-6000

NOTICE

When Government drawings, specifications, or other data are used for any purpose other than in connection with a definitely related Government procurement operation, the United States Government thereby incurs no responsibility nor any obligation whatsoever, and the fact that the government may have formulated, furnished, or in any way supplied the said drawings, specifications, or other data, is not to be regarded by implication or otherwise as in any manner licensing the holder or any other person or corporation, or conveying any rights or permission to manufacture, use, or sell any patented invention that may in any way be related thereto.

This technical report has been reviewed and is approved for publication.

This report is releasable to the National Technical Information Service (NTIS). At NTIS, it will be available to the general public, including foreign nations.




JAMES M. LARSEN  
Metals Behavior Branch  
Metals and Ceramics Division



ALLAN W. GUNDERSON  
Tech Area Manager  
Metals Behavior Branch  
Metals and Ceramics Division

FOR THE COMMANDER:



JOHN P. HENDERSON, CHIEF  
Metals Behavior Branch  
Metals and Ceramics Division

"If your address has changed, if you wish to be removed from our mailing list, or if the addressee is no longer employed by your organization please notify AFWAL/MLLN, W-P AFB, OH 45433 to help us maintain a current mailing list".

Copies of this report should not be returned unless return is required by security considerations, contractual obligations, or notice on a specific document.

## REPORT DOCUMENTATION PAGE

Form Approved  
OMB No 0704-0188  
Exp. Date Jun 30, 1986

|  |       |  |  |  |                |
|--|-------|--|--|--|----------------|
| 1a. REPORT SECURITY CLASSIFICATION<br>Unclassified   |       |  | 1b. RESTRICTIVE MARKINGS   |  |                |
| 2a. SECURITY CLASSIFICATION AUTHORITY  |       |  | 3. DISTRIBUTION/AVAILABILITY OF REPORT<br>Approved for public release;<br>distribution is unlimited                    |  |                |
| 2b. DECLASSIFICATION/DOWNGRADING SCHEDULE  |       |  |  |  |                |
| 4. PERFORMING ORGANIZATION REPORT NUMBER(S)  |       |  | 5. MONITORING ORGANIZATION REPORT NUMBER(S)<br>AFWAL-TR-88-4090  |  |                |
| 6a. NAME OF PERFORMING ORGANIZATION<br>Southwest Research Institute  |       | 6b. OFFICE SYMBOL<br>(if applicable)       | 7a. NAME OF MONITORING ORGANIZATION<br>Air Force Wright Aeronautical Laboratories<br>Materials Laboratory (AFWAL/MLLN) |  |                |
| 6c. ADDRESS (City, State, and ZIP Code)<br>PO Drawer 28510<br>6220 Culebra Road<br>San Antonio, TX 78284   |       |  | 7b. ADDRESS (City, State, and ZIP Code)<br>Wright-Patterson AFB, OH 45433-6533   |  |                |
| 8a. NAME OF FUNDING/SPONSORING ORGANIZATION  |       | 8b. OFFICE SYMBOL<br>(if applicable)       | 9. PROCUREMENT INSTRUMENT IDENTIFICATION NUMBER<br>F33615-85-C-5051  |  |                |
| 8c. ADDRESS (City, State, and ZIP Code)  |       |  | 10. SOURCE OF FUNDING NUMBERS  |  |                |
|  |       |  | PROGRAM ELEMENT NO.<br>62102F  | PROJECT NO.<br>2420                                | TASK NO.<br>01 |
| 11. TITLE (Include Security Classification)<br>Growth of Small Cracks in Aeroengine Disc Materials (U)   |       |  |  |  |                |
| 12. PERSONAL AUTHOR(S)<br>S.J. Hudak, Jr., D.L. Davidson, K.S. Chan - SwRI; A.C. Howland, M.J. Walsh, Rolls-Royce plc  |       |  |  |  |                |
| 13a. TYPE OF REPORT<br>Final Report  |       | 13b. TIME COVERED<br>FROM 8-1-85 TO 1-1-88 |  | 14. DATE OF REPORT (Year, Month, Day)<br>June 1988 |                |
| 15. PAGE COUNT<br>251  |       |  |  |  |                |
| 16. SUPPLEMENTARY NOTATION   |       |  |  |  |                |
| 17. COSATI CODES   |       |  | 18. SUBJECT TERMS (Continue on reverse if necessary and identify by block number)                                      |  |                |
| FIELD  | GROUP | SUB-GROUP                                  |  |  |                |
| 11   | 06    |  |  |  |                |
| 13   | 13    |  |  |  |                |
| 19. ABSTRACT (Continue on reverse if necessary and identify by block number)<br>Growth rate data for small fatigue cracks in fine grained (12 $\mu$ m) and coarse grained (30 $\mu$ m) Astroloy and in coarse grained (42 $\mu$ m) Waspaloy were obtained at temperatures of 25°C, 200°C and 600°C. Expressing the crack growth kinetics in terms of the linear elastic parameter $\Delta K$ , resulted in small cracks growing faster than large cracks in all cases except that of the fine grained Astroloy at elevated temperature. This difference occurred even though the crystallographic nature of cracking in small cracks was shown to be the same as that in large cracks, based on metallographic, selected area electron channeling, and fractographic information. Furthermore, the fracture morphology of small and large cracks also exhibited the same dependence on temperature and applied stress level indicating that the crack propagation mechanism was the same in both cases. Consequently, it was concluded that the observed differences in kinetics were due to differences in mechanical driving force for small and large fatigue cracks. |       |  |  |  |                |
| 20. DISTRIBUTION/AVAILABILITY OF ABSTRACT<br><input checked="" type="checkbox"/> UNCLASSIFIED/UNLIMITED <input type="checkbox"/> SAME AS RPT <input type="checkbox"/> DTIC USERS   |       |  | 21. ABSTRACT SECURITY CLASSIFICATION<br>Unclassified   |  |                |

Contributions to these differences in mechanical driving force were examined using high resolution scanning electron microscopy, coupled with the stereoimaging technique. This technique enabled the quantification of local crack-tip displacements, strains, and crack opening loads during fatigue crack growth. Measurements showed that the crack-tip strain fields, as well as the nature of crack closure, were significantly different for small and large cracks. These observations were consistent with the fact that the linear elastic fracture mechanics concept of small scale yielding was shown to be invalid for small cracks based on the fact that measured crack-tip plastic zone sizes were on the order of the crack size.

In view of this situation, the local crack-tip measurements were used to define an elastic-plastic crack driving force based on the relationship between crack-tip opening displacement and  $\Delta J$ , the cyclic J-integral. To facilitate comparison of small and large crack data,  $\Delta J$  was expressed in terms of an equivalent  $\Delta K$ , termed  $\Delta K_{eq}$ . The value of  $\Delta K_{eq}$  for small cracks was found to depend on significant contributions from plasticity, mixed mode and crack closure, while that for large cracks was found to depend only on crack closure. Expressing the crack growth rates of small and large cracks as a function of  $\Delta K_{eq}$  resulted in kinetics which were independent of crack size, within experimental scatter.

The above results formed the basis of a phenomenological model for the growth of both small and large fatigue cracks in which  $\Delta K_{eq}$  is related to the applied  $\Delta K$ . Since  $\Delta K_{eq}$  cannot currently be computed analytically, the phenomenological model was used to predict the fatigue life of unflawed turbine engine discs. The initial flaw sizes for these calculations were set equal to the material grain size -- a size typical of the intrinsic microstructural defects expected to be found in Ni-based superalloys. The fatigue lives predicted using the phenomenological model were found to be in better overall agreement with measured fatigue lives than those predicted based on the classical linear elastic fracture mechanics approach and large crack data. At longer lives, the latter approach overpredicted the measured lives by several orders of magnitude. This overprediction was shown to be associated with the occurrence of the fatigue crack growth threshold for large cracks,  $\Delta K_{th}$ . Based on these results, it is concluded that  $\Delta K_{th}$  and associated near-threshold growth rate data are not applicable to material selection, design and damage tolerant analyses of turbine engine discs.

## FOREWORD

The current program was conducted through a teaming arrangement between Southwest Research Institute (SwRI) and Rolls-Royce (RR). SwRI was the prime contractor and was responsible for the overall conduct and management of the program, while RR was a subcontractor to SwRI. The RR technical effort was conducted at RR plc in Derby, England, while the subcontract was administered through RR, Inc., Atlanta Engineering Office, with A. B. Thakker serving as the RR Program Manager. The technical responsibilities of SwRI included the experimentation on small cracks, as well as the mechanistic studies and phenomenological model development. RR provided the test materials and generated the mechanical properties and reference fatigue crack growth rate data on large cracks, and conducted most of the fractographic examination. RR also used the model developed by SwRI to predict fatigue lives of available rig-tested turbine discs. This procedure enabled the model assessment to be conducted independent of the model development.

|                    |                                     |
|--------------------|-------------------------------------|
| Accession For      |                                     |
| NTIS GRA&I         | <input checked="" type="checkbox"/> |
| DTIC TAB           | <input type="checkbox"/>            |
| Unannounced        | <input type="checkbox"/>            |
| Justification      |                                     |
| By _____           |                                     |
| Distribution/      |                                     |
| Availability Codes |                                     |
| Dist               | Avail and/or<br>Special             |
| <b>A-1</b>         |                                     |



## TABLE OF CONTENTS

|  | <u>Page</u> |
|--|-------------|
| 1. SUMMARY   | 1-1         |
| 2. INTRODUCTION  | 2-1         |
| 2.1 References   | 2-2         |
| 3. MATERIAL MICROSTRUCTURAL AND MECHANICAL PROPERTIES  | 3-1         |
| 3.1 Microstructural Characterization   | 3-1         |
| 3.2 Mechanical Properties  | 3-5         |
| 3.3 References   | 3-17        |
| 4. FATIGUE THRESHOLD AND LARGE CRACK GROWTH BEHAVIOR   | 4-1         |
| 4.1 Large Crack Testing Procedure  | 4-1         |
| 4.2 Near-Threshold Fatigue Crack Growth Rates<br>in Large Cracks   | 4-2         |
| 4.3 The Influence of Grain Size on Fatigue Threshold   | 4-11        |
| 4.4 Crack Closure in Large Cracks  | 4-15        |
| 4.5 References   | 4-19        |
| 5. GROWTH OF SMALL CRACKS AS A FUNCTION OF $\Delta K$  | 5-1         |
| 5.1 Small Crack Experimental Procedure   | 5-1         |
| 5.2 Stress Intensity Factor For Small Cracks<br>in Bending   | 5-5         |
| 5.3 Effect of Elastic Anisotropy and Mixed-Mode Loading<br>on Stress Intensity Factor for Small Cracks                   | 5-10        |
| 5.4 Effect of Temperature on Initiation and Early<br>Growth of Microcracks   | 5-12        |
| 5.5 Sources of Variability in Small Crack Growth Rates   | 5-19        |
| 5.6 Small Versus Long Crack Growth Rates as a Function<br>of Material, Environment, Temperature and Loading<br>Variables | 5-26        |
| 5.6.1 Effect of Applied Stress Level   | 5-36        |
| 5.6.2 Effect of Environment  | 5-37        |
| 5.6.3 Effect of Material Variables   | 5-37        |
| 5.6.4 Effect of Temperature  | 5-38        |
| 5.7 References   | 5-39        |



## TABLE OF CONTENTS (CONTINUED)

|   | <u>Page</u> |
|---|-------------|
| 6. MECHANISMS OF SMALL CRACK INITIATION AND GROWTH  | 6-1         |
| 6.1 The Role of Pores and Slip Bands in Crack Initiation and Early Growth                   | 6-1         |
| 6.2 The Crystallography of Microcrack Initiation and Growth                                 | 6-10        |
| 6.3 The Fractography of Small Cracks  | 6-23        |
| 6.3.1 Fractography Versus Test Temperatures   | 6-24        |
| 6.3.2 Fractography Versus Alloy Composition   | 6-28        |
| 6.3.3 Fractography Versus Grain Size  | 6-28        |
| 6.3.4 Fractography of Small versus Large Cracks   | 6-28        |
| 6.4 References  | 6-33        |
| 7. CRACK-TIP DEFORMATION AND CRACK CLOSURE IN SMALL CRACKS                                  | 7-1         |
| 7.1 Experimental Techniques   | 7-1         |
| 7.1.1 Initiation of Fatigue Microcracks   | 7-1         |
| 7.1.2 SEM Experiments   | 7-2         |
| 7.1.3 Stereoimaging Analysis  | 7-4         |
| 7.2 Local Crack-Tip Measurements on Small Cracks  | 7-7         |
| 7.2.1 Crack-Tip Displacements   | 7-7         |
| 7.2.2 Crack-Tip Strain and Plastic Zone Size  | 7-14        |
| 7.2.3 Crack Closure in Small Versus Large Cracks  | 7-19        |
| 7.3 References  | 7-27        |
| 8. A PHENOMENOLOGICAL MODEL FOR THE GROWTH OF SMALL CRACKS                                  | 8-1         |
| 8.1 The Relationship Between Cyclic CTOD and $\Delta J$                                     | 8-1         |
| 8.2 Phenomenological Model for the Growth of Small and Large Fatigue Cracks                 | 8-5         |
| 8.3 Small and Large Crack Growth Rates as Functions of $\Delta K_{eq}$ and $\Delta K_{eff}$ | 8-12        |
| 8.4 References  | 8-17        |
| 9. EFFECT OF SMALL CRACK BEHAVIOR ON COMPONENT FATIGUE LIFE                                 | 9-1         |
| 9.1 Analysis of Rig-Tested Discs  | 9-1         |
| 9.2 Comparison of Predicted Versus Measured Disc Lives                                      | 9-3         |
| 9.3 References  | 9-7         |
| 10. DISCUSSION  | 10-1        |
| 10.1 References   | 10-5        |
| 11. CONCLUSIONS   | 11-1        |

## TABLE OF CONTENTS (CONTINUED)

|   | <u>Page</u> |
|---|-------------|
| APPENDIX - FINITE ELEMENT ANALYSES IN NON-ISOTROPIC MATERIALS                             | A-1         |
| A.1 Two-Dimensional Finite Element Models   | A-1         |
| A.1.1 Elastic Properties of Rotated Anisotropic Material                                  | A-3         |
| A.1.2 Calculation of Elastic Strain Energy Release Rate 'G' Using MARC                    | A-9         |
| A.1.3 Plane Elastic Anisotropy  | A-11        |
| A.1.4 Displacement Extrapolation for Calculation of $K_I$ and $K_{II}$                    | A-16        |
| A.1.5 Crack Extension and Branching   | A-18        |
| A.1.6 Angled Edge Crack Models  | A-22        |
| A.1.7 Discussion on 2-Dimensional Analyses  | A-22        |
| A.2 Three-Dimensional Stress Intensity Factors for Cracks in Locally Anisotropic Material | A-27        |
| A.2.1 Three-Dimensional Finite Element Models   | A-27        |
| A.2.2 30 Degree Angled Edge Through-Crack Model   | A-29        |
| A.2.3 Perpendicular Semicircular Surface Crack  | A-29        |
| A.2.4 Elastic Properties of Models  | A-29        |
| A.2.5 Crack Orientation Within Anisotropic Region   | A-32        |
| A.2.6 Elastic Properties of Rotated Anisotropic Material                                  | A-32        |
| A.2.7 Three-Dimensional Elastic Anisotropy  | A-36        |
| A.2.8 Displacement Extrapolation for Calculation of $K_I$ , $K_{II}$ , and $K_{III}$      | A-39        |
| A.2.9 Elastic Strain Energy Method  | A-40        |
| A.2.10 Results of 3-Dimensional Analyses  | A-43        |
| A.2.11 Conclusions  | A-49        |
| A.3 Summary   | A-53        |
| A.4 References  | A-55        |

## LIST OF FIGURES

| <u>Figure</u>   | <u>Page</u> |
|---|-------------|
| 3-1 Microstructure of Waspaloy  | 3-3         |
| 3-2 $\gamma'$ Structure of Waspaloy   | 3-3         |
| 3-3 Microstructure of FG Astroloy   | 3-6         |
| 3-4 $\gamma'$ Structure of FG Astroloy  | 3-6         |
| 3-5 Microstructure of CG Astroloy   | 3-7         |
| 3-6 $\gamma'$ Structure of CG Astroloy  | 3-7         |
| 3-7 Tensile Test Specimen   | 3-8         |
| 3-8 Strain-controlled Low cycle Fatigue Specimen  | 3-8         |
| 3-9 Monotonic (solid lines) and Cyclic (dashed lines) Stress-strain Curves for Waspaloy at Several Temperatures     | 3-12        |
| 3-10 Monotonic (solid lines) and Cyclic (dashed lines) Stress-strain Curves for FG Astroloy at Several Temperatures | 3-13        |
| 3-11 Monotonic (solid lines) and Cyclic (dashed lines) Stress-strain Curves for CG Astroloy at Several Temperatures | 3-14        |
| 3-12 Creep Rupture Test Specimen  | 3-18        |
| 3-13 Stress-rupture Data for Waspaloy, and FG and CG Astroloy at 600°C  | 3-19        |
| 4-1 Temperature Effects in Fine Grain Astroloy  | 4-3         |
| 4-2 Temperature Effects in Coarse Grain Astroloy  | 4-4         |
| 4-3 Effect of Temperature on Near Threshold Crack Growth Behavior of Necklace Astroloy                              | 4-5         |
| 4-4 Effect of Microstructure on Near Threshold Crack Growth Behavior of Astroloy (200°C)                            | 4-6         |
| 4-5 Effect of Microstructure on Near Threshold Crack Growth Behavior of Astroloy (600°C)                            | 4-7         |
| 4-6 Load Ratio Effects in Fine Grain Astroloy (600°C)   | 4-8         |
| 4-7 Load Ratio Effects in Coarse Grain Astroloy (600°C)   | 4-9         |

## LIST OF FIGURES (CONTINUED)

| <u>Figure</u> |   | <u>Page</u> |
|---------------|---|-------------|
| 4-9           | Effect of Environment on Fatigue Crack Growth Rates of Waspaloy (600°C)   | 4-12        |
| 4-10          | Effect of Temperature on Near Threshold Crack Growth Rates of Waspaloy  | 4-13        |
| 4-11          | Correlation of $\Delta K_{th}$ with Grain Size in Astroloy  | 4-14        |
| 4-12          | Definition of Terms Used to Characterize Fatigue Crack Closure  | 4-16        |
| 4-13          | Crack Closure Behavior of Large Cracks in Necklace Astroloy at Various Temperatures, from Soniak and Remy [4.10]  | 4-18        |
| 5-1           | System for Small Crack Testing Using 3-point Bend Specimens   | 5-2         |
| 5-2           | Temperature Profile in Induction-heated Bend Specimen at 650°C  | 5-4         |
| 5-3           | Fatigue Crack Shape as a Function of Crack Size for Various Alloys and Test Temperatures  | 5-6         |
| 5-4           | Dependence of Local Stress ratio ( $R$ ) on Local Cyclic Strain Range ( $\Delta\epsilon$ ) for Three-point Bend Specimens   | 5-8         |
| 5-5           | Measured Strain at the Surface of the Three-point Bend Specimen as a Function of the Normalized Maximum Stress, $S = S_{max}/S_{ys}$  | 5-9         |
| 5-6           | Normalized Mode I Stress Intensity Factor for Inclined Cracks in a Mar-M200 Single-crystal CT Specimen [Ref. 5.4]<br>$a' = 1 + a \cos \theta$ is the Projected Crack Length | 5-11        |
| 5-7           | Comparison of Isotropic and Anisotropic Model I Stress Intensity Factors from Finite Element Model of a Semi-circular Surface Crack   | 5-13        |
| 5-8           | Influence of Relative Applied Stress Level ( $S = S_{max}/S_{ys}$ ) and Temperature on the Cyclic Life of 10x10x70 mm Bend Specimens of CG Astroloy                         | 5-15        |
| 5-9           | Example of Erratic Crack Growth in Ni-base Alloys at 600°   | 5-16        |
| 5-10          | Comparison of Cyclic Lives of Notched ( $k_t = 2.13$ ) Tension  | 5-18        |

## LIST OF FIGURES (CONTINUED)

| <u>Figure</u> |   | <u>Page</u> |
|---------------|---|-------------|
| 5-12          | Comparison of Small Crack Data from Current Heat (□) of Astroloy Versus that from a Previous Heat (▲), Ref. [5.13]  | 5-21        |
| 5-13          | Comparison of Small Crack Data Variability from a Single Data Set Versus the Entire Data Set for CG Astroloy at 25°C  | 5-23        |
| 5-14          | Crack Length (top-curve-right scale) and Crack Growth Rate (lower curve-left scale) for One End of a Small Crack in Coarse Grained Astroloy at 20°C (BF-17, Crack 18) | 5-24        |
| 5-15          | Percentage of Surface Crack Tips Stopped by Grain Boundaries in Waspaloy and Coarse Grained Astroloy at Room Temperature  | 5-25        |
| 5-16          | Effect of Crack Growth Increment on Computed Growth Rates for Small Cracks  | 5-27        |
| 5-17          | Influence of Frequency of Measurement and/or Test Interruption on the Growth Rates of Small Cracks  | 5-28        |
| 5-18          | Comparison of Large and Small Crack Data in CG Astroloy at 25°C for Various Relative Applied Stress Levels and Environments   | 5-29        |
| 5-19          | Comparison of Large and Small Crack Growth Rate Data in CG Astroloy at 600°C for Various Relative Applied Stress Levels and Environments                              | 5-30        |
| 5-20          | Comparison of Large and Small Crack Growth Rate Data in Waspaloy at 600°C for Various Relative Applied Stress Levels and Environments                                 | 5-31        |
| 5-21          | Effect of Alloy Composition on the Crack Growth Rates in Both Small and Large Cracks at 600°C   | 5-32        |
| 5-22          | Comparison of Large (■) and "small" (□, $a = 215-1000 \mu\text{m}$ ) Crack Growth Rates in FG Astroloy at 200°C   | 5-33        |
| 5-23          | Comparison of Large and Small Crack Growth Rates in FG Astroloy at 600°C  | 5-34        |
| 5-24          | Effect of Temperature on the Growth Rates of Small (symbols) and Large (lines) Cracks in CG Astroloy  | 5-35        |

## LIST OF FIGURES (CONTINUED)

| <u>Figure</u>   | <u>Page</u> |
|---|-------------|
| 6-2 Two Views of Fatigue Crack Initiation at a Surface Pore Showing Debris at the Corner of the Pore and Along the Crack Further Away   | 6-4         |
| 6-3 Fatigue Crack Initiated within a Grain, Along a Slip Band: (a) is an Overall View of the Crack Showing no Debris, and (b) is a Grazing Angle View Showing Mode III Displacements                    | 6-5         |
| 6-4 Slip Band Initiated Fatigue Crack Showing the Lack of Debris in the Region of Initiation  | 6-7         |
| 6-5 Relationship Between the $\gamma'$ -precipitate Structure and Slip Lines Showing that Slip is of $\langle 111 \rangle$ Type and is Likely to Result in Both In-plane and Out-of-plane Displacements | 6-8         |
| 6-6 Three Views of a Slip Band Initiated Fatigue Crack Showing Extrusions Having Tongue-like Shapes   | 6-9         |
| 6-7 Electron Channeling Map Showing Orientations of the Surface Normal Directions for those Grains which Initiated Cracks   | 6-12        |
| 6-8 Definition of Geometric Relations   | 6-13        |
| 6-9 Determination of Crack Growth Plane and Slip Direction by Selected Area Electron Channeling   | 6-15        |
| 6-10 Determination of Crack Growth Plane and Slip Direction by Selected Area Electron Channeling  | 6-16        |
| 6-11 Orientations of Low Taylor Factor for fcc Crystals Deforming by $\{111\} \langle 110 \rangle$ slip: (a) $M=2$ , and (b) $M=2.46$   | 6-20        |
| 6-12 Standard Stereographic Triangle Showing Orientations with Low Taylor Factor Values   | 6-21        |
| 6-13 Variation of Normalized Taylor Factors ( $M/\bar{M}$ ) with the Number of Grains   | 6-22        |
| 6-14 Effect of Test Temperature on Fracture Surfaces of Small Cracks in CG Astroloy   | 6-25        |
| 6-15 Effect of Test Temperature on Fracture Surfaces of Small Cracks in Waspaloy Versus CG Astroloy   | 6-26        |
| 6-16 Fracture Surfaces of Small Cracks in CG Astroloy Versus  | 6-27        |

## LIST OF FIGURES

| <u>Figure</u> |   | <u>Page</u> |
|---------------|---|-------------|
| 6-18          | Effect of Grain Size and Temperature on the Fractography of Long Cracks in Astroloy (after Ref. 6.14)                                     | 6-30        |
| 6-19          | Schematic Illustration of Consolidation of Small and Large Crack Growth Rate Data in terms of $\Delta K_{eq}$                             | 6-32        |
| 7-1           | Specimen Design Used to Study Small Cracks Within the SEM   | 7-2         |
| 7-2           | 125 $\mu\text{m}$ crack in Fine Grained Astroloy Initiated at Ambient Temperature, but Grown at 600°C                                     | 7-5         |
| 7-3           | 14 $\mu\text{m}$ long crack in Coarse Grained Astroloy at 20°C  | 7-6         |
| 7-4           | (a) Displacements Measured Around the Tip of the Cracks Shown in the Upper Part of Figure 7-2, Fine Grained Astroloy at 600°C             | 7-8         |
| 7-4           | (b) Displacements Measured Around the Tip of the Cracks Shown in the Lower Part of Figure 7-2, Fine Grained Astroloy at 600°C             | 7-9         |
| 7-5           | Original ( $X' - Y'$ ) and Transformed ( $X-Y$ ) Coordinates for the Measured Displacement Fields at Small Cracks                         | 7-10        |
| 7-6           | Crack Opening Displacements for FG Astroloy at 600°C  | 7-12        |
| 7-7           | Crack Opening Displacements in CG Astroloy at 600°C   | 7-13        |
| 7-8           | Comparison of $\Delta K$ Determined from Measured Crack Displacements with Applied $\Delta K$ for Large Cracks in Several Aluminum Alloys | 7-15        |
| 7-9           | Measured Strain Fields in FG Astroloy at 600°C a) Upper and b) Lower Crack Tips Shown in Figure 7-2                                       | 7-16        |
| 7-10          | Cyclic Plastic Zone Ahead ( $\phi = 0^\circ$ ) of the Small Crack as a Function of Applied $\Delta K$                                     | 7-20        |
| 7-11          | Cyclic Plastic Zone Sizes to the Side ( $\phi = 90^\circ$ ) of Small Cracks as a Function of Applied $\Delta K$                           | 7-21        |
| 7-12          | Ratio of Crack Size to Plastic Zone Size ( $a/r_p$ ) for Small Cracks in Astroloy of Various Sizes  | 7-22        |
| 7-13          | Comparison of Crack Closure Behavior of Small and Large Cracks at Various Temperatures  | 7-23        |
| 7-14          | Crack Closure Behavior of Small and Large Cracks in a 7075 Aluminum Alloy   | 7-15        |

## LIST OF FIGURES (CONTINUED)

| <u>Figure</u> |  | <u>Page</u> |
|---------------|--|-------------|
| 7-15          | Comparison of $K_{op}$ versus $K_{max}$ Data on Small Cracks in Astroloy from the Current Study with Those of Soniak and Remy [7.10]   | 7-26        |
| 8-1           | Operation Definition Used to Determine the Crack-tip Opening Displacement ( $\delta_t$ ) from Numerical Analyses [8.7]   | 8-3         |
| 8-2           | Equivalent Versus Applied $\Delta K$ for Small and Large Cracks in a 7075 Aluminum Alloy   | 8-8         |
| 8-3           | Equivalent Versus Applied $\Delta K$ for Small and Large Cracks in Astroloy at Various Temperatures  | 8-9         |
| 8-4           | Phenomenological Model for the Growth of Small and Large Fatigue Cracks: a) is the Crack Closure Behavior and b) is the Local Mechanical Driving Force Versus Applied $\Delta K$       | 8-11        |
| 8-5           | Comparison of Crack Growth Kinetics of Small ( $\square$ ) and Large ( $\text{—}$ ) Cracks in CG Astroloy at 25°C in Terms of a) Equivalent and b) Effective Stress Intensity Factors  | 8-13        |
| 8-6           | Comparison of Crack Growth Kinetics of Small ( $\square$ ) and Large ( $\text{—}$ ) Cracks in CG Astroloy at 600°C in Terms of a) Equivalent and b) Effective Stress Intensity Factors | 8-14        |
| 8-7           | Comparison of Crack Growth Kinetics in Small ( $\square$ ) and Large ( $\text{—}$ ) Cracks in Waspaloy at 600°C in Terms of a) Equivalent and b) Effective Stress Intensity Factors    | 8-15        |
| 9-1           | Influence of the Small Crack Effect on the Cyclic Life Ratio for Various Disc Temperatures and Failure Locations   | 9-3         |
| 9-2           | Comparison of Measured Disc Lives with Those Predicted Using Small Versus Large Crack Growth Kinetics  | 9-5         |
| 9-3           | Influence of Various Crack Growth Rate "laws" on the Cyclic Life Ratio   | 9-6         |
| A-1           | 2-D Finite Element Model   | A-2         |
| A-2           | Detail of Crack Region   | A-4         |
| A-3           | Rotation of Elastic Constants  | A-8         |
| A-4           | Stiffness of SRR99 at 20°C   | A-10        |
| A-5           | Extension by Node Advance  | A-20        |
| A-6           | Definition of Angular Stress Intensity Factors   | A-21        |



## LIST OF FIGURES (CONTINUED)

| <u>Figure</u>   | <u>Page</u> |
|---|-------------|
| A-7 Strain Energy Release Rate from a) Differential Crack Advance [dca] b) Angular SIF [asif] | A-24        |
| A-8 Strain Energy Release Rate by Angular S.I.F. Method                                       | A-25        |
| A-9 Strain Energy Release Rate by Angular S.I.F. Method                                       | A-26        |
| A-10 3D Brick Quarter Point Crack Tip Element Configuration                                   | A-28        |
| A-11 Edge Crack Mesh  | A-30        |
| A-12 Surface Crack Mesh   | A-31        |
| A-13 Low Index Axes in Relation to Crack Plane  | A-33        |
| A-14 Crack Orientation  | A-34        |
| A-15 Rotation of Elastic Constants  | A-35        |
| A-16 Crack Front Coordinate Axes  | A-37        |
| A-17 Notation for Plane Extension   | A-38        |
| A-18 a) Differential Stiffness Energy Release Calculation - Mesh Direction                    | A-42        |
| A-18 b) Energy Release Rate Calculation, 3D Crack Front                                       | A-42        |
| A-19 30 Degree Angled Edge Through-Crack  | A-45        |
| A-20 30 Degree Angled Edge Through-Crack  | A-46        |
| A-21 30 Degree Angled Edge Through Crack  | A-47        |
| A-22 Semicircular Surface Crack   | A-48        |
| A-23 Semicircular Surface Crack   | A-50        |
| A-24 Semicircular Surface Crack   | A-51        |
| A-25 Semicircular Surface Crack   | A-52        |

## LIST OF TABLES

| <u>Table</u> |  | <u>Page</u> |
|--------------|--|-------------|
| 3-1          | Chemical Composition of Waspaloy   | 3-2         |
| 3-2          | Chemical Composition of Astroloy   | 3-4         |
| 3-3          | Stress-Strain Properties of Waspaloy at Various Temperatures   | 3-9         |
| 3-4          | Stress-Strain Properties of FG Astroloy at Various Temperatures  | 3-10        |
| 3-5          | Stress-Strain Properties of CG Astroloy at Various Temperatures  | 3-11        |
| 3-6          | Monotonic Strain Hardening Data  | 3-15        |
| 3-7          | Cyclic Strain Hardening Data   | 3-16        |
| 6-1          | Orientation Relationships for Cracks in CG Astroloy  | 6-14        |
| 6-2          | Taylor Factor Calculation for Selected Grain Orientations Under Plain Strain Deformation ( $d\epsilon_{zz} = 0$ )                      | 6-18        |
| 7-1          | Crack-Tip Strains and Plastic Zone Sizes for Small Cracks in Astroloy  | 7-18        |
| 8-1          | Summary of Measured Crack-Tip Stress, Strain and Displacement Ranges and Resulting $\Delta K_{eq}$ Values for Small Cracks in Astroloy | 8-6         |
| 8-2          | Material Constants for the Phenomenological Model for the Growth of Small and Large Cracks   | 8-16        |
| A-1          | Elastic Material Properties  | A-5         |
| A-2          | Elastic Strain Energy Release Rate 'G' and Remote Stress for a Strain of $0.3846E-3$   | A-12        |
| A-3          | Relationship Between Plane Strain ( $b_{ij}$ ) and Plane Stress ( $a_{ij}$ ) Elastic Compliance  | A-13        |
| A-4          | Solutions to Characteristic Equation   | A-17        |
| A-5          | $K_I$ and $K_{II}$ for Co-linear Extension Determined by Displacement Extrapolation Method   | A-23        |

## 1. SUMMARY

Growth rate data for small fatigue cracks in fine grained (12  $\mu\text{m}$ ) and coarse grained (30  $\mu\text{m}$ ) Astroloy and in coarse grained (42  $\mu\text{m}$ ) Waspaloy were obtained at temperatures of 25°C, 200°C and 600°C. Expressing the crack growth kinetics in terms of the linear elastic parameter  $\Delta K$  resulted in small cracks growing faster than large cracks in all cases except that of the fine grained Astroloy at elevated temperature. This difference occurred even though the crystallographic nature of cracking in small cracks was shown to be the same as that in large cracks, based on metallographic, selected area electron channeling, and fractographic information. Furthermore, the fracture morphology of small and large cracks also exhibited the same dependence on temperature and applied stress level indicating that the crack propagation mechanism was the same in both cases. Consequently, it was concluded that the observed differences in kinetics were due to differences in mechanical driving force for small and large fatigue cracks.

Contributions to these differences in mechanical driving force were examined using high resolution scanning electron microscopy, coupled with the stereoimaging technique. This technique enabled the quantification of local crack-tip displacements, strains, and crack opening loads during fatigue crack growth. Measurements showed that the crack-tip strain fields, as well as the nature of crack closure, were significantly different for small and large cracks. These observations were consistent with the fact that the linear elastic fracture mechanics concept of small scale yielding was shown to be invalid for small cracks based on the fact that measured crack-tip plastic zone sizes were on the order of the crack size.

In view of this situation, the local crack-tip measurements were used to define an elastic-plastic crack driving force based on the relationship between crack-tip opening displacement and  $\Delta J$ , the cyclic J-integral. To facilitate comparison of small and large crack data,  $\Delta J$  was expressed in terms of an equivalent  $\Delta K$ , termed  $\Delta K_{eq}$ . The value of  $\Delta K_{eq}$  for small cracks was found to depend on significant contributions from plasticity, mixed mode and crack closure, while that for large cracks was found to depend only on

crack closure. Expressing the crack growth rates of small and large cracks as a function of  $\Delta K_{eq}$  resulted in kinetics which were independent of crack size, within experimental scatter.

The above results formed the basis of a phenomenological model for the growth of both small and large fatigue cracks in which  $\Delta K_{eq}$  is related to the applied  $\Delta K$ . Since  $\Delta K_{eq}$  cannot currently be computed analytically, the phenomenological model was used to predict the fatigue life of unflawed turbine engine discs. The initial flaw sizes for these calculations were set equal to the material grain size -- a size typical of the intrinsic microstructural defects expected to be found in Ni-based superalloys. The fatigue lives predicted using the phenomenological model were found to be in better overall agreement with measured fatigue lives than those predicted based on the classical linear elastic fracture mechanics approach and large crack data. At longer lives, the latter approach overpredicted the measured lives by several orders of magnitude. This overprediction was shown to be associated with the occurrence of the fatigue crack growth threshold for large cracks,  $\Delta K_{th}$ . Based on these results, it is concluded that  $\Delta K_{th}$  and associated near-threshold growth rate data are not applicable to material selection, design and damage tolerant analyses of turbine engine discs.

## 2. INTRODUCTION

The approach to insuring the safety, reliability and cost effectiveness of high-performance gas turbine engines has undergone a change from the "safe life" philosophy, based on traditional fatigue crack initiation concepts, to the "damage tolerant" philosophy, based on fracture mechanics concepts. The latter has been formally implemented by the United States Air Force in two separate programs. The Retirement-for-Cause of Turbine Engine Components Program uses fracture mechanics concepts in the life management of critical components of the F100 engine [2.1, 2.2]. The Engine Structural Integrity Program (ENSIP) is broader in scope and establishes a general damage tolerance design specification for critical components of future engines [2.3-2.5]. In both programs, crack-like defects must be assumed to exist in the components at the time of production and analysis and testing is required to demonstrate that these defects will not grow to a critical size, corresponding to catastrophic failure, within the lifetime of the engine.

The above approach is based on the assumption that there exists a unique, geometry-independent relationship between the crack-tip stress intensity factor, defined by linear elasticity, and the rate of fatigue crack propagation. Such a relationship has been demonstrated for large through-thickness cracks which have traditionally been tested in the laboratory [2.6-2.8]. However, more recent results on cracks which are small in relation to either the crack-tip plastic zone size or the material microstructure appear to violate such a relationship [2.9-2.12]. These "small" cracks appear to grow at faster rates than those of large cracks subject to the same elastic stress intensity factor range,  $\Delta K$ . Furthermore, small cracks can propagate at  $\Delta K$  values which are below the threshold  $\Delta K$  value exhibited by large cracks.

Unfortunately, the demarcation between "small" and "large" crack behavior is not well defined. Thus, the precise impact of this anomalous behavior on life prediction has been uncertain. Nevertheless, it is clear that with the advent of improved nondestructive examination techniques this issue will increase in importance. For example, recent analyses have estimated that an improvement in NDE resolution of about a factor of two will

result in an order of magnitude difference in the life predicted using crack growth rates from "small" versus "large" cracks [2.10].

The above situation provided the impetus for the current program. The primary objective of this program was to define the limitations of linear elastic fracture mechanics to treat the growth of small cracks and to identify the underlying physical mechanisms responsible for the anomalously high growth rates exhibited by small cracks. The anticipated benefits from such an effort include an improved basis for life prediction, as well as more realistic material selection criteria.

## 2.1 References

- 2.1 J. M. Hyzak, W. H. Reimann, and J. E. Allison, "The Development of Quantitative NDI for Retirement-for-Cause," Air Force Materials Laboratory, Report AFML-TR-78-198, Wright-Patterson AFB, OH, 1979.
- 2.2 C. G. Annis, Jr., J. S. Cargill, J. A. Harris, Jr., and M. C. Van Wanderham, "Engine Component Retirement-for-Cause: A Nondestructive Evaluation (NDE) and Fracture Mechanics-Based Maintenance Concept," Journal of Met., 1981, pp. 24-28.
- 2.3 W. D. Cowie, "Turbine Engine Structural Integrity Program (ENSIP)," Journal of Aircraft, Vol. 12, 1975, pp. 366-369.
- 2.4 United States Air Force, "Engine Structural Integrity Program," Military Standard 1783, Aeronautical Systems Division, Wright-Patterson Air Force Base, OH, 1984.
- 2.5 T. T. King, W. D. Cowie, and W. H. Reimann, "Damage Tolerant Design Concepts for Military Engines," AGARD Conference Proceedings No. 393, NATO Advisory Group for Aerospace Research and Development, 1985, pp. 31-39.
- 2.6 P. C. Paris and F. Erdogan, "A Critical Analysis of Crack Propagation Laws," ASME J. Basic Engr., December 1963, pp. 528-534.
- 2.7 P. C. Paris, "The Fracture Mechanics Approach to Fatigue," in Proc. of the 10th Sagamore Army Materials Research Conf., Syracuse Univ. Press, 1964, pp. 107-132.
- 2.8 S. J. Hudak, Jr., A. Saxena, R. J. Bucci and R. C. Malcolm, "Development of Standard Methods of Testing and Analyzing Fatigue Crack Growth Rate Data," Air Force Materials Laboratory, Report AFML-TR-78-40, Wright-Patterson Air Force Base, OH, 1978.

- 2.9 S. Pearson, "Initiation of Fatigue Cracks in Commercial Aluminum Alloys and the Subsequent Propagation of Very Short Cracks," Engr. Fracture Mech., Vol. 7, 1975, pp. 235-247.
- 2.10 S. J. Hudak, Jr., "Small Crack Behavior and the Prediction of Fatigue Life," ASME J. of Engr. Mater. and Tech., Vol. 103, 1981, pp. 26-35.
- 2.11 S. Suresh and R. O. Ritchie, "The Propagation of Short Fatigue Cracks," Int. Metal. Rev., Vol. 29, 1984, pp. 445-476.
- 2.12 B. N. Leis, A. T. Hopper, J. Ahmed, D. Broek, and M. F. Kanninen, "Critical Review of the Fatigue Crack Growth of Short Cracks," Engr. Fract. Mech., Vol. 23, 1986, pp. 893-898.
- 2.13 J. Lankford and S. J. Hudak, Jr., "Relevance of the Small Crack Problem to Lifetime Prediction in Gas Turbines," Int. J. Fatigue, Vol. 9, No. 2, 1987, pp. 87-93.

### 3. MATERIAL MICROSTRUCTURAL AND MECHANICAL PROPERTIES

Two nickel-base superalloys typical of those used in gas turbine engine discs were chosen for this study: 1) Astroloy, examined in fine grained (FG) and coarse grained (CG) variants, 2) and Waspaloy. The thermo-mechanical processing of these alloys and resulting monotonic and cyclic stress-strain properties, as well as creep properties, are provided in this section.

#### 3.1 Microstructural Characterization

The Waspaloy used in this program was in the form of a large diameter turbine disc and was produced by Cameron Iron Works using a cast-wrought route. The measured chemical composition is given in Table 3-1. The alloy was melted by a Vacuum Induction Melt/Vacuum Arc Refine (VIM-VAR) process and heat treated as follows:

|          |          |       |            |
|----------|----------|-------|------------|
| Solution | 2 hours  | 1016C | Oil Quench |
| 1st Age  | 4 hours  | 850C  | Air Cool   |
| 2nd Age  | 16 hours | 760C  | Air Cool   |

The Waspaloy grain size, determined in accordance with ASTM E112, was 42  $\mu\text{m}$  (ASTM 5.9). The microstructure, which consisted of equiaxed grains, with occasional large grains up to 200  $\mu\text{m}$  by 100  $\mu\text{m}$ , is shown in Figure 3-1. The  $\gamma'$  structure was also examined, and was a bimodal distribution of spheroidal particles, typically 0.3 and 0.03  $\mu\text{m}$  in diameter (Figure 3-2).

Both the FG and CG Astroloy were produced by a powder metallurgy route involving argon atomization, powder classification and blending followed by Hot Isostatic Pressing (HIP) into billet prior to forging. The powder was supplied and HIP'ed by Wiggin Alloys. The FG discs were forged by Daniel Doncasters, while the CG discs were forged by Landish. The measured chemical composition is given in Table 3-2. All discs were heat treated as follows:

1218°C HIP (30,000 psi)

|          |          |        |          |
|----------|----------|--------|----------|
| Solution | 4 hours  | 1095°C | Air Cool |
| 1st Age  | 24 hours | 650°C  | Air Cool |
| 2nd Age  | 8 hours  | 760°C  | Air Cool |



TABLE 3-1  
CHEMICAL COMPOSITION OF WASPALOY

| <u>Element</u> | <u>Specified Composition</u><br><u>Weight % (ppm)</u> |            | <u>Analysis</u> |
|----------------|---|------------|-----------------|
|                | <u>Min</u>  | <u>Max</u> |                 |
| Carbon         | 0.02  | 0.10       | 0.023           |
| Silicon        | -   | 0.15       | 0.037           |
| Manganese      | -   | 0.10       | 0.02            |
| Phosphorus     | -   | 0.015      | 0.003           |
| Sulphur        | -   | 0.008      | <0.002          |
| Silver         | -   | (5)        | -               |
| Aluminum       | 1.2   | 1.6        | 1.5             |
| Boron          | 0.003   | 0.01       | 0.007           |
| Bismuth        | -   | (1)        | -               |
| Cobalt         | 12.0  | 15.0       | 12.26           |
| Chromium       | 18.0  | 21.0       | 19.52           |
| Copper         | -   | 0.10       | -               |
| Iron           | -   | 2.0        | 0.97            |
| Molybdenum     | 3.5   | 5.0        | 3.82            |
| Lead           | -   | (10)       | -               |
| Titanium       | 2.8   | 3.3        | 3.29            |
| Zirconium      | 0.02  | 0.08       | 0.062           |
| Nickel         | Remainder   |            |                 |



FIGURE 3-1. Microstructure of Waspaloy

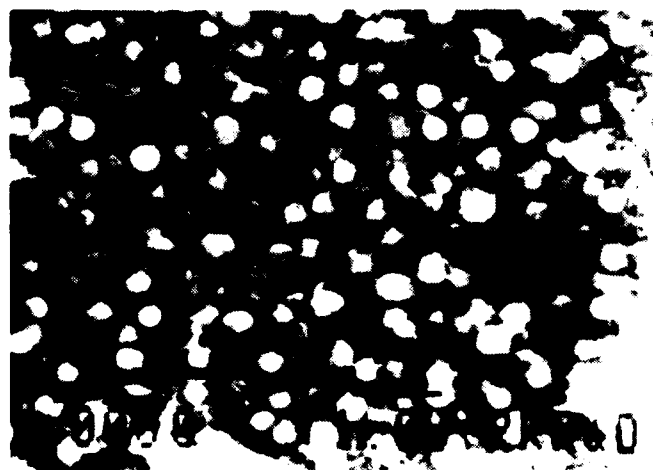


TABLE 3-2  
CHEMICAL COMPOSITION OF ASTROLOY

| Element    | Specified Composition |       | Analysis |        |        |
|------------|-----------------------|-------|----------|--------|--------|
|            | Weight % (ppm)        |       | A3770    | A3771  | AAH2   |
|            | MIN                   | MAX   |          |        |        |
| Carbon     | 0.01                  | 0.035 | 0.023    | 0.025  | 0.026  |
| Silicon    | -                     | 0.2   | 0.016    | 0.014  | 0.021  |
| Manganese  | -                     | 0.15  | -        | 0.010  | 0.020  |
| Phosphorus | -                     | 0.15  | 0.003    | 0.002  | 0.003  |
| Sulphur    | -                     | 0.005 | <0.002   | <0.002 | <0.002 |
| Argon      | -                     | (3)   | -        | -      | -      |
| Silver     | -                     | (5)   | -        | -      | -      |
| Aluminum   | 3.85                  | 4.15  | 4.06     | 4.09   | 3.97   |
| Boron      | 0.015                 | 0.03  | 0.02     | 0.02   | 0.018  |
| Bismuth    | -                     | (0.5) | -        | -      | -      |
| Cobalt     | 16                    | 18    | 17.23    | 17.12  | 17.13  |
| Chromium   | 14                    | 16    | 14.92    | 14.91  | 14.84  |
| Copper     | -                     | 0.1   | -        | -      | 0.02   |
| Iron       | -                     | 0.5   | 0.07     | 0.07   | 0.05   |
| Molybdenum | 4.5                   | 5.5   | 5.05     | 5.05   | 5.07   |
| Nitrogen   | -                     | (50)  | -        | -      | -      |
| Oxygen     | -                     | (150) | -        | -      | -      |
| Lead       | -                     | (10)  | -        | -      | -      |
| Titanium   | 3.35                  | 3.65  | 3.49     | 3.53   | 3.53   |
| Tungsten   | -                     | 0.05  | 0.03     | 0.02   | 0.02   |
| Zirconium  | 0.03                  | 0.06  | 0.042    | 0.040  | 0.047  |
| Nickel     | Balance               |       |          |        |        |

The CG Astroloy received an additional grain growth treatment of 4 hours at 1180°C, before being re-solutioned and re-aged.

The grain sizes of the two Astroloy variants were 12  $\mu\text{m}$  (ASTM 10) for the FG material and 30  $\mu\text{m}$  (ASTM 7) for the CG material. The general microstructure and  $\gamma'$  morphology for the FG Astroloy are shown in Figures 3-3 and 3-4, respectively. Analogous results for the CG Astroloy are shown in Figures 3-5 and 3-6. In the FG material, the  $\gamma'$  existed as large, monolithic particles carried over from forging, (that is, not broken up during solution) with a fine back-ground dispersion of cubic  $\gamma'$ , approximately 0.2  $\mu\text{m}$  on edge. In the CG variant the monolithic  $\gamma'$  was broken down by the additional grain growth treatment. The structure was bimodal and cubic, the particles being 0.5  $\mu\text{m}$  and 0.1  $\mu\text{m}$  on edge.

### 3.2 Mechanical Properties

Tensile tests were performed under both monotonic and cyclic conditions. The specimens utilized are shown in Figures 3-7 and 3-8. The monotonic tests were conducted in accord with BS4A4 Part 1 Section 3, while the cyclic testing was conducted in accord with the method of Pickard and Knott [3.1].

Tabulated summaries of the tensile results at 25°C, 200°C and 600°C are given in Tables 3-3 thru 3-5, with graphic representation given in Figures 3-9 thru 3-11. A tabulation of the strain hardening data is given in Tables 3-6 and 3-7. The values of K and n in Table 3-4 were determined by least squares fitting of the monotonic stress-strain data to the following equation:

$$\sigma = k \epsilon_p^n$$

where  $\sigma$  = the true stress and  $\epsilon_p$  = the true (logarithmic) plastic strain. The cyclic values given in Table 3-7 were similarly obtained using the following equation:

$$\frac{\Delta \sigma}{2} = k \frac{\Delta \epsilon_p}{2}^{n'}$$

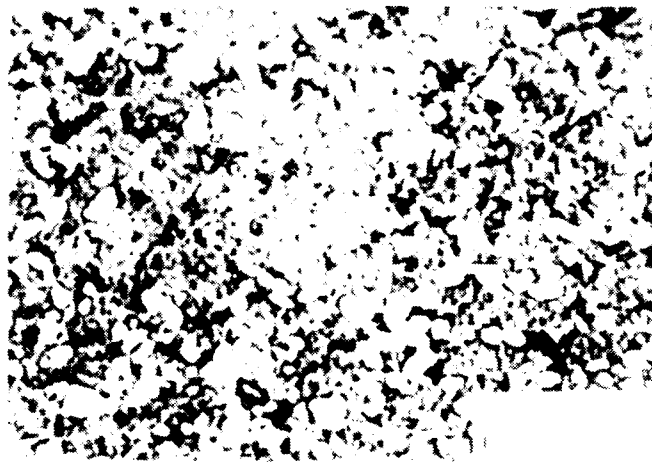


FIGURE 3-3. Microstructure of FG Astroloy



FIGURE 3-4. Y' Structure of FG Astroloy

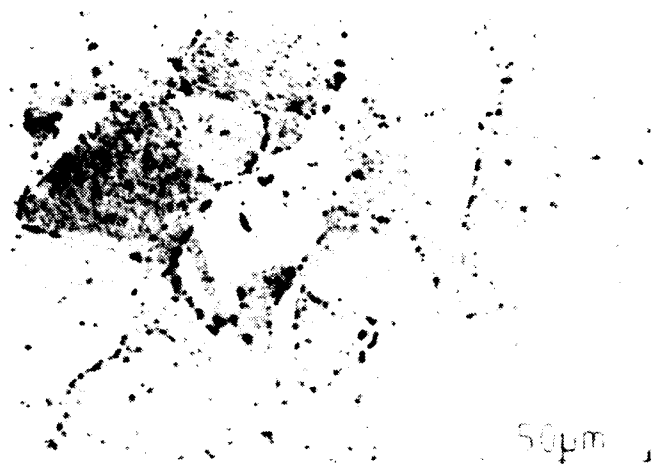


FIGURE 3-5. Microstructure of CG Astroloy



FIGURE 3-6. Y' Structure of CG Astroloy

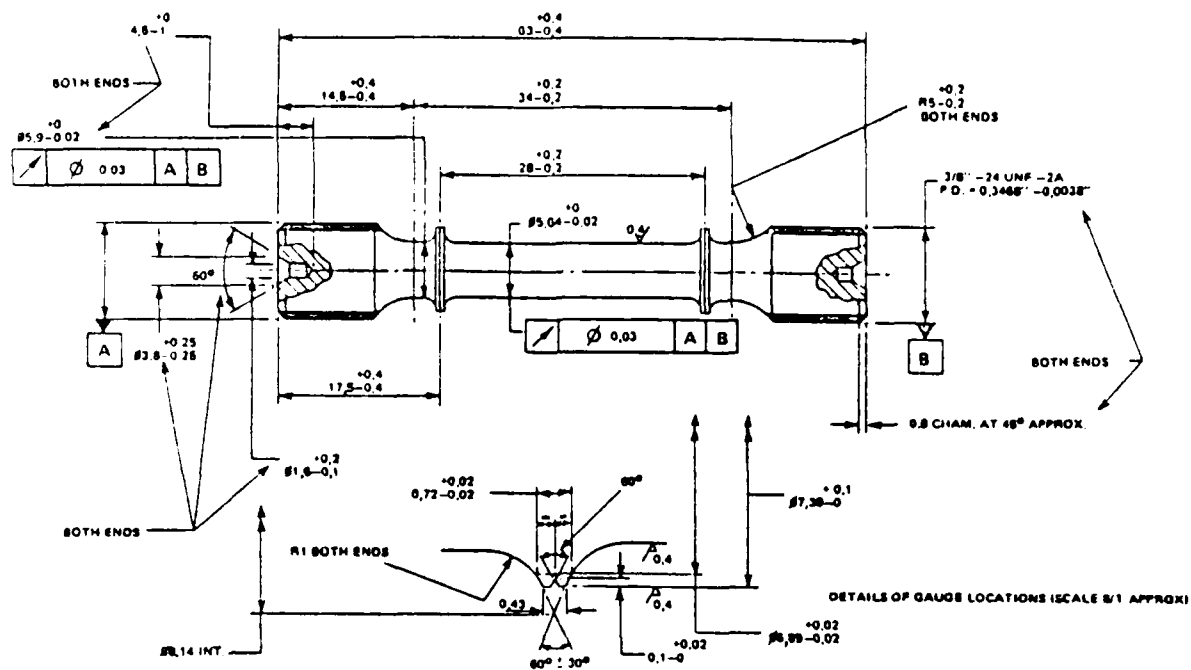


FIGURE 3-7. Tensile Test Specimen  
(dimensions in mm)

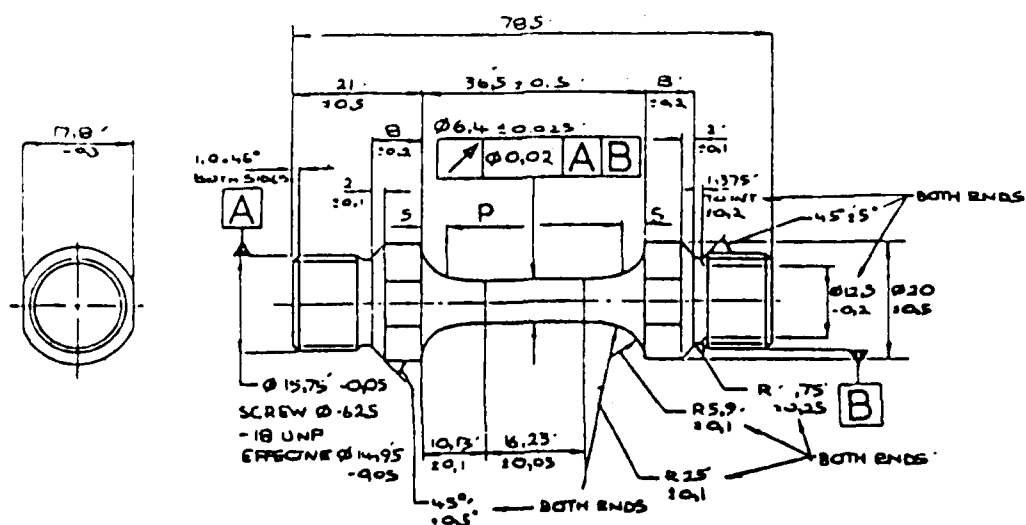


FIGURE 3-8. Strain-controlled low cycle fatigue specimen  
(dimensions in mm)

TABLE 3-3

STRESS-STRAIN PROPERTIES OF WASPALOY AT VARIOUS TEMPERATURES  
(M= Monotonic and C = Cyclic)

| Temperature<br>°C |   | UTS<br>MPa | 0.1%<br>Proof<br>MPa | 0.2%<br>Proof<br>MPa | Modulus<br>GPa | Elongation<br>% | R/A<br>% |
|-------------------|---|------------|----------------------|----------------------|----------------|-----------------|----------|
| 20                | M | 1329       | 890                  | 909                  | 211            | 22              | 28       |
|                   | C |            | 880                  | 930                  | 229            |                 |          |
| 200               | M | 1257       | 824                  | 846                  | 213            | 22              | 29       |
|                   | C |            | 870                  | 900                  | 215            |                 |          |
| 600               | M | 1249       | 759                  | 788                  | 181            | 19              | 25       |
|                   | C |            | 765                  | 800                  | 197            |                 |          |



TABLE 3-4

## STRESS-STRAIN PROPERTIES OF FG ASTROLOY AT VARIOUS TEMPERATURES

(M = Monotonic and C = Cyclic)

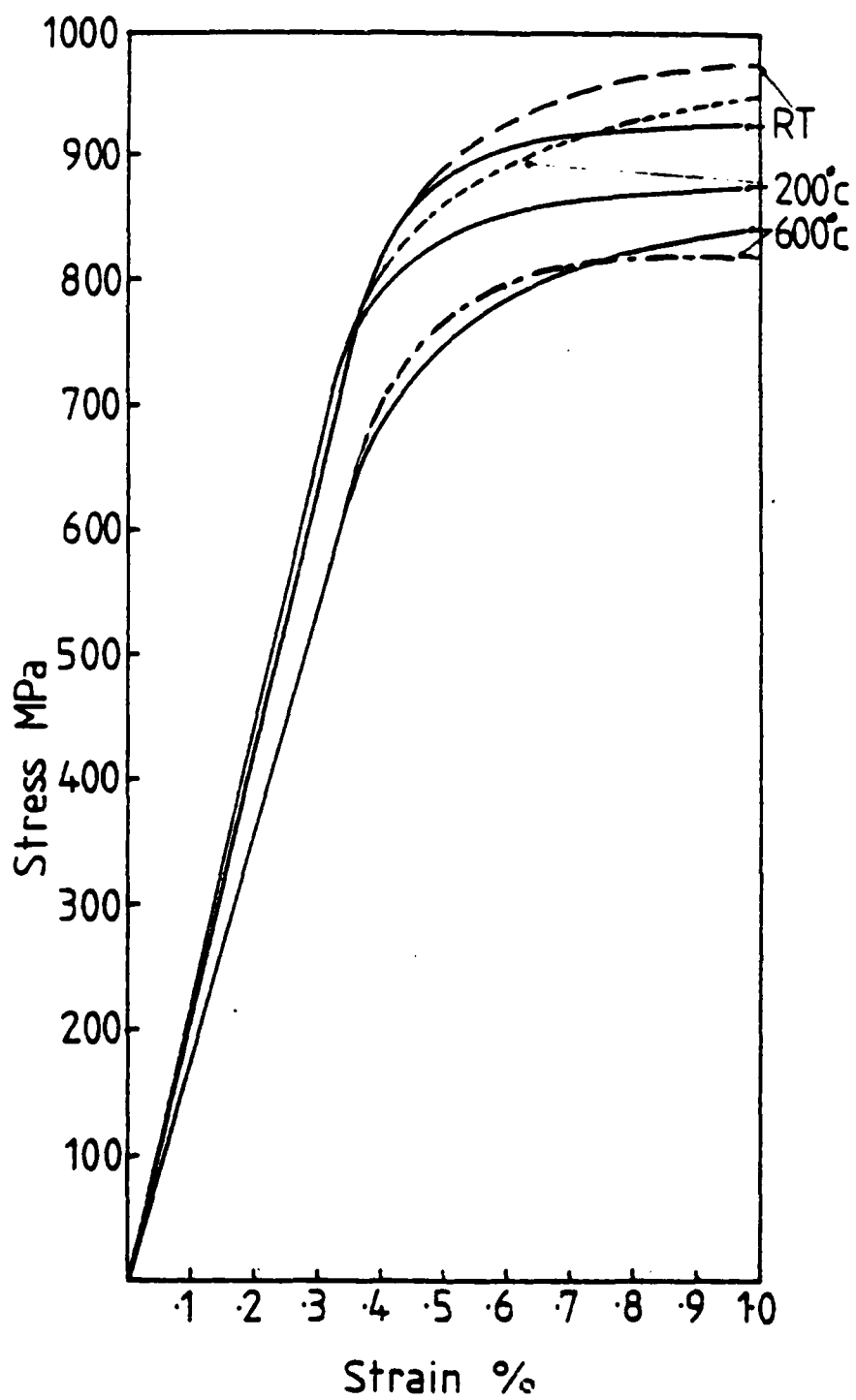
| Temperature<br>°C |   | UTS<br>MPa | 0.1%<br>Proof<br>MPa | 0.2%<br>Proof<br>MPa | Modulus<br>GPa | Elongation<br>% | R/A<br>% |
|-------------------|---|------------|----------------------|----------------------|----------------|-----------------|----------|
| 20                | M | 1516       | 1057                 | 1057                 | 214            | 27              | 32       |
|                   | C |            | 995                  | 1018                 | 221            |                 |          |
| 200               | M | 1394       | 943                  | 954                  | 215            | 18              | 17       |
|                   | C |            | 1025                 | 1065                 | 204            |                 |          |
| 600               | M | 1411       | 940                  | 971                  | 186            | 20              | 25       |
|                   | C |            | 985                  | 1025                 | 195            |                 |          |

TABLE 3-5

## STRESS-STRAIN PROPERTIES OF CG ASTROLOY AT VARIOUS TEMPERATURES

(M = Monotonic and C = Cyclic)

| Temperature<br>°C |   | UTS<br>MPa | 0.1%<br>Proof<br>MPa | 0.2%<br>Proof<br>MPa | Modulus<br>GPa | Elongation<br>% | R/A<br>% |
|-------------------|---|------------|----------------------|----------------------|----------------|-----------------|----------|
| 20                | M | 1398       | 884                  | 905                  | 223            | 28              | 33       |
|                   | C |            | 880                  | 905                  | 209            |                 |          |
| 200               | M | 1334       | 846                  | 864                  | 209            | 25              | 27       |
|                   | C |            | 940                  | 980                  | 205            |                 |          |
| 600               | M | 1303       | 828                  | 862                  | 166            | 23              | 28       |
|                   | C |            | 820                  | 865                  | 168            |                 |          |



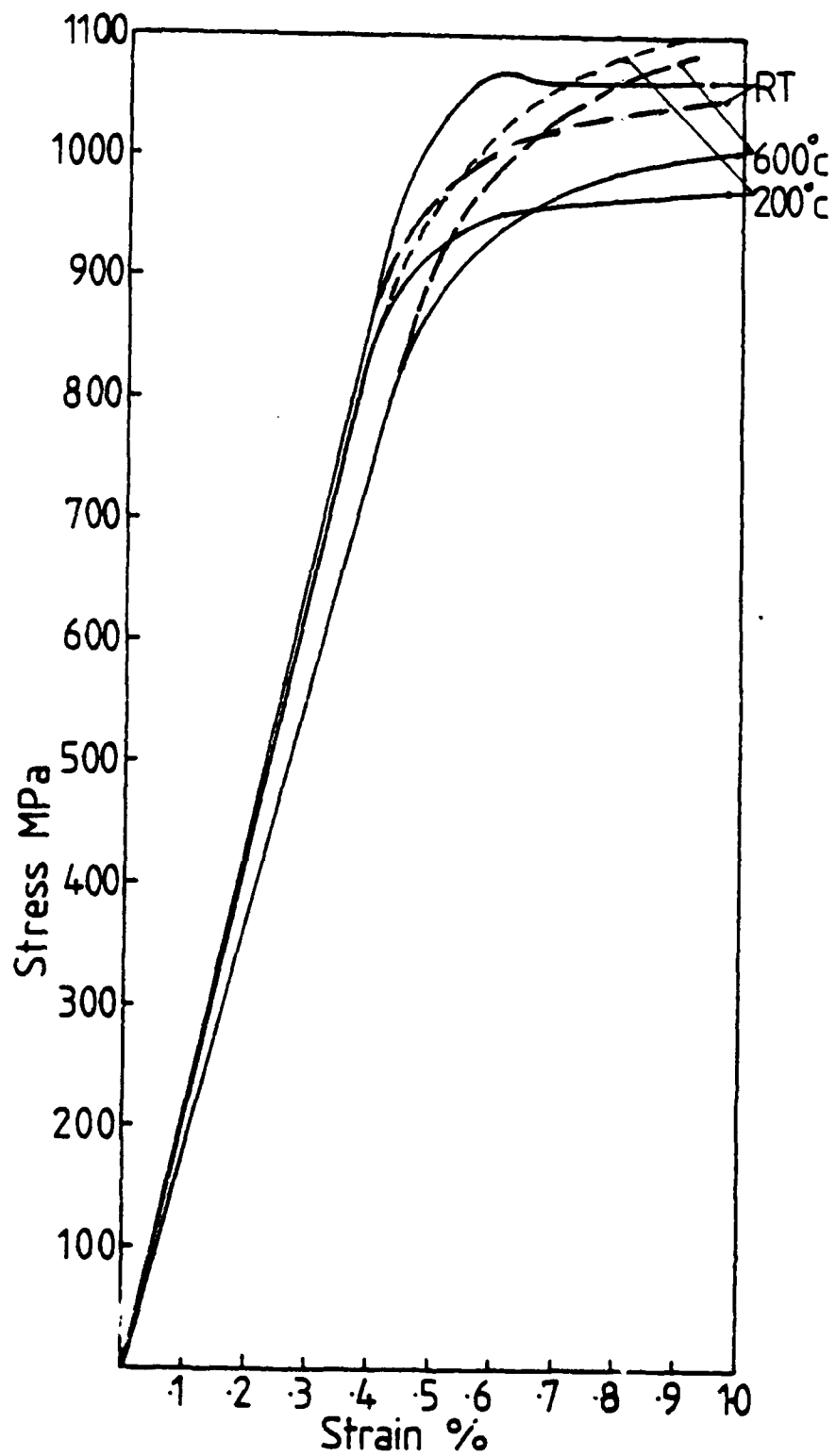


FIGURE 3-10. Monotonic (solid lines) and cyclic (dashed lines) stress-strain curves for FG Astroloy

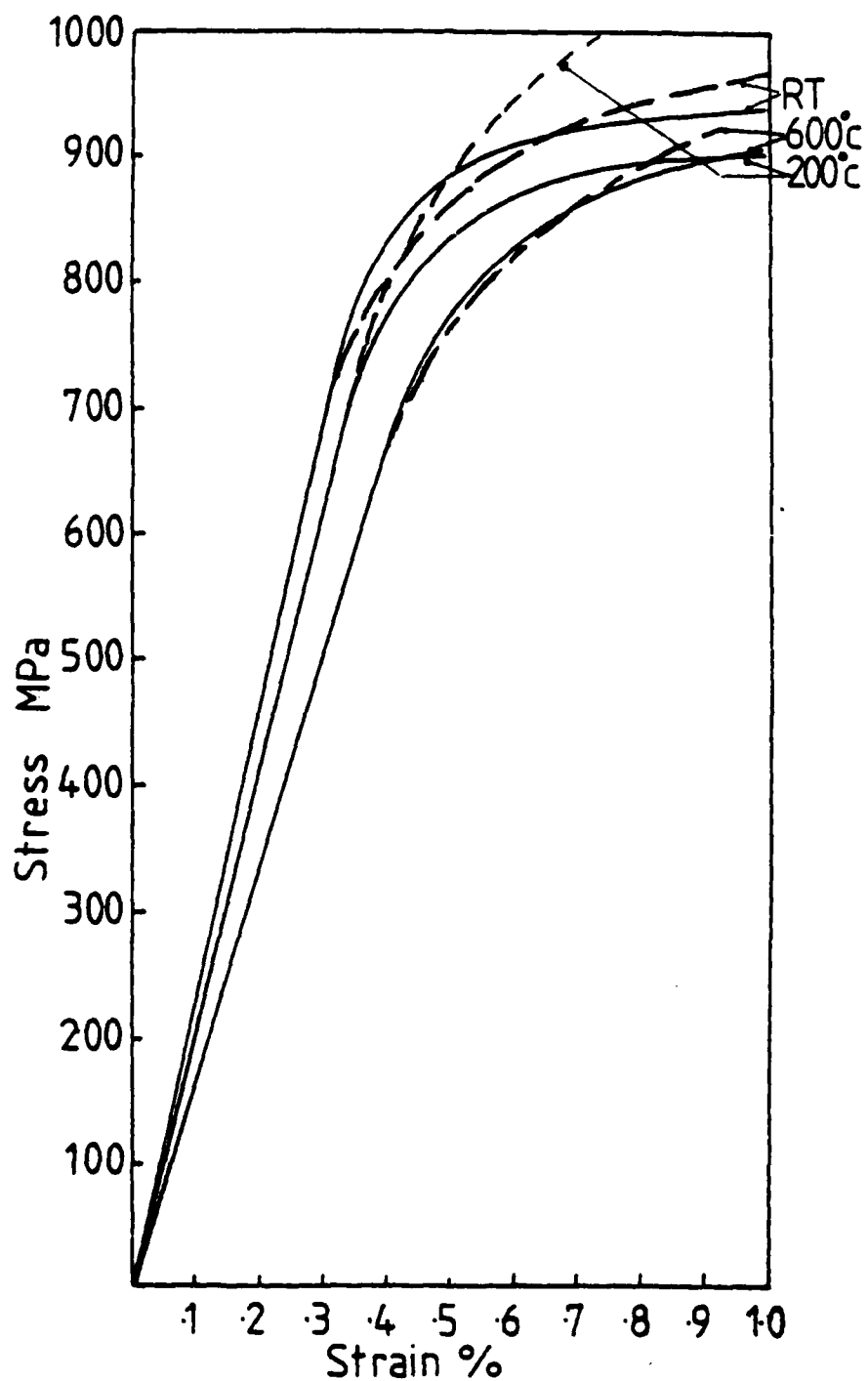


FIGURE 3-11. Monotonic (solid lines) and cyclic (dashed lines) stress-strain curves for CG Astroloy at several temperatures.

**TABLE 3-6**  
**MONOTONIC STRAIN HARDENING DATA**

| Material    | Temp | E   | k      | n     | Correlation<br>Coefficient |
|-------------|------|-----|--------|-------|----------------------------|
| Waspaloy    | 20   | 211 | 1207.8 | 0.043 | 0.98                       |
|             | 200  | 215 | 1051.4 | 0.033 | 0.99                       |
|             | 600  | 181 | 1099.2 | 0.053 | 0.99                       |
| FG Astroloy | 20   | 214 | 1162.3 | 0.018 | 0.92                       |
|             | 200  | 214 | 1218.1 | 0.038 | 0.94                       |
|             | 600  | 185 | 1231.6 | 0.036 | 0.98                       |
| CG Astroloy | 20   | 222 | 1191.1 | 0.042 | 0.99                       |
|             | 200  | 205 | 1068.5 | 0.033 | 0.99                       |
|             | 600  | 168 | 1245.8 | 0.059 | 0.99                       |

**TABLE 3-7**  
**CYCLIC STRAIN HARDENING DATA**

| Material               | Temp | E   | k'     | n'    | Correlation<br>Coefficient |
|------------------------|------|-----|--------|-------|----------------------------|
| Waspaloy               | 20   | 229 | 1375.3 | 0.064 | 0.99                       |
|                        | 200  | 215 | 1420.6 | 0.075 | 0.98                       |
|                        | 600  | 197 | 963.7  | 0.029 | 0.69                       |
| FG Astroloy<br>(A3771) | 20   | 216 | 1372.8 | 0.052 | 0.96                       |
|                        | 200  | 207 | 1591.5 | 0.065 | 0.98                       |
|                        | 600  | 192 | 2604.1 | 0.150 | 0.95                       |
| FG Astroloy<br>(A3770) | 20   | 225 | 1464.8 | 0.064 | 0.97                       |
|                        | 200  | 201 | 1539.2 | 0.061 | 0.98                       |
|                        | 600  | 198 | 2423.4 | 0.140 | 0.96                       |
| CG Astroloy            | 20   | 220 | 1274.3 | 0.059 | 0.99                       |
|                        | 200  | 221 | 1642.0 | 0.089 | 0.99                       |
|                        | 600  | 183 | 1480.0 | 0.094 | 0.94                       |

Constant load creep strain to rupture tests were conducted at 600°C for all three materials to define the stress rupture curve between 50 and 500 hours. The test specimen utilized is shown in Figure 3-12. The plotted rupture data are shown in Figure 3-13.

The tensile and creep properties of the Waspaloy and the FG Astroloy were considered to be typical for materials form forgings of these sizes. The CG Astroloy exhibited tensile and creep properties which were somewhat below typical levels, but nevertheless above the specification minimum levels. Thus, the three forgings supplied form a solid basis for the current study.

### 3.3. References

- 3.1 A. C. Pickard and J. F. Knott, "Effect of Testing Method on Cyclic Hardening Behavior of Face Centered Cubic Alloys," ASTM Symposium on Low Cycle Fatigue, October 1985, in press.





FIGURE 3-12. Creep Rupture Test Specimen  
(dimensions in mm)

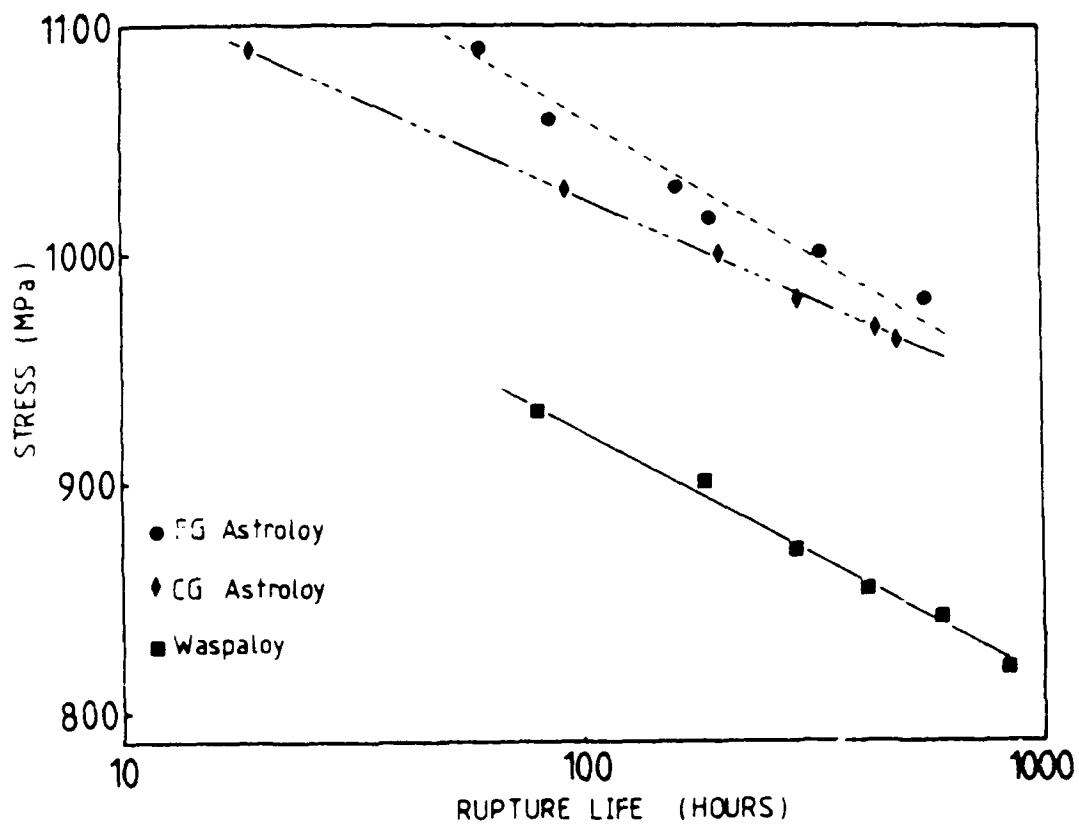


FIGURE 3-13. Stress-rupture data for Waspaloy, and FG and CG Astroloy at 600°C.

## 4. FATIGUE THRESHOLD AND LARGE CRACK GROWTH BEHAVIOR

### 4.1 Large Crack Testing Procedure

The experiments were performed to a Rolls-Royce procedural specification which is broadly similar to the ASTM draft specification for the determination of  $\Delta K_{th}$ . This load shedding technique utilizes load reductions of 5%, growing the crack at least three times the calculated maximum plastic zone size prior to further reductions in load. As the threshold is approached, the load reductions are decreased in magnitude until they reach the limit of the machines sensitivity. The threshold condition was defined as no detectable growth in  $10^7$  cycles. After the threshold is established, the alternating load is increased at constant load ratio to that expected to yield a growth rate of  $10^{-7}$  mm/cycle and the crack allowed to grow freely under constant load amplitude.

Standard compact-type specimens having an effective width of 26 mm and a thickness of 13 mm were used to obtain the large crack data. Threshold and crack growth testing was performed on a 100 kN capacity Amsler vibrophore electro-resonant fatigue machine at a cyclic frequency of 130 Hz. The crack length was determined by a D.C. potential drop technique as described by Hicks and Pickard [4.1]. Crack length was also determined optically during the test as a back up to that determined by the potential drop method.

After termination of the tests, the specimens were heat tinted (where required) and the final crack length measured at five points across the crack front. The average final crack length, and the final crack voltage were used to calibrate the potential drop to a crack length polynomial function, enabling an accurate post-test determination of the threshold and subsequent crack growth rates. Crack growth data were not determined for the decreasing  $\Delta K$  phase of the tests.

Crack growth rates were determined using a three point secant method as follows:

$$\frac{da}{dN}_i = \frac{a_{i+1} - a_{i-1}}{N_{i+1} - N_{i-1}}$$

The corresponding value of  $\Delta K$  was computed using  $a_i$ .

#### 4.2 Near-Threshold Fatigue Crack Growth Rates in Large Cracks

The effects of temperature on threshold and near threshold growth rates are summarized in Figures 4-1 through 4-3. In the FG Astroloy material, the threshold conditions is independent of temperature, but with fatigue crack growth rates at higher stress intensities becoming faster with increased temperature. This latter feature is considered to be a manifestation of oxide induced closure [4.2]. In CG Astroloy (Figure 4-2) a trend of increasing threshold with decreasing temperature was noted. In a comparison of the coarse and fine grain variants of Astroloy it is apparent that the threshold values at 600°C are quite similar, indicative perhaps of an equivalence of surface roughness. The effects of temperature in the necklaced variant are shown in Figure 4-3. In the absence of any RT data, the data for CG Astroloy has been included. A comparison of the necklace data with that of the FG and CG Astroloy again reveals good correlation at 600C with increasing discrepancies at lower temperatures. The variations in threshold and near threshold crack growth with microstructure are shown in Figures 4-4 and 4-5 for 200°C and 600°C, respectively. The effects of load ratio at 600°C are shown in Figures 4-6 and 4-7 for FG and CG Astroloy, respectively. At  $R = 0.1$ , thresholds for both microstructural variants offer comparatively good agreement, as might be expected, since at 600°C the dominant mode of material deformation at the crack tip is wavy slip producing a comparatively smooth transgranular fracture surface with little variation in fracture surface roughness between microstructural variants. In keeping with this, the threshold condition will be dominated by oxide induced closure, which manifests itself as a grain size independent threshold. The high load ratio data ( $R = 0.5$ ) is perhaps a more representative indication of the true resistance of the material to the growth of a fatigue crack, with the fine grain material being marginally superior.

The near threshold growth rates of CG Astroloy in air and vacuum, are contrasted in Figure 4-8. The threshold condition in vacuum is generally recognized as being higher than its air counterpart, and in this case as having a significantly higher knee. Work by Beevers [4.3] on both Waspaloy and Astroloy has indicated threshold behavior at 200°C in vacuum to be variable, due to load history effects, and having an enhanced tendency towards a planar slip deformation mechanism. The behavior at 600°C, while no longer dominated

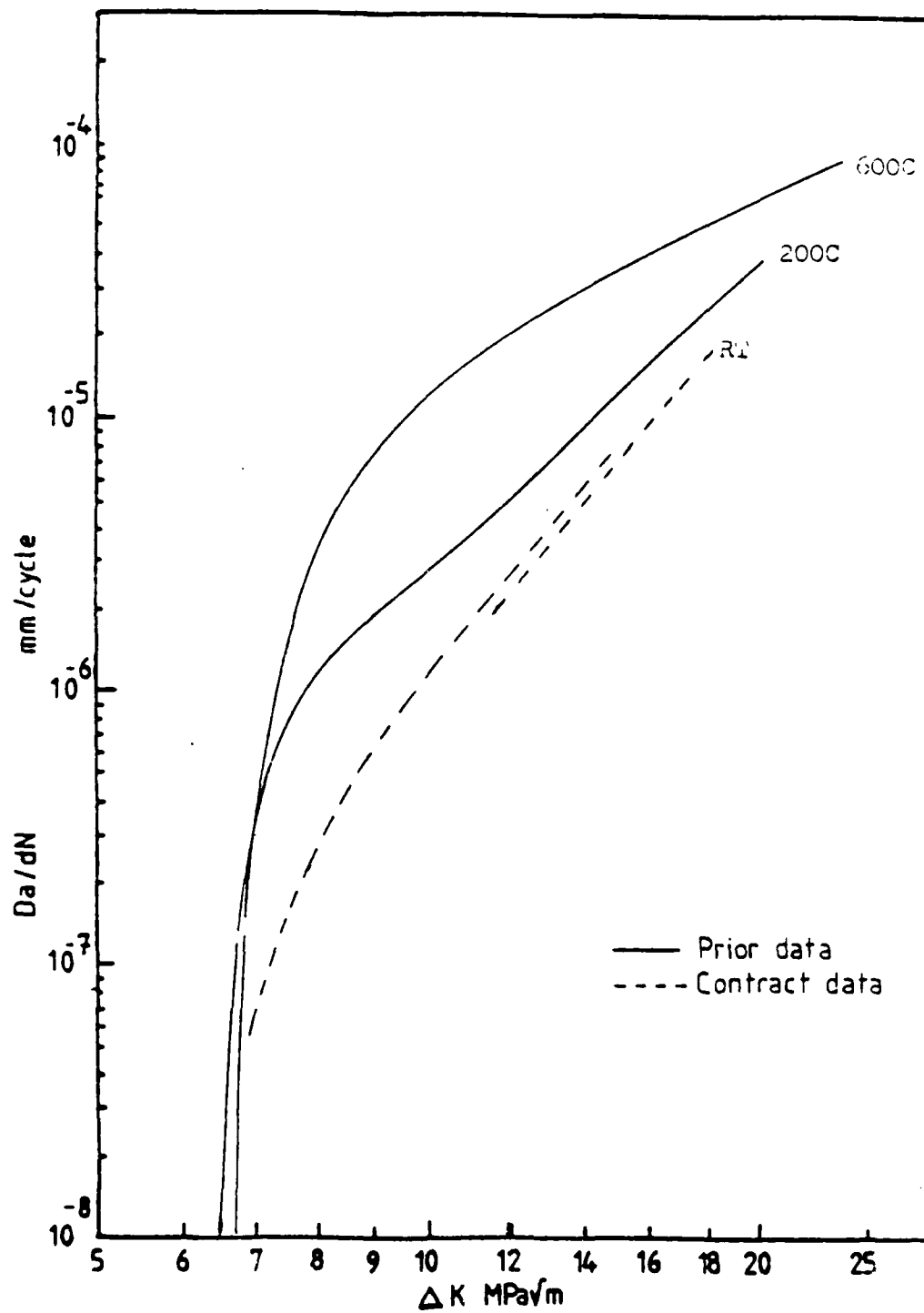


FIGURE 4-1. Temperature Effects in Fine Grain Astroloy

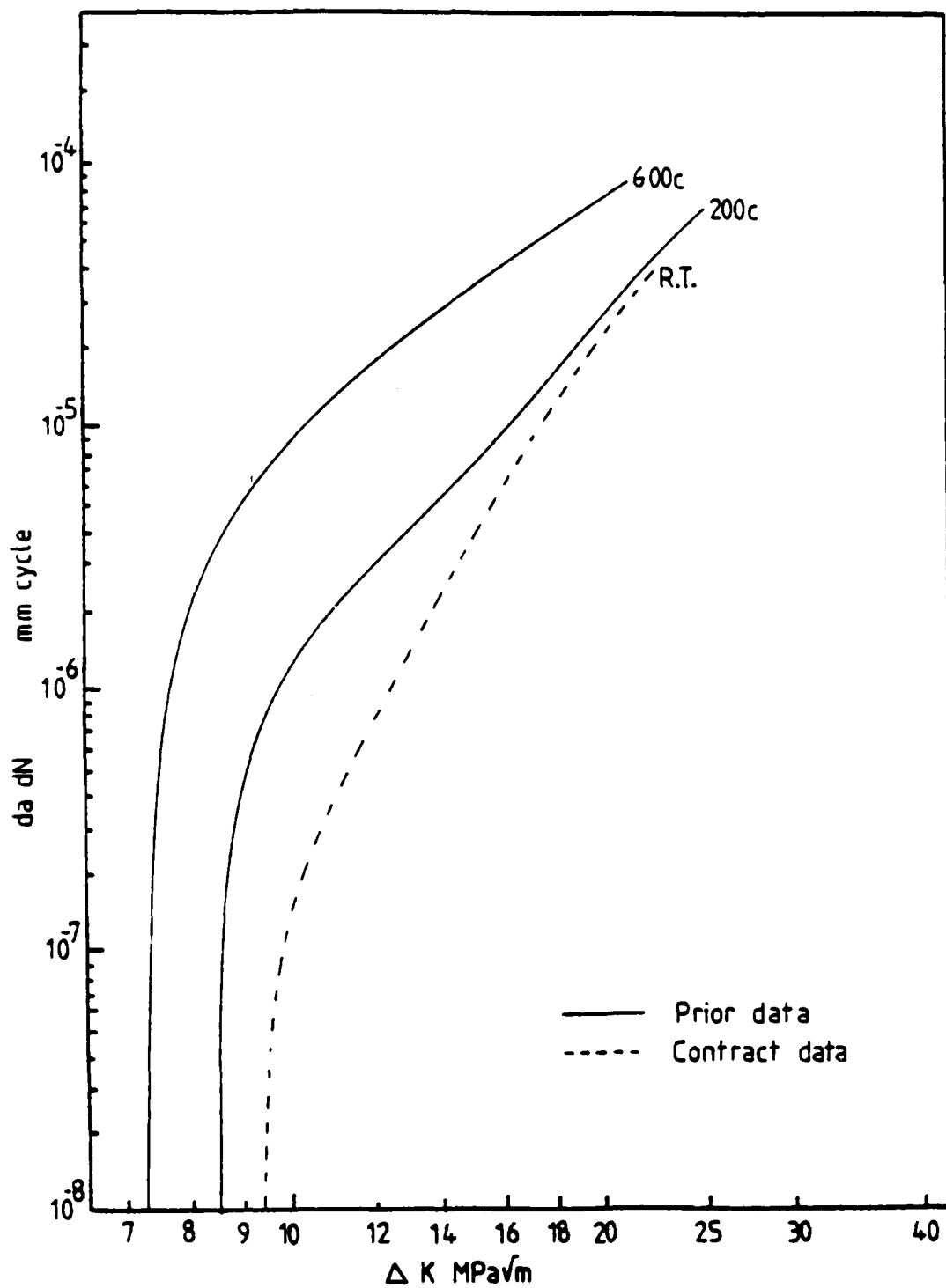


FIGURE 4-2. Temperature Effects in Coarse Grain Astroloy

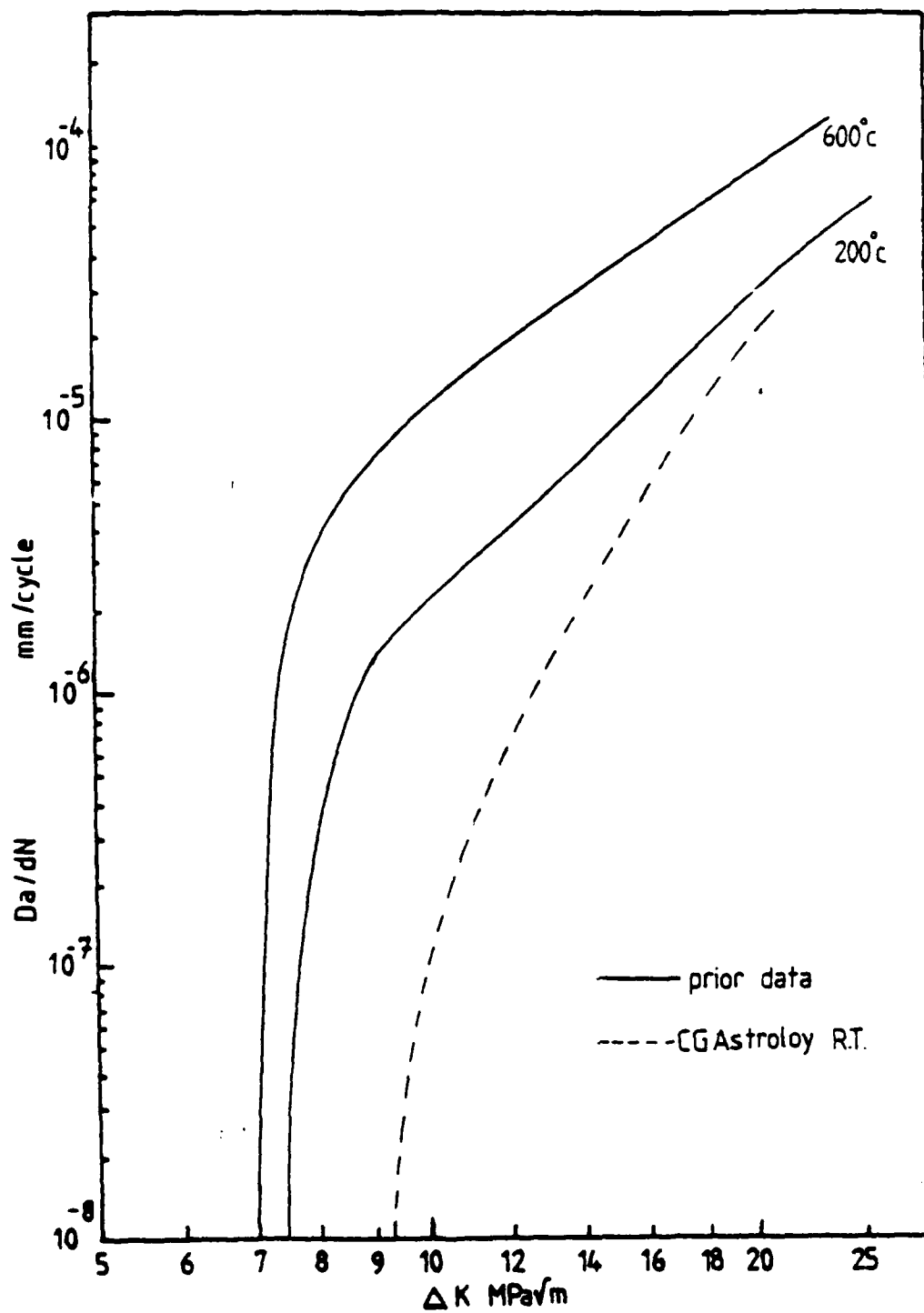


FIGURE 4-3. Effect of temperature on near threshold crack growth behavior of necklace Astroloy.

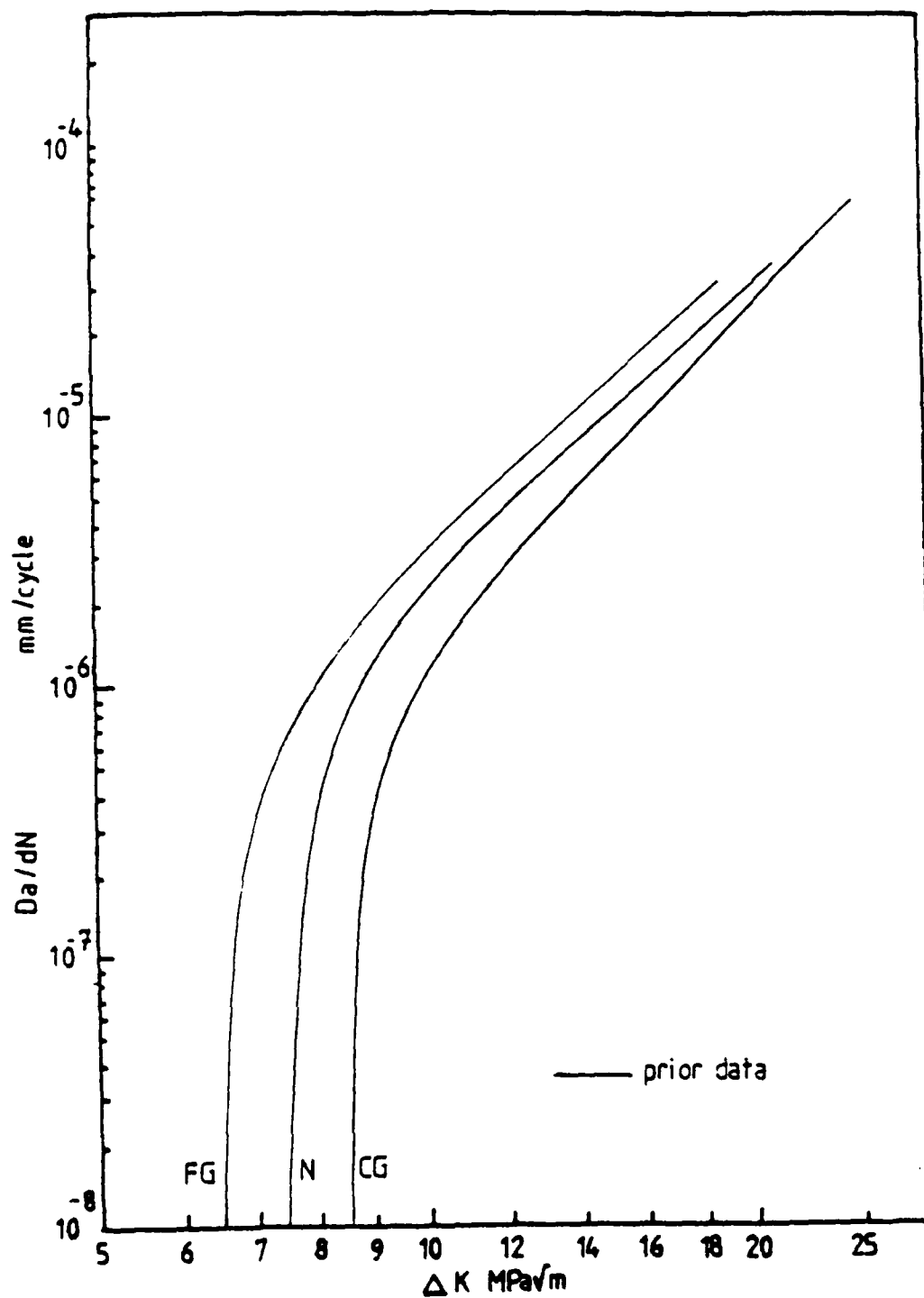


FIGURE 4-4. Effect of microstructure on near threshold crack growth behavior of Astroloy (200°C).



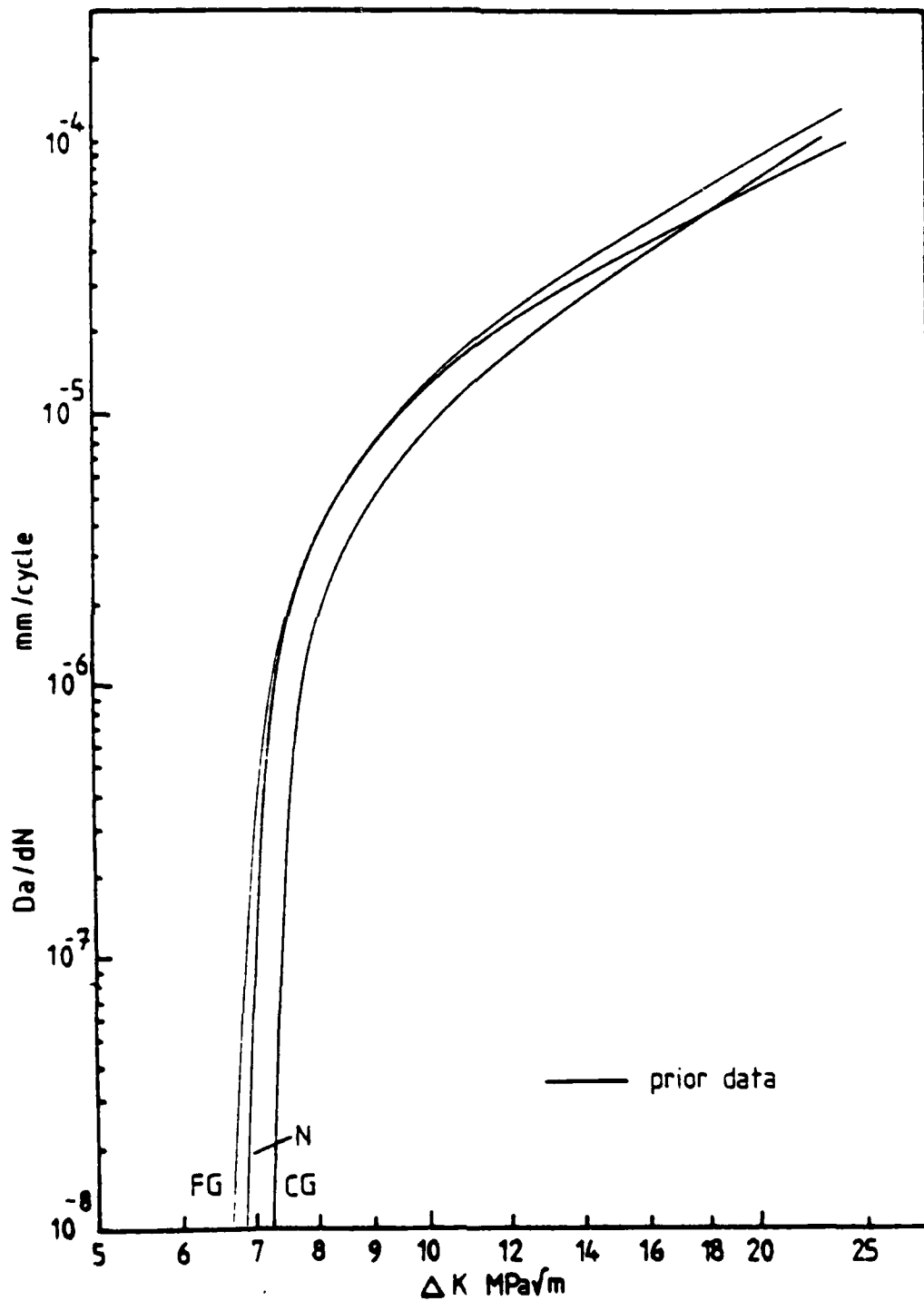


FIGURE 4-5. Effect of microstructure on near threshold crack growth behavior of Astroloy (600°C).

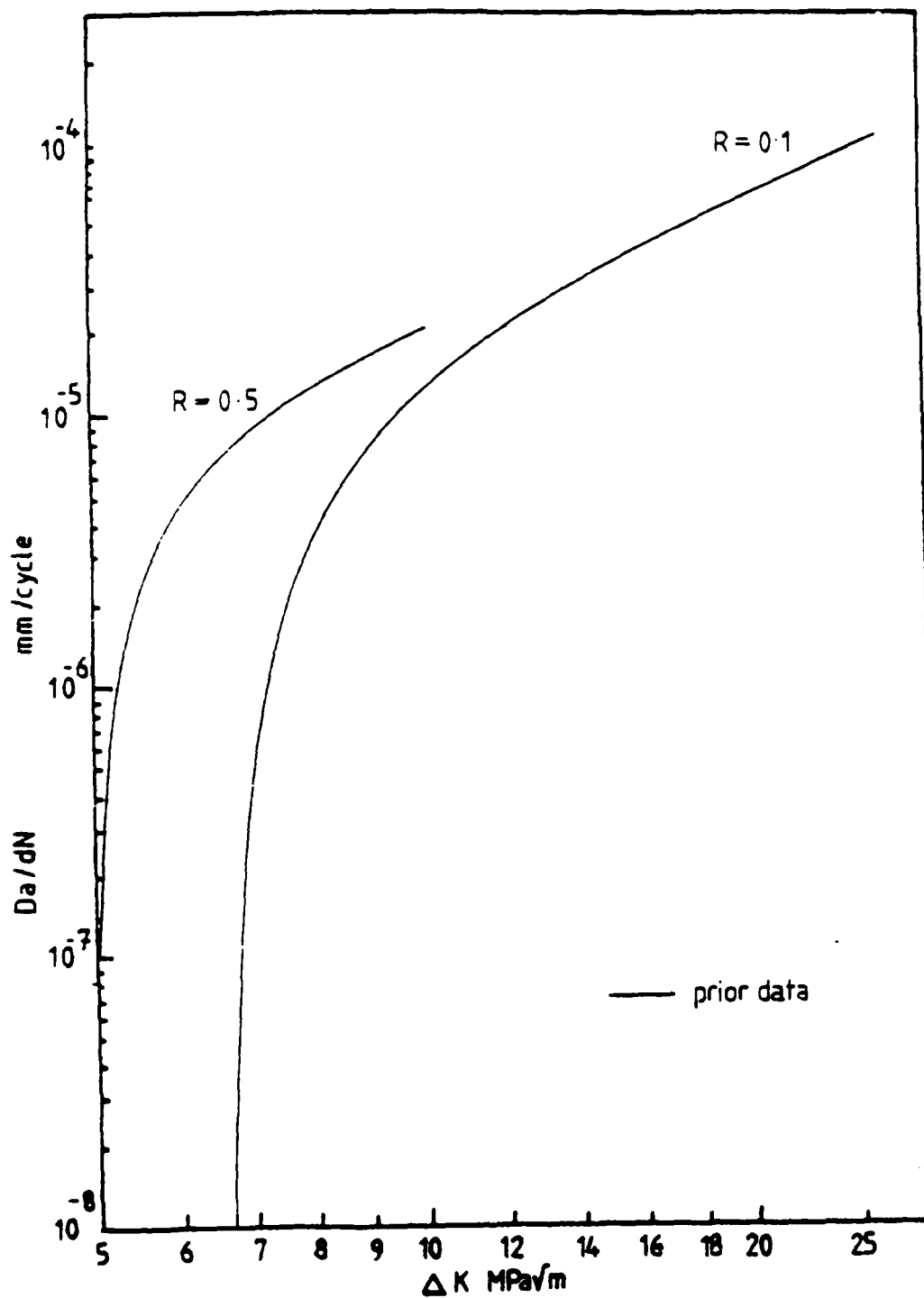


FIGURE 4-6. Load Ratio Effects in Fine Grain Astroloy (600°C)

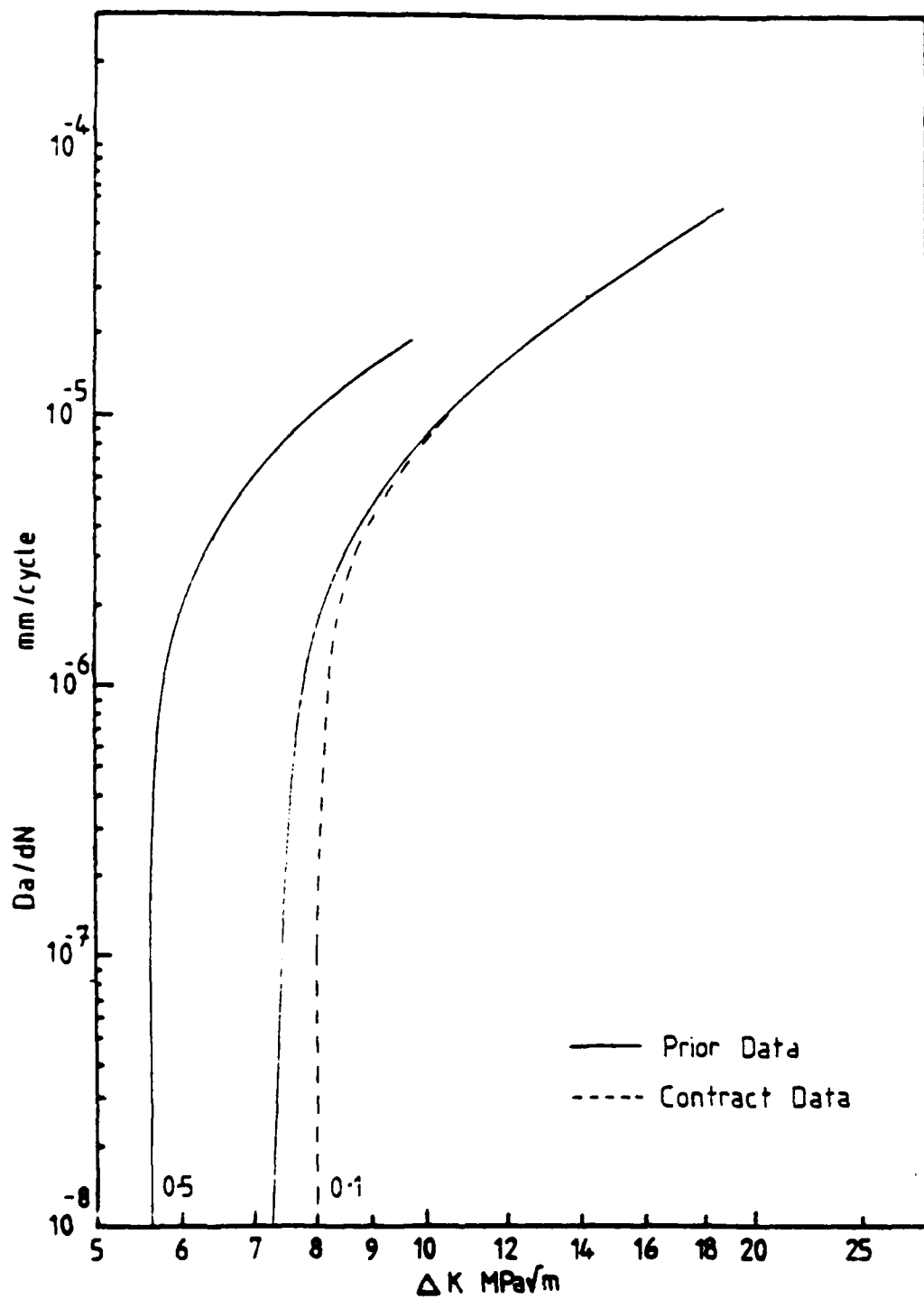


FIGURE 4-7. Load Ratio Effects in Coarse Grain Astroloy (600°C)

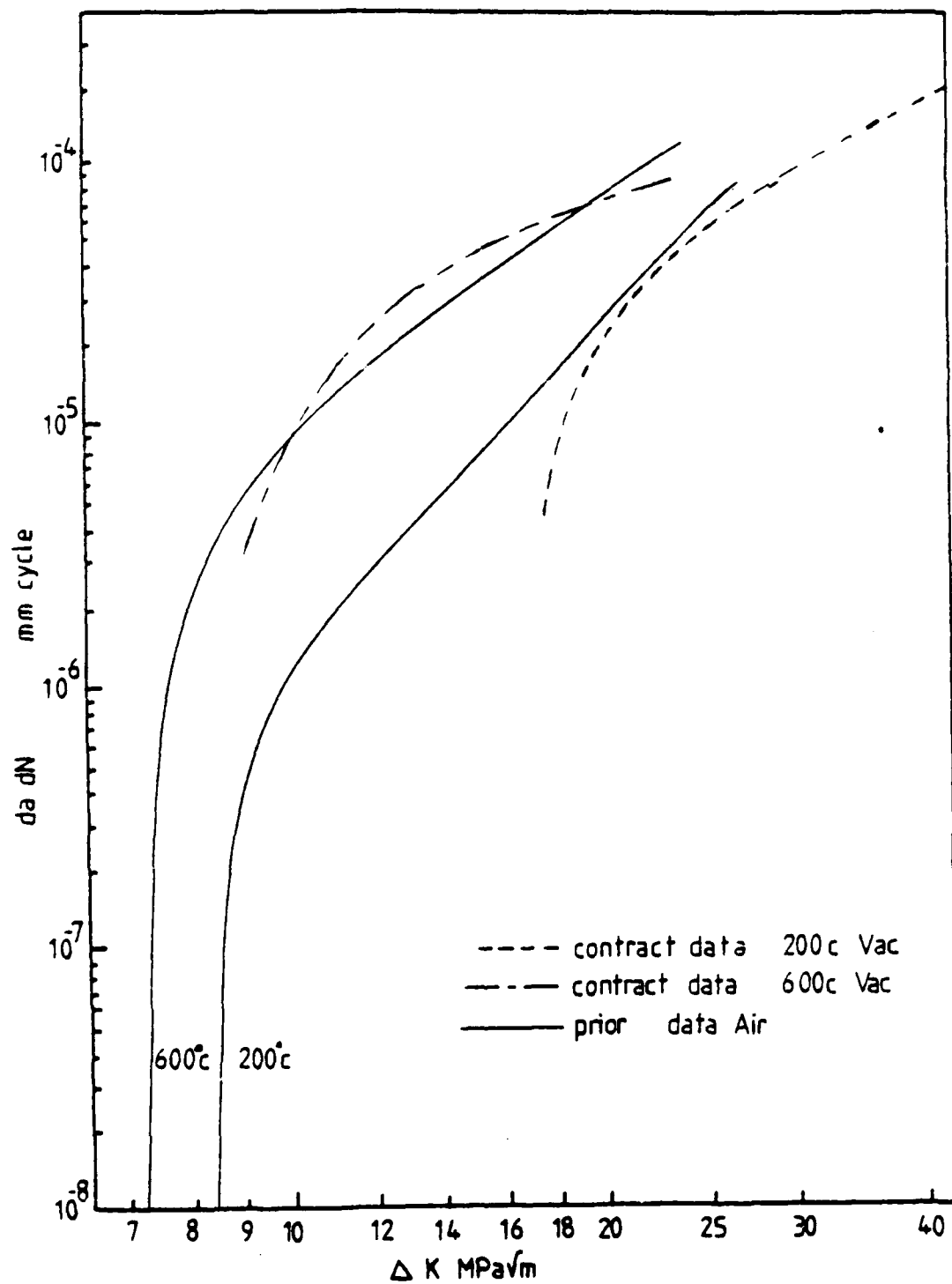


FIGURE 4-8. Effect of environment and temperature on near threshold crack growth rates of Coarse Grain Astroloy.

by such a tendency towards faceted fracture does remain similar in nature with an indication of a higher threshold and lower growth rates in the Paris regime. Although the range of growth rates explored was not as extensive as the 200°C vacuum test, corroboration of the lower growth rates in vacuum comes from the test data for Waspaloy at 550°C in air and vacuum, (Figure 4-9) where growth rates in air are a factor of two faster than the vacuum growth rates.

Crack growth data for Waspaloy is shown in Figure 4-10 along with the growth rates measured for coarse grain Astroloy of 30  $\mu\text{m}$  grain size. The behavioral trends are similar to those seen in CG Astroloy (Figure 4-2), although it should be emphasized that the threshold conditions measured were lower for the RT test than the 600°C test. The 600°C behavior is almost identical to the 600°C behavior of the 30  $\mu\text{m}$  grain size Astroloy, with threshold again being dominated by oxide induced closure, while the RT growth rates are slightly faster than the 30  $\mu\text{m}$  Astroloy due to the differences in yielding behavior, and the fact that the Waspaloy, while coarser in grain size, did not produce facets in the near threshold regime to the same extent as the 30  $\mu\text{m}$  grain size Astroloy.

#### 4.3 The Influence of Grain Size on Fatigue Threshold

The room temperature CG Astroloy data obtained in the current study exhibits significantly lower  $\Delta K_{th}$  values than that obtained previously for a different heat of CG Astroloy [4.4, 4.5]. Several factors are believed to contribute to this difference as follows: First, the material used in the previous study was "As-HIP'ed", and particularly prone to facetting on {111} planes at RT. Secondly, the average grain size in the previous study was 50  $\mu\text{m}$  as opposed to 30  $\mu\text{m}$  in the current study. When the above factors are considered, the differences in the measured thresholds are not unexpected. Figure 4-11 plots the measured thresholds from this and other studies [4.4, 4.6] of Astroloy against grain size. The correlation between points is very good, and certainly puts the measured values into perspective. Although the mechanism by which grain size influences the fatigue crack growth rate is not completely understood, the fractographic information is consistent with the operation of roughness-induced and oxide-induced mechanisms of crack closure.

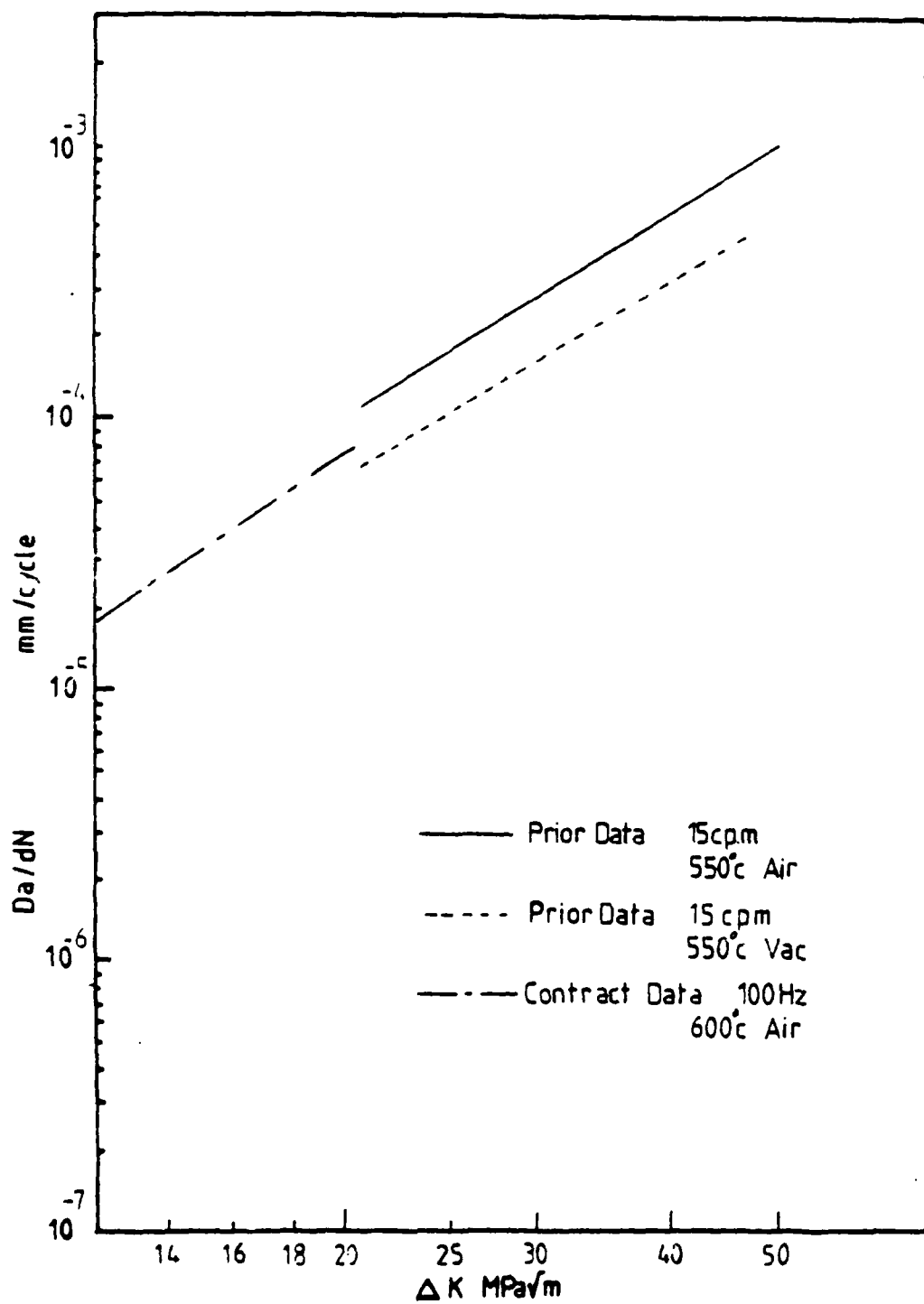
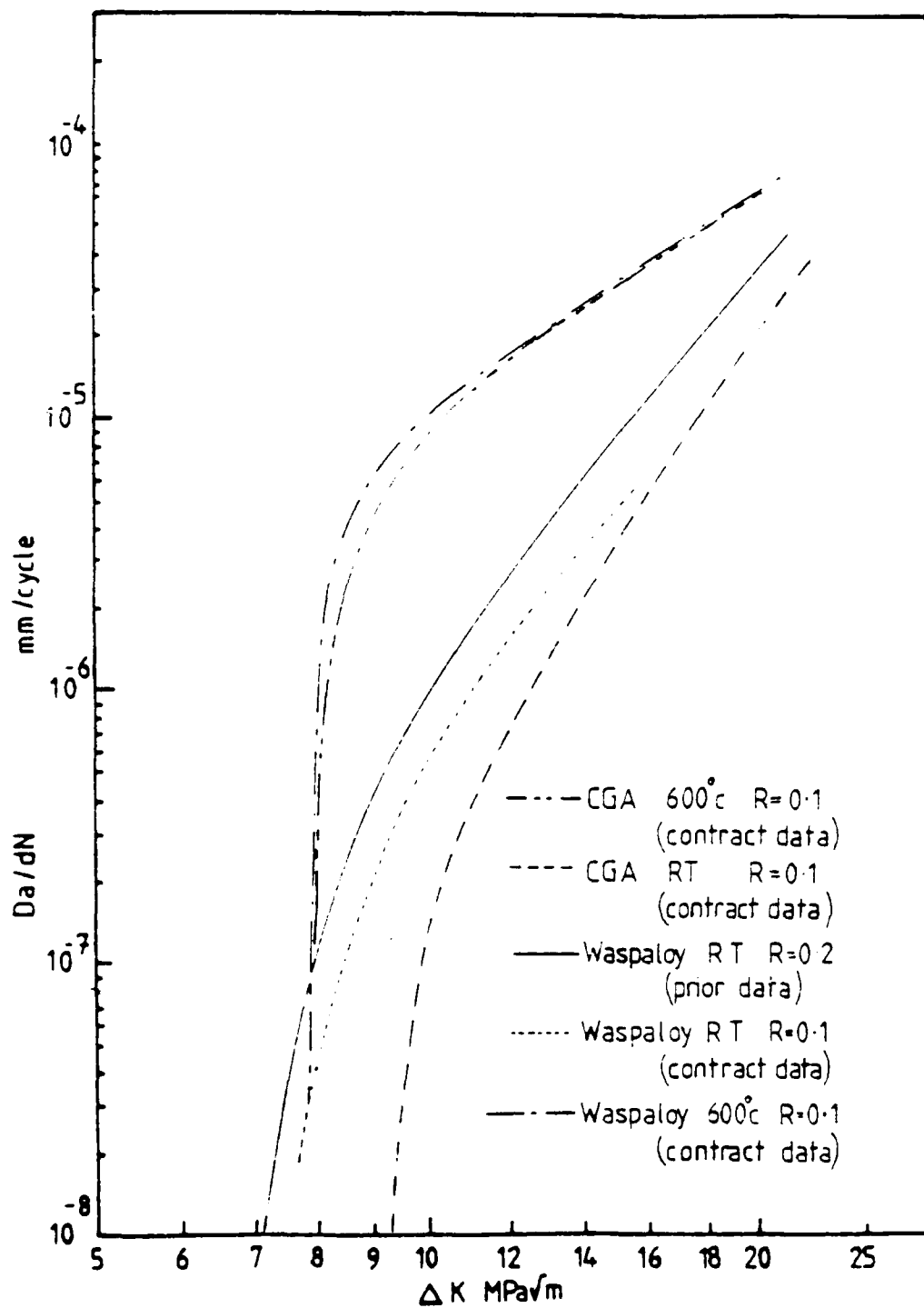


FIGURE 4-9. Effect of environment on fatigue crack growth



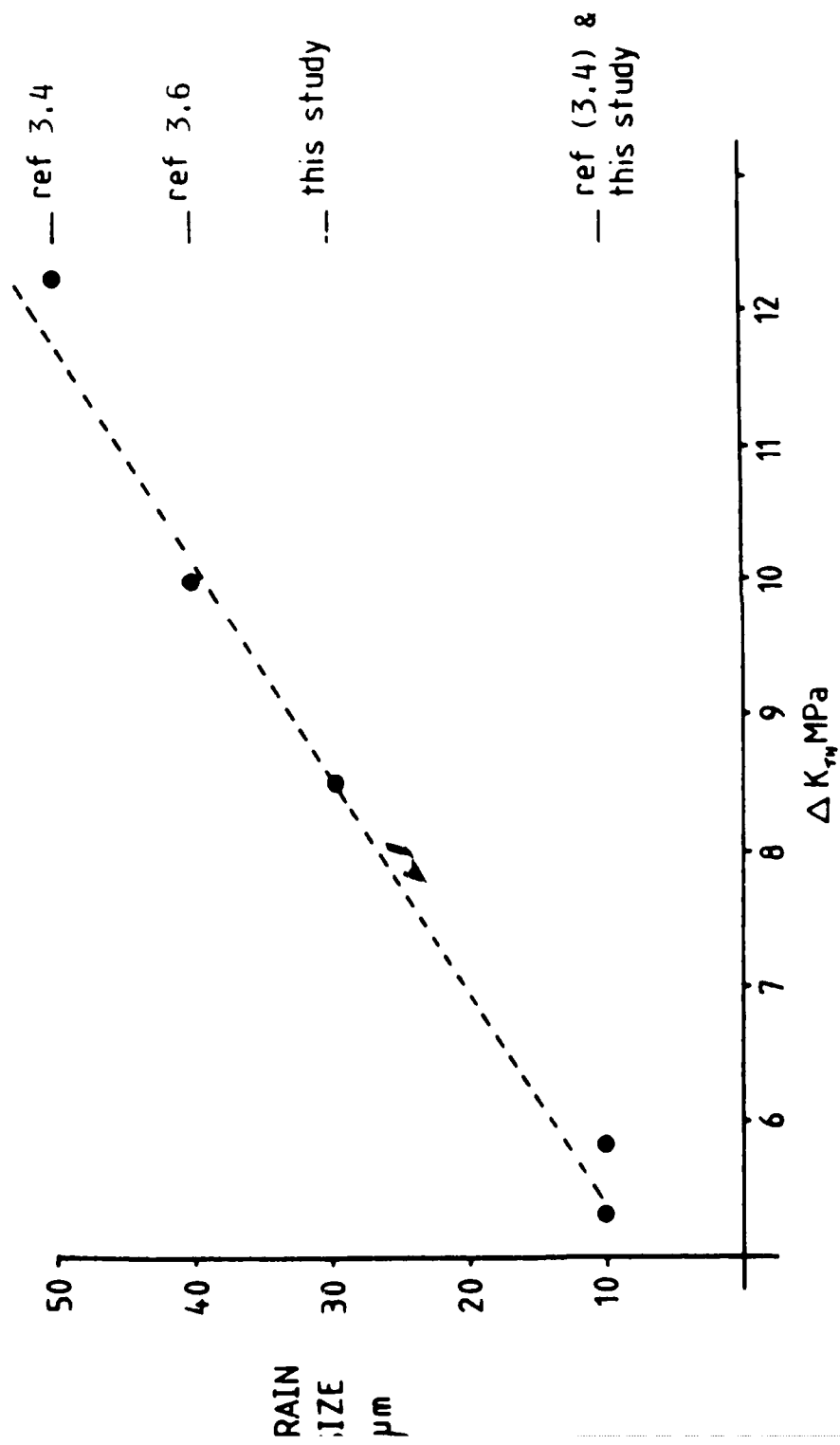


FIGURE 4-11. Correlation of  $\Delta K_{th}$  with Grain Size in Astroloy



#### 4.4 Crack Closure in Large Cracks

Crack closure results are of interest to understanding certain trends exhibited by the previous crack growth rates in large cracks. In addition, the basic differences in the extent of crack closure developed by large and small cracks need to be taken into account in attempting to formulate a driving force for crack growth which is independent of crack size. Fundamental crack closure concepts are briefly reviewed below, in preparation for a summary and reinterpretation of literature data on crack closure in Astroloy large cracks.

From the basic definition of crack closure, as defined originally by Elber [4.7], we have:

$$\Delta K_{eff} = K_{max} - K_{op} = \Delta K - \Delta K_{cl} \quad (4-1)$$

where:  $\Delta K_{cl} = K_{op} - K_{min}$

where the definitions of the above parameters is given in Figure 4-12. Although the load required to open the crack ( $P_{op}$ ) is the basic measurement in any crack closure study, this measurement is often expressed in terms of any one of several dimensionless closure parameters, including:  $R_{eff} = P_{op}/P_{max} = K_{op}/K_{max}$ , or  $\Delta K_{eff}/\Delta K$ . However, based on the definition in Eq. (4-1) these parameters are related as follows:

$$\Delta K_{eff}/\Delta K = (1 - R_{eff})/(1 - R) \quad (4-2)$$

Recently, Hudak and Davidson [4.8] have found that crack closure could be described by the following relatively simple relationship for several different materials and a wide range of fatigue loading variables:

$$\Delta K_{eff}/\Delta K = 1 - K_0/K_{max} \quad (4-3)$$

where  $K_0$  is a material constant. Eq. (4-3) is based on crack closure data obtained using the stereoimaging technique which enables high resolution measurements to be made local to the crack-tip (see Section 7.1). This technique allows the determination of the load required to fully open the crack, to within a fraction of a micron from its tip. Nevertheless, when remote techniques are used to measure the opening load, such as changes in specimen

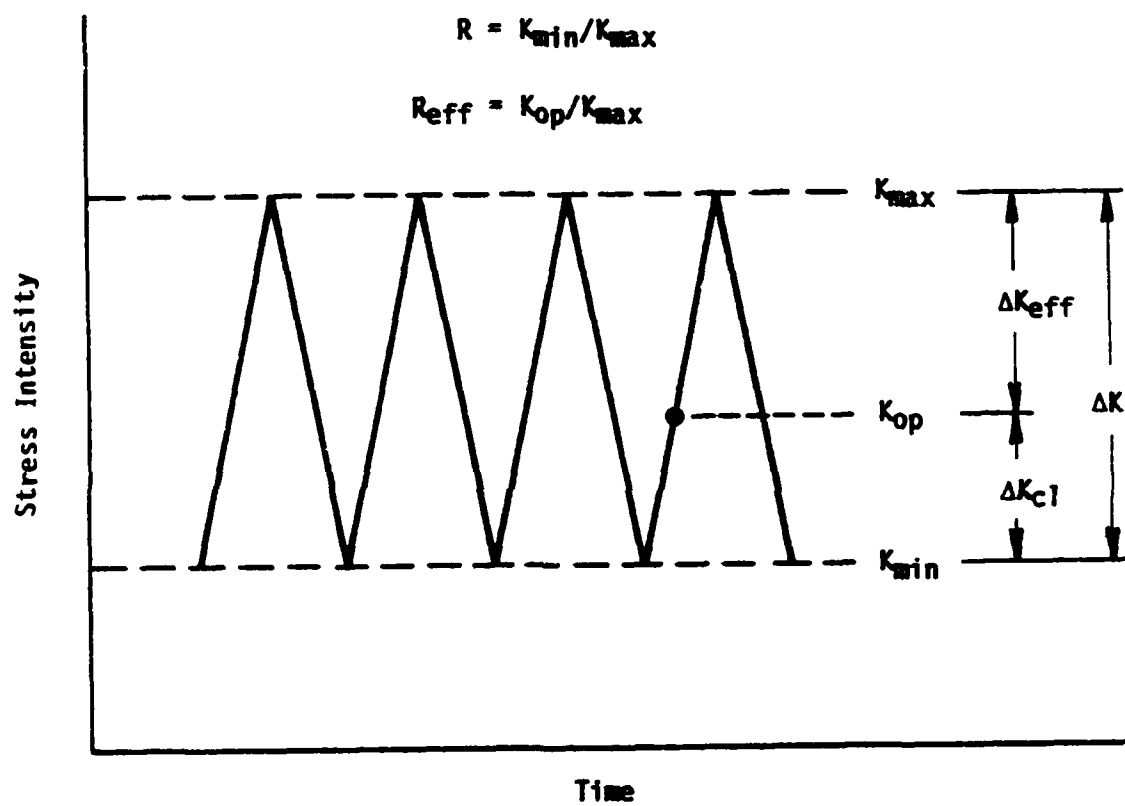


FIGURE 4-12. Definition of terms used to characterize fatigue crack closure.

compliance, a similar relationship is also found. However, the latter techniques often detect less closure, primarily due to their lack of precision with regard to events close to the crack-tip.

Combining Eqs. (4-1) and (4-3), along with the basic definition  $\Delta K = (1 - R)K_{\max}$ , gives:

$$\Delta K_{cl} = K_0(1 - R) \quad (4-4)$$

It is significant to note that the above observation appears to hold for large cracks subjected to a wide range of applied  $\Delta K$  (or  $K_{\max}$ ) and  $R$  values. It should also be noted that for the special case of  $R = 0$  (and  $K_{\min} = 0$ ), Eq (4-4) reduces to:

$$K_{op} = K_0 \quad (4-5)$$

The above relationship is consistent with observations on a variety of materials that  $K_{op}$  is relatively constant for  $R$  near zero; for example, see Ref. [4.9].

Although crack closure measurements were not obtained for large crack in the current study, available literature data of Soniak and Remy on necklace Astroloy at 20°C and 650°C [4.10] have been analyzed using Eqs. (4-3) and (4-4). These results, summarized in Figure 4-13, indicate relatively good agreement with the above equations, although considerable scatter is evident in the elevated temperature data.

The data in Figure 4-13 show measurably less crack closure (higher  $\Delta K_{eff}/\Delta K$  values) at 650°C than at 25°C. This result is consistent with the crack growth rates measured in the present study, as well as with the fractography in Ni-base alloys which shows noticeably flatter surfaces at the elevated temperature (See Section 6.3). The latter observation supports the previous hypothesis of Hicks et al [4.11] that crack closure in these alloys is controlled by fracture surface roughness. Thus, the observed temperature dependence of the long crack growth rates appears to be due to differences in the effective driving force for crack growth, as well as to expected differences in the intrinsic resistance to fatigue crack growth.

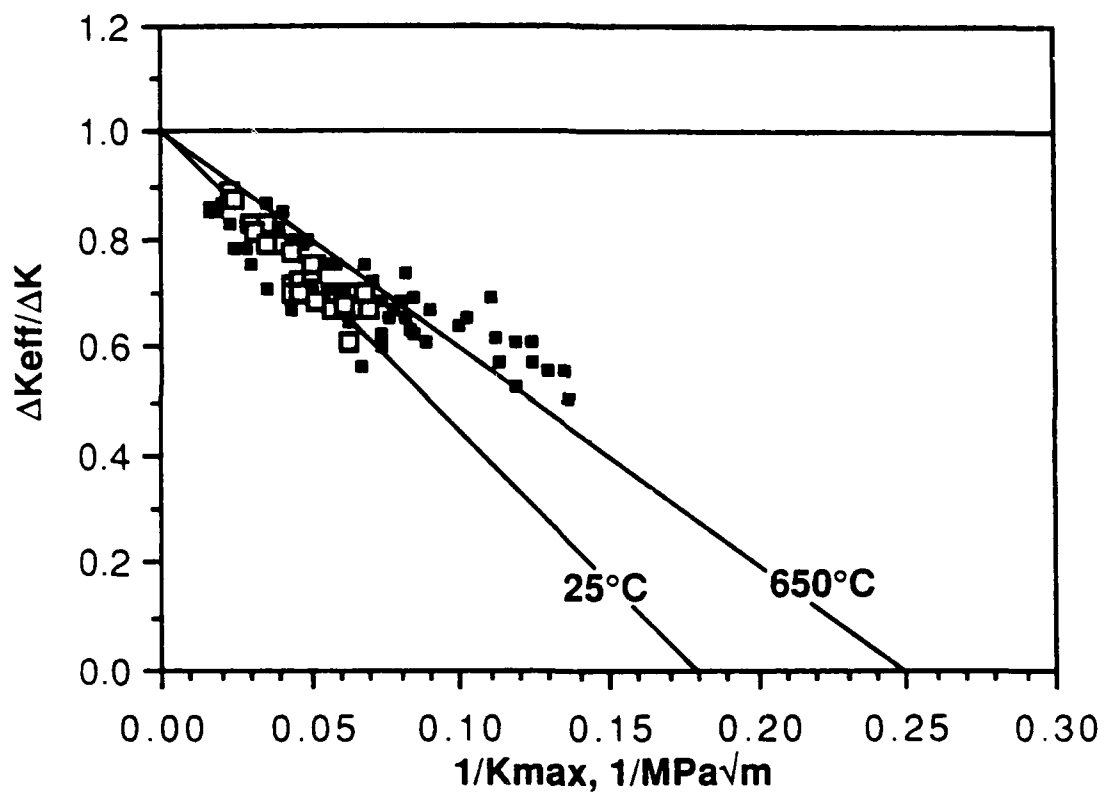


FIGURE 4-13. Crack closure behavior of large cracks in necklace Astroloy at various temperatures, from Soniak and Remy [4.10].

The intercepts along the abscissa in Figure 4-13 correspond to  $\Delta K_{CI}$  values of 4-6 MPa $\sqrt{m}$  at 25°C and 3-5 MPa $\sqrt{m}$  at 650°C. These results are discussed further in Section 7, where they are compared with crack closure measurements on small cracks.

#### 4.5 References

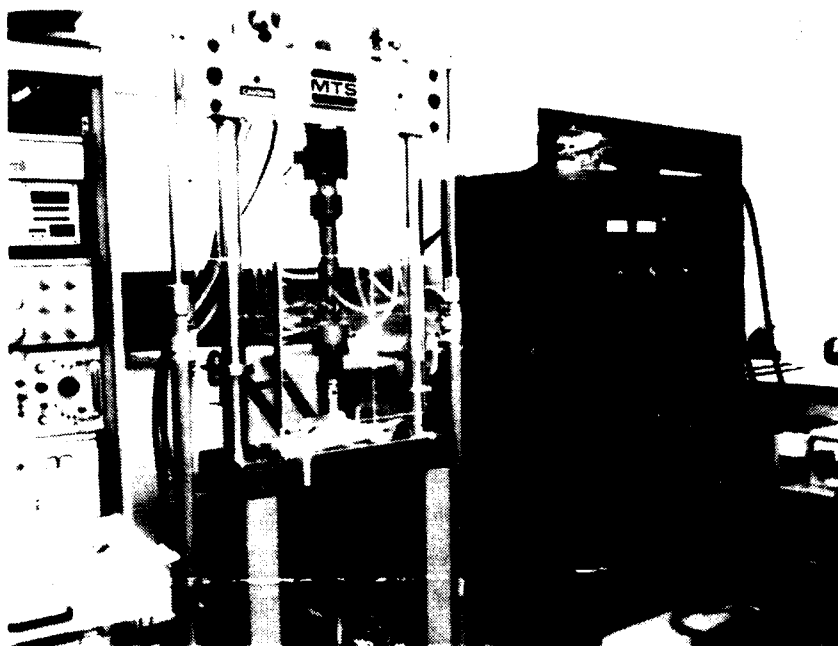
- 4.1 M. A. Hicks and A. C. Pickard, "A Comparison of Theoretical and Experimental Methods of Calibrating the Electrical Potential Drop Technique for Crack Length Determination," Intn. J. of Fracture, Vol. 20, 1982, pp. 91-101.
- 4.2 S. Suresh, G. F. Zamitski and R. O. Ritchie, "Oxidation and Crack Closure: An Explanation for Near Threshold Corrosion Fatigue Crack Growth Behavior," Met. Trans., Vol. 12A, 1981, pp. 1435-1443.
- 4.3 C. J. Beevers, Personal Communication, 1985.
- 4.4 M. A. Hicks and J. E. King, "Temperature Effects on Fatigue Thresholds and Structure Sensitive Crack Growth in a Nickel-Base Superalloy," Intn. J. Fatigue, Vol. 5, 1983, pp. 67-74.
- 4.5 C. W. Brown, J. E. King and M. A. Hicks, "Effect of Microstructure on Long and Short Crack Growth in Nickel-Base Superalloys," Metal Science, Vol. 18, 1984, pp. 374-380.
- 4.6 J. E. King, "Surface Damage and Near Threshold Fatigue Crack Growth in a Nickel Base Superalloy in Vacuum," Fat. Engr. Matls. and Structures, Vol. 5, 1982, pp. 177-188.
- 4.7 W. Elber, "Fatigue Crack Closure Under Cyclic Tension," Engr. Fract. Mech., Vol. 2, 1970, pp. 37-45.
- 4.8 S. J. Hudak, Jr. and D. L. Davidson, "The Dependence of Crack Closure on Fatigue Loading Variables," in Mechanics of Closure, ASTM STP 982, Eds. J. C. Newman and W. Elber, 1987, pp. 121-138.
- 4.9 J. E. Allison, "On the Measurement of Crack Closure During Fatigue Crack Growth," in Fracture Mechanics: Eighteenth Symposium, ASTM STP 945, Eds. D. T. Read and R. P. Reed, 1987.
- 4.10 F. Sonick and L. Remy, "Behavior of Long and Short Fatigue Cracks in a Powder Metallurgy Superalloy at Room and High Temperature," in Fatigue '87, Eds. R. O. Ritchie and E. A. Starke, Jr., EMAS, 1987, pp. 351-360.
- 4.11 M. A. Hicks and J. E. King, "Temperature Effects on Fatigue Thresholds and Structure Sensitive Crack Growth in a Nickel-Base Superalloy," Int. J. Fatigue, Vol. 5, No. 2, 1983, pp. 67-74.

## 5.0 GROWTH OF SMALL CRACKS AS A FUNCTION OF $\Delta K$

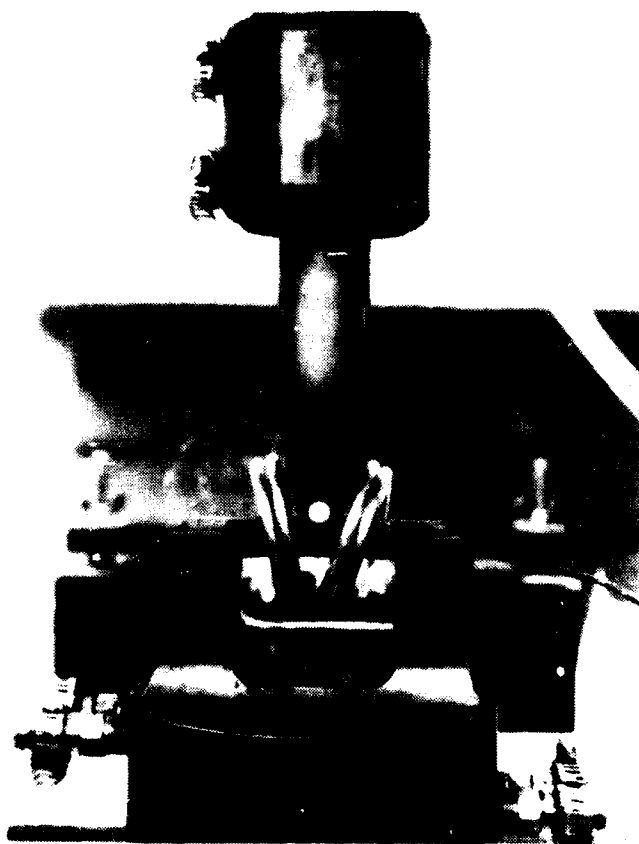
This section compares small crack data obtained using naturally initiated surface cracks in three-point bend specimens with the large crack data of Section 4. These results are also compared with the additional small crack data from Section 7 which were obtained in the scanning electron microscope. This initial comparison is made within the framework of linear elastic fracture mechanics, although it is recognized that this approach may be inadequate for small cracks. Nevertheless, it does provide a convenient basis for initial comparison of the influence of material, environmental and loading variables in a format which is consistent with most other small crack studies. The development and evaluation of a more appropriate driving force for the growth of small cracks is presented in Sections 7 and 8. Since the success of any small crack study is dependent on the experimental techniques employed, particularly at elevated temperature, these techniques are discussed below prior to presenting the experimental results.

### 5.1 Small Crack Experimental Procedure

Data on the growth of small cracks at both room temperature and elevated temperature were obtained using 10x10x70 mm specimens loaded in three point bending as shown in Figure 5-1. These specimens were prepared using low-stress machining. In addition, to eliminate residual stresses which may have remained after machining, the gage section was electropolished in a solution of 25 percent nitric acid in methanol at -30°C. Typically a 130  $\mu$ m-thick layer of material was removed during electropolishing. Induction heating was used to conduct the elevated temperature testing. To accommodate the induction heating both the upper and lower bend fixtures were water cooled. Contact between the upper fixture and the specimen was achieved using a ceramic tup in order to eliminate localized induced heating in this region of the specimen. The configuration of the induction heating coils was also optimized to minimize temperature gradients in the central region of the specimen. Thermal transients arising from room air currents were minimized by placing a plexiglass box around the center of the test machine as shown in Figure 5-1. With this system, the temperature in the region of the specimen



(a) Overview of test system and induction heater.



(b) Close-up of specimen and loading fixtures.

containing the small cracks was constant to within  $\pm 3^{\circ}\text{C}$  as indicated by results in Figure 5-2 from thermocouple measurements obtained for a prescribed temperature of  $650^{\circ}\text{C}$ .

All cracks were naturally initiated from the electropolished surface of the specimen. Generally two or three independent cracks occurred and were monitored using surface replication at intervals of 10,000 to 20,000 cycles. Replicas were subsequently coated with vapor-deposited silver and crack lengths were measured using a light microscope at magnifications of 200X to 1000X. Although this technique involved periodic interruption of the experiment, and cooling in the case of the elevated temperature experiments, this inconvenience was outweighed by the fact that reliable data were obtained on multiple cracks as small as  $10\text{ }\mu\text{m}$  in length. The detection of the smallest cracks was possible due to the fact that larger, more readily detectable cracks could be easily found and back-tracked on previous replicas. The fact that cracks naturally initiated at either voids or persistent slip bands in favorably oriented grains enabled interactions between these microstructural features and the growth of small cracks to be studied.

The above specimen geometry and loading mode proved to have the following advantages for small crack testing: First, due to the stress gradient in the bend specimen, cracks initiated at the surface, rather than at subsurface pores and inclusions; whereas, subsurface crack initiation is often a problem in tensile loading. Secondly, the localization of the maximum bending moment at the center of the specimen in 3-point bending facilitated the detection and monitoring of microscopic cracks by limiting the area over which cracks initiated. Finally, the simplicity of specimen design and fixturing is both economical and promoted efficient heating and cooling during elevated temperature experiments. The major disadvantage of the technique was the fact that the average crack initiation lives were longer than those which would be expected under tensile loading. This difference is believed to be partly statistical -- that is, due to the fact that less volume of highly stressed material occurs in the bend specimen, thereby reducing the probability of encountering favorable initiation sites in the region of highest stress. In addition, at high applied stresses contained plastic deformation near the surface of the bend specimen caused compressive stresses to be generated which reduced the local mean stress and tensile stress range as discussed below.



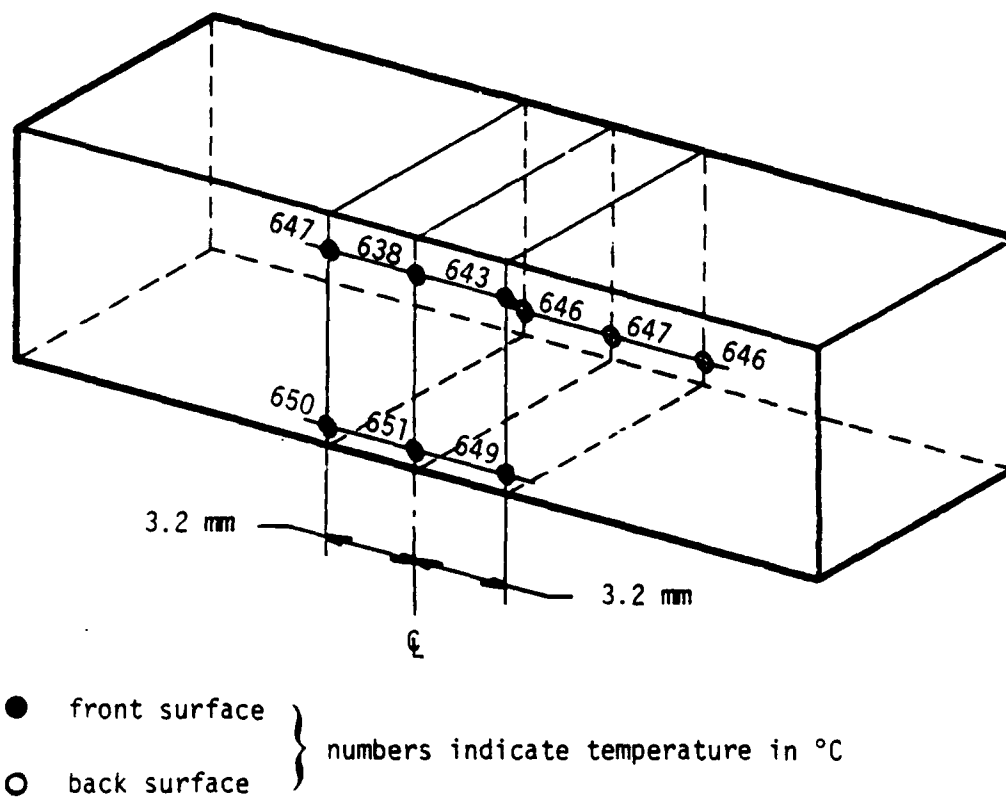


Figure 5-2. Temperature profile in induction-heated bend specimen at 650°C.

## 5.2 Stress Intensity Factor for Small Surface Cracks in Bending

The following simplified stress intensity factor expression, derived from Pickard's [5.1] three-dimensional finite element analyses of surface cracks in rectangular bars, was used to analyze the growth of small cracks in the bend bar experiments:

$$\Delta K = 1.155 \{1 - 0.5(a/W)\} \{S_{\max}(1 - R)/(1 - R_0)\} \sqrt{\pi a} \quad (5.1)$$

where:  $\Delta K$  = the stress intensity factor range, at the position where the crack intersects the specimen surface

$a$  = the half-crack length (or crack depth for the case of a semicircular crack)

$W$  = the half-height of the specimen

$S_{\max}$  = the maximum "outer-fiber" stress computed for three-point bending

$R$  = the stress ratio, given by the ratio of the applied minimum to maximum load

$R_0$  = the local stress ratio during fatigue loading, given by the ratio of local minimum to maximum stress. (As discussed below, this ratio can differ from  $R$ )

The relative simplicity of Eq. (5.1) compared to the general solution given in Ref. [5.1] arises from the fact in the current experiments the relative crack length was always less than 1 mm, thus  $a/W < 0.2$ , and the crack aspect ratio ( $a/c$ ) was approximately equal to one. Under these conditions Eq. (5.1) represents the original finite element results to within 0.5 percent.

The assumption that the crack remained semicircular ( $a/c = 1$ ) as it grew was assessed by post-mortem examination of the fracture surfaces. The determination of the crack shape was relatively easy for experiments conducted at elevated temperature since the fracture surfaces exhibited a color gradient due to differences in oxide thickness. Results from these microscopic examinations are summarized in Figure 5-3. Although considerable scatter in the aspect ratio is evident, no consistent trend emerged with respect to alloy composition or test temperature, indicating that the nominal crack shape is controlled by specimen geometry and loading mode. Most importantly, the average aspect ratio is consistent with the assumed crack shape used in the analysis.

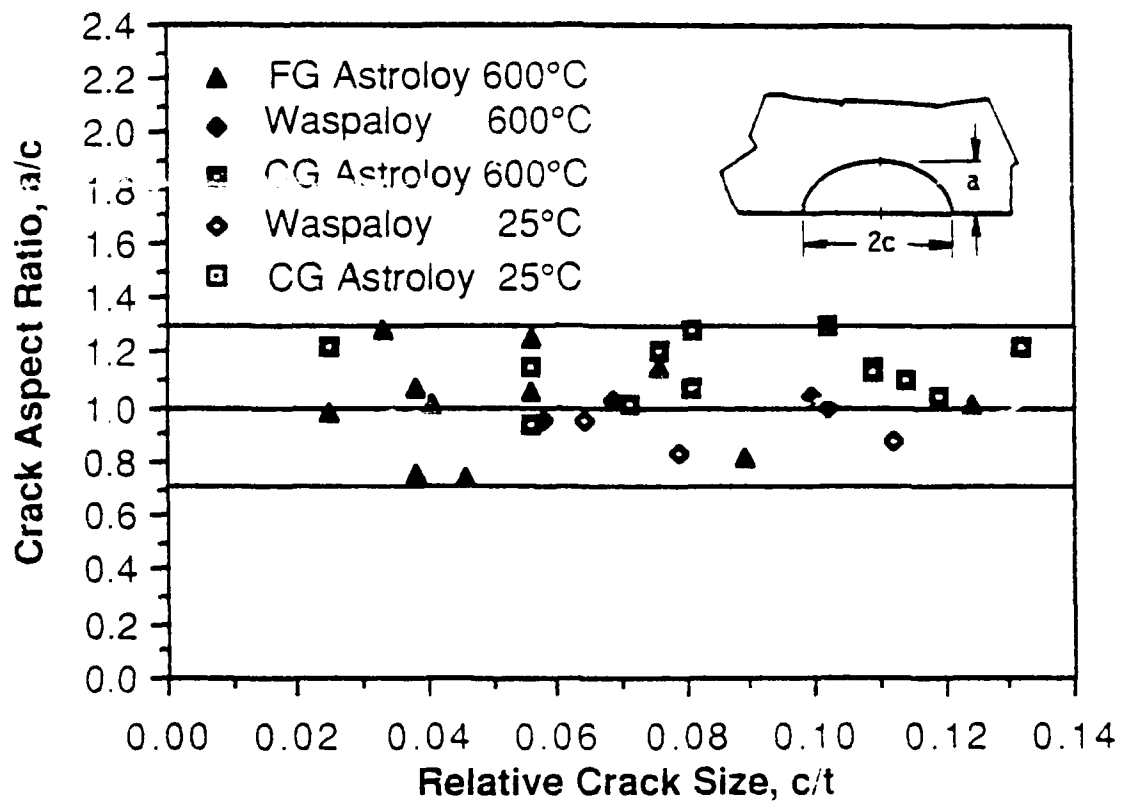


Figure 5-3. Fatigue crack shape as a function of crack size for various alloys and test temperatures.  
( $t$  = specimen thickness)

All experiments were conducted such that the bend specimen was nominally elastic. However, due to the stress gradient in the specimen, localized plastic deformation sometimes occurred in the surface region of the specimen where cracks initiated and grew. (This behavior is analogous to the localized deformation which can occur in notched geometries.) The primary result of this contained plasticity at the surface of the specimen was an alteration in the local mean stress.

The above process was quantified using strain gage measurements on an uncracked CG Astroloy specimen cycled at different load (strain) ranges. As shown in Figure 5-4, the local stress ratio ( $R_o$ ) decreased and became negative as the applied strain range increased. The values of  $R_o$  in the CG Astroloy bend specimen were computed from the measured strains using the monotonic and stable cyclic stress-strain relations provided in Section 3. Since information on cyclic stress relaxation could not be included in these computations, they provide an upper-bound estimate of the local stress ratio in the bend specimen. The additional influence of cyclic stress relaxation on the local mean stress can be estimated from the measurements of Lindholm et al [5.2], obtained on the superalloy B1900+Hf tested under cyclic strain-control. Since uniaxial tensile specimens were used in this study, the mean stress could be measured directly. The difference between these results and those obtained for the bend bar is primarily due to cyclic stress relaxation. It is interesting to note that the measured results are in good agreement with values computed from the Bodner-Partom constitutive relations and show a limiting case of fully-reversed cycling ( $R_o = -1$ ).

The results in Figure 5-4 including relaxation were assumed to apply to all of the Ni-base superalloys examined in the current program. This assumption is consistent with the fact that the extent of mean stress relaxation is known to primarily depend on the magnitude of the cyclic plastic strain range for a given class of materials [5.3]. The value of strain experienced in the bend bars for various materials and temperatures was assumed to scale with material strength level as shown in Figure 5-5. Thus, for a given applied normalized stress  $S = S_{max}/S_{ys}$ , the strain was obtained from Figure 5-5, and the corresponding local mean stress from Figure 5-4. Since the crack is not expected to grow while the local stress is compressive, the local stress ratio was used to eliminate the local compressive stress from the

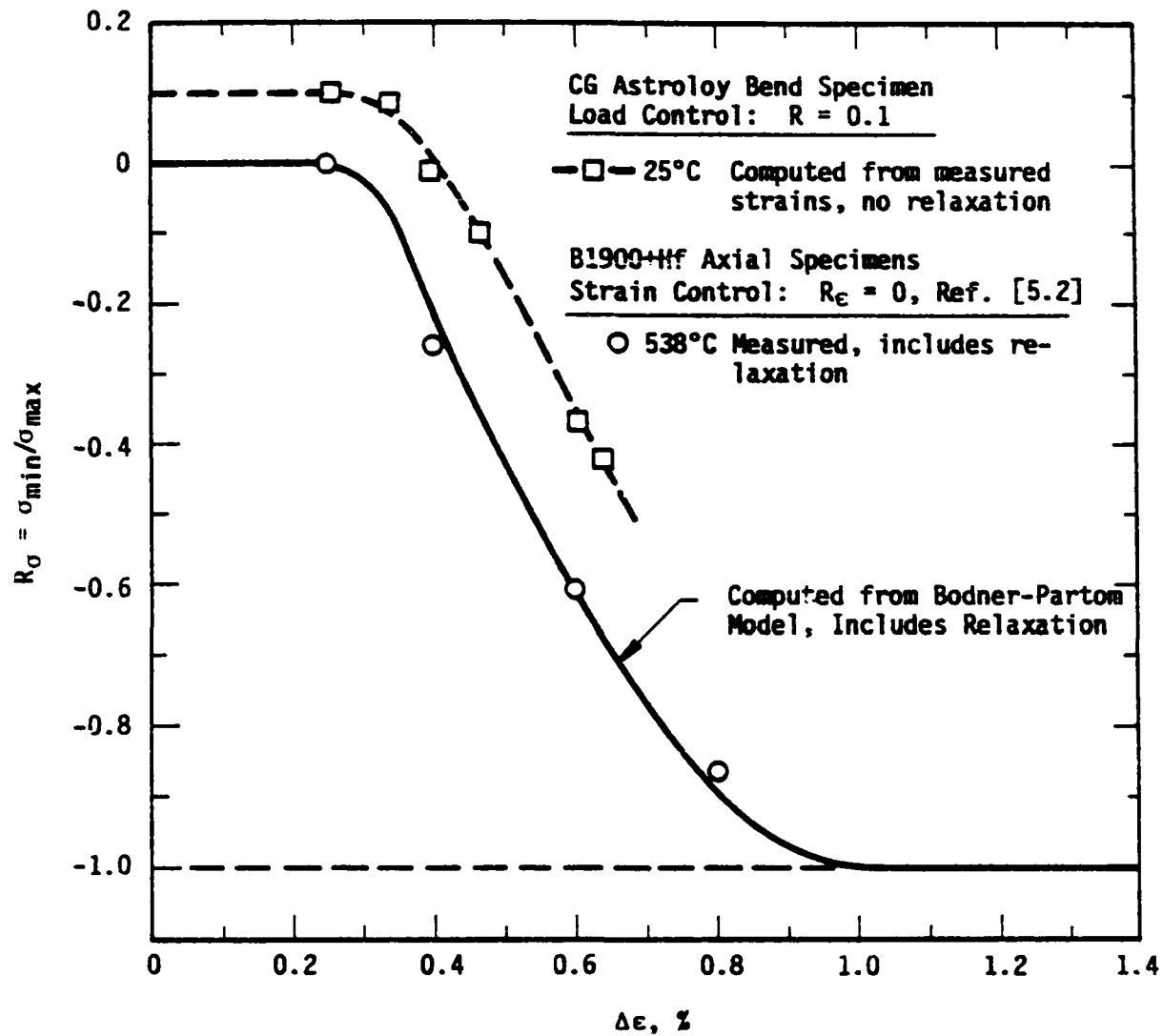


Figure 5-4. Dependence of local stress ratio ( $R_\sigma$ ) on local cyclic strain range ( $\Delta\epsilon$ ) for three-point bend specimens.

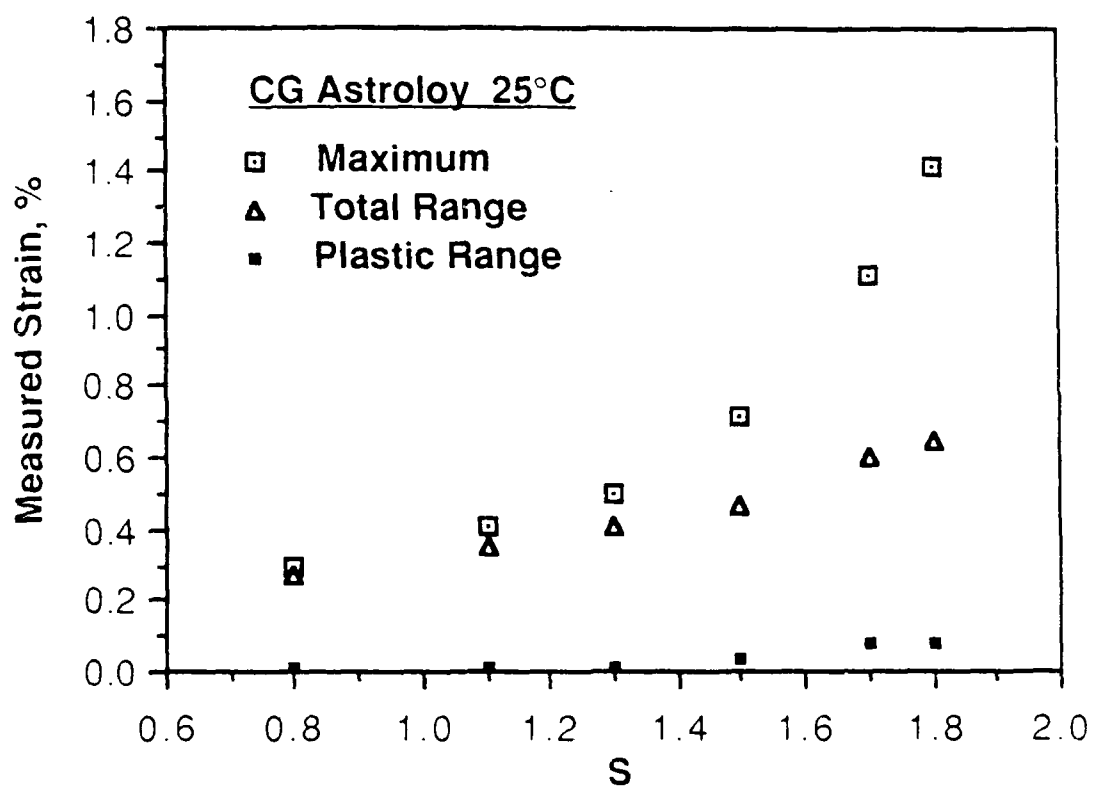


Figure 5-5. Measured strain at the surface of the three-point band specimen as a function of the normalized maximum stress,  $S = S_{\max}/S_{\text{sys}}$ .

computation of  $\Delta K$  by reducing the applied stress by the factor  $1/(1 - R_p)$ , as indicated in Eq. 5.1.

### 5.3 Effect of Elastic Anisotropy and Mixed Mode Loading on the Stress Intensity Factor for Small Cracks

As shown in Section 6, the crystallographic nature of the cracking encountered in small cracks causes cracks to be inclined at an angle  $\theta$  with respect to the remote loading direction -- for example, see Table 6-1. This inclined crystallographic crack growth introduces mixed-mode, anisotropic effects which need to be considered in analyzing small crack data. The effect of these factors on the stress intensity factor for small cracks was assessed based on anisotropic finite element (FE) analyses conducted by RR under the present program (see Appendix), as well as the anisotropic boundary-integral-equation (BIE) results of Chan and Cruse [5.4].

The two dimensional BIE results of Chan and Cruse [5.4] on Mar-M200 single crystal compact specimens are shown in Figure 5-6. Here the normalized stress intensity factor is given as a function of the projected relative crack size, where:  $a'$  is the projected crack length,  $b$  is the specimen thickness,  $W$  is the effective specimen width, and  $P$  is the applied load. The similarity of results for normal cracks ( $\beta = 0^\circ$ )\* with two crystallographic orientations ( $\alpha = 0^\circ$  and  $45^\circ$ ) indicates that the effect of elastic anisotropy on the stress intensity factor is insignificant. This conclusion is also supported by the fact that these results were found to be in excellent agreement with the elastic isotropic results recommended by ASTM for the compact specimen geometry [5.5]. In addition, as shown in Figure 5-6, results for cracks at various inclined crack angles  $\beta$  were also found to be similar for small values of  $\beta$  and small relative projected crack sizes. These results suggest that elastic anisotropic effects can be ignored for conditions encountered in the present study and that mixed mode effects can be approximated by employing the projected crack length to compute the dominant Mode I stress intensity factor using Eq. 5.1.

Based on the results of Chan and Cruse [5.4], and the currently observed crack growth inclinations, it is estimated that the stress intensity factor

\* Note that  $\beta$  in Figure 5-6 and  $\theta$  in Table 6-1 are related as follows:  
 $\beta = \theta - 90^\circ$ .

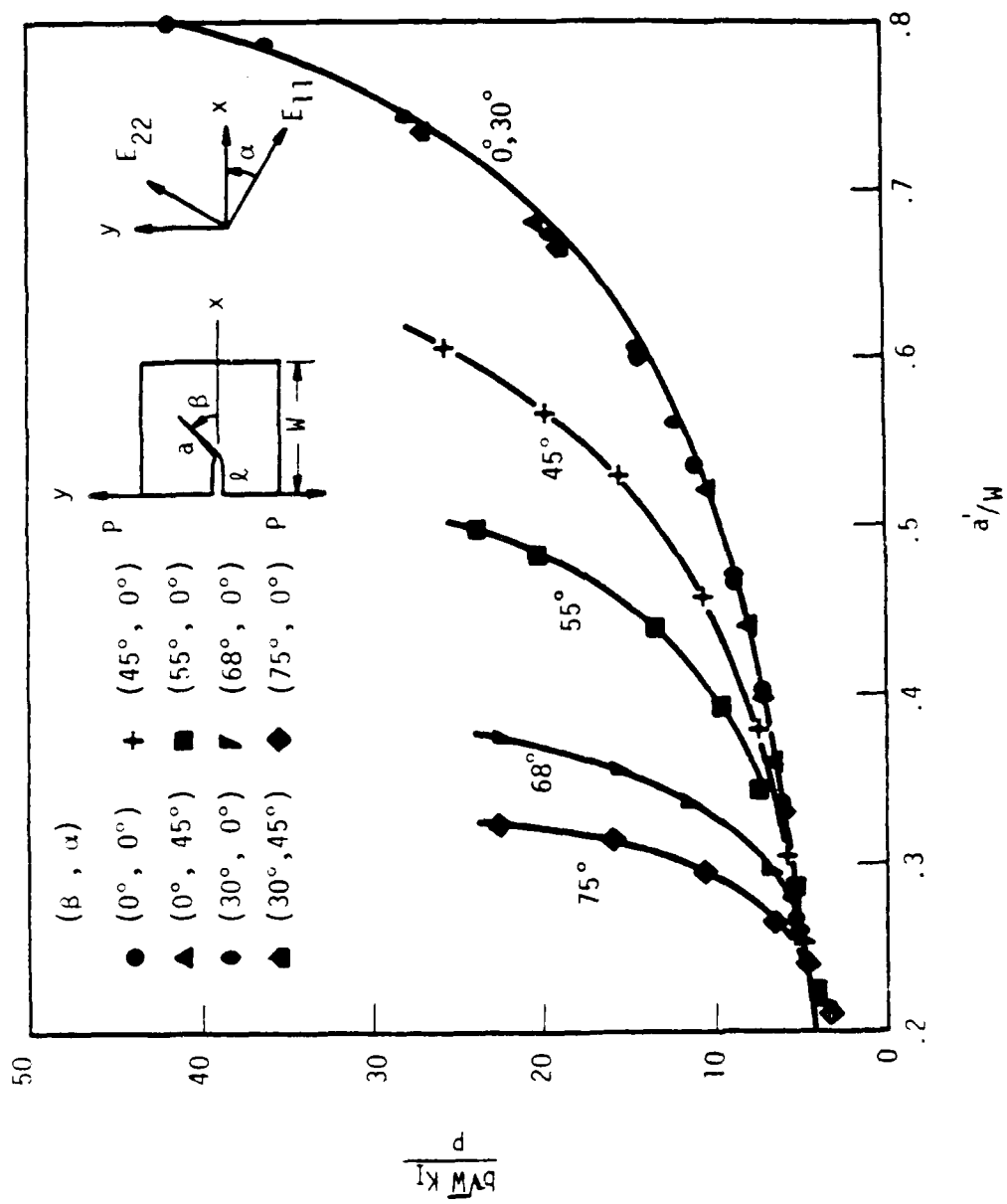


FIGURE 5-6. Normalized Mode I stress intensity factor for inclined cracks in a Mar-M200 single-crystal CT specimen (Ref. 5.4)  
 $a' = l + a \cos \beta$  is the projected crack length.



for Mode II will always be less than the 35 percent of the Mode I value. Since the overall elastic driving force under mixed mode loading in single crystals Ni-based alloys has been shown to be governed by the strain energy release rate [5.6-5.7], which is proportional to  $\Delta K_I^2 + \Delta K_{II}^2$ , the Mode II contribution will be less than 6 percent of the total elastic driving force. This contribution has been neglected in analyzing the results from the current study.

An obvious limitation of the above results is the fact that they are for long-thru cracks in a specimen geometry which differs from those used in the present study. Thus, the ultimate objective of the FE analyses conducted by RR under the present program was to examine the importance of material anisotropy for the three-dimensional case of surface cracks. The approach taken was a systematic one which included both two-dimensional and three-dimensional FE modeling of cracks in anisotropic bodies and of cracks in local regions of anisotropy within an otherwise isotropic body. Computational details of this approach are provided in the Appendix, while the results which are significant to the analysis of small cracks are summarized below.

Results of the finite element analyses, for several different anisotropic orientations, revealed an increase in the stress intensity factor compared to the isotropic case. However, as shown in Figure 5-7, on average these results differ by only 5 percent. This same figure shows that this difference is small compared to the variation in stress intensity factor which occurs for various positions along the semicircular crack front, characterized by the angle  $\delta$ . Thus, the issue of elastic anisotropy is less important than that of selecting the proper isotropic stress intensity factor along the crack front to characterize the crack driving force. In the current study, the value at the position where the crack intersects the specimen surface was used. This value was found to provide the best overall agreement between fatigue crack growth results from the largest surface cracks and from the long thru cracks.

#### **5.4 Effect of Temperature on the Initiation and Early Growth of Microcracks**

The initiation and early growth of microcracks at room temperature was relatively easy to accomplish in the three-point bend specimens. For example,

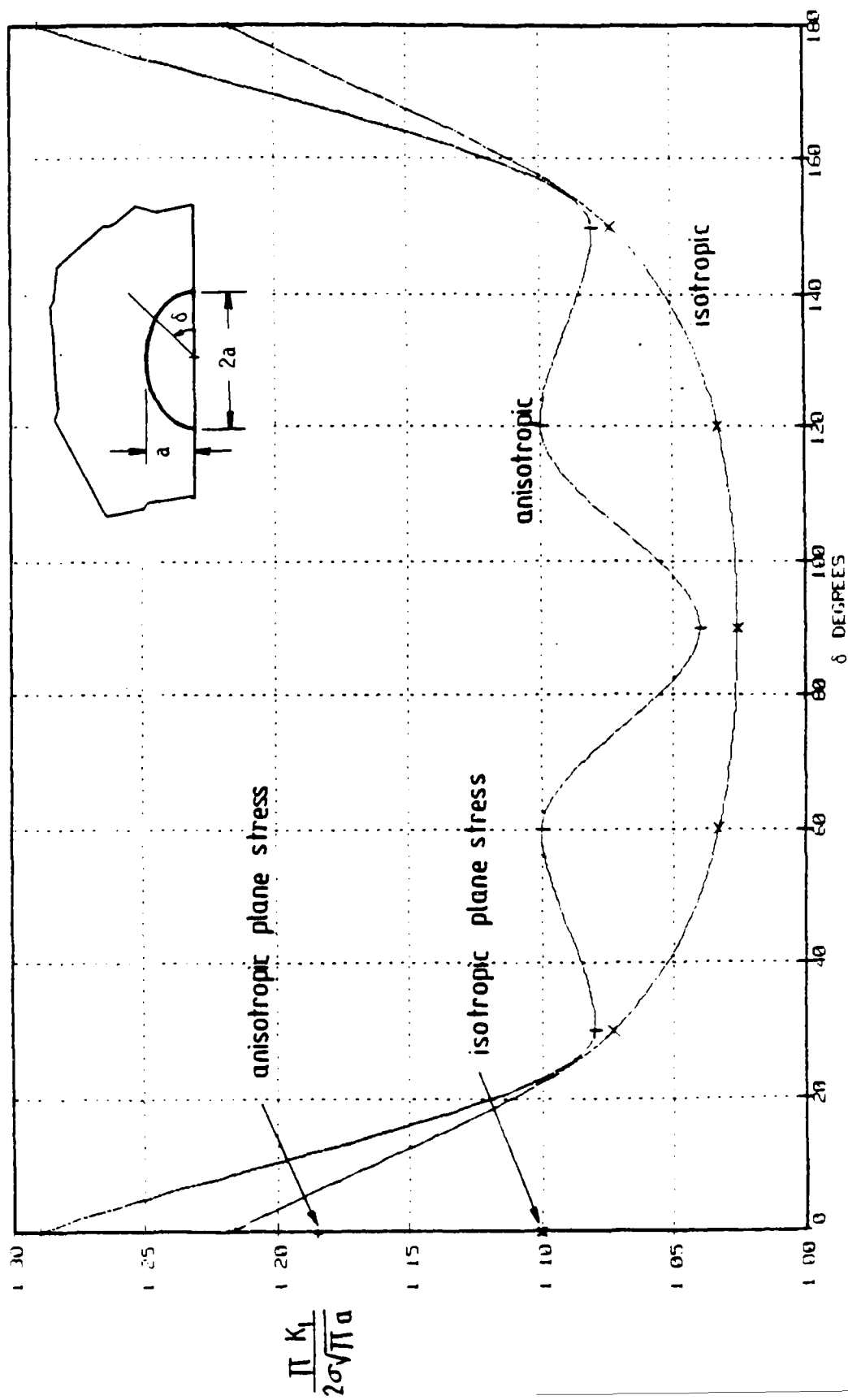


Figure 5-7. Comparison of isotropic and anisotropic Model I stress intensity factors from finite element model of a semicircular surface crack.

when the maximum (outer fiber) bending stress was about equal to the materials yield strength, microcracks of 15 to 20  $\mu\text{m}$  in total surface length were obtained in about  $10^5$  cycles. The subsequent growth of these cracks was also relatively easy to monitored since it occurred over 70 percent to 85 percent of the total cyclic life of the specimen. However, the initiation and early growth of microcracks at elevated temperature was considerably more difficult to produce. As indicated by the S-N data in Figure 5-8, applied stresses had to be increased by about 40 percent in order to produce cyclic lives comparable to those experienced at room temperature.

In order to facilitate the acquisition of data at elevated temperature, microcracks were in many cases initiated at room temperature before increasing the temperature for the remainder of the experiment. However, even with this procedure the growth of microcracks was erratic at elevated temperature in all three materials examined. An example of this erratic behavior is given by the CG Astroloy data summarized in Table 5-1. Fatigue precracking at room temperature was conducted at  $S = 1.21$  and  $R = 0.1$  for 160,000 cycles to insure that growing cracks were present. Although several cracks initiated under these conditions, Table 5-1 only provides information on the dominant crack which eventually caused the specimen to fail. This particular crack initiated from a pore on the electropolished surface of the specimen. Shortly after the temperature was increased from room temperature to  $600^\circ\text{C}$ , the crack arrested and remained dormant for most of the remaining specimen life. During this period the applied stress was gradually increased in steps. Following the final increase to  $S = 1.45$ , the crack grew rapidly and resulted in specimen failure in only 25,000 cycles. Similar behavior was also observed at higher applied stresses, as shown in Figure 5-9. In this case, the crack initiated in only 30,000 cycles due to the high stress ( $S = 1.8$ ), but then remained dormant for about 120,000 cycles before the growth rate increased several orders of magnitude, resulting in failure of the specimen.

The above behavior made it difficult to monitor crack growth at  $600^\circ\text{C}$  using the replication technique. This problem was eventually overcome after numerous specimens were tested, thereby enabling the periods of initiation and dormancy to be estimated. Using this experience, the replication interval was reduced at the appropriate time so that adequate data could be obtained.

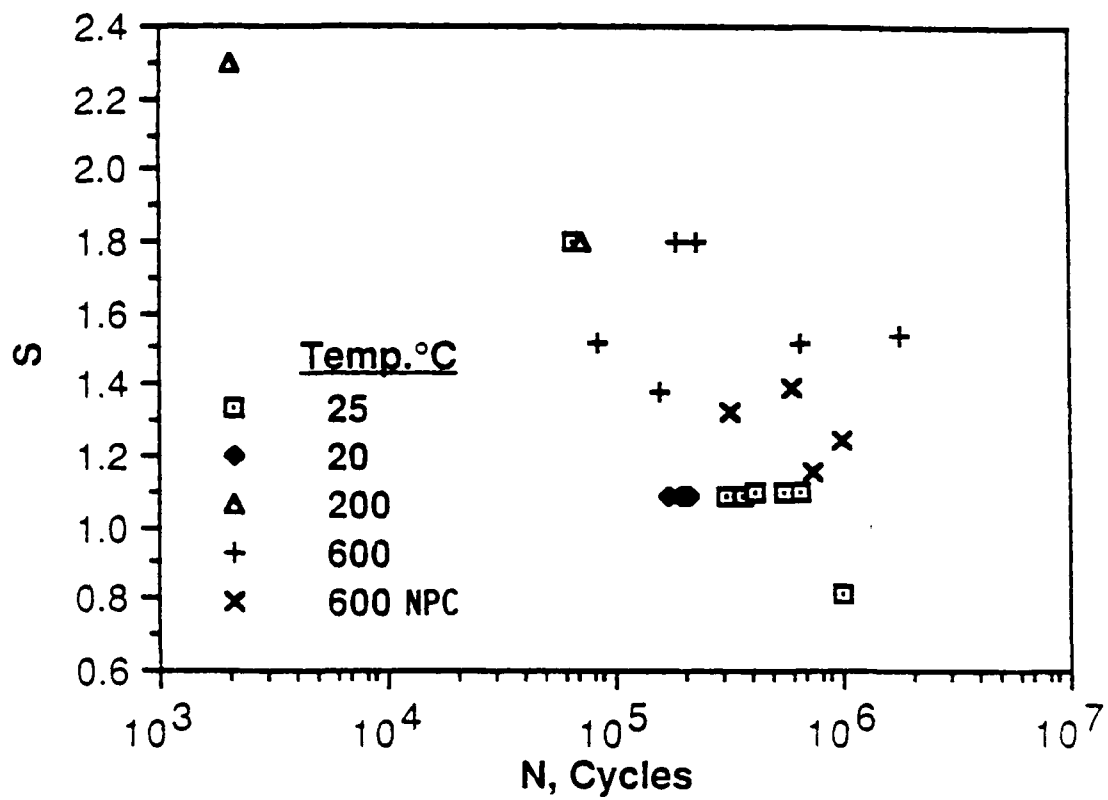


Figure 5-8. Influence of relative applied stress level ( $S = S_{max}/S_{ys}$ ) and temperature on the cyclic life of 10x10x70 mm bend specimens of CG Astroloy. (NPC = non-propagating crack)

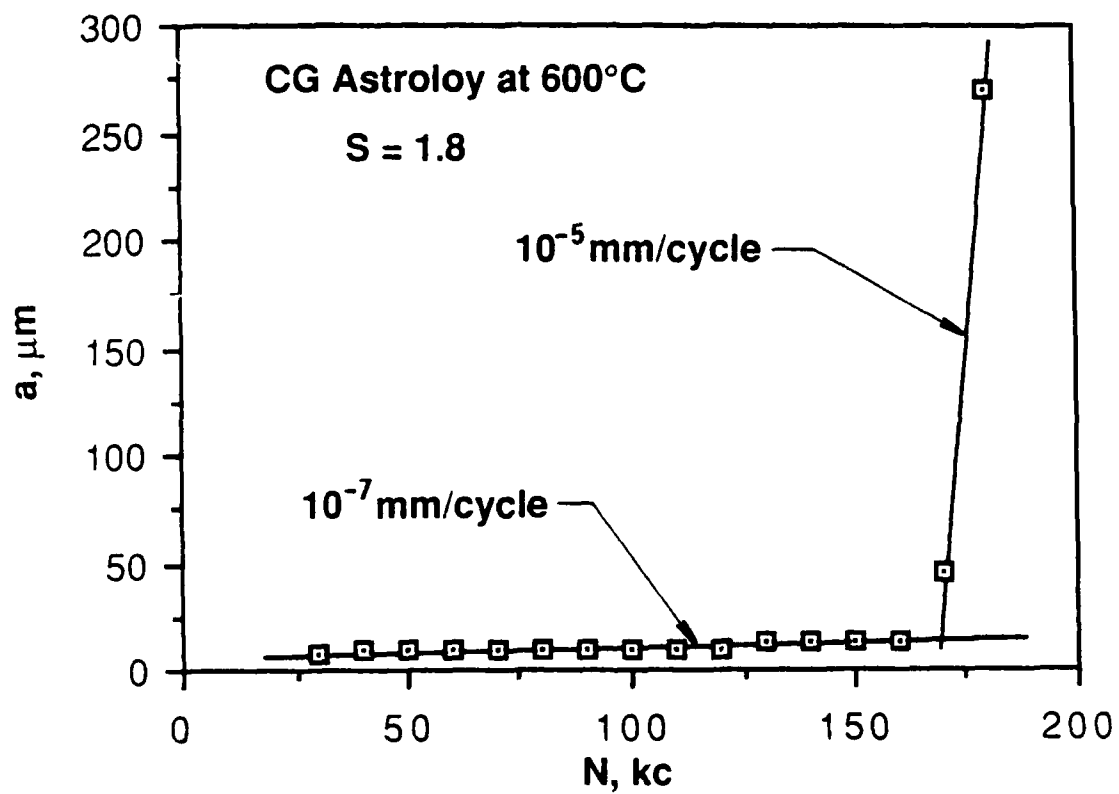


Figure 5-9. Example of erratic crack growth in Ni-base alloys at 600°C.

The cyclic lives obtained using the three-point bend specimens (Figure 5-8) are longer than those which one would expect in gas turbine discs. This difference is believed to be due to differences in the crack initiation lives between small laboratory specimens and actual components which result from: 1) differences in surface finish, and 2) a statistical size effect. As discussed in Refs. [5.8], actual components contain a variety of manufacturing defects such as dents and scratches which often serve as mechanical stresses concentrations for crack initiation. Such defects are generally not present in laboratory specimens -- for example, the specimens used in the current study were polished both mechanically and electrochemically. Furthermore, the relatively small size and mode of loading of the bend specimens resulted in a limited amount of highly stress material being sampled. Thus, the probability of this highly stressed region containing a void or other microstructural defect which would assist in the nucleation of a crack was also relatively small. Consequently, many of the cracks in the small laboratory specimens initiated at persistent slip bands in favorably oriented surface grains, rather than at material defects. The above arguments are consistent with the data in Figure 5-10 which compares cyclic lives of the three point bend specimens with those from much larger tensile specimens containing simulated bolt holes [5.9]. Note that the lives in the latter case are significantly shorter. Interestingly, the apparent fatigue limit in the bolt-hole specimen corresponds to the stress in the smooth specimen which produced non-propagating cracks (NPC) which were the size of one or two grains.

Although the precise mechanism responsible for the long periods of crack dormancy, following crack initiation, at elevated temperature is not clearly defined, several mechanisms can be postulated. Initially, the possibility of a decrease in the effective crack driving force due to oxide-induced crack closure [5.10, 5.11] was considered. However, the importance of this mechanism was subsequently discounted when the same erratic crack growth behavior occurred during experiments conducted in  $10^{-5}$  torr vacuum at 600°C, where oxidation was absent. The fractographic observations of Section 6 show that the sharpness of the crystallographic facets decrease as temperature was increased from 25°C to 600°C, thereby suggesting that multiple slip becomes

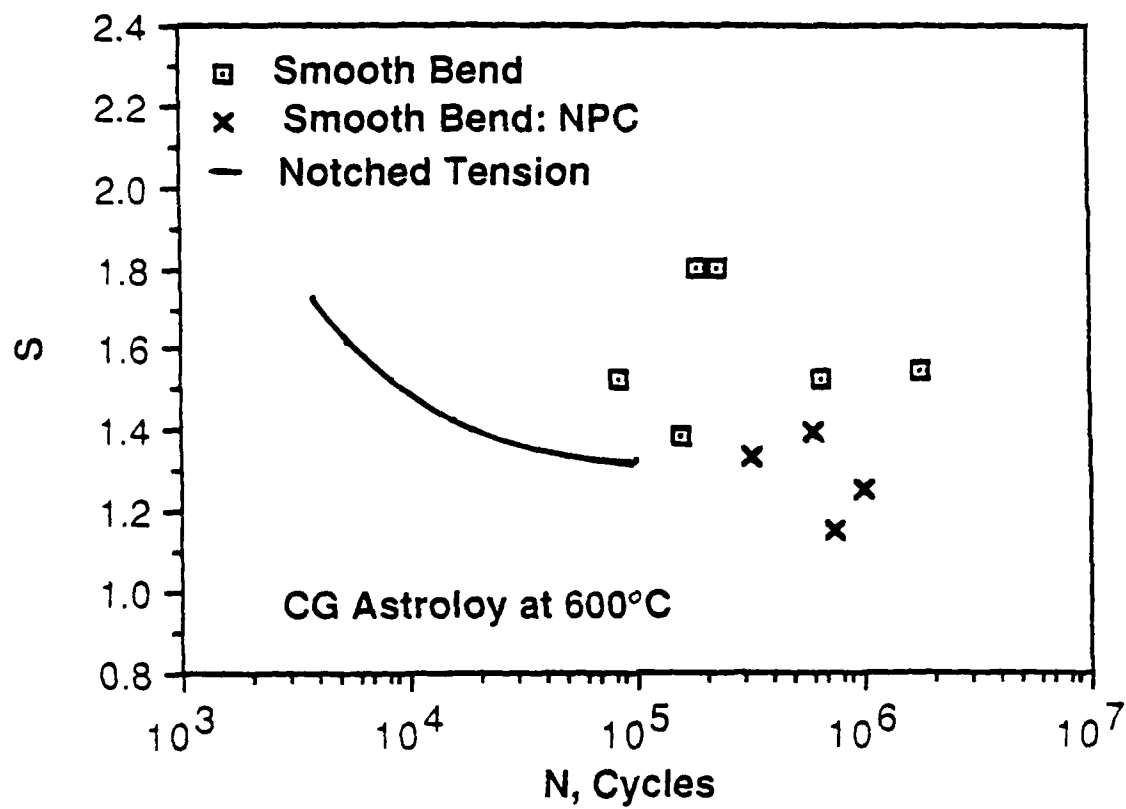


Figure 5-10. Comparison of cyclic lives of notched ( $k_t = 2.13$ ) tension specimens and smooth ( $k_t = 1$ ) bend specimens in Astroloy at 600°C. (NPC = non-propagating crack)

elevated temperature since the fracture surfaces exhibited a color gradient due to differences in oxide thickness. Results from these microscopic examinations are summarized in Figure 5-3. Although considerable scatter in the aspect ratio is evident, no consistent trend emerged with respect to alloy composition or test temperature, indicating that the nominal crack shape is controlled by specimen geometry and loading mode. Most importantly, the average aspect ratio is consistent with the assumed crack shape used in the analysis.

5-5

activated at the higher temperature. It was also observed, through periodic replication, that the dormant cracks at 600°C exhibited a time-dependent increase in the Mode I crack opening displacements. The resulting crack-tip blunting and stress relaxation which one would associate with this process is consistent with the operation of multiple slip at elevated temperature. Although details of this process remain sketchy, it would seem to be related to the difficulty encountered in growing microcracks at elevated temperature.

#### **5.5 Sources of Variability in Small Crack Growth Rates**

One of the characteristics of small cracks is their large variability in crack growth rates, relative to those which occur in long cracks. For example, variability of a factor of ten, or more, is common in small cracks, whereas for long cracks in the same growth rate regime a factor of two is typical [5.12]. For both practical and fundamental reason, it is of interest to assess whether this difference arises from basic differences in the growth mechanisms of large versus small cracks or from differences in the precision of measurement used in each case.

In order to examine the above issue, as well as validate the small crack measurement procedure used in the current study, a series of replicate experiments was performed on CG Astroloy at room temperature. Information was obtained on the specimen-to-specimen, lab-to-lab, and heat-to-heat variability, as well as the influence of crack measurement interval and data analysis procedure on the variability in small crack growth rates.

To examine the reproducibility of data from lab-to-lab several small crack experiments were conducted at both SwRI and RR using the same test procedure described in Section 5.1. As shown in Figure 5-11, there was no discernable difference between results from the two laboratories, although the variability in rates was in both cases about a factor of ten. Similar agreement is found between the current RR data and those generated previously at RR on a different heat of CG Astroloy [5.13], as indicated in Figure 5-12. For comparison, Figure 5-12 also gives the corresponding long crack data for these same two heats of Astroloy. As discussed previously the long crack data appear to be dependent on grain size, whereas the small crack data are relatively independent of grain size.



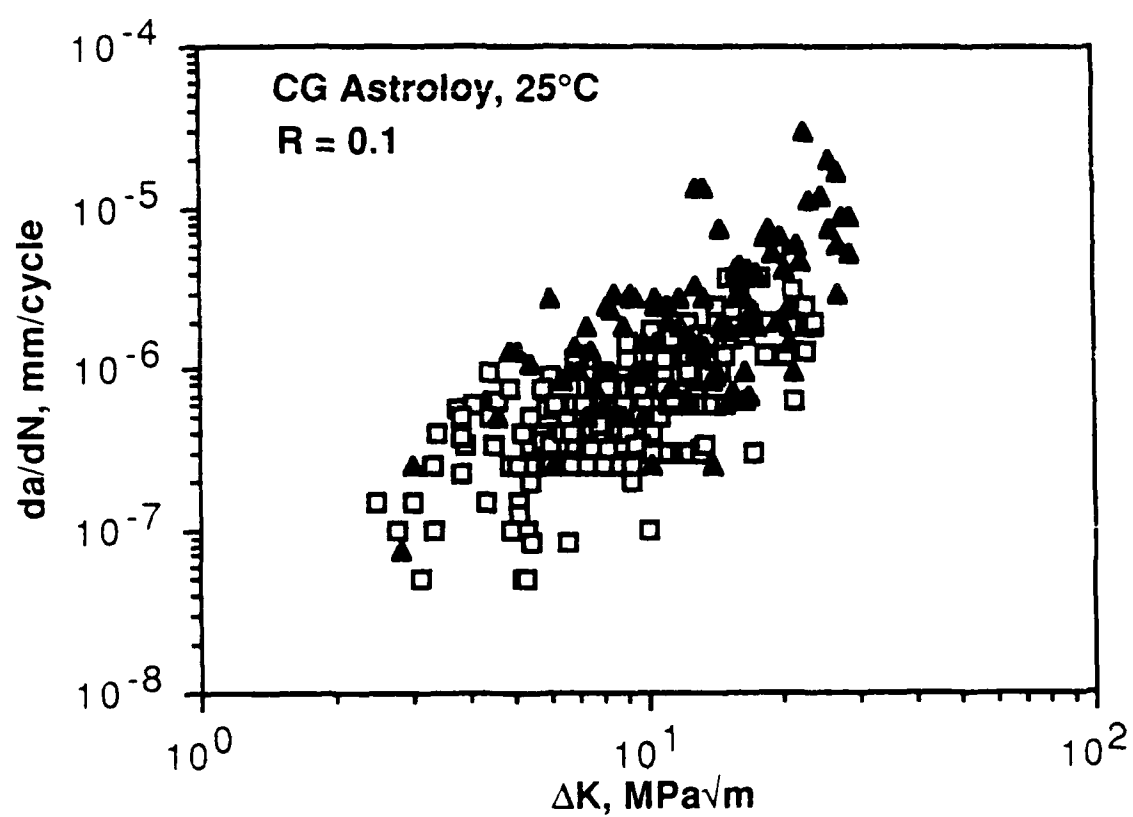


Figure 5-11. Comparison of small crack growth obtained at SwRI ( $\square$ ) and RR ( $\blacktriangle$ ).

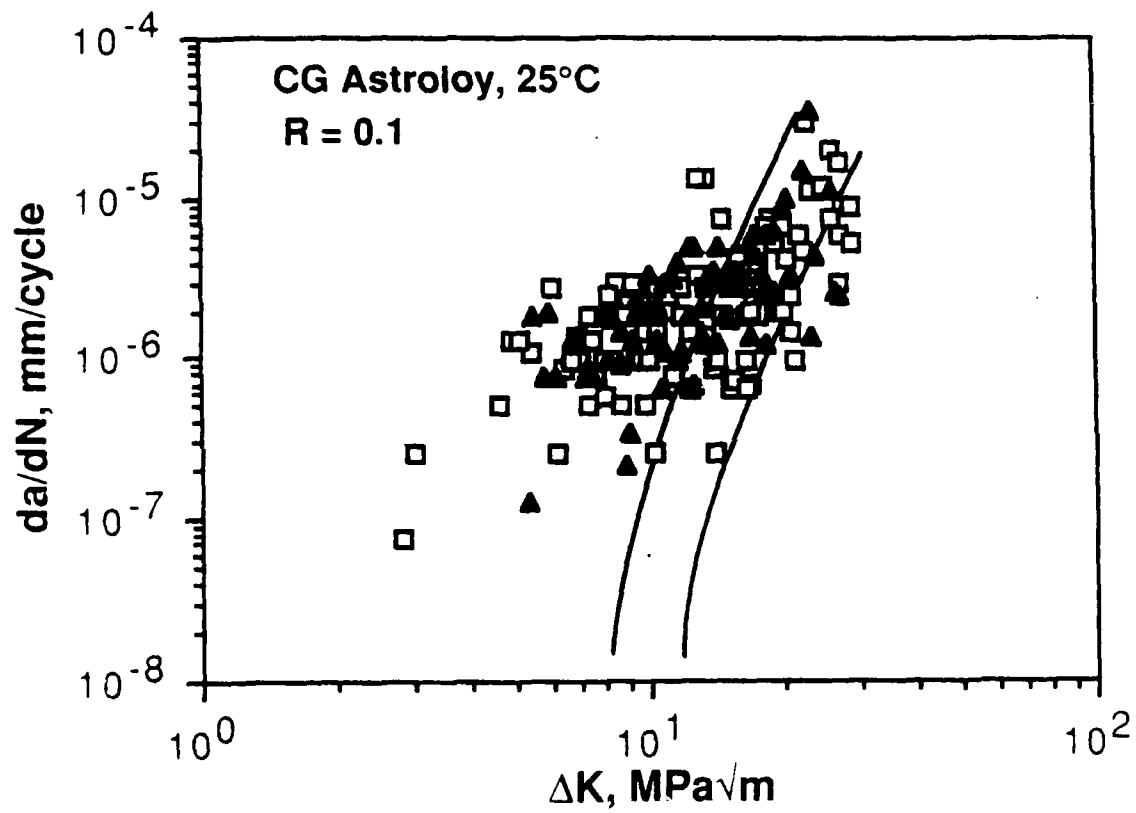


Figure 5-12. Comparison of small crack data from current heat ( $\square$ ) of Astroloy versus that from a previous heat ( $\blacktriangle$ ), Ref. [5.13].

As shown in Figure 5-13, the variability in growth rates from a single small crack is equal to that exhibited by the entire data set consisting of 7 different cracks from three replicate specimens. Thus, the observed variability in the small crack data is not due to a lack of reproducibility from specimen-to-specimen. This characteristic variability is believed to be primarily due to the incremental manner in which cracks grow and not to errors in crack length measurement. For example, cracks often appear to stop growing for tens of thousands of cycles, even when high resolution measurement techniques are used. Estimating the precision of crack length measurement with the current replication technique to be  $1\text{ }\mu\text{m}$  gives a growth rate during these apparent dormant periods of less than  $1 \times 10^{-7}$  mm/cycle.

A detailed analysis of this irregular growth was performed on three specimens of CG Astroloy tested at  $20^{\circ}\text{C}$  in order to examine the potential role of interactions between the growing crack and microstructural features. Temporary crack arrests occurred, on average, each 95,000 cycles and lasted for 20,000 to 30,000 cycles. Results from one of the three specimens which best illustrates the variety of interactions which can occur are shown in Figure 5-14. As indicated, although arrests were sometimes observed at either grain boundaries or triple points, this was not always the case. In fact, arrests only appeared to be associated with such interactions about 25 percent of the time. The present observations also showed that whether or not the crack changed crystallographic plane as it crossed the grain boundary had no bearing on the ability of the grain boundary to arrest the crack. Thus, contrary to what one might expect, the relative misorientation of adjacent grains does not appear to influence the ability of a grain boundary to arrest a small crack. The frequency with which grain boundary arrests were observed in CG Astroloy is in good agreement with recent observations at Rockwell [5.14] on Waspaloy, Figure 5-15. Interestingly, the Rockwell data show that grain boundary arrests occur more frequently as the grain size decreases. This factor may have contributed to the difficulties encountered in obtaining small crack data in FG Astroloy.

An obvious limitation of the above analysis is the fact that observations were restricted to crack growth within the surface grains. If a stronger correlation between temporary crack arrests and grain boundaries exists it would have to involve interactions among adjacent grains. In this

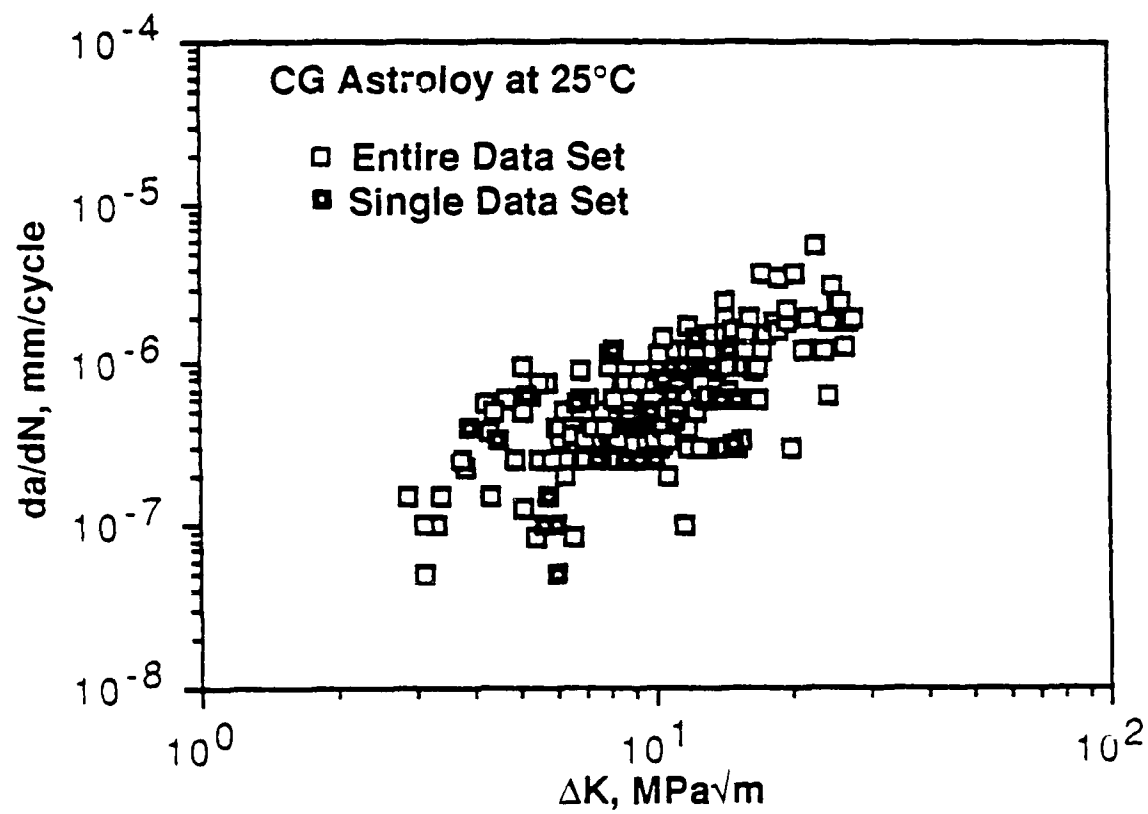


Figure 5-13. Comparison of small crack data variability from a single data set versus the entire data set for CG Astroloy at 25°C.

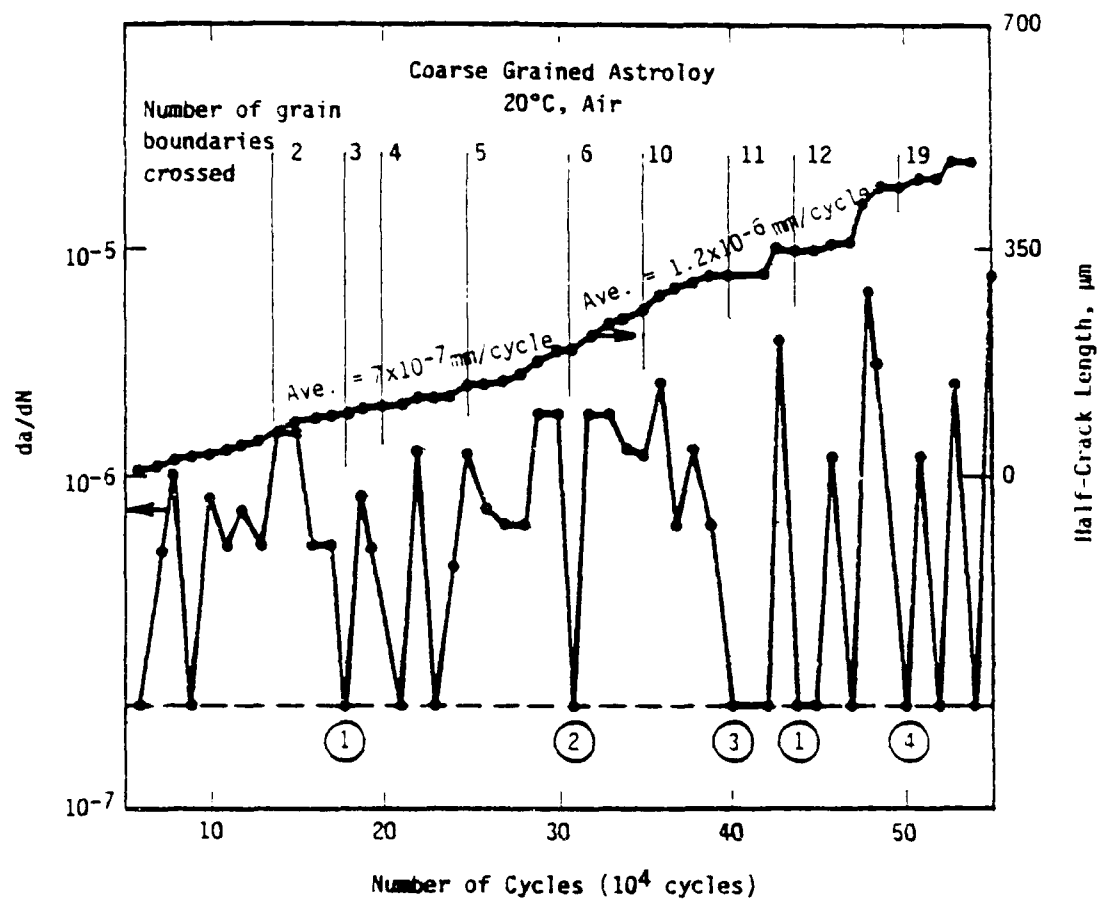


Figure 5-14. Crack length (top-curve-right scale) and crack growth rate (lower curve-left scale) for one end of a small crack in Coarse Grained Astroloy at 20°C (BF-17, Crack 18). The number of grain boundaries crossed are indicated across the top. The dashed line is the minimum value of crack growth rate detectable by the measurement technique; however, it does represent temporary crack arrest. Circled numbers indicate crack arrest at microstructural features as follows:

- ① arrest at triple point
- ② arrest at GB, with subsequent growth along another direction
- ③ arrest at GB, then growth along grain boundaries
- ④ arrest at point slightly beyond a GB

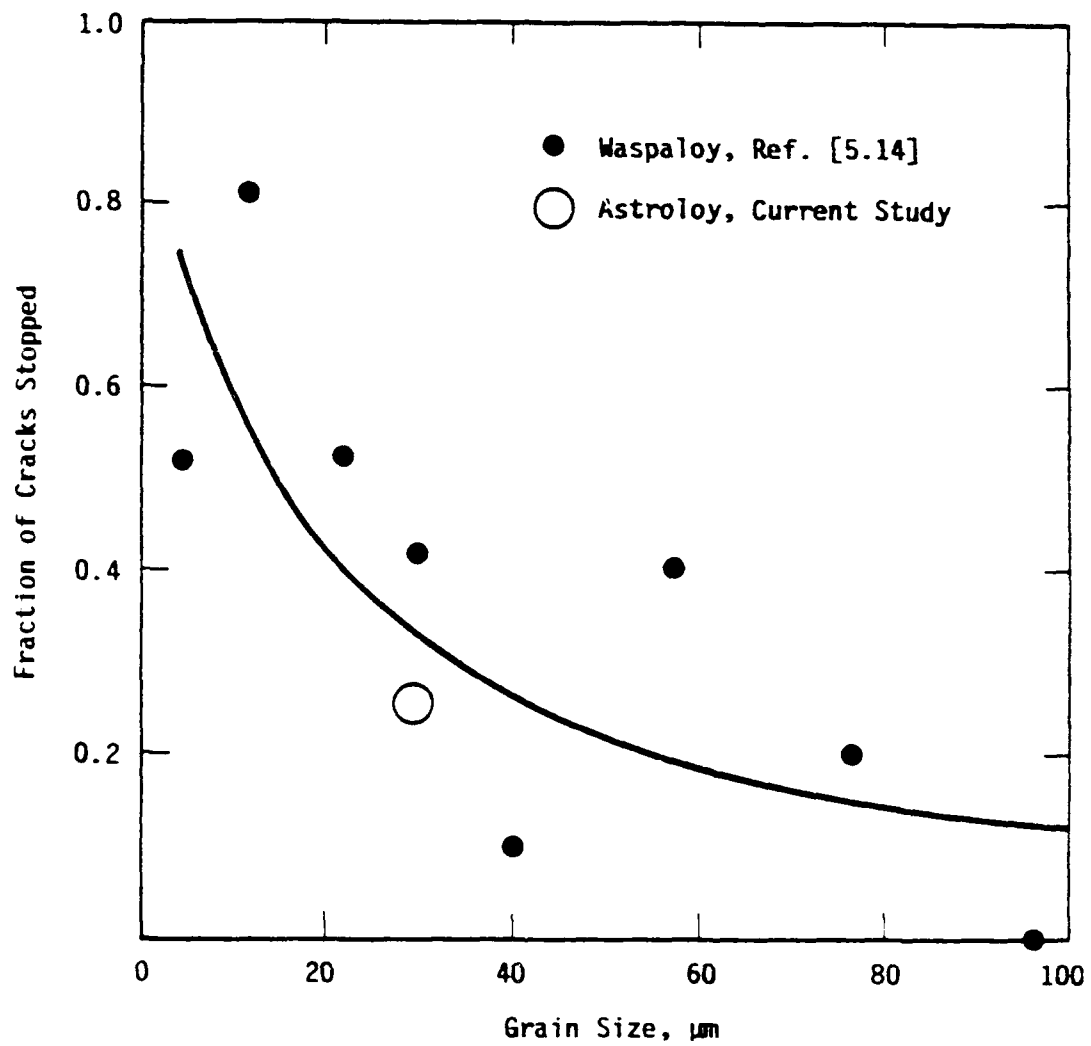


Figure 5-15. Percentage of surface crack tips stopped by grain boundaries in Waspaloy and coarse grained Astroloy at room temperature.

way arrest at a grain boundary below the surface might influence what was observed at the surface, thereby accounting for the majority of cases when arrests at the surface appeared not to be associated with a grain boundary

As one might expect, the data variability can be reduced by averaging crack growth rates over larger intervals of cycles (or crack length) as shown in Figure 5-16. Interestingly, using larger interval to analyze the data produces variability which is comparable to that obtained on large cracks in this growth rate regime. This observation, combined with the fact that large cracks exhibit this same irregular growth when observed at high resolution [5.15], suggests that the observed difference in the variability of crack growth rates between large and small cracks is due primarily to differences in the precision of measurement. Thus, it would also appear that the basic mechanism of crack extension is the same for both large and small cracks thereby supporting the view that the small crack effect is due to differences in the mechanical driving force for long and small cracks.

The possible influence of periodic test interruptions and surface replication on the the growth of small cracks was also examined by varying the sampling interval between 10,000 and 50,000 cycles. However, so as not to confound the interpretation of these results by the above mentioned influence of crack growth increment, all results were compared using data analyzed with a common cycle interval of 50,000 cycles. As shown in Figure 5-17, the frequency of test interruption and measurement had little influence on the measured growth rates. The largest deviation in rates was about a factor of two and occurred at the highest  $\Delta K$  values examined. The source of this difference in rates is not currently understood. However, if the deviation is due to the interruption of cycling (rather than to the replication process itself) the slower rates should be typical of those which occur in actual discs since these are also subjected to periodic unloadings during service.

#### **5.6 Small Versus Long Crack Growth Rates as a Function of Material, Environment, Temperature and Loading Variables**

Fatigue crack growth rates for small and long cracks, expressed as a function of  $\Delta K$ , are compared in Figures 5-18 thru 5-24 for several applied stress levels, environments, test temperatures, and material conditions. In nearly all cases, the classical small crack effect was observed -- that is,

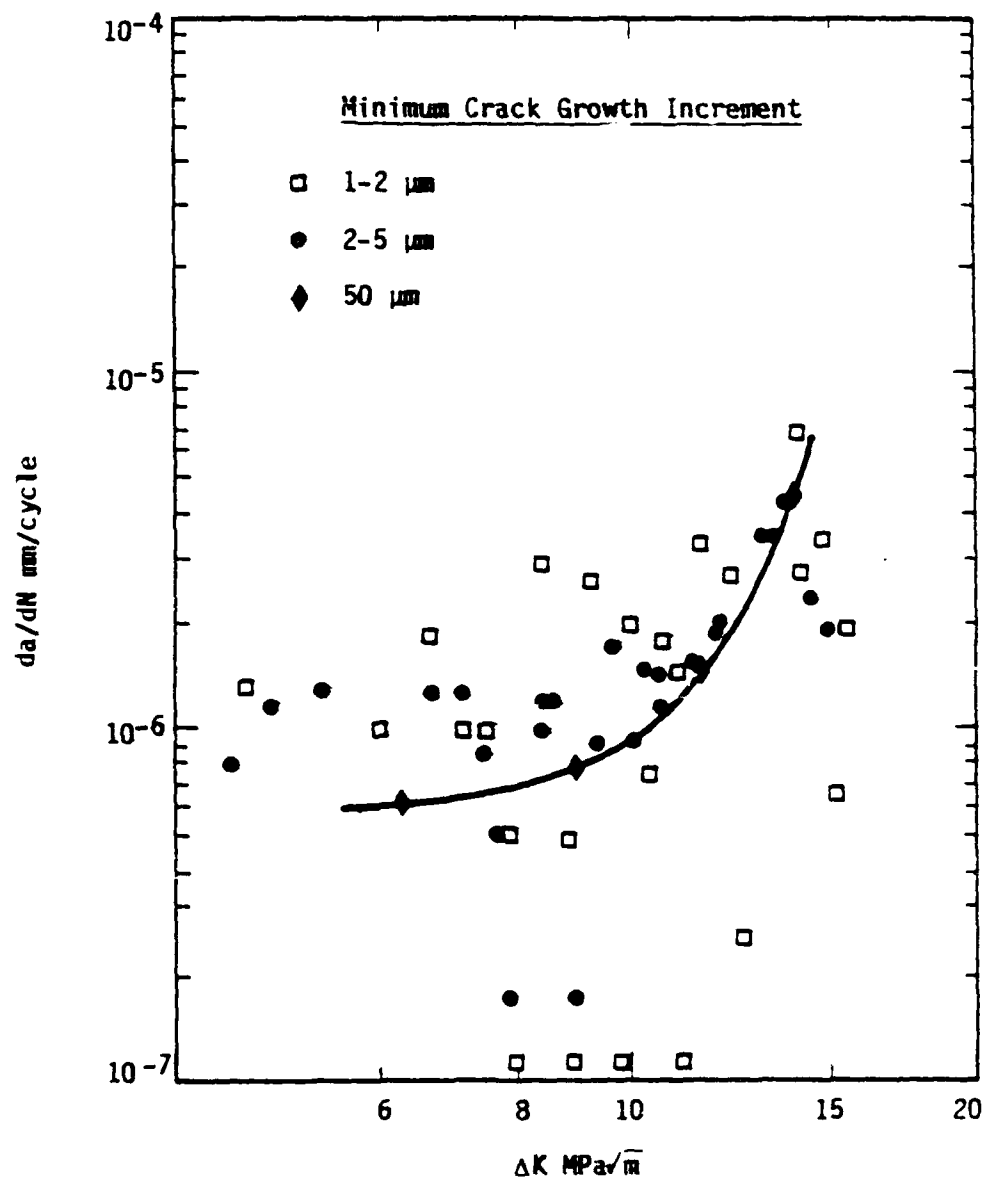


Figure 5-16. Effect of crack growth increment on computed growth rates for small cracks.



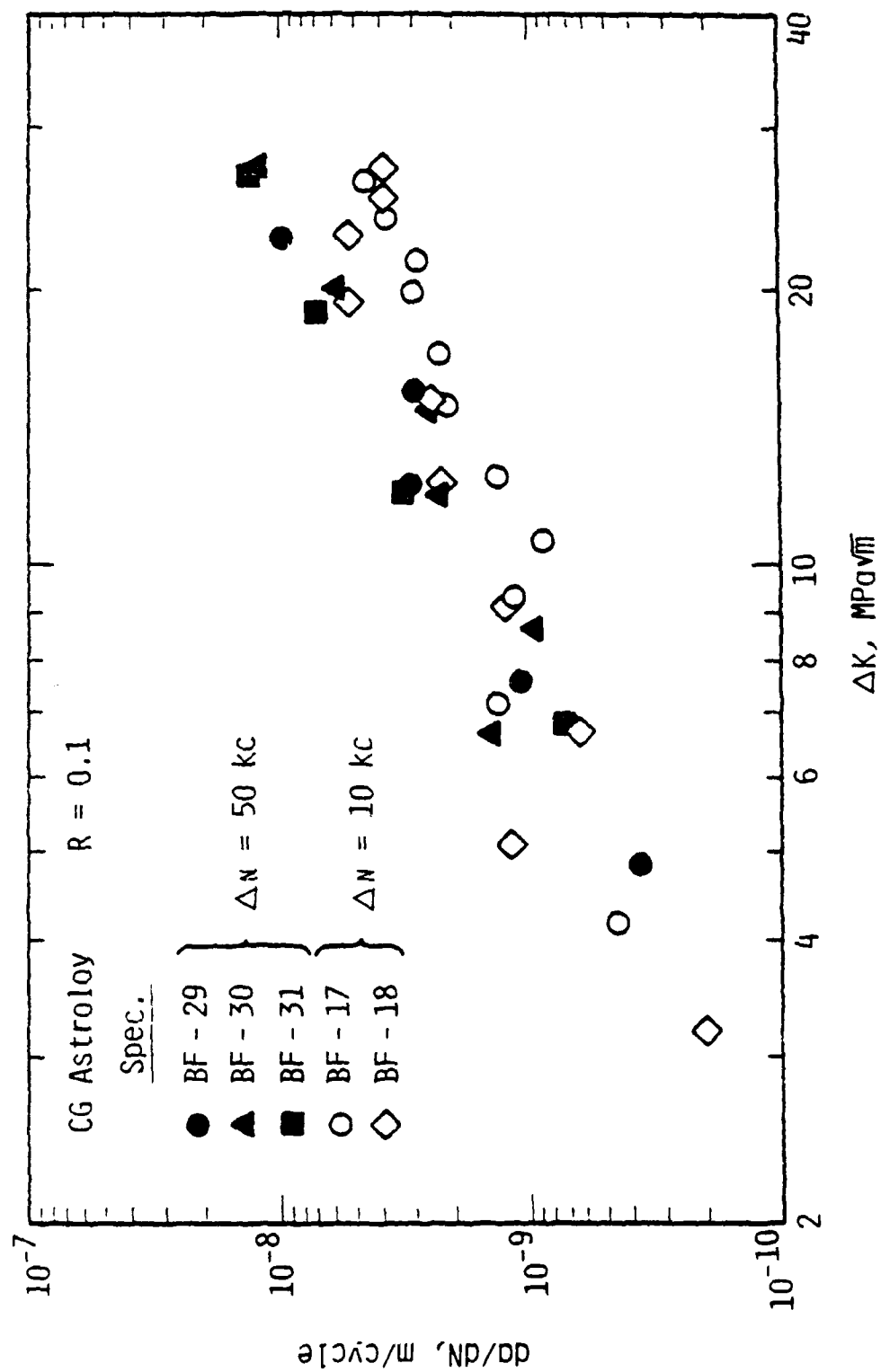


Figure 5-17. Influence of frequency of measurement and/or test interruption on the growth rates of small cracks.

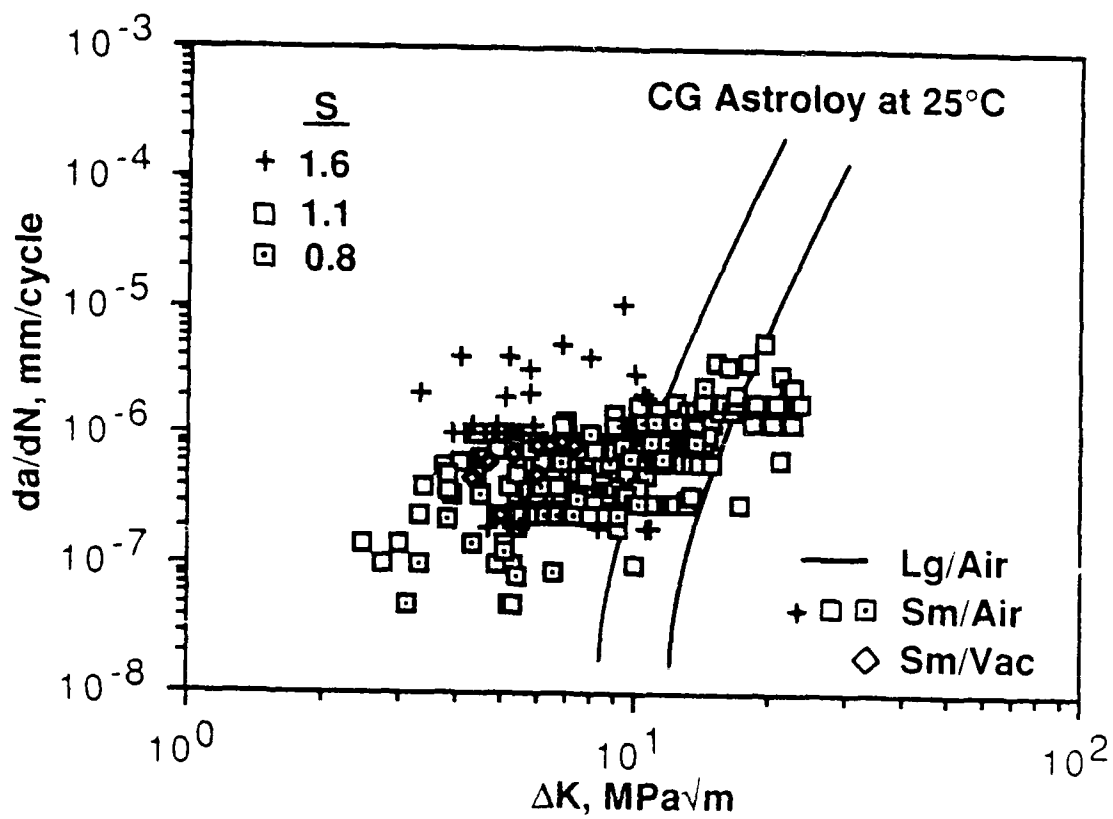


Figure 5-18. Comparison of large and small crack data in CG Astroloy at 25°C for various relative applied stress levels and environments.

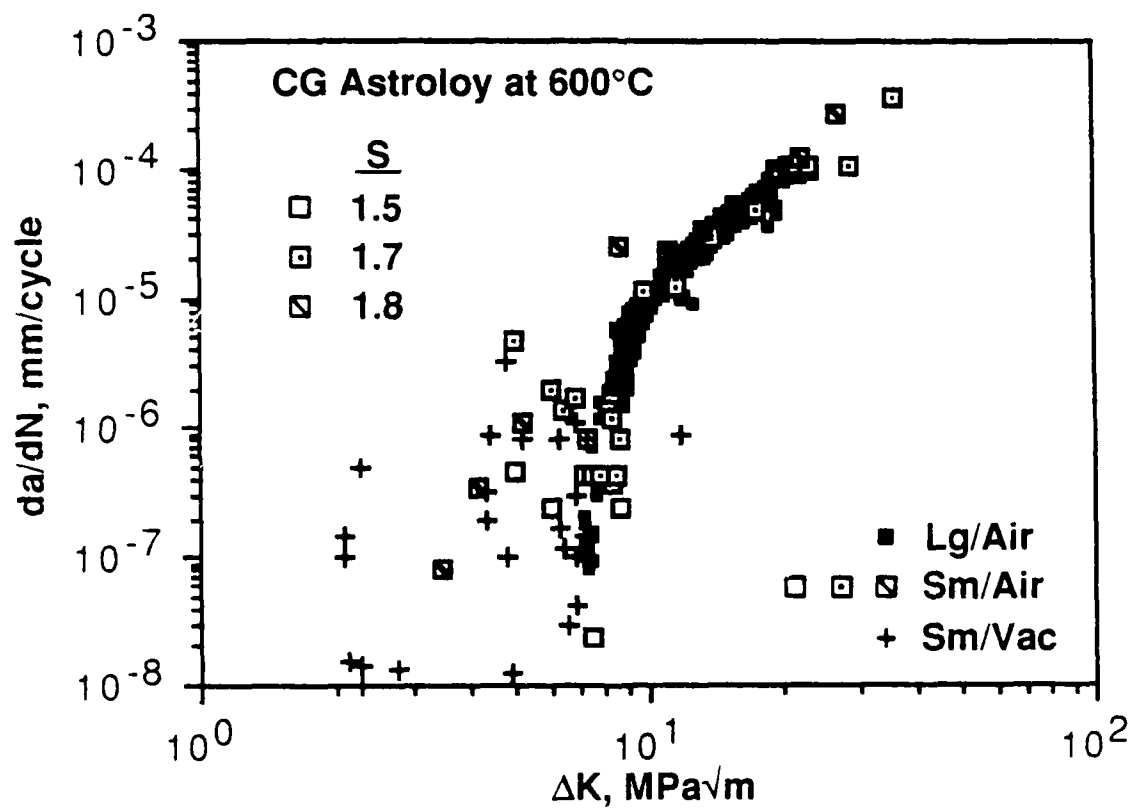


Figure 5-19. Comparison of large and small crack growth rate data in CG Astroloy at 600°C for various relative applied stress levels and environments.

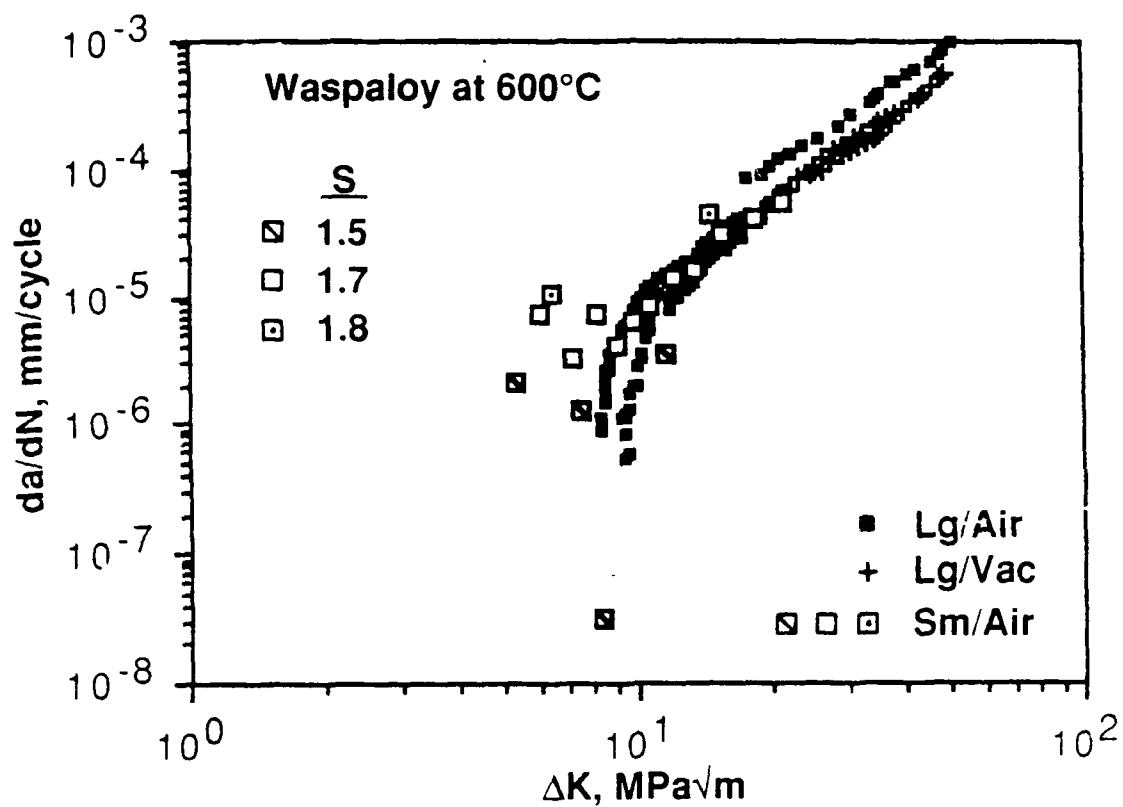


Figure 5-20. Comparison of large and small crack growth rate data in Waspaloy at 600°C for various relative applied stress levels and environments.

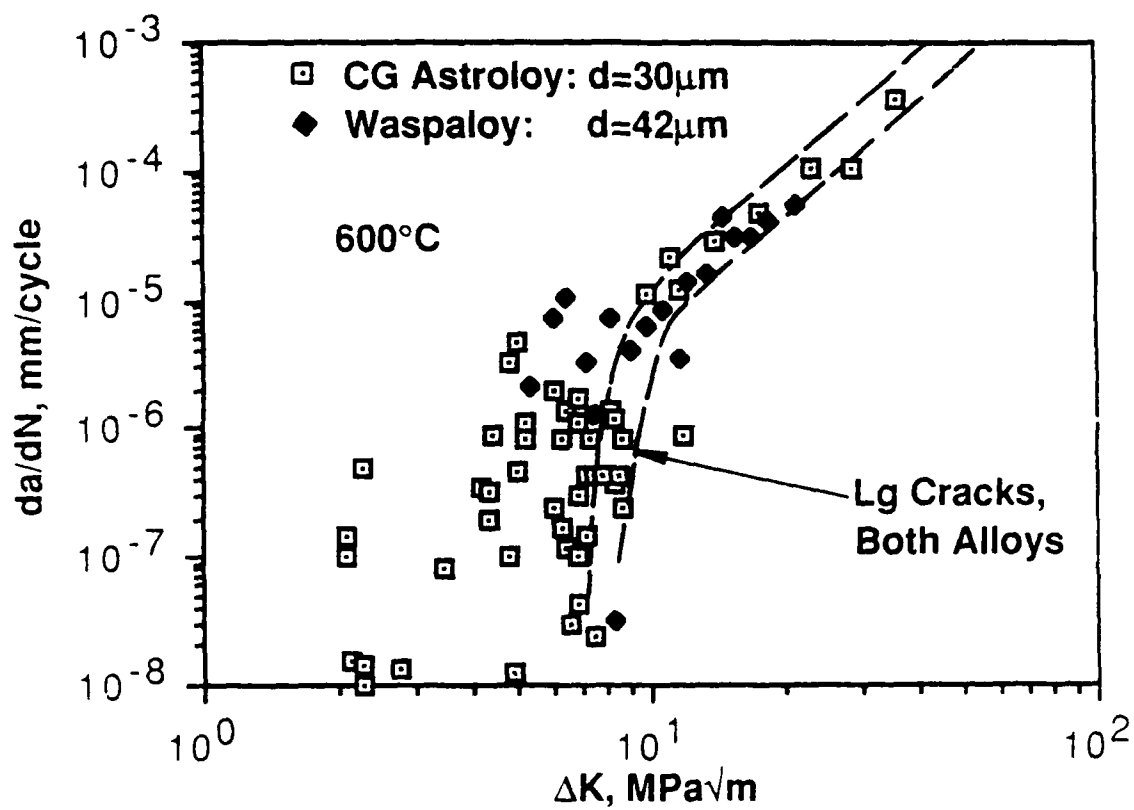


Figure 5-21. Effect of alloy composition on the crack growth rates in both small and large cracks at  $600^\circ\text{C}$ .

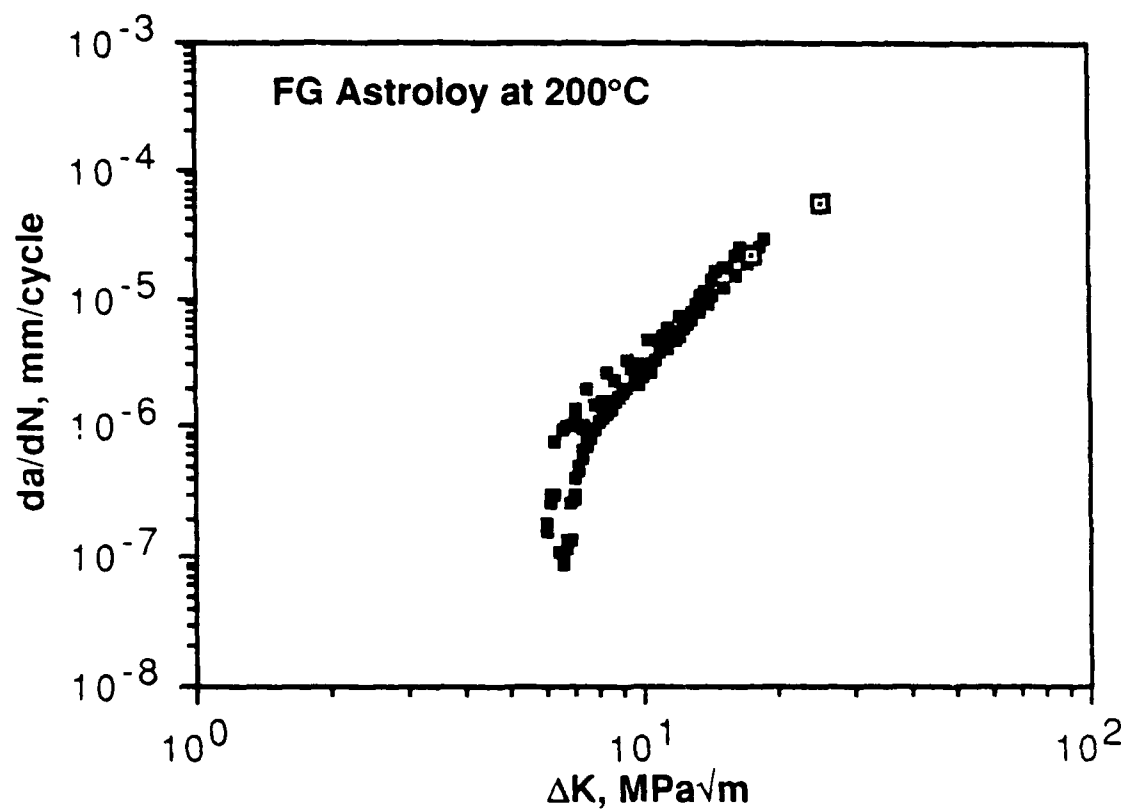


Figure 5-22. Comparison of large (■) and "small" (□,  $a = 215\text{-}1000\text{ }\mu\text{m}$ ) crack growth rates in FG Astroloy at 200°C.

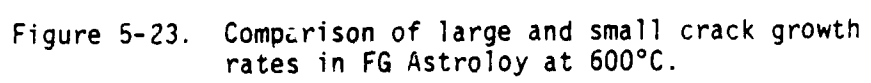


Figure 5-23. Comparison of large and small crack growth rates in FG Astroloy at 600°C.

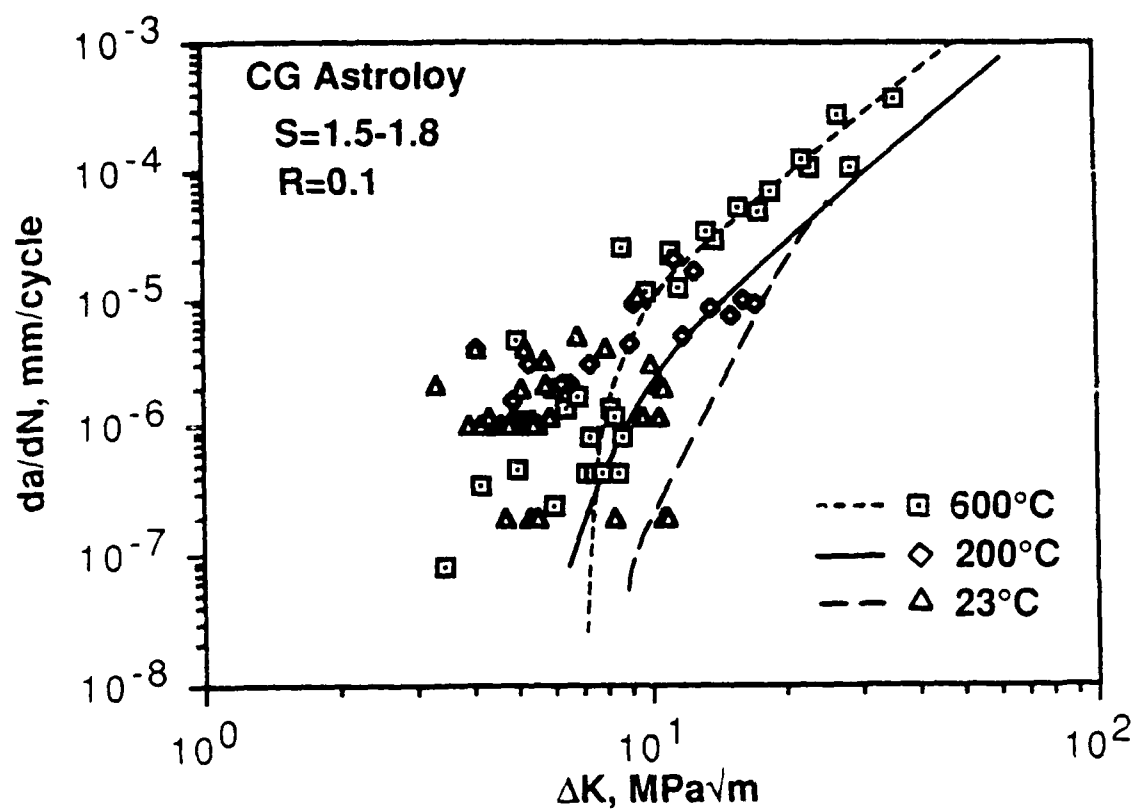


Figure 5-24. Effect of temperature on the growth rates of small (symbols) and large (lines) cracks in CG Astroloy.



small cracks exhibited faster rates than did large cracks, at a given  $\Delta K$  value, and grew at  $\Delta K$  values below the long crack threshold stress intensity,  $K_{th}$ .

#### **5.6.1 Effect of Applied Stress Level**

Figure 5-18 and Figures 5-19 and 5-20 show the influence of applied stress on the kinetics of small crack growth at temperatures of 25°C and 600°C, respectively. The applied stress level in these figures is expressed in terms of the relative stress,  $S$ , defined as the ratio of the applied stress to material yield strength ( $S_{max}/S_{ys}$ ). The CG Astroloy data at 25°C in Figure 5-18 shows that  $S$  values of 0.8 and 1.1 give similar results, while growth rates at  $S = 1.6$  are significantly faster, at a given value of  $\Delta K$ . On the other hand, as shown in Figures 5-19 and 5-20, growth rates in both CG Astroloy and Waspaloy at 600°C are relatively insensitive to  $S$  for values ranging from 1.5 to 1.8. Elevated temperature data are not available at lower  $S$  values due to the difficulty in initiating and growing cracks at 600°C, while data at higher  $S$  values were not obtained since  $S = 1.8$  was the limit for global elastic response of the bend specimens. If data were available over a wider range of  $S$  values at 600°C, results similar to those obtained at room temperature would be expected.

The above results suggests that the influence of  $S$  on small crack growth kinetics is small at low  $S$  values, larger at intermediate  $S$  values, and saturates at higher  $S$  values. The latter behavior is consistent with the alteration of the local stress state due to localized yielding at the surface of the bend specimen as described in Section 5.2. This localized yielding causes an increase in  $S$  to be counteracted by a decrease in the local mean stress (Figure 5-4) and concomitant decrease in the local stress range which is effective in opening the crack.

It is significant to point out that the dependence of the small crack growth kinetics on applied stress level suggests that  $\Delta K$  provides an inadequate characterization of the mechanical driving force for small cracks. This occurs in spite of the fact that the overall specimen response is elastic and is presumably due to the fact that the small scale yielding requirement of linear-elastic fracture mechanics also requires that the extent

of plasticity be small compared to the crack size -- a condition which is violated in most small crack experiments, as discussed in greater detail in Section 7.

#### **5.6.2 Effect of Environment**

Figures 5-18 and 5-19 also provide a comparison of small crack data obtained in two different environments -- vacuum versus air. The air data were obtained using the three-point bend specimen described in Section 5.1, while the vacuum data were obtained using the single edge notch specimen described in Section 7.1. No measurable difference in rates were observed. This fact is believed to be due the relatively high cyclic frequency of 10 Hz which was employed, thereby precluding any significant interaction with the environment, even at 600°C. This interpretation is consistent with the fact that no significant difference was observed between the growth rate of long cracks in air and vacuum tests, below  $1 \times 10^{-4}$  mm/cycle (Section 4). At higher growth rates, the long crack data obtained in air are about a factor of two faster than the vacuum data.

#### **5.6.3 Effect of Material Variables**

Figure 5-21 compares small and large crack data from CG Astroloy and Waspaloy at 600°C. The long crack data for both alloys fall within a relatively narrow scatter band. However, if one were to carefully examine these long crack results, a small difference between the two alloys actually occurs which is consistent with the influence of grain size which was discussed previously in Section 4. In contrast, no measurable difference was observed between the small crack results in the two alloys at 600°C. This observation is consistent with the room temperature results of Brown et al [5.13] on these same alloys which showed small crack results to be relatively insensitive to grain size, as well as  $\gamma'$  morphology.

Results on FG Astroloy at 200°C, Figure 5-22, show good agreement between the small surface crack data and long crack data. The lack of the crack size effect in this case is likely due to the fact that the surface crack length ( $2a = 430$  to  $2000 \mu\text{m}$ ) was always significantly larger than the  $12 \mu\text{m}$  grain size of this material. This conclusion is in agreement with the

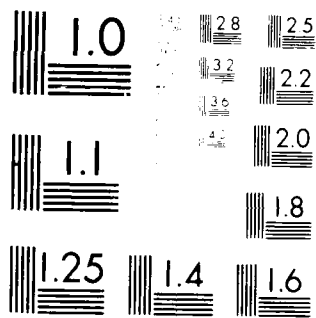
AD-A199 842 GROWTH OF SMALL CRACKS IN AEROENGINE DISC MATERIALS(U) 2/3

SOUTHWEST RESEARCH INST SAN ANTONIO TX

Y HUDAK ET AL JUN 88 AFMAL-TR-88-4890

UNCLASSIFIED F33615-85-C-5051

F/G 11/6.1 NL



MICROCOPY RESOLUTION TEST CHART  
 NATIONAL BUREAU OF STANDARDS-1963-A

room temperature data of Brown et al [5.13] which showed that a small crack effect in FG Astroloy of this same grain size was limited to cracks which were smaller than about 300  $\mu\text{m}$ .

As shown in Figure 5-23, results on FG Astroloy at 600°C also did not exhibit the classical small crack effect. Only the smallest crack sizes, corresponding to the lowest  $\Delta K$  values, exhibited rates which were faster than the long crack data. Curiously, as the surface crack enlarged the rates decreased below those of the long-thru cracks, instead of merging with the long crack data. This difference in rates is not likely to be due to the difference in environment in view of the similarity in rates observed in air versus vacuum in CG Astroloy at 600°C, Figure 5-19. The overall trend in the above results is remarkably similar to the room temperature results of Lankford et al [5.16] on PM alloy IN-100 having a grain size of 3 to 7  $\mu\text{m}$ . However, the current results appear to be inconsistent with the room temperature data of Brown et al [5.13] which showed FG Astroloy to exhibit rates which were comparable to those in CG Astroloy, both of which were significantly faster than the long crack rates. Obviously, additional experiments are needed to resolve this dicotomy in the small crack data in fine grained material. Unfortunately, these data are extremely difficult to acquire due to the small crack sizes involved and the difficulty in initiating cracks in fine grained materials.

#### 5.6.4 Effect of Temperature

Figure 5-24 summarizes the effect of temperature on the growth of small and large cracks in CG Astroloy. At room temperature, only small crack results at  $S = 1.6$  are included so as not to confound the comparison with the previously discussed effect of applied stress level. As one might expect, the large crack growth rates increase with increasing temperature over most of the  $\Delta K$  regime. The major exception to this trend occurs in the near-threshold regime where the 600°C data cross-over the 200°C data and consequently exhibits a higher  $\Delta K_{th}$  value. This cross-over of the near-threshold growth rates with increasing temperature is consistent with recent observations in other Ni-base superalloys [5.17, 5.18]. At low  $\Delta K$  values, the small crack growth rates do not exhibit a clear trend with respect to temperature. However, as the small cracks enlarge, they merge with the long crack data and

The complexity of the temperature dependence for both long and small cracks is believed to be related to changes in the character of the deformation with increasing temperature. Specifically, as indicated in Section 6.3, the change in fracture surfaces for both small and long cracks from those having highly angular facets to those which are smoother and flatter suggests that slip becomes more homogeneous with increasing temperature. These results appear to be consistent with observations made during low cycle fatigue of Ni-base alloys which shown the deformation to become more homogeneous at elevated temperature, presumably due to the thermal activation of cross-slip and climb, particularly for materials with coarse grains and fine precipitates [5.19 - 5.22]. Thus, although slip is still predominantly planar, it can apparently occur on intersecting  $\langle 111 \rangle$  planes to produce a wavy appearance. These processes are also consistent with the observed time-dependent deformation of small cracks which arrested at 600°C after growing through the first few grains (Section 5.4).

Although the above explanation of the complex temperature dependence of crack growth in these alloys is plausible, certain details of the deformation mechanism attending crack growth remain unclear. For example, as shown in Section 7, the deformation fields at small cracks are relatively homogeneous at all temperatures, thus the relation between the crystallographic nature of the crack path and the near-tip deformation field is not fundamentally understood.

In spite of this incomplete mechanistic understanding, the current results clearly demonstrate that the small crack effect is not just a low temperature phenomenon, thus it can be of potential practical importance to life prediction in aeroengine components. This issue is examined in Section 9.

## 5.7 References

- 5.1 The Application of 3-Dimensional Finite Element Methods to Fracture Mechanics and Fatigue Life Prediction, A. C. Pickard, Engineering Materials Advisory Services, Ltd., West Midlands, U.K.
- 5.2 U. S. Lindholm, K. S. Chan, S. R. Bodner, R. M. Weber, K. P. Walker and B. N. Cassenti, "Constitutive Modeling for Isotropic Materials (HOST) - Second Annual Status Report," NASA CR-174980, July 1985.

- 5.3 JoDean Morrow and G. M. Sinclair, "Cycle-Dependent Stress Relaxation," ASTM STP 237, 1958, pp. 83-109.
- 5.4 K. S. Chan and T. A. Cruse, "Stress Intensity Factors for Anisotropic Compact-Tension Specimens with Inclined Cracks," Engineering Fracture Mechanics, Vol. 23, No. 5, 1986, pp. 863-874.
- 5.5 ASTM E 647: "Standard Test Method for Constant-Load-Amplitude Fatigue Crack Growth Rate Above  $10^{-8}$  m/cycle," Annual Book of ASTM Standards, Vol. 03.01, 1986, pp. 714-736.
- 5.6 K. S. Chan, J. E. Hack, and G. R. Leverant, "Fatigue Crack Growth in MAR-M200 Single Crystals," Met. Trans., Vol. 18A, April 1987, pp. 581-591.
- 5.7 K. S. Chan and G. R. Leverant, "Elevated-Temperature Fatigue Crack Growth Behavior of MAR-M200 Single Crystals," Met. Trans., Vol. 18A, April 1987, pp. 593-602.
- 5.8 A. C. Pickard, M. A. Hicks and R. H. Jeal, "Fatigue '87 Overview Lecture: Applications of Fatigue Analyses: Aircraft Engines," in Fatigue '87, Eds. R. O. Ritchie and E. A. Starke, Jr., Engineering Materials Advisory Service, U.K., 1987.
- 5.9 Rolls-Royce, unpublished results.
- 5.10 A. T. Stewart, "The Influence of Environment and Stress Ratio on Fatigue Crack Growth at Near Threshold Stress Intensities in Low Alloy Steels," Eng. Fract. Mech., Vol. 13, 1980, pp. 463-478.
- 5.11 R. O. Ritchie, S. Suresh and C. M. Moss, "Near-Threshold Fatigue Crack Growth in 2-1/2 Cr-Mo Pressure Vessel Steel in Air and Hydrogen," J. of Engineering and Materials Technology, Trans. ASME, Series H., Vol. 102, 1980, pp. 293-299.
- 5.12 W. G. Clark and S. J. Hudak, Jr., "Variability in Fatigue Crack Growth Rate Testing," J. of Testing and Evaluation, JTEVA, Vol. 3, No. 6, 1975, pp. 454-476.
- 5.13 C. W. Brown, J. E. King and M. A. Hicks, "Effects of Microstructure on Long and Short Crack Growth in Nickel Base Superalloys," Metal Science, Vol. 18, July 1984, pp. 374-380.
- 5.14 W. J. Pardee et al, "Quantitative Nondestructive Evaluation (NDE) for Retirement-For-Cause," Rockwell International Science Center, Report No. 5C5283.16FR, Final Report on DARPA Contract No. MDA 903-80-C-0641, 1984.
- 5.15 D. L. Davidson and J. Lankford, "The Breakdown of Crack-Tip Microstructure During Fatigue Crack Extension in Aluminum Alloys," in High Strength Powder Metallurgy Aluminum Alloys, Eds. G. J. Hildeman and M. J. Koczak, TMS/AIME, 1986.

- 5.16 J. Lankford, T. S. Cook and G. P. Sheldon, "Fatigue Microcrack Growth in a Nickel-Base Superalloy," Int. J. of Fracture, Vol. 17, April 1981, pp. 143-155.
- 5.17 J. L. Yuen, P. Rox and W. D. Nix, "Effect of Oxidation Kinetics on the Near Threshold Fatigue Crack Growth Behavior of a Nickel Base Superalloy," Met. Trans., Vol. 15A, September 1984, pp. 1769-1775.
- 5.18 R. H. Van Stone and D. D. Krueger, "Closure and Near-Threshold Crack Growth in Nickel-Base Superalloys," Paper Presented at the 19th National Symposium on Fracture Mechanics, San Antonio, TX, June 1986.
- 5.19 M. Clavel, C. Levaillant and A. Pineau, "Influence of Micromechanisms of Cyclic Deformation and Elevated Temperature on Fatigue Behavior," in Creep-Fatigue Environment Interactions, Eds. R. M. Pelloux and N. S. Stoloff, TMS/AIME, Warrendale, PA, 1980, pp. 24-45.
- 5.20 R. V. Miner, J. Gayda and R. D. Maier, "Fatigue and Creep-Fatigue Deformation of Several Nickel-Base Superalloys at 650°C," Met. Trans., Vol. 13A, October 1982, pp. 1755-1765.
- 5.21 B. A. Lerch, N. Jayaraman and S. D. Antolovich, Mater. Sci. Eng., Vol. 66, 1984, pp. 151-166.
- 5.22 J. E. King, "Fatigue Crack Propagation in Nickel-Base Superalloys -- Effects of Microstructure, Load Ratio and Temperature," Mat. Sci. and Tech., Vol. 3, September 1987, pp. 750-764.



## 6.0 MECHANISMS OF SMALL CRACK INITIATION AND GROWTH

This section presents information on the basic mechanisms of fatigue crack initiation and growth in the Ni-base alloys examined in this study. Results are summarized in three parts: First the role of pre-existing pores and persistent slip bands on the initiation and early growth of small cracks is considered. Next, the orientation relationship between these cracks and the underlying crystallography within individual grains is determined. These results not only serve to elucidate the initiation process, but also provide information essential to understanding subsequent growth of small cracks since the displacement modes experienced by these cracks are controlled by their orientation within the crystallites. Finally, the morphology of the fracture surfaces are examined as a function of the primary material, loading and environmental variables studied in this program. This information proved to be particularly useful in understanding the similarities and differences in the growth mechanisms of small and long cracks, as well as the complex temperature dependence of their growth rates.

### 6.1 The Roles of Pores and Persistent Slip Bands In Crack Initiation and Early Growth

Many of our basic concepts of fatigue crack initiation and early growth of microcracks have come from mechanistic studies of model system, such as single crystals of copper or iron-silicon -- for example, see Refs. [6.1 thru 6.4]. These basic studies have emphasized the role of persistent slip bands and the subsequent formation of surface intrusions and extrusions in nucleating cracks. The primary objective of this portion of the current work was to assess whether or not this crack initiation mechanism is applicable to Ni-based superalloys. Although this effort concentrated on CG Astroloy at room temperature, general features of the observations are believed to be applicable to FG Astroloy and Waspaloy.

The experimental procedures were the same as those used to study the local deformation at microcracks (Section 7.1), with one important modification. Namely, replication was not used during the current experiments so as not to damage the extrusions, since these features are known to be fragile

loading to about 80 percent of its expected fatigue life, then observed directly within the SEM at various tilt angles.

In all cases, fatigue cracks were found to initiate within persistent slip band, occasionally these bands were formed at surface pores. Observation from eight cracks may be classified into 5 categories, each illustrated by a figure, as follows:

1. Pore initiated crack showing no extrusions or debris. A low magnification view of two fatigue cracks that initiated at adjacent pores and linked together through subsequent growth is shown in Figure 6-1(a), while Figure 6-1(b) shows a detail of a crack traversing a pore. The cubic shape of  $\gamma'$ -precipitates at the bottom of the pore suggests that the crack plane is of the  $\langle 111 \rangle$  type.
2. Pore initiated crack showing debris or tongue-like extrusions and Mode III displacements. A lower magnification view is shown in Figure 6-2(a) at a lower tilt angle, while Figure 6-2(b) is a higher magnification view at a higher tilt angle. The figure shows debris, or extrusions, coming from the corner of the pore and from a small crack nearby. Evidently, the small crack showing the more profuse and continuous extrusions initiated, but did not grow. In contrast, the larger crack evidences debris, less continuous in nature than at the small crack, at isolated locations along its length.
3. Slip band initiated cracks showing Mode III opening but no debris or extrusions. A low magnification view of the whole crack is shown in Figure 6-3(a). The direction of the loading axis is unknown for this crack, observations from similar cracks showed that they were usually at an angle of  $40-55^\circ$  to the loading axis (see Section 6.2). The white object projecting above the surface on the figure may also be seen on the left side of Figure 6-3(b) which is a view looking down the crack from a grazing angle to the surface. Note that this crack is open, similar to the cracks shown in Figures 6-1 and 6-2, and that some Mode III may be seen

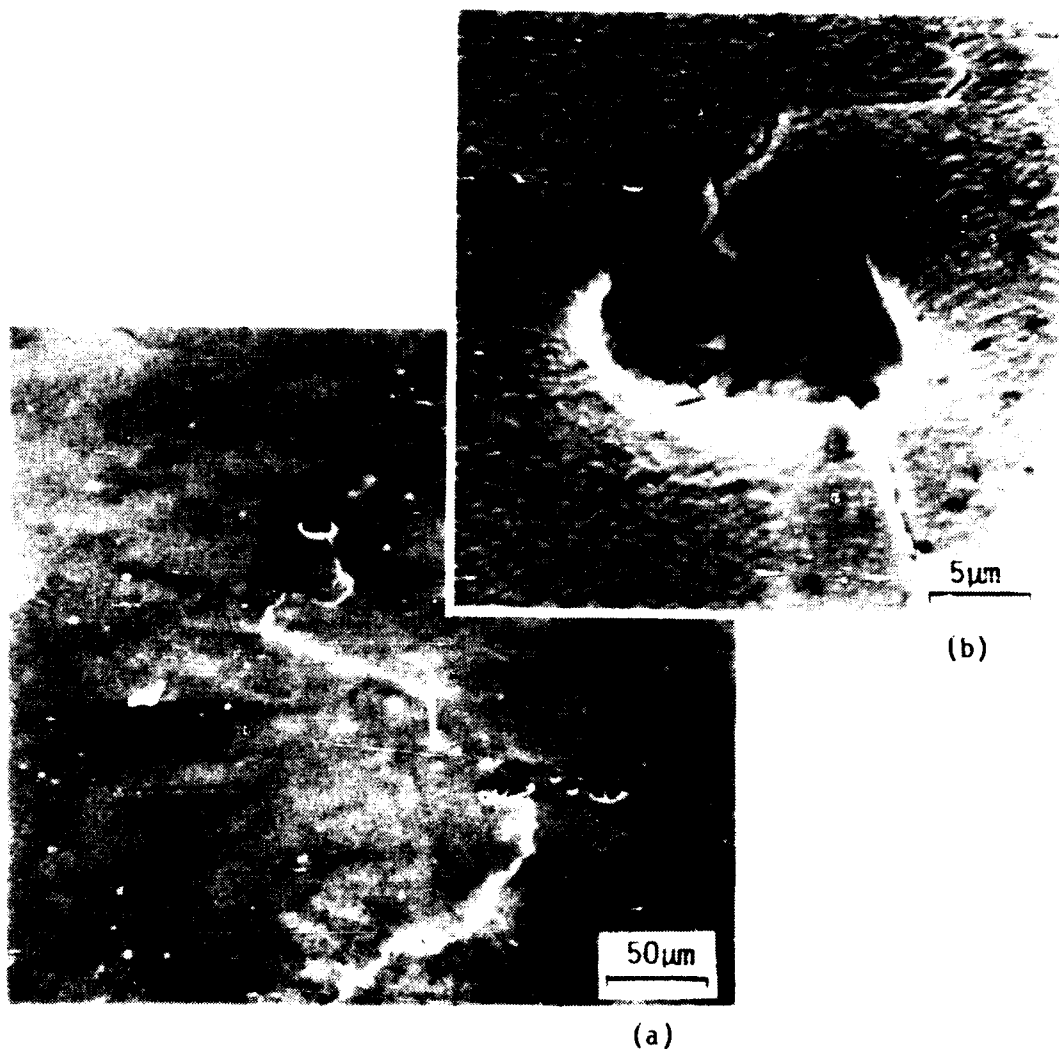


FIGURE 6-1. Fatigue crack initiation at surface pores in CG Astroloy showing (a) an overview of the crack with some debris along the lower part of the crack, and (b) a higher magnification view of one of the initiation sites.

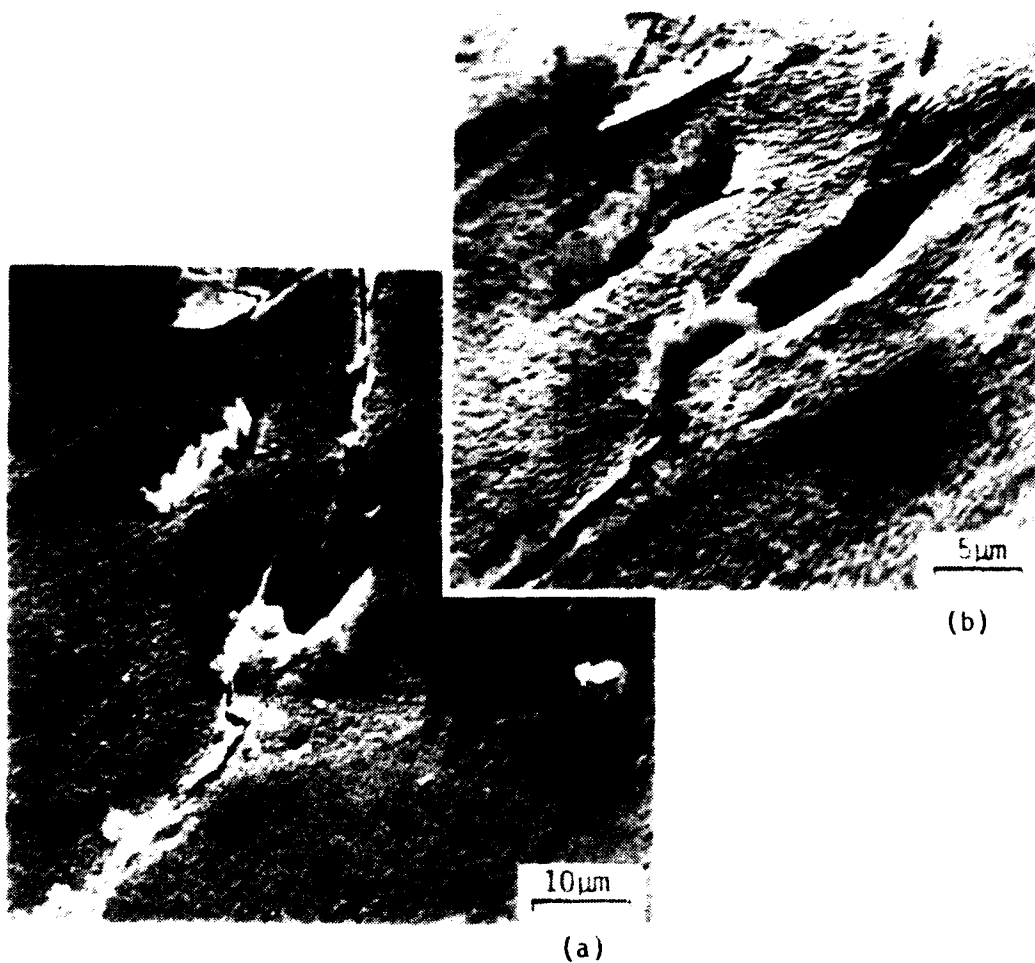


FIGURE 6-2. Two views of fatigue crack initiation at a surface pore showing debris at the corner of the pore and along the crack further away. The tilt of (a) is lower than (b), which shows better the somewhat "tongue-like" nature of the debris. Note the large amount of debris extruded from the very small crack adjacent to the main crack. This crack apparently initiated but did not grow.

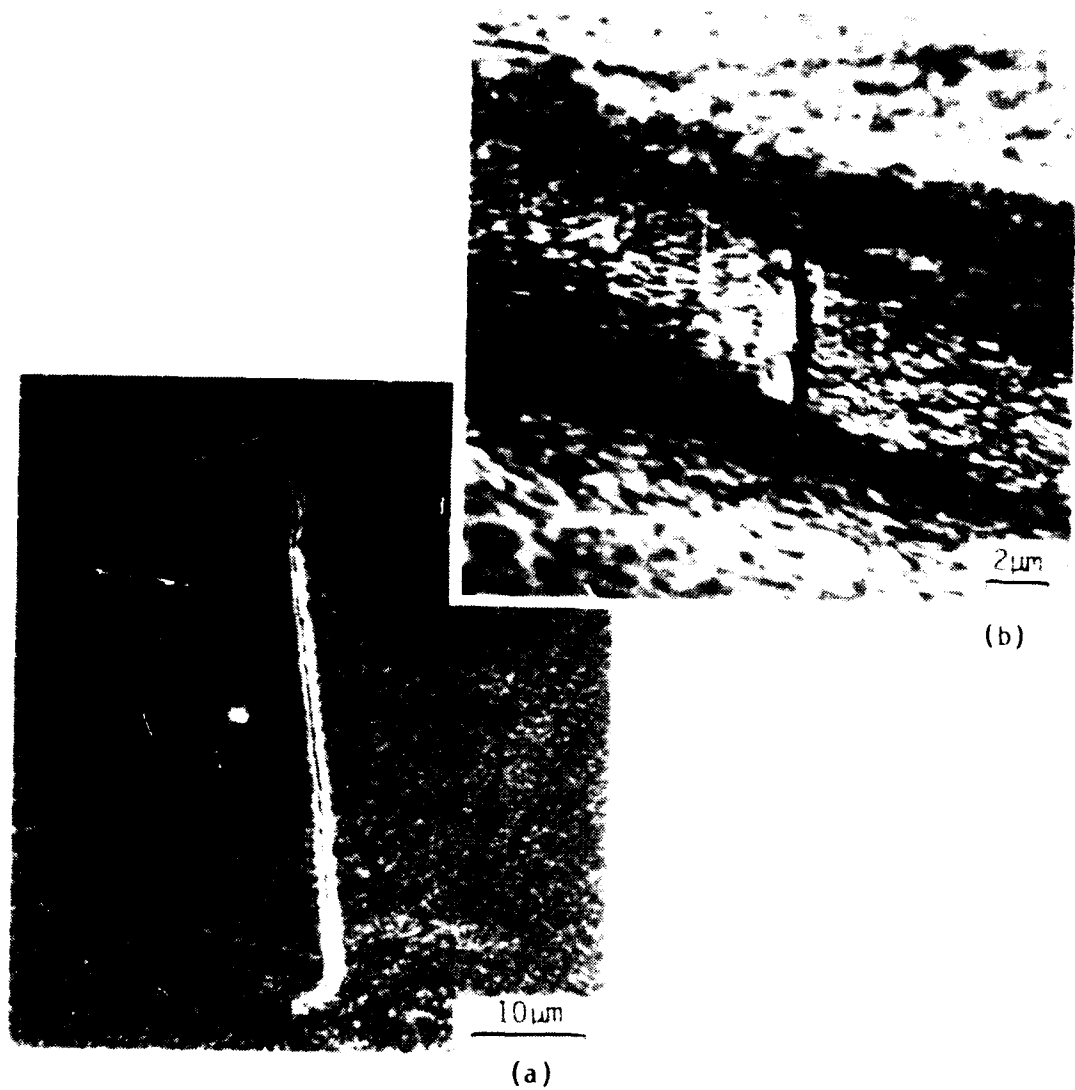


FIGURE 6-3. Fatigue crack initiated within a grain, along a slip band: (a) is an overall view of the crack showing no debris, and (b) is a grazing angle view showing Mode III displacements.

4. Slip band initiated crack showing Mode III, and having associated debris. An overall view of the crack is shown in Figure 6-4(a). The initiation site was along one of the slip bands evident in the one grain showing extensive slip. A higher magnification view of this region is shown in Figure 6-4(b), which shows the crack crossing two boundaries. At one boundary, the crack continued across the adjacent grain in the same direction, but finally changed direction drastically, continuing along the grain boundary. The other end of the crack also changed direction radically, but debris accompanied this part of the crack and nearly obscured the crack path over a short region. This debris does not have the nature of organized extrusions, which have also been termed "tongues" such as shown accompanying the small crack in Figure 6-2. Presumably the debris generated by this crack resulted from the change in direction of the crack, which caused crack face rubbing. The Mode III opening of the crack is likely to have ejected this debris from within the crack.

Figure 6-5 shows the relationship between the slip lines and the  $\gamma_2$ -precipitates. These precipitates are cube-shaped, with sides of the cube lying along  $\{100\}$ ; thus the square shapes of the precipitates indicate that the surface of observation is on or near the  $\{100\}$ . Slip lines cut across these precipitates on the diagonal, indicating slip on  $\{111\}$  which are inclined to the surface at an angle of approximately 35 degrees. Slip could be along either of the two  $\langle 110 \rangle$  Burgers vectors lying on the  $\{111\}$  and inclined to the surface at 45 degrees, or the third  $\langle 110 \rangle$  Burgers vector in the plane of the surface. The topography of the surface shown in Figure 6-5, which was also confirmed by stereophotographs, indicates that at least part of the slip was out of the plane of the surface. Therefore, some Mode III displacements very likely accompanied the crack of Figure 6-4.

5. Slip initiated cracking accompanied by tongue-like extrusions. The only crack clearly having the same type of extrusions as those reported in single crystals is shown in Figure 6-6. Photographs (a) thru (c) are shown at progressively larger amounts of tilt, each of which more

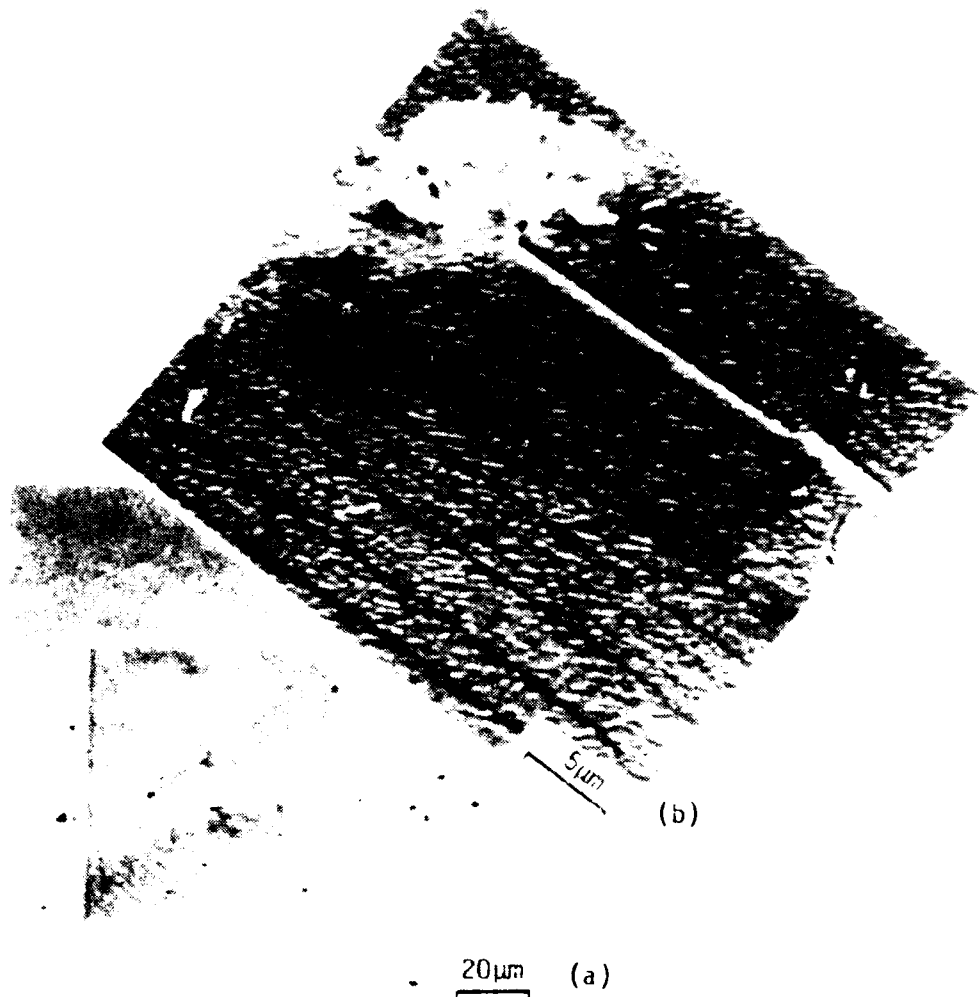


FIGURE 6-4. Slip band initiated fatigue crack showing the lack of debris in the region of initiation. The limited debris is associated with the irregular path of the crack formed on traversing one of the grain boundaries.

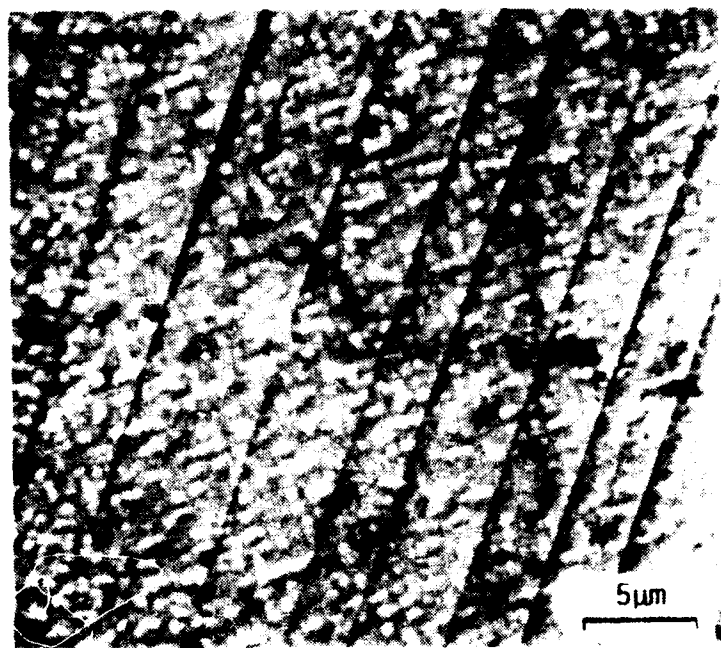


FIGURE 6-5. Relationship between the  $\gamma'$ -precipitate structure and slip lines showing that slip is of  $\langle 111 \rangle$  type and is likely to result in both in-plane and out-of-plane displacements.



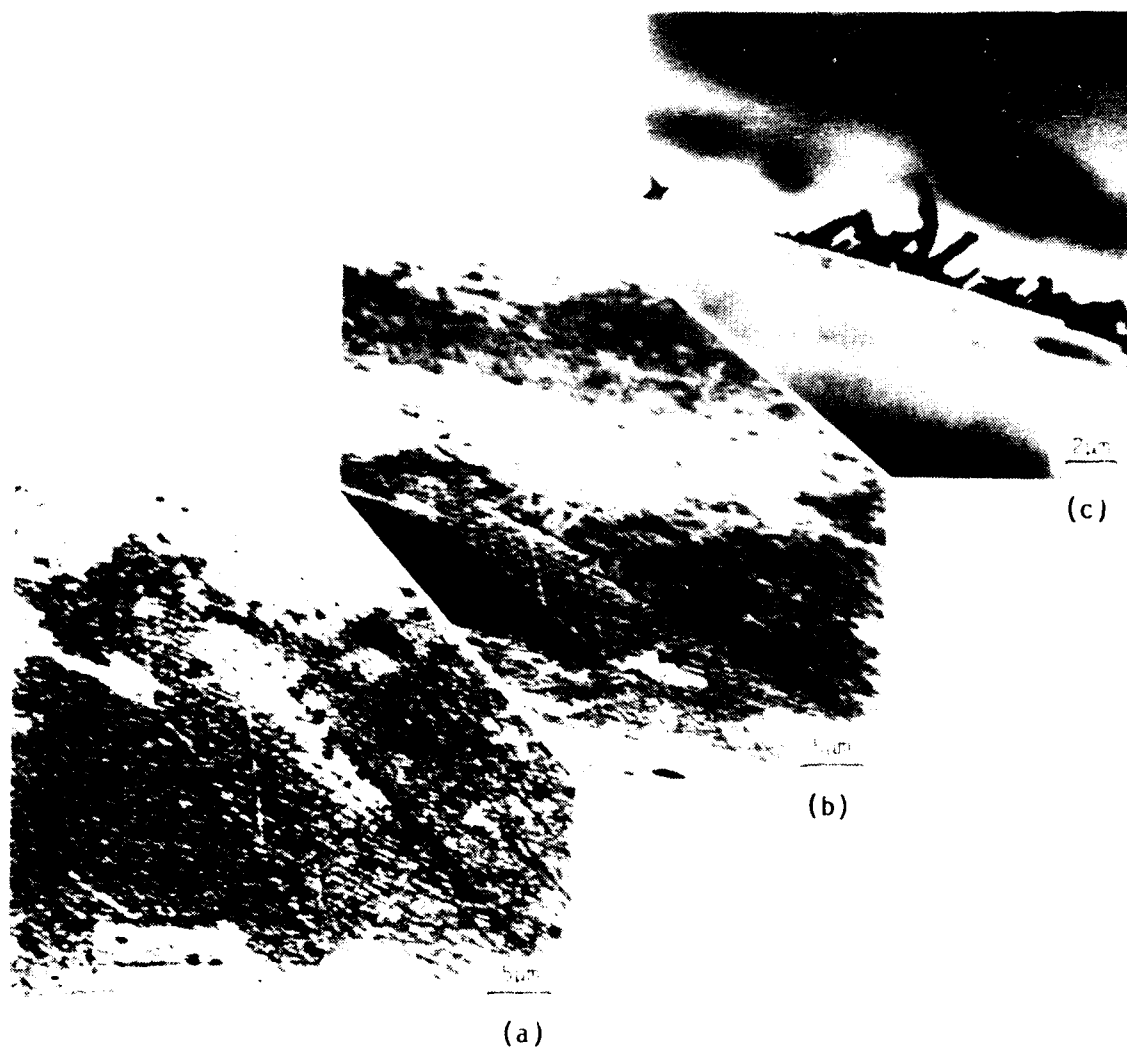


FIGURE 6-6. Three views of a slip band initiated fatigue crack showing extrusions having tongue-like shapes. These micrographs were made at a decreasing angle of incidence, with (c) being at a grazing angle to the surface. This crack appears to have initiated within a single grain at the intersection of two slip systems and shows little evidence for Mode III displacements.

Figures 6-4 and 6-5. This is believed to be partly due to the tilt used in the photographs and partly due to the fact that the surface plane of the specimen does not appear to be a low index plane, as determined from the shape of the precipitates. The grain in which this crack initiated extends from the line of blocky  $\gamma'$ -precipitates in the left-center of Figure 6-6(a) to the line of blocky  $\gamma'$ -precipitates very near the top of the photograph. Two different slip systems are evident within this grain, one near the lower left boundary, which has resulted in the slip lines pointing vertically in the photograph, and the other running approximately parallel to the crack plane at the upper right of the figure. The crack appears to have formed approximately at the intersection of these two slip systems. Although one might expect this intersection to be a twin boundary, the shapes of the precipitate particles do not support this expectation. If this were the case, it would parallel the observation of Neumann [6.4], who found cracks in single crystals of copper growing in twin boundaries which were accompanied by tongue-like extrusions.

In conclusion, it has been shown that fatigue cracks in CG Astroloy start due to slip initiated, either in favorably oriented grains, or at surface pores. For cracks initiated within grains, slip on  $\{111\}$  crystallographic planes probably occurs along several  $\langle 110 \rangle$  directions simultaneously, causing both in-plane and out-of-plane displacements. Under some circumstances, this can cause the appearance of extrusions of material having a tongue-like morphology, but such extrusions are by no means necessary for crack formation. Debris may also be extruded from small cracks at or near initiation sites, but this debris is a consequence of crack formation rather than the cause of it. Debris apparently occurs due to crack face rubbing, probably accompanied by Mode III displacements. Tongues may be considered just another form of debris, or they may be caused by some more organized mechanism, such as has been detailed by Neumann [6.4].

## **6.2 The Crystallography of Microcrack Initiation and Growth**

The primary objective of this portion of the work was to examine the orientation relationship between microcracks and the underlying crystallo-

channeling technique [6.5] was used to determine this information. The test procedure was similar to that given in Section 7.1. However, just prior to commencing the electron channeling work, the specimen was given an additional brief electropolish to remove any oxide which might have formed during the experiment; the material removed by this process was insufficient to destroy the cracked grains. Since the average grain size of this material was 30  $\mu\text{m}$  and the spot size used for making selected area electron channeling patterns (SACP) was 15  $\mu\text{m}$ , information was obtained from within individual grains. The fact that SACP could be measured meant that the dislocation density in the cracked grains was below about  $10^7/\text{sq. cm}$ . Previous estimates have shown that this dislocation density corresponds to a cumulative strain on the surface of no greater than about 10 percent [6.6]. Naturally, the localized strain within the slip band is expected to be much higher.

It was possible to obtain SACP of sufficient clarity to determine the orientation of 10 grains containing cracks. A summary of the orientations of the grain normals is shown in the stereographic triangle of Figure 6-7. This figure also shows a face centered cubic channeling map (made from a copper single crystal) which was used for orienting the SACP from Astroloy. Orientations of surface normals of grains forming cracks were grouped near  $\langle 100 \rangle$ ,  $\langle 001 \rangle$  and  $\langle 113 \rangle$ .

By knowing the angular rotation between the SEM micrograph of the cracked grain, the orientation of the SACP, and the geometric relationship of the crack to the loading axis, it was possible to derive relationships between the crack plane, loading axis, grain surface normal and slip direction. Definitions of these angular relations are shown in Figure 6-8. The associated angles derived for each of the oriented grains are given in Table 6-1, with examples shown in Figures 6-9 and 6-10. The grain shown in Figure 6-9 was chosen as an example because the crack initiated at the pore, seen as a black hole in the backscattered electron image of Figure 6-9(a). As shown in Figure 6-9(c), the orientation of that grain is near the  $\langle 110 \rangle$ . The remainder of the angular relations are shown in Figure 6-9(d). The other mode of crack initiation, that caused by slip band formation within a grain, is illustrated in Figure 6-10. Note that in both illustrations, one of the slip directions was always within 40 degrees of the surface normal, indicating that Mode III crack opening was likely.



FIGURE 6-7. Electron channeling map showing orientations of the surface normal directions for those grains which initiated cracks.

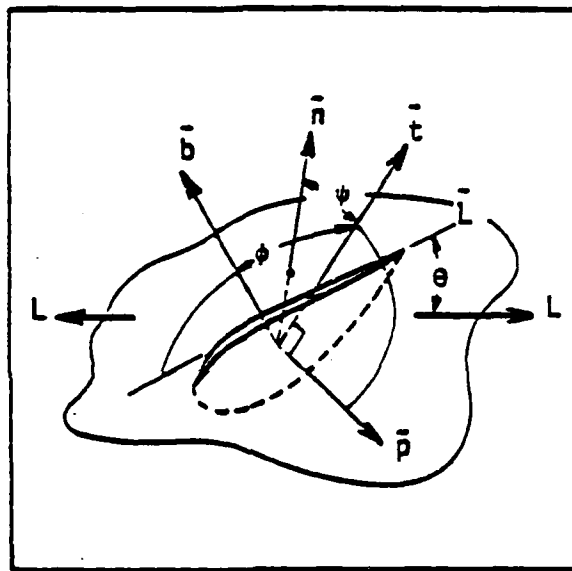


FIGURE 6-8. Definition of geometric relations between:

- $\vec{L}$  - loading direction
- $\vec{L}$  - crack direction
- $\vec{n}$  - surface normal
- $\vec{p}$  - crack plane normal
- $\vec{t}$  - crack plane tangent
- $\vec{b}$  - slip direction

plane of  $\psi$  is defined by  $\vec{n}$ ,  $\vec{t}$ ,  $\vec{p}$   
 plane of  $\phi$  is defined by  $\vec{t}$ ,  $\vec{b}$ ,  $\vec{L}$ .

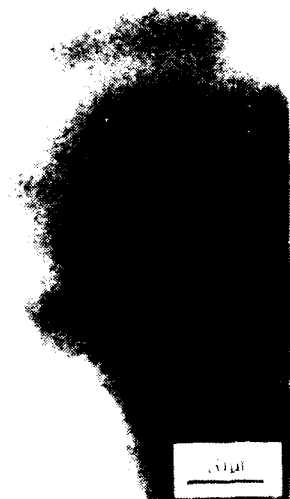
TABLE 6-1

ORIENTATION RELATIONSHIPS FOR CRACKS IN CG ASTROLOY  
(See Figure 6-8 for Definition of Orientation Parameters)

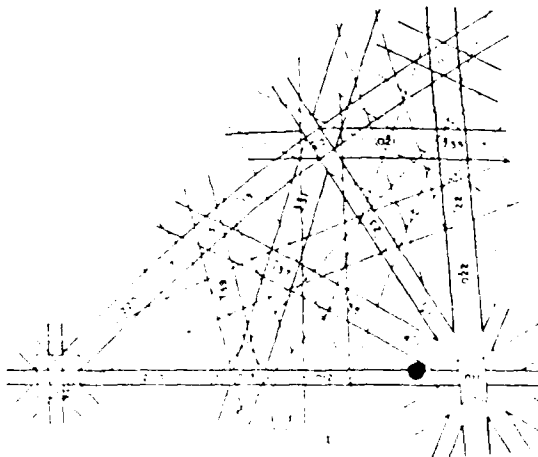
| <u>Crack<br/>Number</u> | <u>Length<br/>(<math>\mu\text{m}</math>)</u> | <u>No. Grains<br/>Crossed</u> | <u>end</u> | $\theta$<br><u><math>L-\bar{L}</math></u> | $\psi$<br><u><math>\bar{n}-\bar{t}</math></u> | $\phi$<br><u><math>\bar{t}-\bar{s}</math></u> |
|-------------------------|--|-------------------------------|------------|---|---|---|
| 4                       | 240  | 1                             | 1          | 55  | 33  | 31  |
|                         |  | 3                             | 2          | 68  | 33  | 31  |
| 5                       | 102  | 2                             | 1          | 64  | 0   | 7   |
| 7                       | 167  | 2.3                           | 1          | 48  | 6   | 31  |
| 3                       | 78   | 1.2                           | 1          | 64  | 17  | 31  |
| 6                       | 59   | 1                             | 1          | 53  | 0   | 13  |
| 8                       | 102  | 1                             | 1          | 47  | 7   | 7   |
|                         |  | 2                             | 2          | 85  | 0   | 5   |
| 10                      | 51   | 2.3                           | 1          | 43  | 9   | 6   |



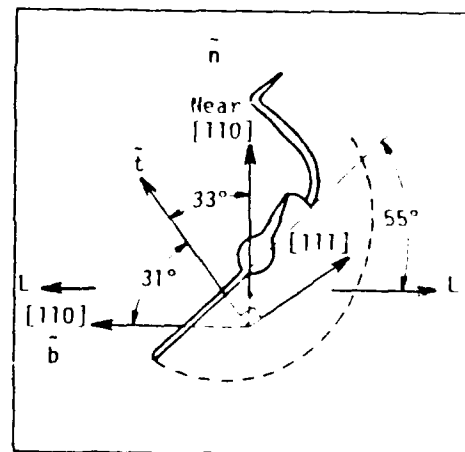
(a)



(b)



(c)



(d)

FIGURE 6-9. Determination of crack growth plane and slip direction by selected area electron channeling. (a) backscattered electron image of crack, showing grain pattern and location of the channeling pattern shown in (b). Note there is a rotation between the pattern and image which has not been shown in this illustration. (c) shows the location (large dot) of the surface normal to the grain within a stereographic triangle, and (d) is a sketch of the angular relations derived for this crack. For further definition of the vectors shown, consult Figure 6-8.

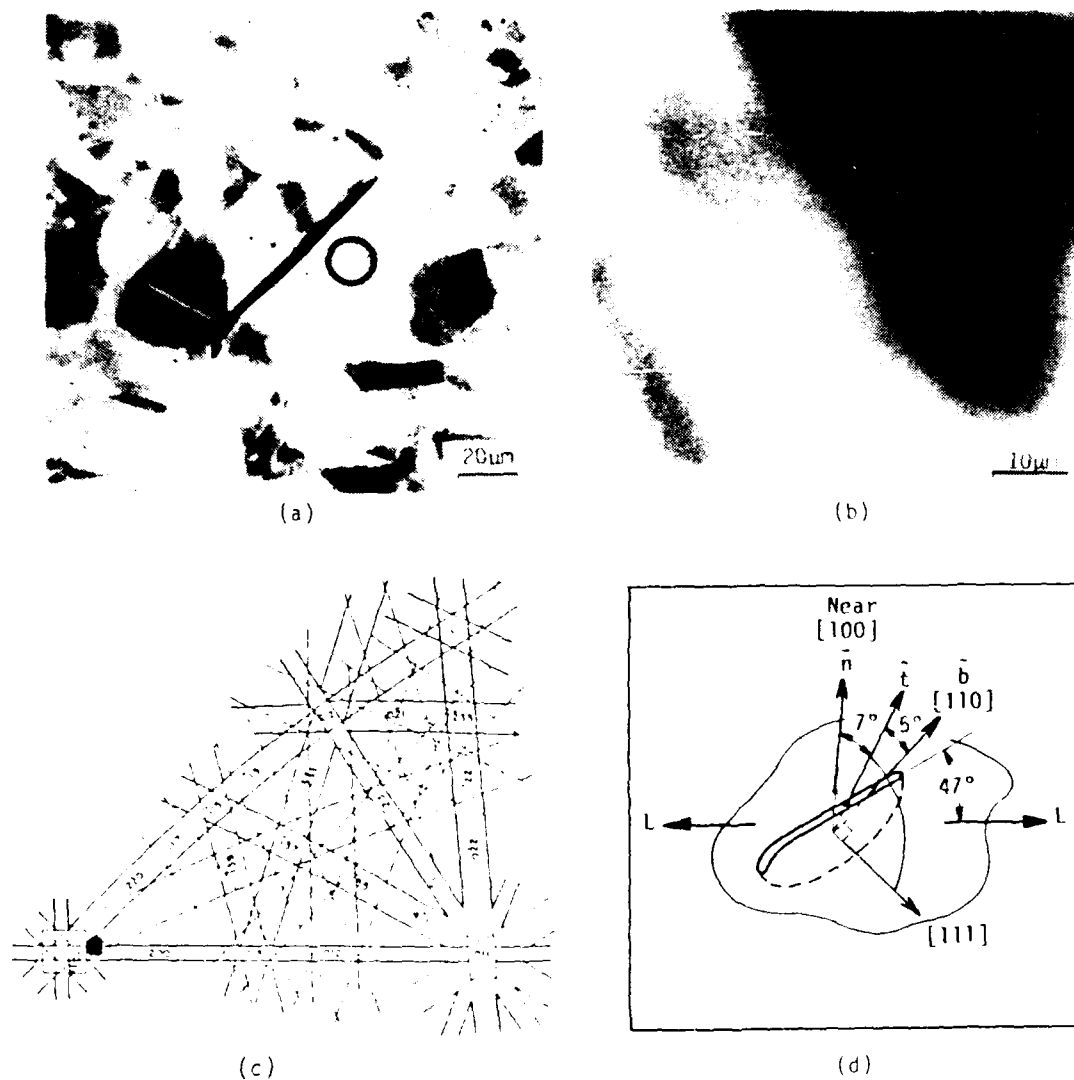


FIGURE 6-10. Determination of crack growth plane and slip direction by selected area electron channeling. (a) backscattered electron image of crack, showing grain pattern and location of the channeling pattern shown in (b). Note there is a rotation between the pattern and image which has not been shown in this illustration. (c) shows the location (large dot) of the surface normal to the grain within a stereographic triangle, and (d) is a sketch of the angular relations derived for this crack. For further definition of the vectors shown, consult Figure 6-8.



Clustering of the surface normals of grains containing fatigue cracks occurs in several regions of the standard stereographic triangle. This suggests that there are preferred grain orientations for crack initiation in Astroloy. Fatigue cracks in Astroloy were observed to initiate at slip bands in grains which do not contain pores, as well as at slip bands emanating from pores; therefore, the role of preferred grain orientation in initiation of fatigue cracks in this alloy is somewhat unclear. However, this can be examined by considering the Taylor factors of individual grains within which fatigue cracks initiated.

The appropriate value of the Taylor factor,  $M$ , for a given grain orientation can be computed on the basis of the Bishop-Hill approach [6.6, 6.7]. In particular, the Taylor factor calculations have been performed using [6.7, 6.8]:

$$M = \frac{1}{\tau d\epsilon_{yy}} [-B d\epsilon_{11} + A d\epsilon_{22} + 2 F d\epsilon_{23} + 2 G d\epsilon_{31} + 2 H d\epsilon_{12}] \quad (6-1)$$

in which  $d\epsilon_{yy}$  is the incremental plastic strain in the principal loading ( $y$ ) axis;  $A, B, F, G$ , and  $H$  represent the stress states capable of activating the same shear stress on five or more slip systems. Although Astroloy is comprised of  $\gamma'$  ( $L_{12}$  structure) in a  $\gamma$  (fcc) matrix, the predominate slip systems at room temperature are  $\{111\} \langle 110 \rangle$ , i.e., they are similar to those in cubic metals such as aluminum and copper. The number of these stress states is fifty-six for cubic metals which slip on  $\{111\} \langle 110 \rangle$  slip systems. The values of  $A, B, F, G$ , and  $H$  are given in Ref. [6.7]. The plastic strain components ( $d\epsilon_{11}$ ,  $d\epsilon_{12}$ , etc...) in Eq. (6-1) are obtained by transforming the imposed plastic strains ( $d\epsilon_{xx}$ ,  $d\epsilon_{yy}$ , and  $d\epsilon_{zz}$ ) into the cube axes (1, 2, and 3 axes) of the crystals. In this case, the loading direction is the  $y$ -axis and the  $z$ -axis is parallel to the surface normal of an individual grain. According to Bishop-Hill [6.6, 6.7], the appropriate stress state for Eq. (6-1) is the one which maximizes the external work. The value of  $M$  for a given grain orientation is therefore obtained by maximizing the right-hand side of Eq. (6-1).

Table 6-2 shows the results of the Taylor factor calculation for selected grain orientations for fcc crystals deforming by  $\{111\} \langle 110 \rangle$  slip under the plane strain condition ( $d\epsilon_{xx} = -d\epsilon_{yy}$ ,  $d\epsilon_{zz} = 0$ ). It should be noted

TABLE 6-2

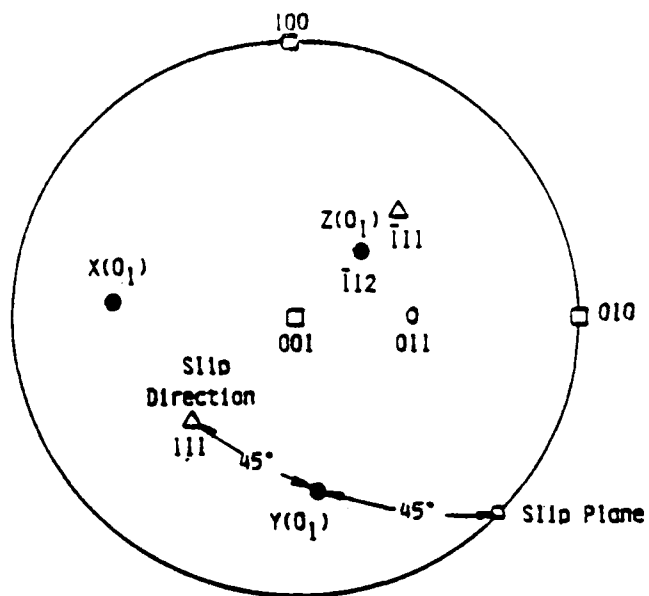
TAYLOR FACTOR CALCULATION FOR SELECTED GRAIN ORIENTATIONS UNDER PLAIN STRAIN DEFORMATION ( $d\epsilon_{zz}=0$ ). The average value of  $M$  for all possible orientations is  $M = 3.53$ .

| Orientation | X                                 | Y                                 | Z                   | M     | $M/\bar{M}$ |
|-------------|-----------------------------------|-----------------------------------|---------------------|-------|-------------|
| $0_1$       | $6^\circ$ off $[021]$             | $6^\circ$ off $[201]$             | $[\bar{1}12]$       | 2.0   | 0.565       |
| $0_2$       | $4^\circ$ off $[13\bar{3}]$       | $2^\circ$ off $[\bar{7}1\bar{1}]$ | $[011]$             | 2.258 | 0.640       |
| $0_3$       | $4^\circ$ off $[\bar{1}3\bar{3}]$ | $2^\circ$ off $[\bar{7}\bar{1}1]$ | $[011]$             | 2.258 | 0.640       |
| $0_4$       | $[001]$                           | $[010]$                           | $[001]$             | 2.449 | 0.693       |
| $0_5$       | $[1\bar{1}0]$                     | $[001]$                           | $[110]$             | 2.449 | 0.693       |
| $0_6$       | $[1\bar{1}1]$                     | $[110]$                           | $[\bar{1}12]$       | 4.082 | 1.155       |
| $0_7$       | $[\bar{1}12]$                     | $[1\bar{1}1]$                     | $[\bar{1}\bar{1}1]$ | 3.674 | 1.040       |
| $0_8$       | $[1\bar{1}0]$                     | $[110]$                           | $[001]$             | 4.899 | 1.386       |
| $0_9$       | $[1\bar{1}2]$                     | $[110]$                           | $[1\bar{1}\bar{1}]$ | 3.266 | 0.924       |

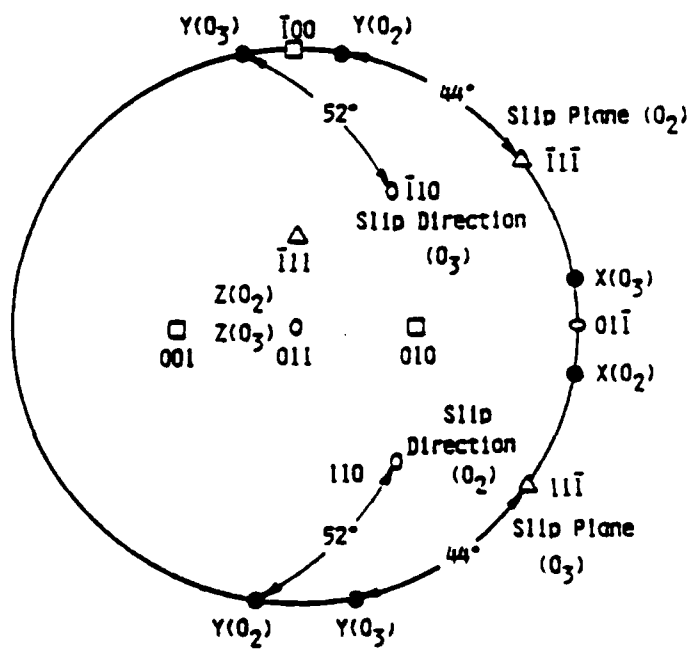
that the Taylor factors for some of the orientations in Table 6-2 were previously reported by Chin et al [6.8]. The present results are identical to those reported by Chin et al. Also included in Table 6-2 are some of the "weakest" orientations ( $O_1$ ,  $O_2$ , and  $O_3$ ) which result in low  $M$  values. The lowest possible value for  $M$  is 2, and it is observed in the grain orientation  $O_1$ . The  $M$  values for orientations  $O_2$  (and  $O_3$ ) and the  $[001]$  orientation are 2.26 and 2.45, respectively. These "weakest" orientations, summarized in the standard stereographic projection shown in Figure 6-11, are unique because the plane strain condition can be satisfied by activating the highest stressed slip system only. The predicted "weakest" orientations are compared in Figure 6-12 with the orientations of grains within which small cracks were initiated. The results indicate that most of the observed orientations are within 5 degrees of the "weakest" orientations; the worst cases are within 10 degrees.

A conclusion which can be drawn from the results shown in Figure 6-12 is that slip in coarse-grained Astroloy, and thus fatigue cracks, tends to initiate within grains having the "weakest" orientations. This seems to be true for slip initiating from pores or within the grains. This behavior can be easily understood since in the present experiments the applied maximum stress was above the proportional limit, but below the macroscopic cyclic yield stress ( $S = 0.8$ ), thus only grains with low Taylor factors can exceed the critical resolved shear stress required to activate slip. Once nucleated within slip bands, small fatigue cracks propagate in a microplastic field since they are entirely embedded within slip bands which extend across individual grains. Fatigue crack propagation can cease (either permanently or temporary) or continue as the microcracks approach the grain boundaries, depending on whether or not the crack tip can propagate slip onto contiguous grains.

In order to gain insight into the effect of statistical variation of the yield strength of individual grains on crack initiation, Taylor factors were computed for grains whose orientations were selected randomly. The number of grains was varied from one to twenty, and each calculation was repeated for fifty sets of randomly selected grain orientations. Results of  $M$  values normalized by the average  $M$  value,  $\bar{M}$ , for all possible orientations, shown as a function of number of grains in Figure 6-13, indicate that a large statistical



(a)



(b)

FIGURE 6-11. Orientations of low Taylor factor for fcc crystals deforming by  $\{111\} \langle 110 \rangle$  slip: (a)  $M=2$ , and (b)  $M=2.46$ . For

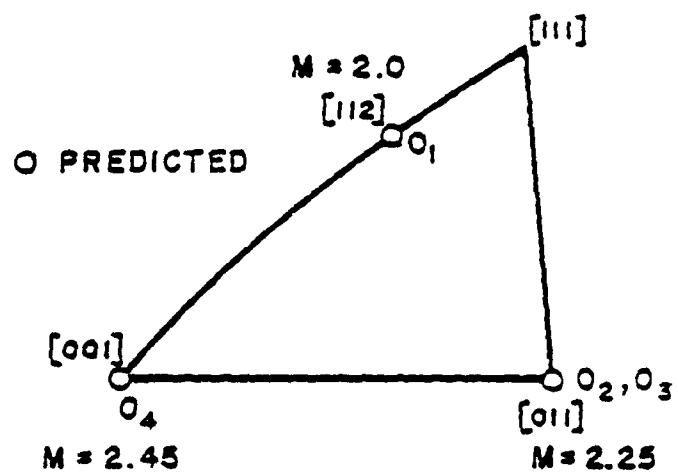


FIGURE 6-12. Standard stereographic triangle showing orientations with low Taylor factor values.

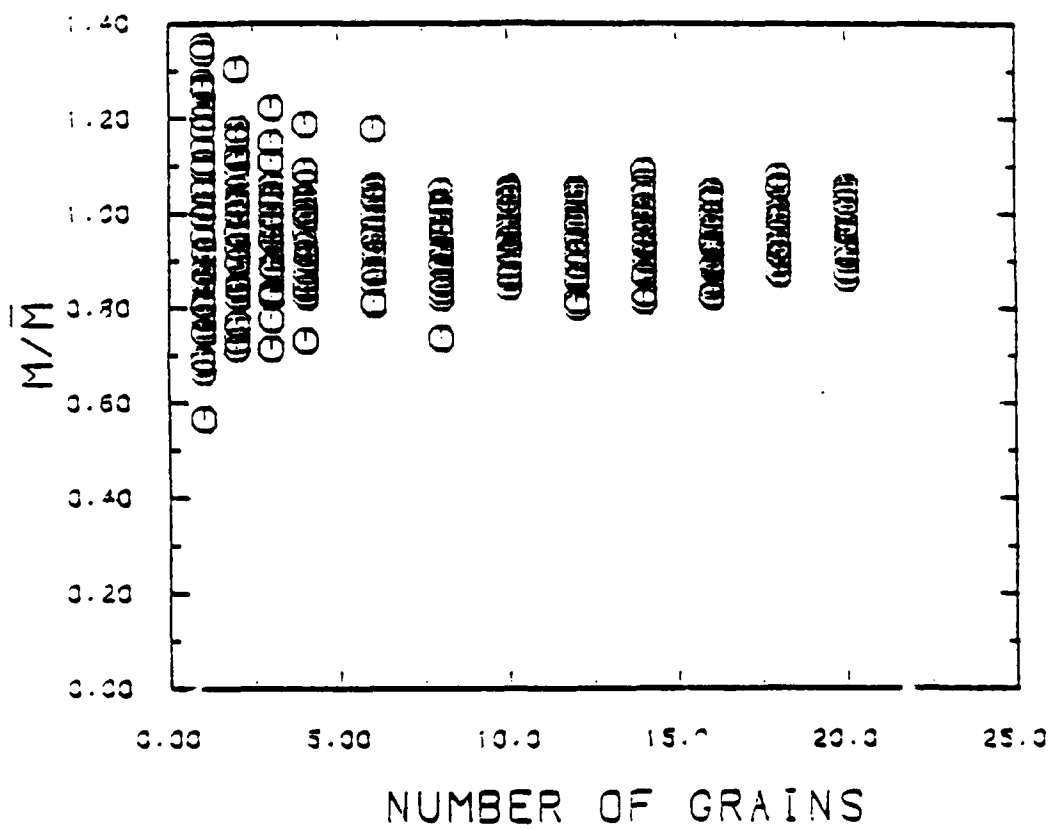


FIGURE 6-13. Variation of normalized Taylor factors ( $M/\bar{M}$ ) with the number of grains.

variation in yield strength is expected in the plastic zone when only one grain is interrogated by the crack tip. This statistical variation of yield strength decreases as the number of grains affected by the crack tip is increased. Thus, the effect of grain orientation is expected to play a prominent role in crack initiation, as well as in the subsequent erratic growth of small fatigue cracks.

In conclusion, fatigue cracks in Astroloy at room temperature initiate preferentially in grains which were weakest by virtue of the fact that their crystallographic orientations favor  $\{111\} \langle 110 \rangle$  slip. These grains were found to have surface normals near the  $[100]$   $[110]$  and  $[113]$  directions and exhibit the lowest Taylor factors. This preferred orientation was also observed for the one out of seven cases (in the current experiment) where a crack initiated from a pre-existing surface pore.\* Thus, crystallographic orientation is an important factor in governing where the crack initiates, as well as its mode of growth. However, it may also be possible for metallurgical defects to initiate cracks in less favorably oriented grains, depending on the nature, geometry, size and distribution of such defects. Manufacturing defects would also be expected to play a similar role in crack initiation in actual aero-engine components as discussed in Section 5.4.

It is significant to note that the crystallographic orientation determined here for small cracks in Astroloy is the same as those observed near the fatigue threshold in long cracks in Astroloy using fracture surface etching [6.9 - 6.11], as well as those in other Ni-base superalloys determined using a variety of techniques [6.12 - 6.14].

### **6.3 Fractography of Small Cracks**

The fracture surface morphology of small cracks was characterized as a function of test temperature, alloy composition and grain size by examining the fractured bend specimens from Section 5. These results assist in understanding the influence of these variables on the small crack growth rates. More importantly, however, the results are compared with known large crack behavior to elucidate possible differences in the crack growth mechanisms in small and large cracks.

### 6.3.1 Fractography Versus Test Temperature

Test temperature had a pronounced effect on the fracture surface morphology of small cracks as indicated by the results in Figure 6-14 on CG Astroloy. The initial fracture surfaces at 25°C were highly crystallographic exhibiting sharp, angular facets. In contrast, crack growth at 600°C, while still initially crystallographic, is significantly flatter and smoother than that at 25°C. Consequently, the relationship between facet size and grain size, which is clearly evident at 25°C, is indistinguishable at the elevated temperature. At both temperatures, the extent of crystallographic cracking decreased as the cracks enlarged, although a transition crack size can be identified in each case. This transition crack size was larger at room temperature than at 600°C ( $a = 400 \mu\text{m}$  versus  $200 \mu\text{m}$ ).

The above change in the fracture surface morphology with temperature also occurred in Waspaloy. However, as indicated in Figure 6-15 the extent of the sharp, angular faceting at 25°C was noticeable less in Waspaloy than in CG Astroloy. In accord with subsequent discussion, this difference is believed to be due to the fact that the room temperature Waspaloy specimen was tested at a significantly higher level of applied stress ( $S = 1.7$  versus  $1.1$ ).

The dramatic influence of test temperature on the nature of the crystallographic crack growth was particularly evident in cases where the temperature was changed during the experiment. This is shown in Figure 6-16 which contains higher magnification fractographs of the crack initiation sites in CG Astroloy and Waspaloy. In both cases cracks were initiated at 25°C until a crack of about one-to-two grain sizes was detected, then the temperature was increased to 600°C for the remainder of the experiment. The transition from the sharp angular facets at 25°C to the flatter, smoother facets at 600°C is clearly evident. Interestingly, this transition corresponds to the point in the experiment where the cracks often arrested for a significant period of time, as described in Section 5.4.

The above changes appear to be consistent with observed changes in the homogeneity of slip in Ni-based alloys with temperature. Specifically, increasing temperature, as well as strain, is known to activate processes such as cross slip and climb which thereby serve to homogenize the deformation [6.16 - 6.20]. Such thermally activated processes would be expected to



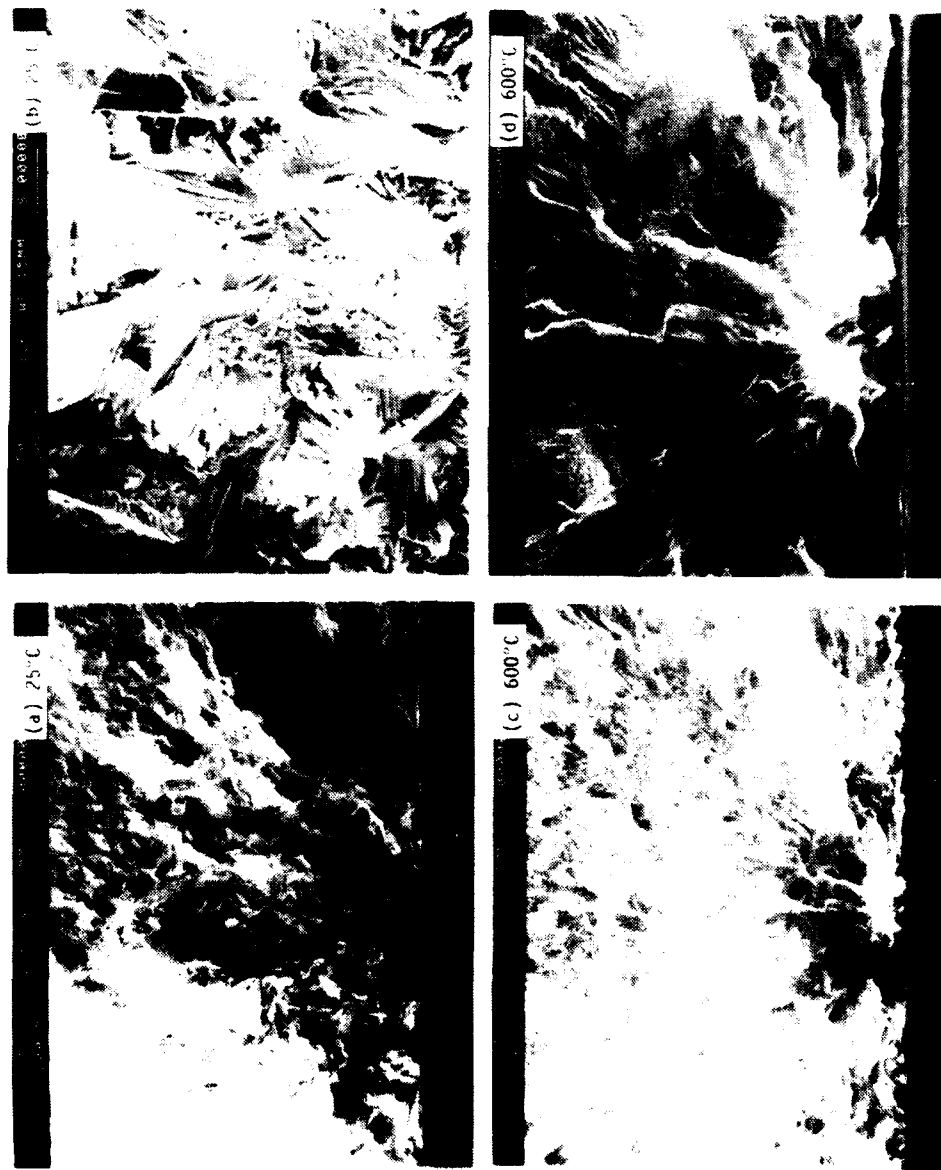


FIGURE 6-14. Effect of test temperature on fracture surfaces of small cracks in CG Astroloy.

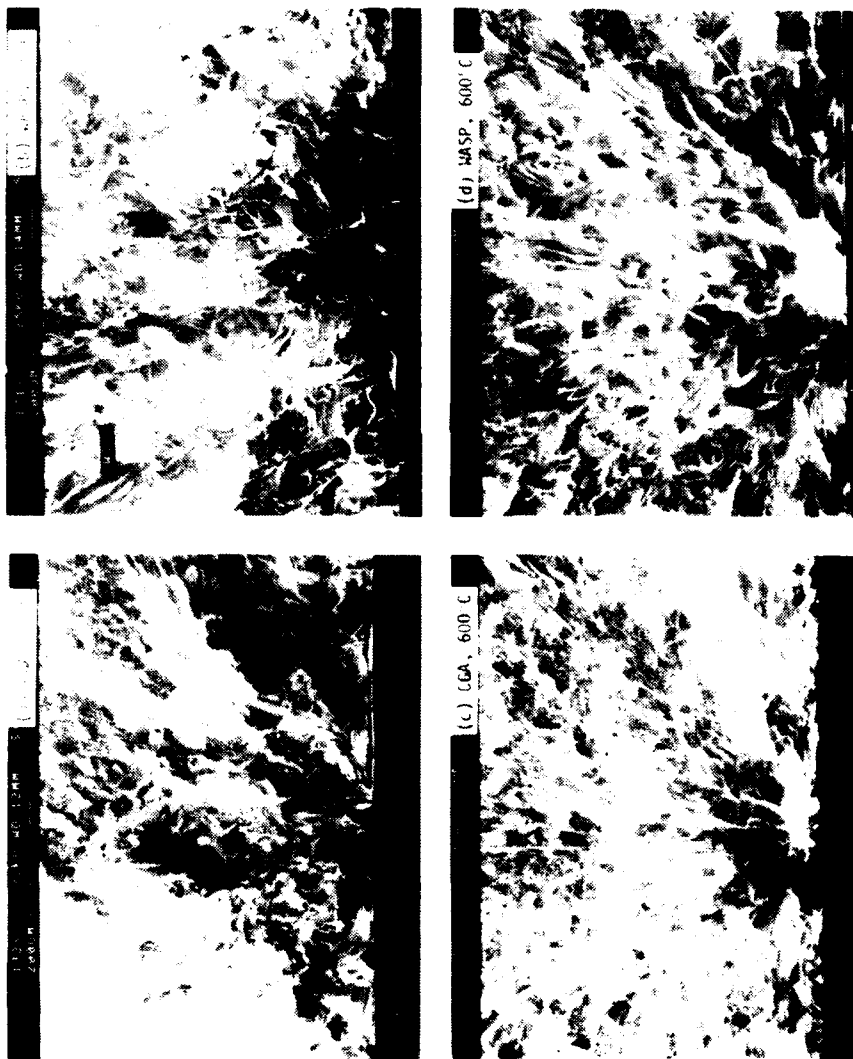


FIGURE 6-15. Effect of test temperature on fracture surfaces of small cracks in Waspaloy versus CG Astroloy.

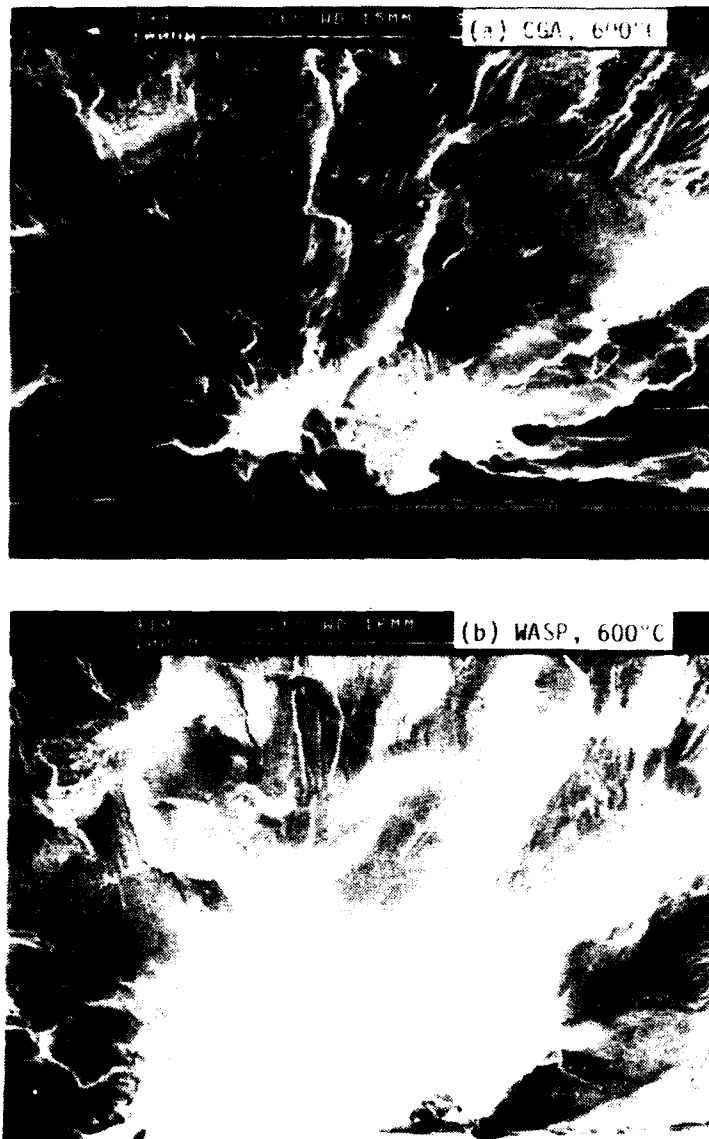


FIGURE 6-15. Fracture surfaces of small cracks in CGA alloy versus Waspalloy. Both cracks were initiated at 250°C (1-2 grains) and subsequently grown at 600°C.

### **6.3.2 Fractography Versus Alloy Composition**

Figures 6-15 and 6-16 also provide a comparison of the influence of alloy composition on the fracture surface morphology since the grain sizes are similar in both CG Astroloy (30  $\mu\text{m}$ ) and Waspaloy (42  $\mu\text{m}$ ). Fracture surfaces in both alloys are strikingly similar, exhibiting the same temperature dependence as well as change from faceted to non-faceted crack growth with increasing crack size. The only noticeable difference in fracture appearance is that the facets in Waspaloy appear more ductile than those in CG Astroloy, Figure 6-16. This difference is understandable, since Waspaloy is the weaker of the two alloys, the enhanced strength of Astroloy being gained through additional precipitation hardening.

The overall commonality of fracture appearance of Waspaloy and Astroloy is consistent with the fact that the growth rate behavior of small cracks in these two alloys is similar at both room temperature [6.21] and elevated temperature (Figure 5-22).

### **6.3.3 Fractography Versus Grain Size**

As shown in Figure 6-17 for the case of Astroloy, the primary role of grain size on the fracture surface morphology is to alter the size of the crystallographic facets. This is clearly evident at 25°C, but less so at 600°C since the smooth, flat surfaces produced at this temperature largely obscure the grain boundaries. Nevertheless, as the crack enlarges and non-crystallographic cracking becomes more predominant at 600°C, the fracture surface of the fine grain material exhibits a noticeable finer structure than that of the coarse grained material.

### **6.3.4 Fractography of Small Versus Large Cracks**

The above mentioned trends in fracture morphology with temperature, alloy composition and grain size are similar to those which have previously been observed for long, thru-thickness cracks in Ni-base alloys in the near-threshold regime [6.9 - 6.11]. An example of the latter, taken from Ref. [6.11], is shown in Figure 6-18 for both FG and CG Astroloy at 25°C and 600°C. Comparing Figure 6-17 with Figure 6-16, and accounting for the

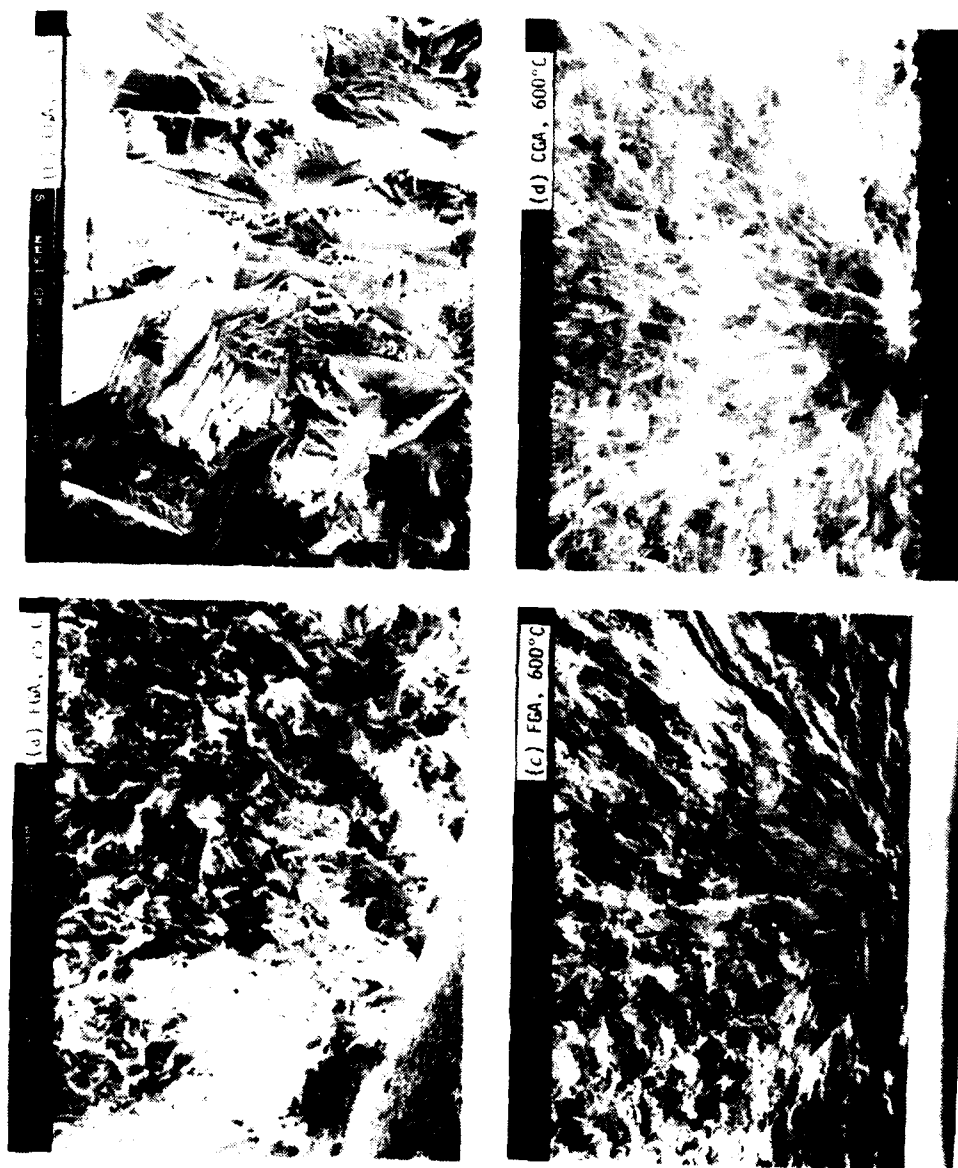


FIGURE 6-17. Effect of grain size and temperature on the fractography of small cracks in Astroloy.

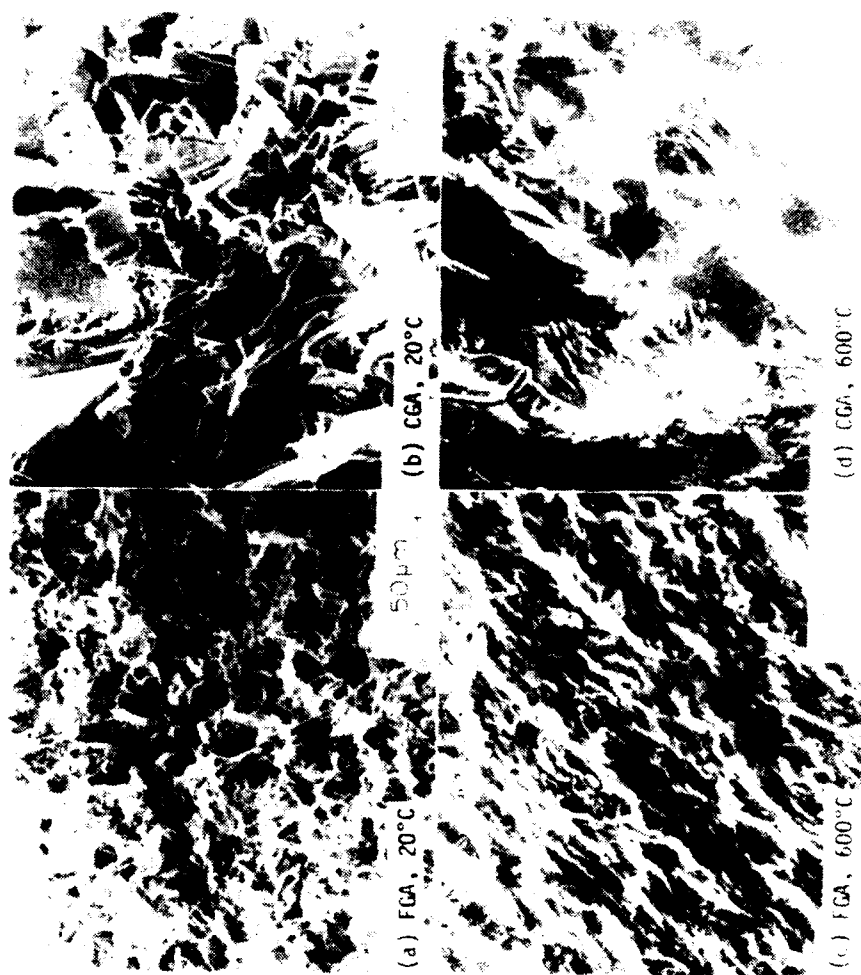


FIGURE 6-18. Effect of grain size and temperature on the fractography of long cracks in Astroloy (after Ref. 6.14). Note similarity with small crack fractography in Figure 6-17.

dependence of the fracture surface is similar in both crack size regimes. This similarity is particularly noticeable in the coarse grained material.

As discussed previously in relation to the observed temperature dependence, the fracture surface morphology should be related to the homogeneity of slip, which is known to change with both temperature and extent of deformation. Thus, a more exact comparison of the fracture surfaces of small and long cracks should be done at equivalent values of the mechanical driving force -- that is, at equivalent magnitudes of the local crack-tip strain.

In long, thru-thickness cracks in Ni-base superalloys it is well documented that crystallographic faceting is favored at low  $\Delta K$ , while non-crystallographic (classical striated) growth is favored at high  $\Delta K$  [6.9, 6.22]. In fact, it has been proposed that the transition between the two crack growth processes occurs when the cyclic plastic zone becomes equal to the grain size [6.22]. However, it should be pointed out that these studies have computed the cyclic plastic zone size based on the applied  $\Delta K$  value. This procedure is likely to have over-estimated the actual cyclic plastic zone size due to the significant crack closure which occurs in large cracks, as shown in Section 4.4. As shown in Section 7, small cracks also exhibit closure, but to a much lesser extent than do long cracks. This difference in crack closure behavior together with inelastic and mixed-mode effects in small cracks, causes the mechanical driving force for small and large cracks to differ. Thus, a more sensible comparison of fracture features should be made in terms of an equivalent  $\Delta K$ , (defined in Section 8), which takes these factors into account for both small and large cracks.

Figure 6-19 illustrates the general relationship between the applied  $\Delta K$  and the equivalent  $\Delta K$ , designated  $\Delta K_{eq}$ . As indicated,  $\Delta K_{eq}$  is less than  $\Delta K$  for long cracks near the threshold, while the opposite is true for small cracks. Consequently, the respective  $\Delta K_{eq}$  values for small and long cracks are much more similar than indicated by their applied  $\Delta K$  values. This similarity in  $\Delta K_{eq}$ , which if properly formulated should characterize the near-tip deformation state in both crack regimes, is believed to account for the similarities in crack growth mechanisms in small and long cracks.

In addition, differences in constraint from neighboring grains in small versus large cracks may favor crystallographic crack growth in small

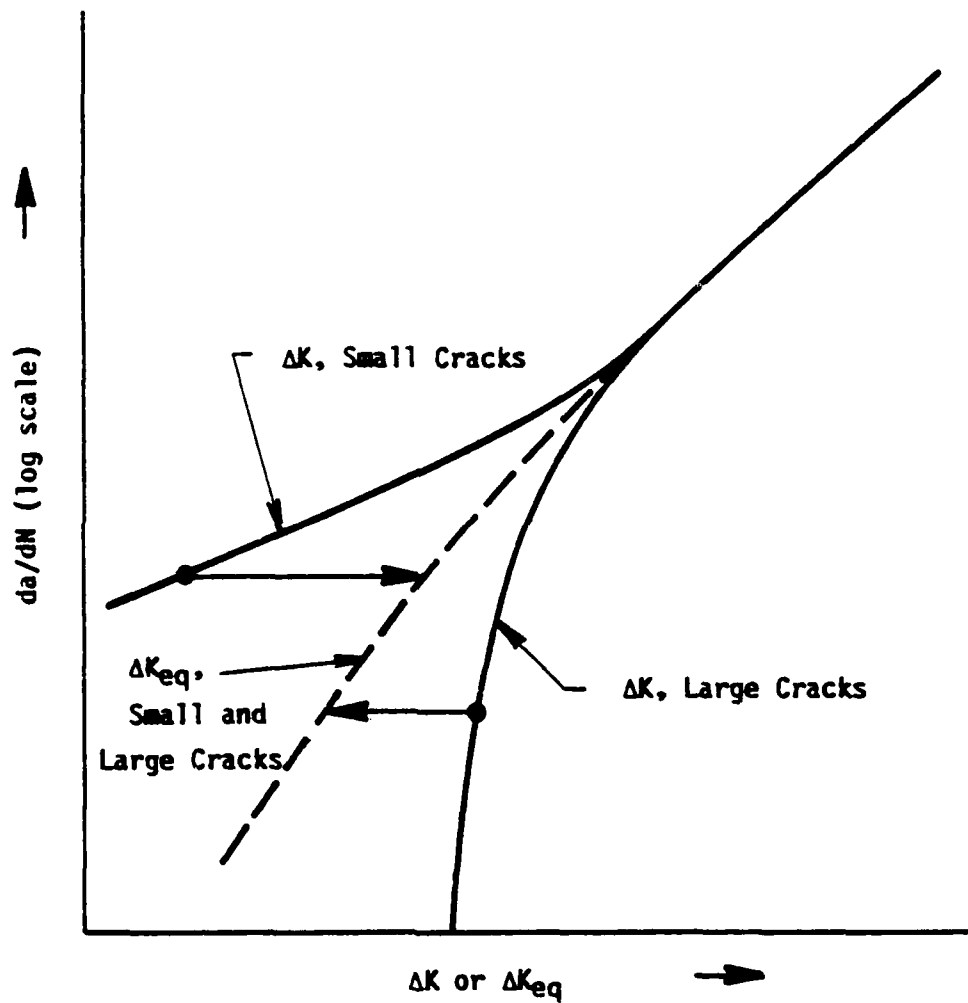


FIGURE 6-19. Schematic illustration of consolidation of small and large crack growth rate data in terms of  $\Delta K_{eq}$ .



the first few grains they can deform and crack in an optimum manner dictated by the particular orientation of each grain (Section 6.2). In contrast, both large surface cracks and long thru cracks are constrained to deform and crack in concert with a large number of grains thereby favoring slip on multiple planes which gives rise to a flatter fracture surface having fewer sharp facets.

In conclusion, the fractography of small cracks is consistent with the orientation relationship established in Section 6.2. Perhaps more importantly, both these observations are consistent with known crack propagation mechanisms in long cracks. Thus, the resolution of the "anomalous" behavior of small cracks appears to require a proper reformulation of the mechanical driving force -- a task undertaken in Sections 7 and 8.

#### 6.4 REFERENCES

- 6.1 R. Wang, H. Mughrabi, S. McGovern, and M. Rapp, Mater. Sci. and Engng., 65 (1984) 219-233.
- 6.2 J. Polak, T. Lepisto, and P. Kettunen, Mater. Sci. and Engg., 74 (1985) 85-91.
- 6.3 M. E. Fine and I. B. Kwon, Small Fatigue Cracks, Ed. by R.O. Ritchie and J. Lankford, TMS-AIME, Warrendale, PA, 1986, pp 29-40.
- 6.4 P. Neumann and A. Tonnessen, Fatigue '87, Vol. 1, Ed. by R. O. Ritchie and E. A. Starke, Jr., Eng. Mater. Advisory Serv. Ltd, 1987, pp 3-22.
- 6.5 D. L. Davidson, Intern. Metals Reviews, 29 (1984) pp. 75-95.
- 6.6 J.F.W. Bishop and R. Hill, Phil. Mag., Vol. 42, (1951) pp. 414-27, pp. 1298-1307.
- 6.7 J.F.W. Bishop, Phil. Mag., (1953) pp. 51-64.
- 6.8 G. Y. Chin, E. A. Nesbitt, and A J. Williams, Acta Met., Vol. 14, (1966) pp. 467-476.
- 6.9 J. E. King, "Effects of Grain Size and Microstructure on Threshold Values and Near Threshold Crack Growth in Powder-Formed Ni-Base Superalloy," Metal Science, Vol. 16, July 1982, pp. 345-355.
- 6.10 M. A. Hicks and J. E. King, "Temperature Effects on Fatigue Thresholds and Structure Sensitive Crack Growth in a Nickel-Base Superalloy," Int. J. of Fatigue, Vol. 5, April 1983, pp. 67-74.

- 6.11 J. E. King, "Fatigue Crack Propagation in Nickel-Base Superalloys- Effects of Microstructure, Load Ratio, and Temperature," Materials Science and Technology, Vol. 3, Sept. 1987, pp. 750-764.
- 6.12 M. Gell and G. R. Leverant, Acta Met., Vol. 16, 1968, p. 553.
- 6.13 D. J. Duquette and M. Gell, Met. Trans., Vol. 2, 1971, pp. 1325- .
- 6.14 K. Sadananda and P. Shahinian, "Analysis of Crystallographic High Temperature Fatigue Crack Growth in a Nickel Base Alloy," Met. Trans., Vol. 12A, 1981, pp. 343-351.
- 6.15 J. N. Vincent and L. Remy, "Temperature Dependence of the Pseudo-Cleavage Mechanism in the Threshold Regime of a Superalloy," in Fatigue Thresholds, Vol. 1, Eds. J. Backlund, A. F. Blom and C. J. Beevers, EMAS, 1982, pp. 441-454.
- 6.16 M. Gell and G. R. Leverant, in STP 520, ASTM, 1973, pp. 37-67.
- 6.17 S. Bashir, P. Taupin and S. D. Antolovich, "Low Cycle Fatigue of AS-HIP and HIP + Forged Rene 95," Met. Trans, Vol. 10A, 1979, pp. 1481-1490.
- 6.18 M. Clavel, C. Levailant and A. Pineau, "Influence of Micromechanisms of Cyclic Deformation at Elevated Temperature on Fatigue Behavior," in Creep-Fatigue-Environment Interactions, Eds. R. M. Pelloux and N. S. Stoloff, TMS/AIME, Warrendale, PA, 1980, pp. 24-45.
- 6.19 R. V. Miner, J. Gayda and R. D. Maier, "Fatigue and Creep-Fatigue Deformation of Several Nickel-Base Superalloys at 650°C," Met. Trans., Vol. 13A, Oct. 1982, pp. 1755-1765.
- 6.20 B. A. Lerch, N. Jayaramau and J. D. Antolovich, Mater. Sci. and Eng., Vol. 66, pp. 151-166.
- 6.21 C. W. Brown, J. E. King and M. A. Hicks, "Effects of Microstructure on Long and Short Crack Growth in Nickel Base Superalloys," Metal Science, Vol. 18, July 1984, pp. 374-380.
- 6.22 C. J. Beevers, "Fatigue Crack Growth Characteristics at Low Stress Intensities of Metals and Alloys," Metal Science, Vol. 11, 1977, pp. 362- 367.

## 7. CRACK-TIP DEFORMATION AND CRACK CLOSURE IN SMALL CRACKS

The work summarized in this section was designed to elucidate the physical processes which contribute to crack size effects in Ni-base alloys under fatigue loading. This was accomplished using high resolution observations and quantitative measurements obtained within a scanning electron microscope (SEM) equipped with a special fatigue loading stage. The local displacements at the tips of small cracks were quantified by combining the SEM observations with the techniques of stereoinaging. These local displacement measurements, combined with crack closure measurements, provided the basis for the crack driving force determined in Section 8. While most of the data presented in this section are on the Ni-base superalloys of primary interest in this study, supplemental results obtained from reanalysis of previously available data on an aluminum alloy are also presented.

### 7.1 Experimental Techniques

The local deformation and closure of small fatigue cracks was measured within a SEM using either of two cyclic loading stages capable of operating at either room temperature or elevated temperature. Details of the design and operation of these units can be found in Refs. 7.1 and 7.2.

The specimen design used for the SEM experiments is shown in Figure 7-1. All specimens were prepared using low-stress machining. In addition, to eliminate any residual stresses remaining after machining, the gage section of the specimens were further prepared by electropolishing in a solution of 25 percent nitric acid in methanol at  $-30^{\circ}\text{C}$ . Typically, this procedure removed a 40  $\mu\text{m}$ -thick layer of material from the specimen. This procedure also revealed the microstructure of the material thereby providing a frame of reference for the observation of small cracks, as well as surface features necessary for stereoinaging.

#### 7.1.1 Initiation of Fatigue Microcracks

All fatigue cracks were naturally initiated by loading the gage section of the specimen in Figure 7-1 in three-point bending. As in the experiments of Section 5, this procedure was used to localize the initiated

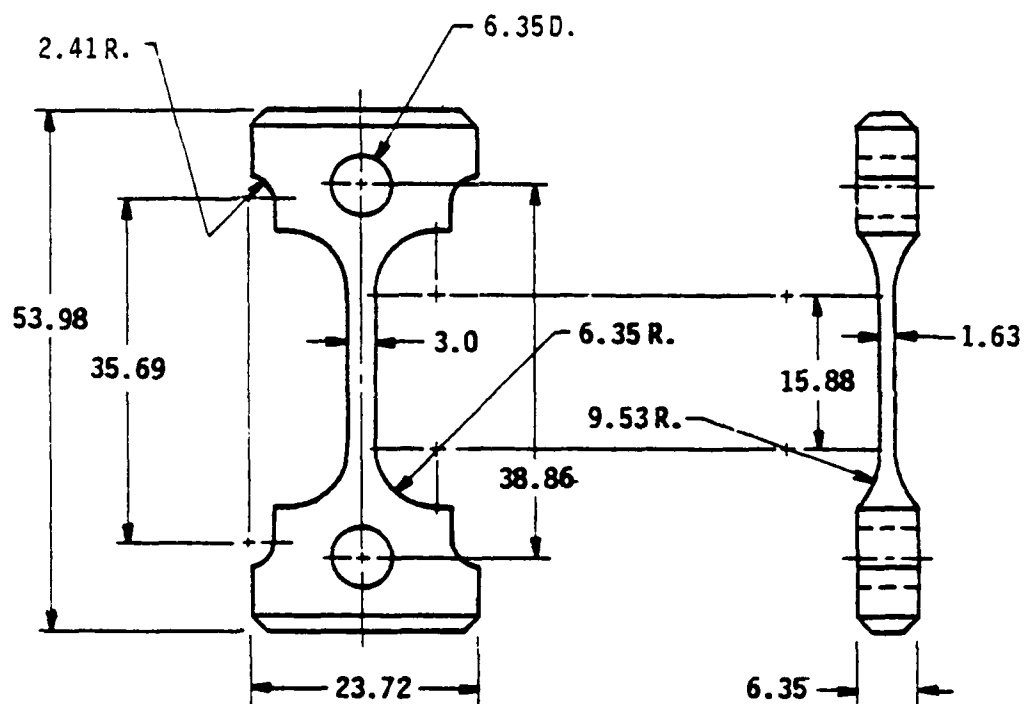


FIGURE 7-1. Specimen design used to study small cracks within the SEM. Dimensions are in mm.

cracks thereby simplifying their detection. For expedience, crack initiation was conducted in a room temperature laboratory air environment (50 percent R. H.) using a laboratory servo-hydraulic test machine cycled under a 10 Hz sinusoidal waveform and a load ratio (R) of 0.1. The maximum (outer fiber) bending stresses were 85 to 98 percent of the proportional limit of the material, as determined from strain gage measurements.

Crack initiation was detected using plastic replicas obtained periodically under both minimum and maximum load. Replicas were metal coated and examined using optical microscopy at 500X. This procedure usually revealed either no cracks or several cracks; rarely did only a single crack initiate. However, multiple cracks were usually widely separated and did not interfere with one another until considerable growth had occurred. As described in Section 6, these cracks were found to initiate either at slip within grains or at surface pores. Occasionally, the slip which initiated the crack could be traced back to the very first loading cycle.

#### 7.1.2 SEM Experiments

Following the initiation of a detectable crack, the specimens were switched to tension-tension loading ( $R = 0.1$ ) in vacuum -- either in a laboratory test machine equipped with a vacuum rig, or within the cyclic loading stage of the SEM. At room temperature this transition occurred without noticeable change in the crack growth rate. However, when this transition involved increasing the test temperature to 600°C, cracks arrested for many thousands of cycles, then eventually resumed growth without warning. This behavior was identical to that which was observed in the experiments of Section 5 and greatly hindered data acquisition at the elevated temperature.

To overcome this difficulty, the initial portion of the 600°C experiments had to be conducted entirely within the SEM where cracks could be constantly monitored at high resolution. During this period, the cyclic load range was gradually increased until the cracks remained open for a significant portion of the loading cycle and crack growth was observed. This procedure typically resulted in a 30 percent increase in the stress, relative to the precracking stress. During this procedure, the cyclic frequency was maintained at 3 Hz in order to preclude measurable creep deformation. Once cracks

were growing at 600°C, the specimen was periodically transferred from the SEM to the laboratory test machine (at 1 MPa vacuum) to lengthen cracks prior to reinsertion into the SEM for further observation.

### 7.1.3 Stereoimaging Analysis

Periodically, during growth of the small cracks, photographs of the entire crack and each of the crack tip regions were made at both minimum and maximum load. Examples of these photographs are shown in Figures 7-2 and 7-3. Cracks in FG Astroloy initiated primarily at pores, Figure 7-2, whereas cracks in CG Astroloy initiated primarily at persistent slip bands, Figure 7-3.

Photographs were analyzed using the stereoimaging technique (7.2), which is an optical method of measuring relative displacements by comparing two photographs of the same region, each obtained at a different displacement state. Using this procedure, the crack-tip displacement field was quantified using high resolution photogrammetric equipment. From these measurements, it was a simple matter to compute crack opening displacements. Furthermore, by taking gradients within the displacement field three elements of the symmetric, in-plane strain tensor were also computed using finite-strain formulation. These strains were used to determine the magnitude of crack-tip strain and the distributions of strain parallel and perpendicular to the loading direction (7.3, 7.4). Plastic zone sizes were also computed by extending these distribution functions to the cyclic elastic limit, defined as twice the cyclic yield stress divided by the elastic modulus.

The stereoimaging technique was also used to determine the load at which the crack was fully opened to its tip. This procedure entailed photographing the crack-tip region at minimum load,  $P_{min}$ , and at progressively higher proportions of the maximum load,  $P_{max}$ . By first observing the photographs of  $P_{min}$  and  $P_{max}$  in a stereoviewer, it was possible to determine the location of the crack tip to within about 0.1  $\mu m$ . At loads below that required for crack opening to the tip, only a portion of the crack appeared open, and with increasing load, this distance decreased until the crack was completely open to the tip. The load at which this occurred was defined as

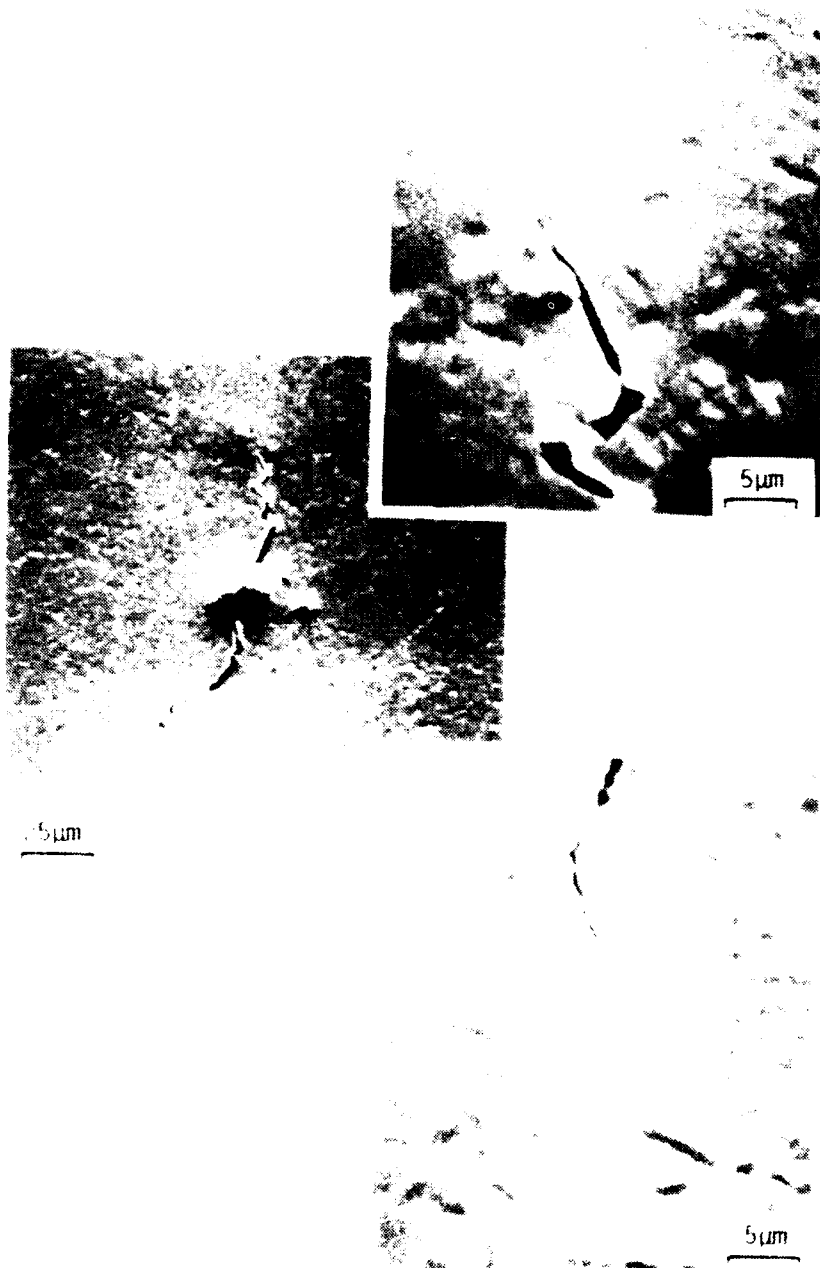


FIGURE 7-2. 125  $\mu$ m crack in Fine Grained Astroloy initiated at ambient temperature, but grown at 600°C. Initiation site was at the pore. Photographs were made at 6000 $\times$ .

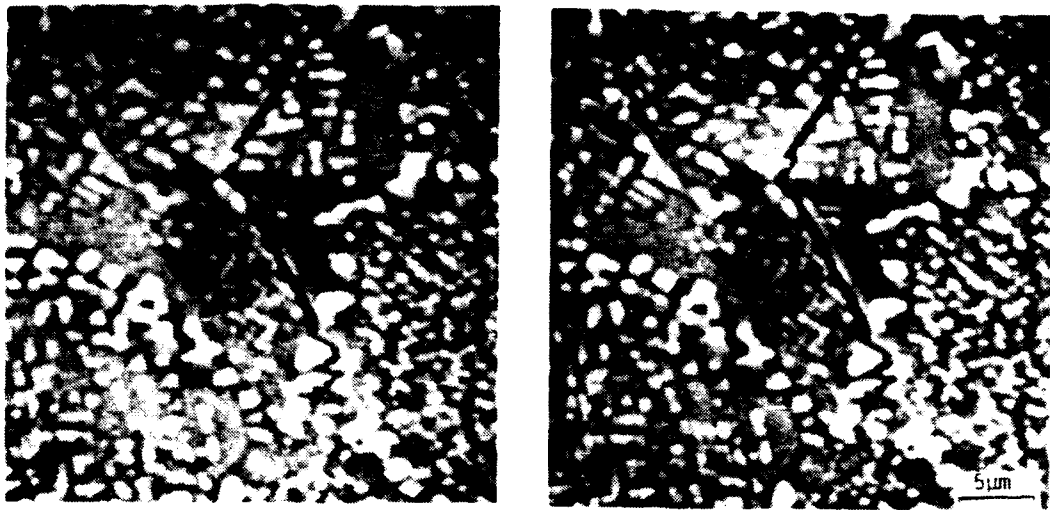


FIGURE 7-3. 14  $\mu\text{m}$  long crack in Coarse Grained Astroloy at 20°C. Crack was slip band initiated.



the crack opening load,  $P_{op}$ . It was usually possible to determine the value of  $P_{op}$  to 10-15 percent of  $P_{max}$ .

By viewing photographs both parallel and perpendicular to the loading axis, a value of applied load corresponding to the onset of Mode I opening ( $P_{op}$ ), as well as the onset of Mode II sliding ( $P_s$ ) could be determined. Occasionally, for large cracks and low  $\Delta K$  values, crack-tip sliding was found to precede crack-tip opening (that is,  $P_s < P_{op}$ ); however, for small cracks this was not the case. In selected cases, Mode III displacements were also determined by comparing photographs of the specimen inclined at two different angles with respect to the electron beam.

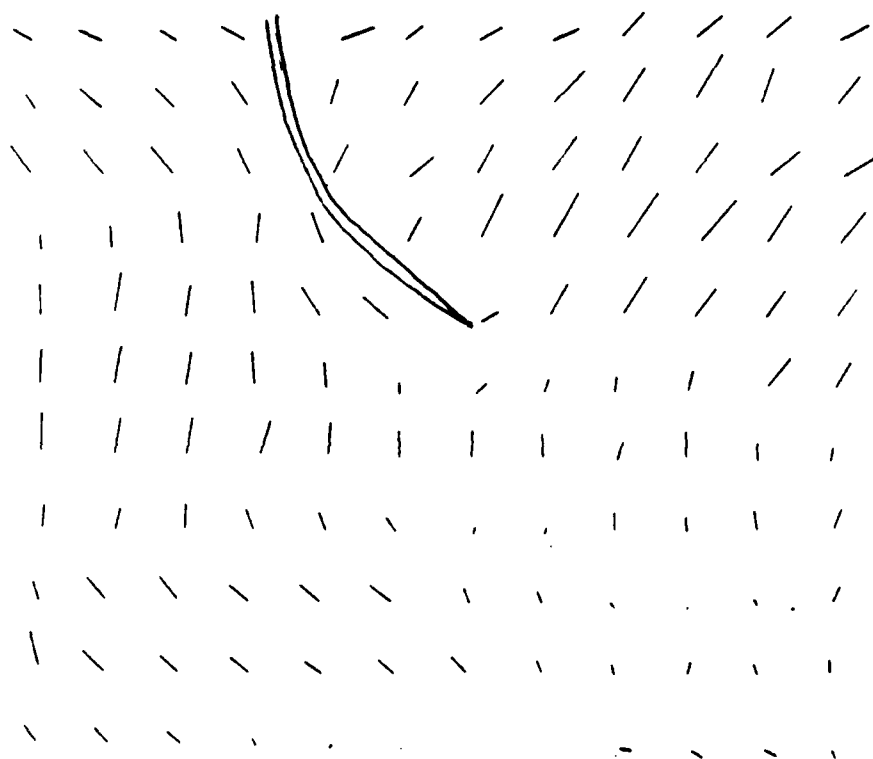
## **7.2 Local Crack-Tip Measurements on Small Cracks**

The crack tip displacements strains and crack opening loads were determined for small surface cracks of various sizes in CG Astroloy at 25°C and in CG and FG Astroloy at 600°C. Detailed results are presented for selected cases to illustrate the nature of the results obtained and summaries of important parameters are provided for the remainder of cases.

### **7.2.1 Crack-Tip Displacements**

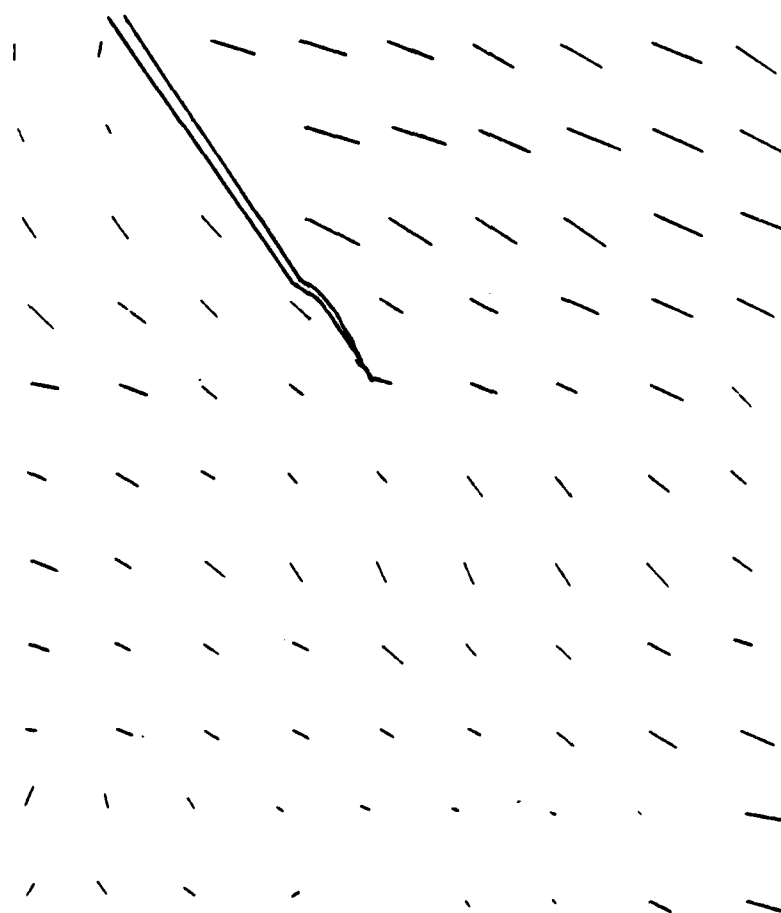
Figure 7-4 provides an example of a typical displacement field determined from stereoimaging. These results were obtained for the small crack in FG Astroloy at 600°C shown in Figure 7-2. All displacements are with respect to a reference point ahead of the crack tip at a remote location which experienced little or no deformation. These displacements are indicative of a biaxial crack-tip deformation field and are surprisingly homogeneous in view of the highly planar slip character of this alloy. Similar results were observed in CG Astroloy and both 25°C and 600°C.

As indicated in Section 6, small cracks were rarely normal to the applied loading direction due to their preferred orientation within the crystallite. Thus, cracks were generally inclined at some angle with respect to the original  $x'-y'$  coordinate system of the stereoimaging measurements, as shown in Figure 7-4. In order to resolve displacements into Modes I and II, the measured displacements were transformed from the original  $x'-y'$  system into an  $x-y$  system as shown in Figure 7-5.



2.00 microns

2.00 micron  
displacement



2.00 microns

2.00 micron  
displacement

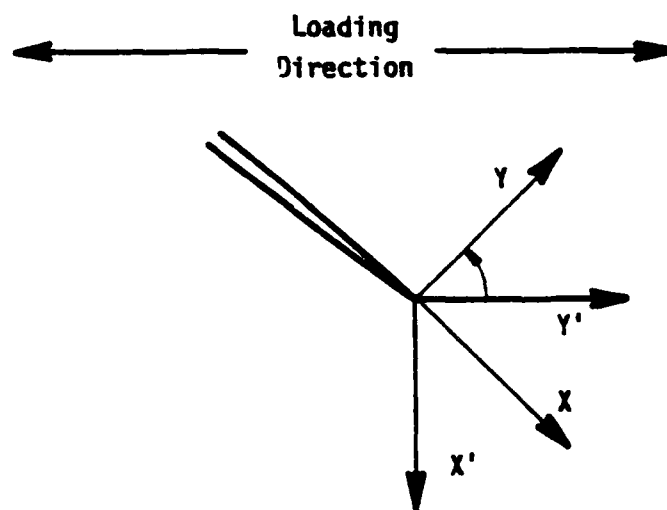


FIGURE 7-5. Original ( $X' - Y'$ ) and transformed ( $X - Y$ ) coordinates for the measured displacement fields at small cracks.

An example of Mode I and Mode II crack opening displacements (COD) in the x-y coordinate system is given in Figure 7-6. Once again, these results are for the small crack in FG Astroloy shown in Figure 7-2 and correspond to the original displacement field of Figure 7-4. The magnitude of the Mode II displacements in this particular case is relatively small since the crack was nearly normal to the loading direction. In contrast, the Mode II displacements are significant for a crack, such as that shown previously in Figure 7-3, which is inclined at an appreciable angle to the loading axis. For example, cracks inclined at an angle of 40°-50° to the loading axis exhibited nearly equal Mode I and Mode II displacements, as shown in Figure 7-7 for a crack in CG Astroloy at 600°C. This mixture of Modes I and II is in good agreement with results obtained from two dimensional elastic analysis of inclined edge cracks using the boundary force methods [7.5]

Perhaps the most interesting feature of the above COD values is the fact that they are a linear function of square root of the distance from the crack tip and thus can be described by:

$$\text{COD} = C_0 \sqrt{r} \quad (7-1)$$

where  $C_0$  is the slope of the lines in Figures 7-6 and 7-7, and  $r$  is the distance from the crack tip. The above  $r$ -dependence of the COD is precisely what one would expect for an elastic crack where, for example, the Mode I displacement ranges are given by:

$$\text{COD}_I = \frac{\Delta K \sqrt{r}}{E \sqrt{2\pi}} [8(1+\nu)(1-\nu)] \quad (7-2)$$

where  $\Delta K$  is the Mode I stress intensity factor defined by linear elasticity and  $\nu$  is Poisson's ratio. By combining Eqs. (7-1) and (7-2), it would appear that  $\Delta K$  can be computed from the slope of lines found in Figures 7-6 and 7-7, provided the cracks conform to the linear elastic fracture mechanics concept of small scale yielding (SSY). However, based on the size of the measured plastic zone in relation to the crack size, this is not likely to be the case for small cracks as described in Section 7.2.2. Thus, the  $\sqrt{r}$  dependence of COD appears to be fortuitous.

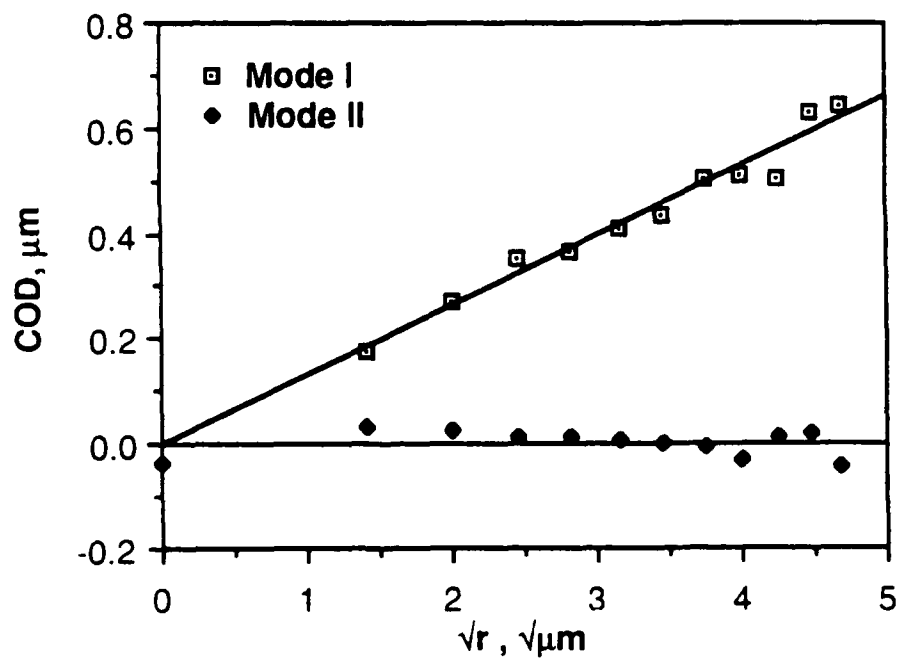
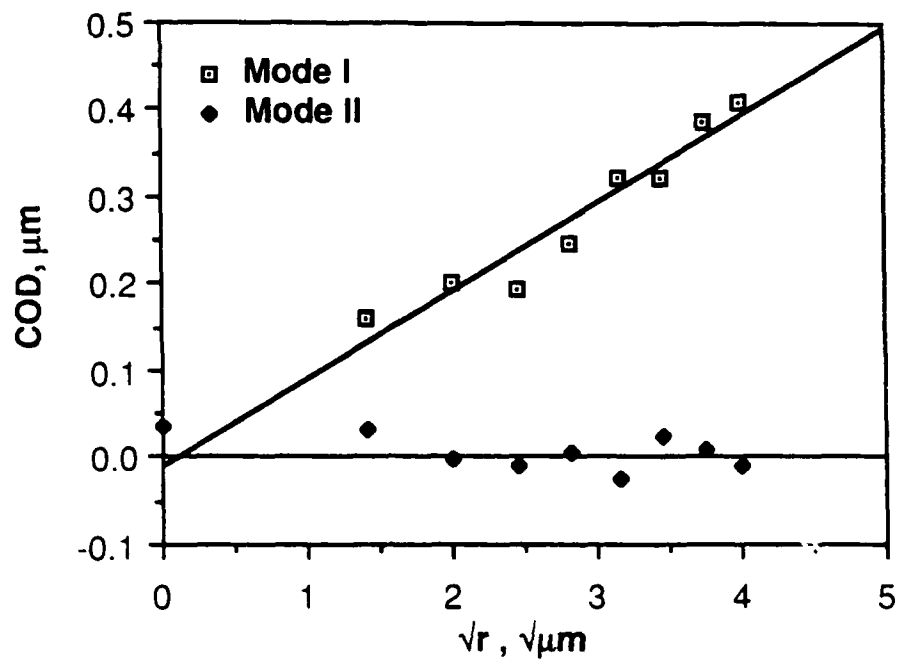


FIGURE 7-6. Crack opening displacements for FG Astroloy at 600°C. Upper and lower figures corre-

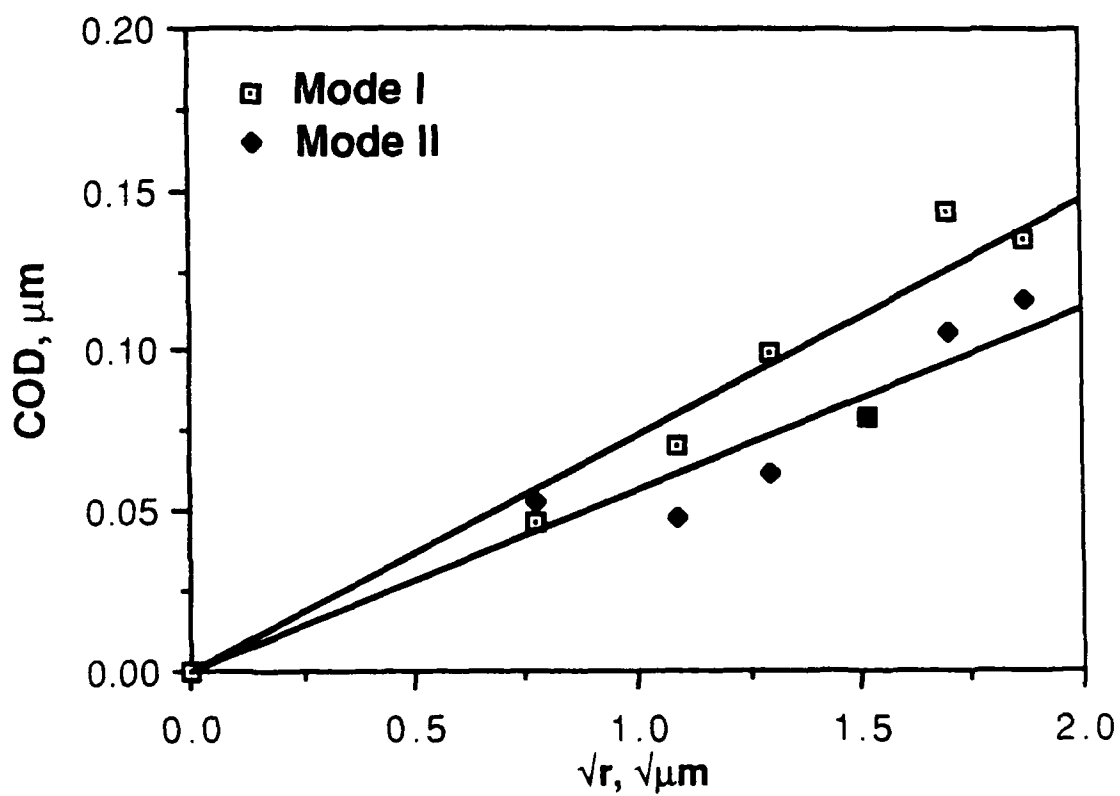


FIGURE 7-7. Crack opening displacements in CG Astroloy at 600°C. Large Mode II displacements are due to the fact that the crack is inclined with respect to the loading axis.

In order to better understand the above observations, Eqs. (7-1) and (7-2) were applied to the analysis of large cracks in 7075 and 7091 aluminum alloys which conformed to the SSY condition. Displacements measured using stereoimaging were again found to exhibit the  $\sqrt{r}$ -dependence. However, the  $\Delta K$  values computed from the measured displacements, termed  $\Delta K(\text{disp.})$  differed from those computed from applied load and crack size using the standard elastic stress intensity factor equations. As shown in Figure 7-8, the difference between  $\Delta K(\text{disp.})$  and the applied  $\Delta K$  was found to increase with increasing applied  $\Delta K$ . The reason for this discrepancy is thought to be related to the influence of the fatigue crack extension process, and associated crack-tip plasticity and crack closure, on the near-tip displacement field. Thus, even when SSY prevails, the local displacements at growing fatigue cracks do not conform to the analytical results from elastic analysis of monotonically loaded, stationary cracks. Nevertheless, when SSY prevails, these local events appear to scale with  $\Delta K$ , as evidenced by the ability of  $\Delta K$  to provide a geometry-independent measure of the crack growth kinetics of large cracks, at least under constant amplitude loading.

#### **7.2.2 Crack-Tip Strain and Plastic Zone Size**

An example of the maximum shear strain distributions at the tips of a small crack in FG Astroloy at 600°C (Figure 7-2) are given in Figure 7-9. The strain field is surprisingly homogeneous in view of the slip character of this material. Thus, multiple slip must be occurring on numerous {111} planes within the crack-tip plastic zone. Although stereoimaging is capable of defining the average crack-tip strain field, it cannot resolve slip details which occur on a much finer scale. Thus, it is not surprising that the criterion controlling which of these {111} slip planes the crack will follow is not obvious from examining the strain field. Similar strain fields were observed in CG Astroloy at both 25°C and 600°C and gave no indication of the change in fracture morphology with temperature which was evident in the fractographic results of Section 6.3.

These strain distributions for small cracks in Ni-base superalloys are similar to those found for small cracks in aluminum alloys (7.6), in that there is a large component of strain roughly parallel to the direction of loading. This distribution of strain is different than that found for



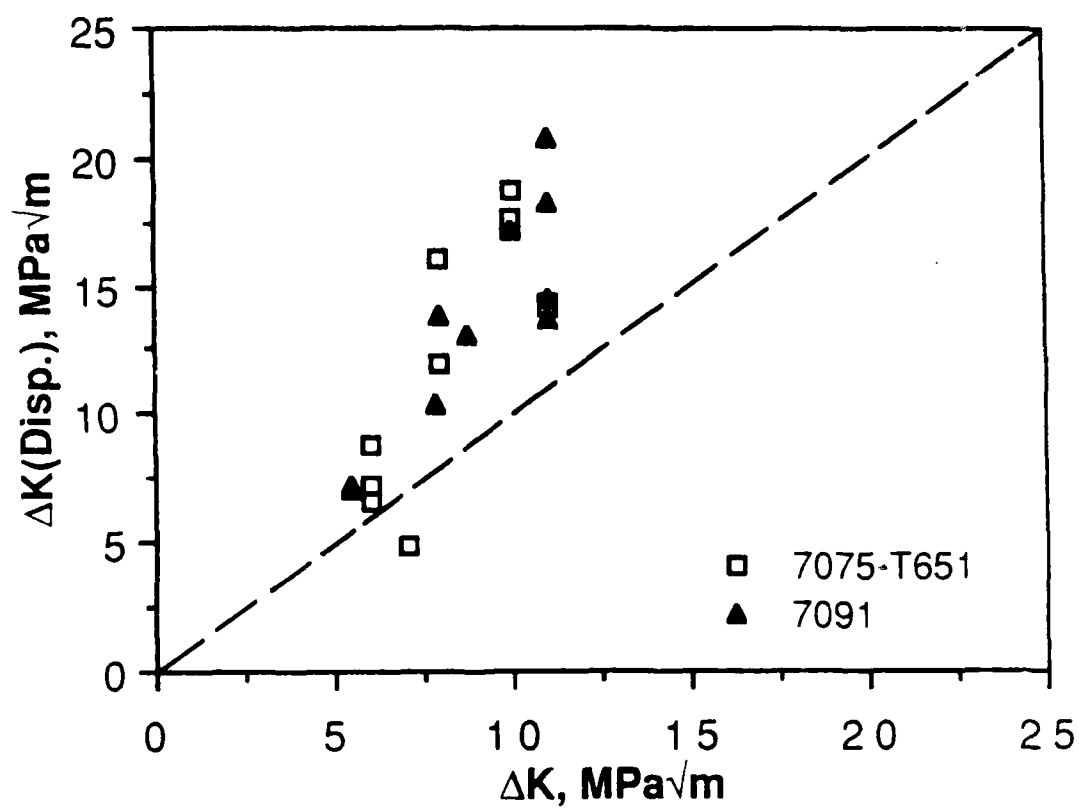
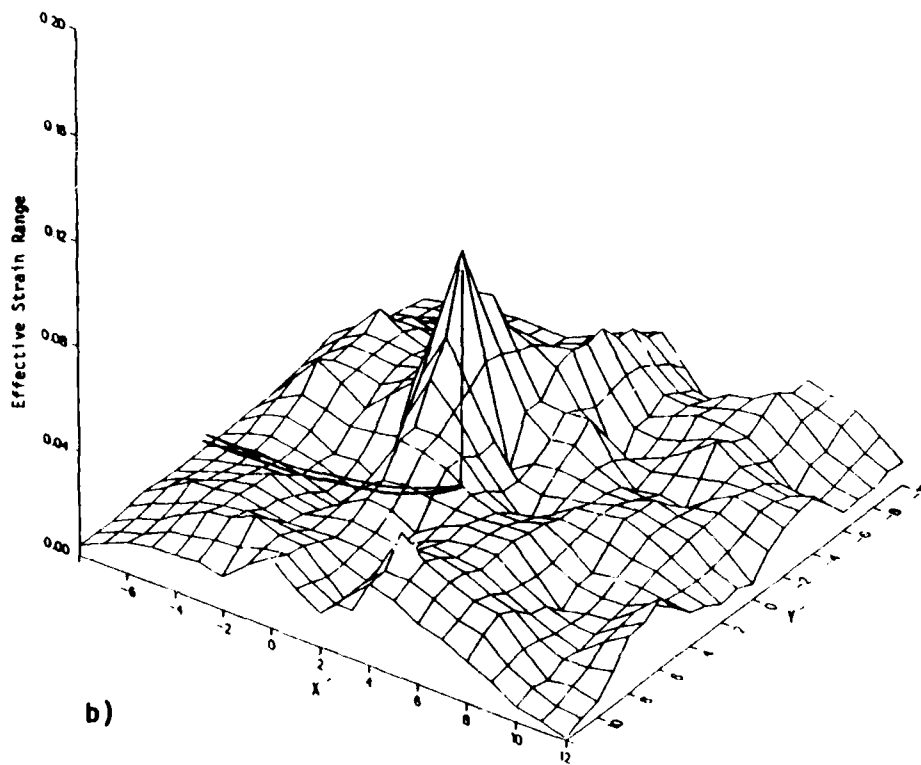
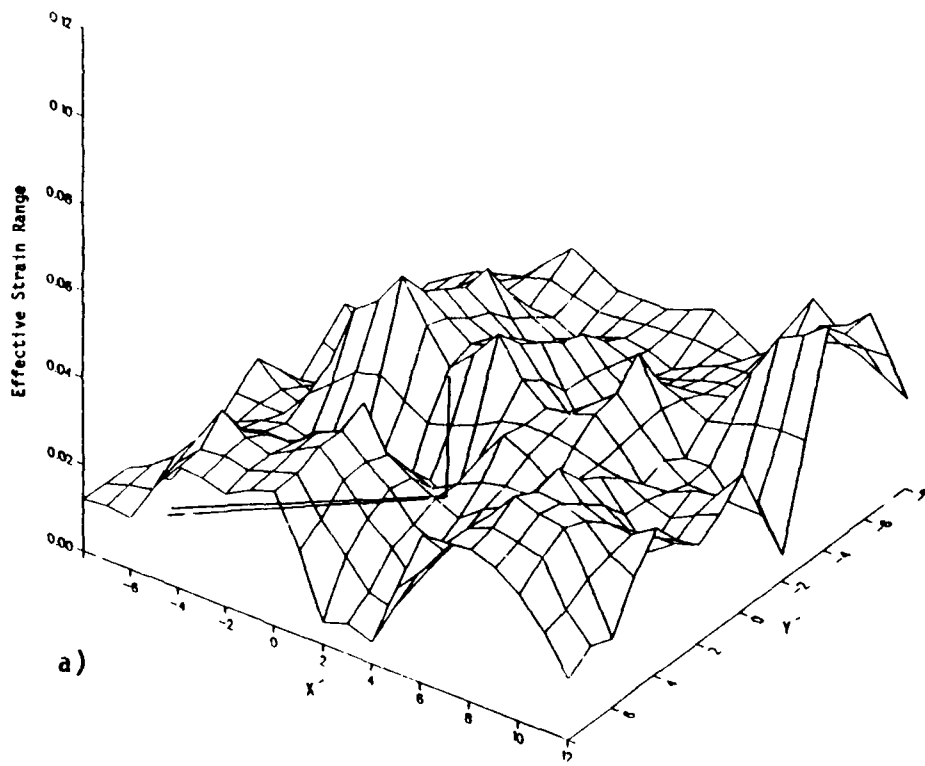


FIGURE 7-8. Comparison of  $\Delta K$  determined from measured crack displacements with applied  $\Delta K$  for large cracks in several aluminum alloys.



large cracks (7.7, 7.8) where a higher level of strain is found ahead of the crack tip. These differences in strain distribution between large and small fatigue cracks appear to depend on whether or not SSY prevails and are believed to be fundamental to understanding the small crack problem. Furthermore, the similarity in strain distribution between small cracks in superalloys and in aluminum alloys indicates the commonality in crack-tip mechanics for these two materials.

Strain distributions for large fatigue cracks have been found to be of the following functional form:

- 1) Perpendicular to the loading axis ( $\phi = 0^\circ$ ) [7.7]

$$\Delta \epsilon'(r) = A' + M' \ln(r+B') \quad (7-3)$$

or

$$\Delta \epsilon'(r) = \frac{A}{(r+B)^m} \quad \text{and } m = 1/(1+n') \quad (7-4)$$

- 2) Parallel to the loading axis ( $\phi = 90^\circ$ ) [7.8]:

$$\Delta \epsilon'(r) = \frac{1}{(1+r)} \quad (7-5)$$

where  $r$  = distance from the crack tip,  $\Delta \epsilon'(r)$  = (strain value at  $r$ )/(strain value at  $r = 0$ ),  $n'$  = the cyclic hardening exponent given in Section 4, and  $A'$ ,  $M'$ ,  $B'$ ,  $A$  and  $B$  are material constants. Considering the variability in the measured strain data, it is not possible to determine whether Eq.(7-3) or Eq.(7-4) provides the better representation of the data.

For small cracks in both CG and FG Astroloy at 25°C and 600°C, Eq.(7-4) has been found to fit the data reasonably well, but it is likely that Eq.(7-3) would also fit since these two functions are very similar near the crack tip. The validity of Eq. (7-5) for small cracks has not been examined.

Crack-tip plastic zone sizes ( $r_p$ ) for  $\phi = 0^\circ$  and  $90^\circ$  were computed by fitting the measured strain data for small cracks in Astroloy to the above equations. These results are summarized in Table 7-1 along with the crack sizes, applied  $\Delta K$  values and crack-tip strain ranges,  $\Delta \epsilon(0)$ . Although the validity of Eq. (7-5) has not been verified for the specific case of small cracks in Astroloy, it has been assumed to be valid for the purposes of comparing plastic zone sizes. The plastic zone sizes for  $\phi = 0^\circ$  and  $90^\circ$  are

TABLE 7-1  
CRACK-TIP STRAINS AND PLASTIC ZONE SIZES  
FOR SMALL CRACKS IN ASTROLOY

| Crack<br>Length (2a), $\mu\text{m}$ | $\Delta K$<br>$\text{MPa}/\text{m}$ | Crack-Tip<br>Strain, $\Delta\epsilon(0)$ | $r_p$ , $\mu\text{m}$ |                   |
|-------------------------------------|-------------------------------------|--|-----------------------|-------------------|
|                                     |                                     |  | $\phi = 0^\circ$      | $\phi = 90^\circ$ |
| CG Astroloy, 25°C                   |                                     |  |                       |                   |
| 45                                  | 4.9                                 | 0.042                                    | 5.6                   | 4.0               |
|                                     | 5.9                                 | 0.032                                    | 13.1                  | 3.0               |
| 67                                  | 5.9                                 | 0.120                                    | 15.3                  | 14.0              |
|                                     |                                     | 0.050                                    | 10.4                  | 5.0               |
| 71                                  | 5.4                                 | 0.0046                                   | 7.1                   | -                 |
|                                     |                                     | 0.0054                                   | 7.9                   | -                 |
| 72                                  | 6.2                                 | 0.016                                    | 4.9                   | 1.0               |
|                                     |                                     | 0.049                                    | 10.4                  | 5.0               |
| 102                                 | 6.5                                 | 0.068                                    | 21.1                  | 7.0               |
| CG Astroloy, 600°C                  |                                     |  |                       |                   |
| 42                                  | 4.4                                 | 0.038                                    | 5.9                   | 3.0               |
|                                     |                                     | 0.029                                    | 6.6                   | 2.0               |
| 54                                  | 5.1                                 | 0.060                                    | 7.6                   | 5.0               |
|                                     |                                     | 0.127                                    | 12.1                  | 11.0              |
| 66                                  | 5.4                                 | 0.107                                    | 30.5                  | 9.0               |
|                                     |                                     | 0.115                                    | 17.0                  | 10.0              |
| FG Astroloy, 600°C                  |                                     |  |                       |                   |
| 106                                 | 7.7                                 | 0.046                                    | 20                    | 3.0               |
|                                     |                                     | 0.057                                    | 25                    | 4.0               |
| 133                                 | 8.8                                 | 0.093                                    | 24                    | 8.0               |
|                                     |                                     | 0.043                                    | 28                    | 3.0               |
| 230                                 | 11.9                                | 0.036                                    | 29                    | 3.0               |
|                                     |                                     | 0.071                                    | 43                    | 6.0               |

plotted as a function of  $\Delta K$  in Figures 7-10 and 7-11, respectively. In neither case does  $r_p$  follow the parabolic relationship with  $\Delta K$  expected from analytical SSY results. The large variation in  $r_p$  versus  $\Delta K$ , particularly for  $\phi = 90^\circ$  (Figure 7-11) occurs because of the lack of symmetry observed in the deformation field of actual cracks.

In order to assess the extent to which the SSY concept applies to these small cracks, the ratio of crack size to plastic zone size ( $a/r_p$ ) for  $\phi = 0$  was examined. These results, given as a function of crack size in Figure 7-12, show that  $a/r_p$  was typically 2 to 4, but overall ranged from 1 to 8. These values are considerably smaller than that of  $a/r_p > 50$  which is generally thought to be required to insure SSY [7.9]. Consequently, an elastic-plastic crack-tip parameter is needed to adequately describe the driving force for the growth of small cracks. Such a parameter is considered in Section 8.

### 7.2.3 Crack Closure in Small Versus Large Cracks

The stereomaging technique was also used to measure the load required to fully open the tip of small cracks,  $P_{op}$ . These values were used to determine relative effective stress intensity factors,  $\Delta K_{eff}/\Delta K$ , using the following relationship derivable from basic crack closure definitions (see Section 4.4):

$$\Delta K_{eff}/\Delta K = (1 - P_{op}/P_{max})/(1 - R) \quad (7-6)$$

Results for small cracks are shown in Figure 7-13, along with the Soniak and Remy [7.10] data from large cracks which were previously discussed in Section 4.4. As indicated, values of  $\Delta K_{eff}/\Delta K$  for small cracks are relatively constant over a wide range of  $K_{max}$  (or  $\Delta K$ ) and are not measurably sensitive to material condition or test temperature. These small crack results are described by the following simple relationship:

$$\Delta K_{eff}/\Delta K = \beta \quad (7-7)$$

where  $\beta = 0.35$  for both FG and CG Astroloy at 25°C and 600°C. In contrast, as indicated in Figure 7-13, the long crack results in Astroloy are sensitive to both  $K_{max}$  and test temperature.

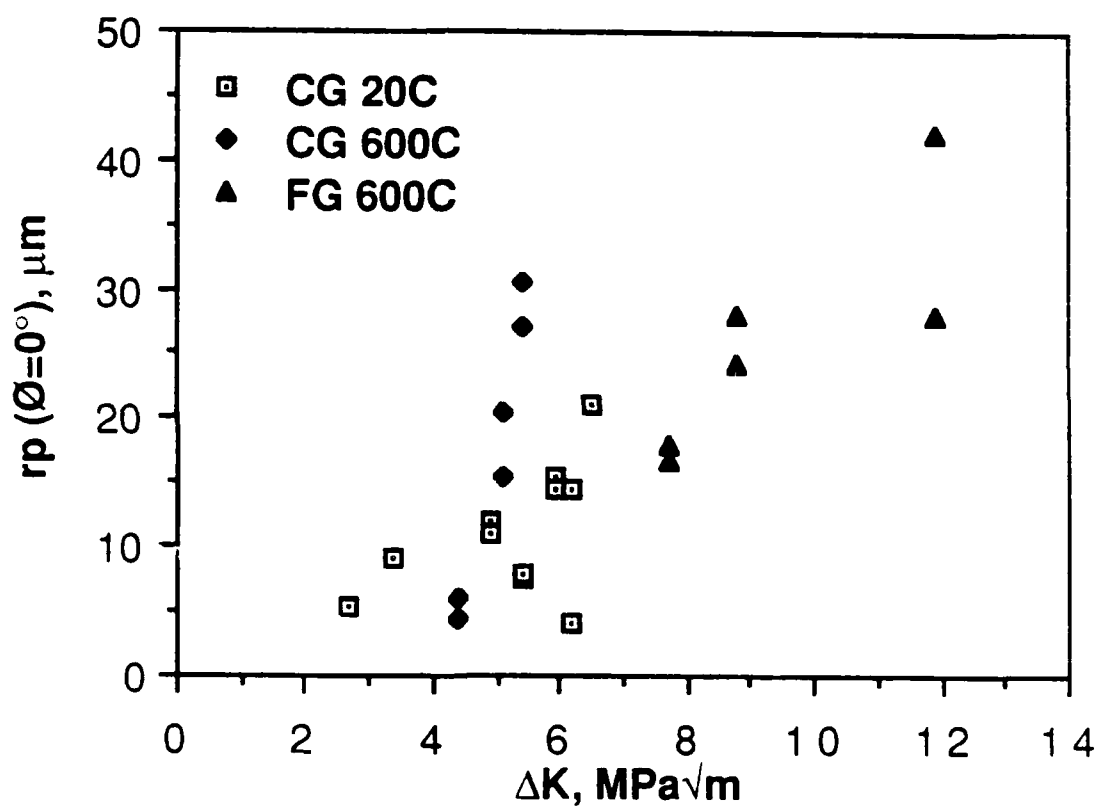


FIGURE 7-10. Cyclic plastic zone ahead ( $\phi = 0^\circ$ ) of the small crack as a function of applied  $\Delta K$ .

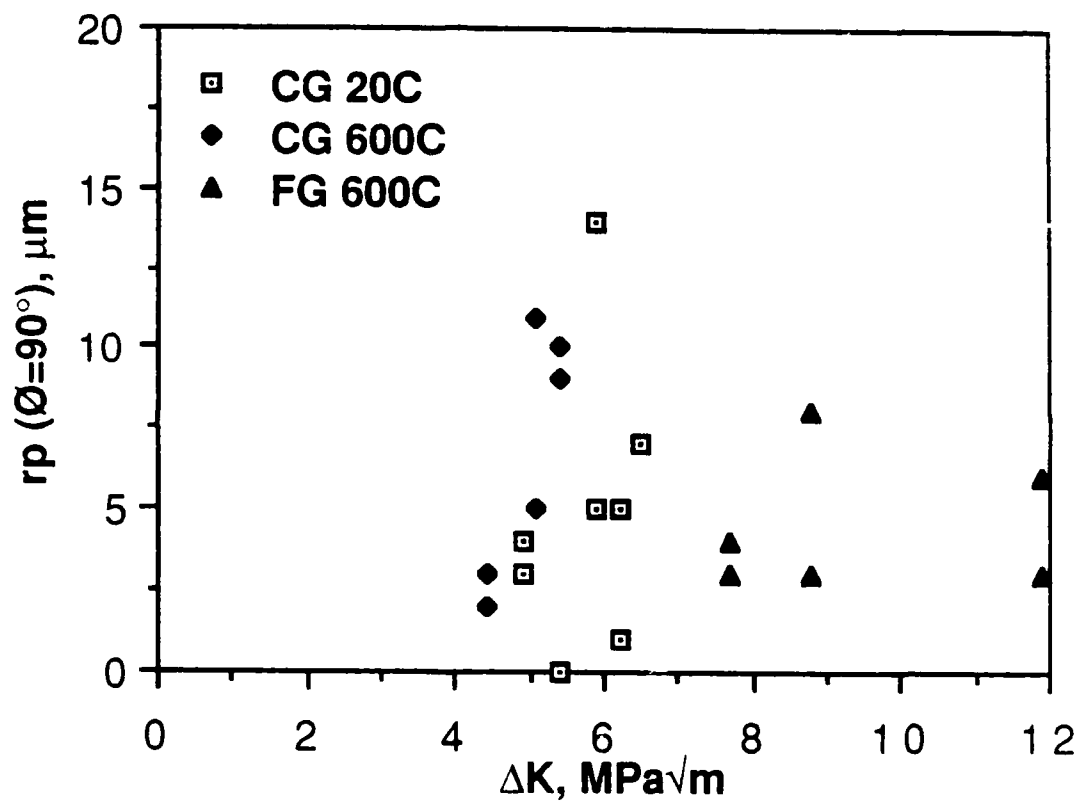


FIGURE 7-11. Cyclic plastic zone sizes to the side ( $\phi = 90^\circ$ ) of small cracks as a function of applied  $\Delta K$ .

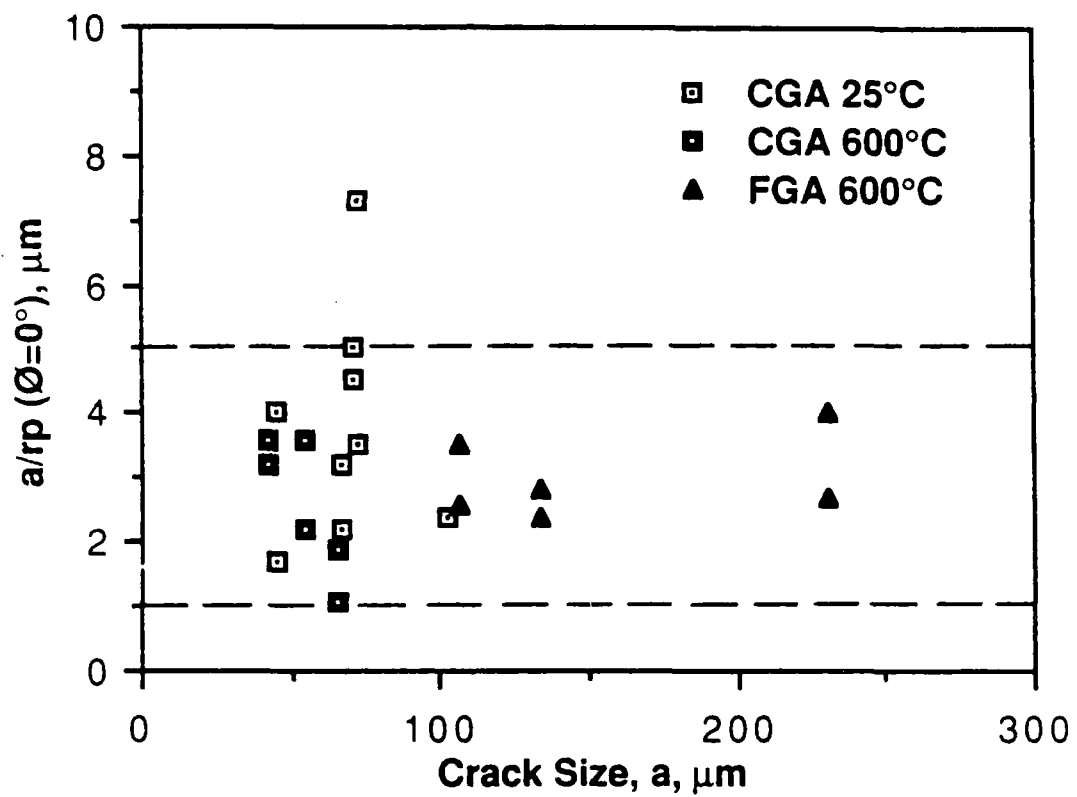


FIGURE 7-12. Ratio of crack size to plastic zone size ( $a/r_p$ ) for small cracks in Astroloy of various sizes.



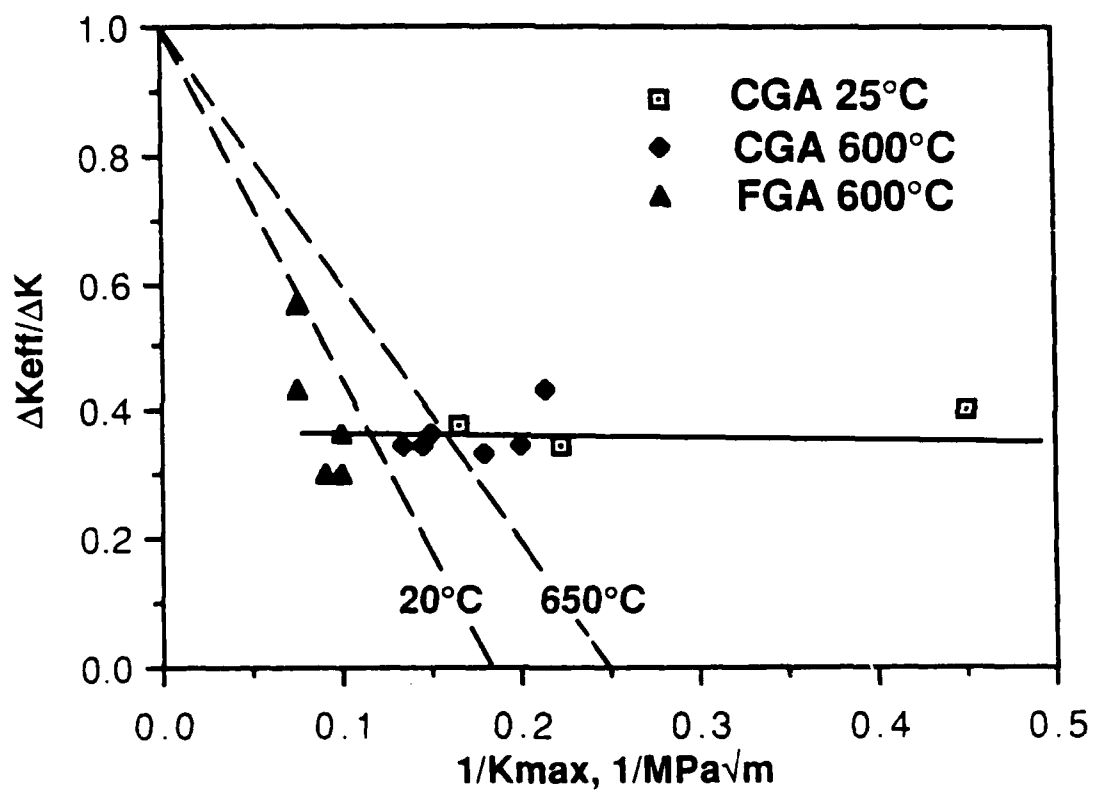


FIGURE 7-12. Comparison of crack closure behavior of small and large cracks at various temperatures. The dashed lines are from the large crack data of Soniak and Remy given in Section 4.4.

The above results in the Ni-base alloys are qualitatively similar to those observed recently in a 7075 aluminum alloy [7.11] as shown in Figure 7-14. In this case, both the small and large crack results were obtained using stereoimaging. These high resolution measurements clearly show that significantly more closure occurs in large cracks, than in small cracks, as  $K_{max}$  is decreased and  $\Delta K$  approaches the large crack threshold for fatigue crack growth.

Combining Eqs (7-6) and (7-7), and noting the identity  $P_{op}/P_{max} = K_{op}/K_{max}$ , gives:

$$K_{op}/K_{max} = 1 - (1-R) \beta \quad (7-8)$$

Thus, for a given  $R$ ,  $K_{op}/K_{max}$  is also constant for small cracks. This relationship is in agreement with recent small crack data of Soniak and Remy [7.10] on necklace Astroloy. The Soniak and Remy data for  $R = 0.1$  are shown in Figure 7-15. These data are consistent with the current results in that crack closure in small cracks was found to be insensitive to temperature. The deviation from Eq. 7-8 which occurs above a  $K_{max}$  of about 20 MPa $\sqrt{m}$  is believed to be due to the fact that the small cracks have grown to the length where they now exhibit closure more typical of large cracks. Furthermore, the fact that these data have a slope  $R$  is consistent with the linear relationship between  $\Delta K_{eff}/K$  versus  $1/K_{max}$  shown for large cracks in Figures 7-13 and 7-14.

For comparison, Figure 7-13 also contains the current results on Astroloy. Although both sets of results exhibit the same functional relationship, the current results give a higher  $K_{op}/K_{max}$  than do those of Soniak and Remy. The larger amount of crack closure given by the current data are believed to result from the fact that these measurements were acquired local to the crack tip, while those of Soniak and Remy are based on compliance measurements made remote from the crack tip. This interpretation is consistent with recent measurements of Su and Sharp [7.12], obtained using a laser-based interferometric displacement gage, which showed that  $K_{op}/K_{max}$  for small fatigue cracks in a 2024-T3 aluminum alloy increased significantly as the measurement location was moved toward the crack tip.

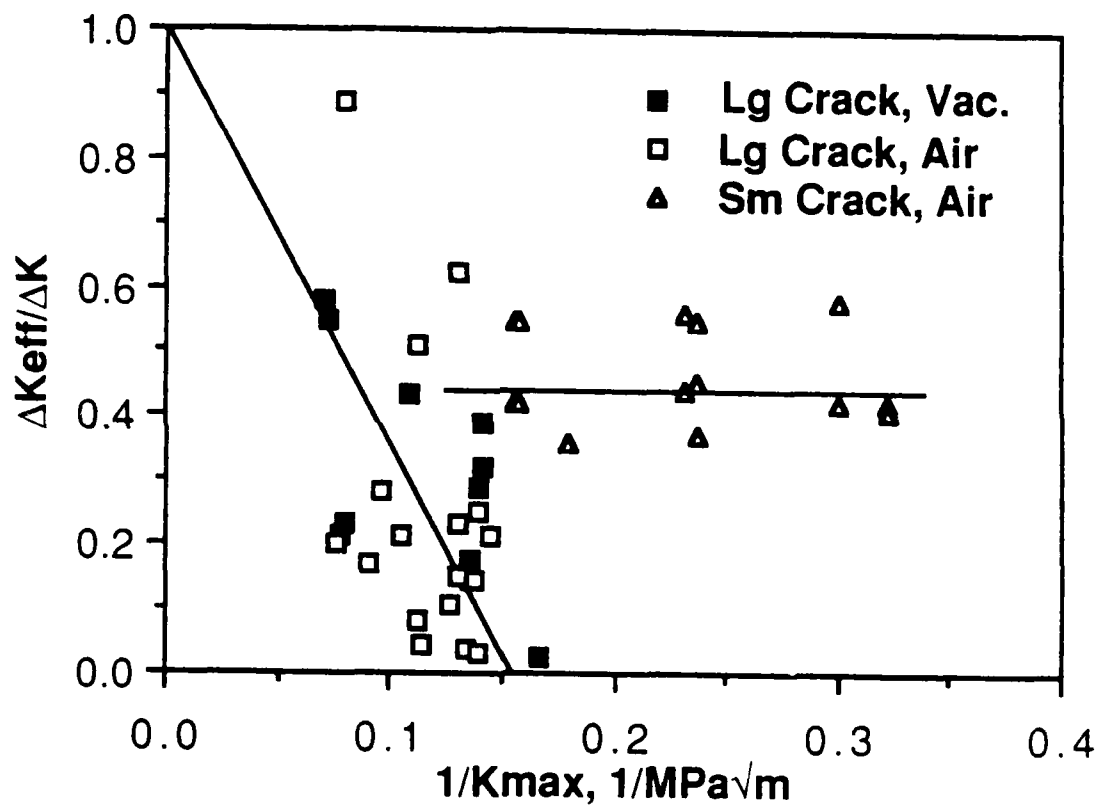


FIGURE 7-14. Crack closure behavior of small and large cracks in a 7075 aluminum alloy.

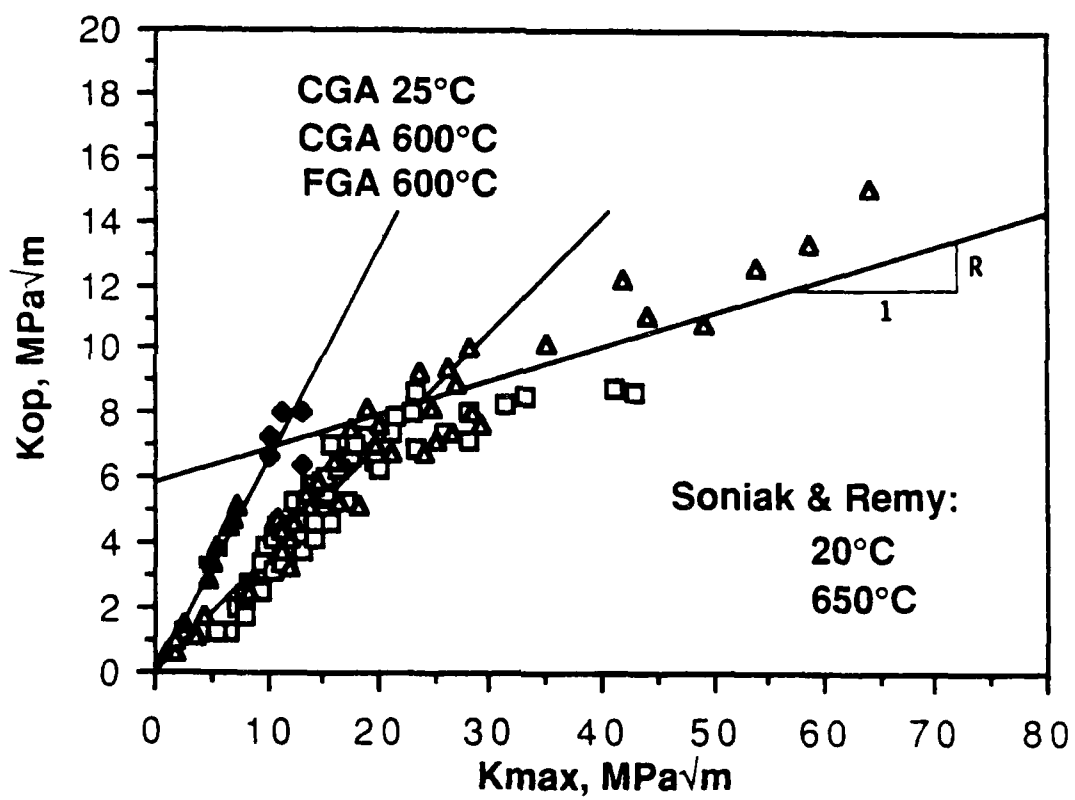


FIGURE 7-15. Comparison of  $K_{op}$  versus  $K_{max}$  data on small cracks in Astroloy from the current study with those of Soniak and Remy [7.10]. Note that the latter data exhibit large crack closure behavior above  $K_{max} \approx 20 \text{ MPa}\sqrt{m}$ .

### 7.3 References

- 7.1 D. L. Davidson and A. Nagy, "A Low Frequency Cyclic Loading Stage for the SEM," J. of Physics, Vol. E11, 1978, pp. 207-210.
- 7.2 A. Nagy, J. B. Campbell and D. L. Davidson, Review of Scientific Instruments, Vol. 55, 1984, pp. 778-782.
- 7.3 D. R. Williams, D. L. Davidson and J. Lankford, "Fatigue Crack Tip Plastic Strains by the Stereoimaging Technique," Exp. Mech., Vol. 20, 1980, p. 134.
- 7.4 D. L. Davidson, D. R. Williams and J. E. Buckingham, "Crack Tip Stresses as Computed from Strains Determined by Stereoimaging," Exp. Mech., June 1983, p. 242.
- 7.5 P. W. Tan, I. S. Raju and J. C. Newman, Jr., "Boundary Force Method for Analyzing Two-Dimensional Cracked Bodies," NASA Tech. Memo. 87725, NASA-Langley Research Center, May 1986.
- 7.6 J. Lankford and D. L. Davidson, "The Role of Metallurgical Factors in Controlling the Growth of Small Fatigue Cracks," in Small Fatigue Cracks, Eds. R. O. Ritchie and J. Lankford, TMS/AIME, 1987, pp. 51-71.
- 7.7 D. L. Davidson, Eng. Fract. Mech., Vol. 25, 1986, pp. 123-132.
- 7.8 D. L. Davidson, Met. Trans., Vol. 18A, 1987, in press.
- 7.9 W. F. Brown, Jr. and J. E. Srawley, "Plane Strain Crack Toughness Testing of High Strength Metallic Materials," ASTM STP 410, 1969.
- 7.10 F. Soniak and L. Remy, "Behavior of Long and Short Fatigue Cracks in a Power Metallurgy Superalloy at Room and at High Temperature," Fatigue '87, Eds. R. O. Ritchie and E. A. Starke, Jr., EMAS, 1987, pp. 351-360.
- 7.11 D. L. Davidson, "Small and Large Cracks in Aluminum Alloys," Acta Met., to be published.
- 7.12 X. Su and W. N. Sharpe, Jr., "An Experimental Study of Closure Behavior of Naturally Initiated Small Cracks," ibid, pp. 343-350.

## 8. A PHENOMENOLOGICAL MODEL FOR THE GROWTH OF SMALL CRACKS

This section uses the local crack-tip displacement measurements of the previous section to determine the mechanical driving force for the growth of small cracks based on the relationship between crack-tip opening displacement and  $\Delta J$ , the cyclic J-integral. To facilitate comparison with large crack data these results are expressed in terms of an equivalent stress intensity factor,  $\Delta K_{eq}$ . Since these results are based on local crack-tip measurements they contain the influence of mixed-mode loading, plasticity and crack closure. However, since these same factors cannot currently be computed for growing fatigue cracks subjected to cyclic loading,  $\Delta K_{eq}$  cannot simply be determined from knowledge of crack size, component geometry and remote loading. Thus, a phenomenological model is formulated in order to relate  $\Delta K_{eq}$  to the applied  $\Delta K$ . The ability of  $\Delta K_{eq}$  to produce crack growth kinetics which are independent of crack size is also assessed by comparing crack growth rates for both small and large cracks as a function of  $\Delta K_{eq}$ . The engineering utility of this approach is subsequently examined in Section 9.

### 8.1 The Relationship Between Cyclic CTOD and $\Delta J$

It is of interest to relate the cyclic CTOD values measured by stereoinaging to a crack-tip field parameter in attempting to establish a driving force for the growth of small fatigue cracks under elastic-plastic loading. Available elastic-plastic solutions for stationary cracks under monotonic loading are briefly reviewed since they provide guidance for the adoption of an operational relationship between the cyclic CTOD and  $\Delta J$ .

Hult and McClintock [8.1] have provided an analytical solution for a stationary crack under antiplane shear in an elastic-perfectly plastic material under small scale yielding. The relationship between Rice's J-integral [8.2] and CTOD for this case is as follows:

$$J_{III} = \pi/4(\tau_0 d_t) \quad (8-1)$$

where:  $J_{III}$  is the J-integral in Mode III,  $d_t$  = the crack tip sliding displacement under Mode III loading, and  $\tau_o$  = the yield stress in shear. It is interesting to note that the constant  $\pi/4$  in Eq. (8-1) is about 60 percent greater than the value of  $1/2$  obtained by Bilby, Cottrell and Swinden [8.3] using a strip-yield model [8.4].

For the case of Mode I loading, the asymptotic solutions of Hutchinson [8.5] and Rice and Rosengren [8.6] define the plastic crack-tip field for a power-hardening material experiencing proportional loading according to deformation theory of plasticity. One difficulty with this so-called HRR field is that the crack opening displacement tends to zero as the crack-tip is approached. To overcome this difficulty, Tracy [8.7], following Rice's suggestion, proposed that the CTOD,  $d_t$ , be operationally defined as shown in Figure 8-1. This definition, combined with the displacement equation for the HRR field, gives:

$$J = (1/d_n) \sigma_{ys} d_t \quad (8-2)$$

where:  $\sigma_{ys}$  = the tensile yield stress; and  $d_t$  is the operationally defined CTOD. The factor  $d_n$  depends primarily on stress state and strain hardening exponent, and mildly on the materials yield strain, as determined by Shih [8.8] using finite element analysis. For the case of plane strain and the range of cyclic strain hardening exponents for the materials and temperatures of interest to the present study ( $n = 0.145$  to  $0.029$ ),  $d_n$  is between 1.4 and 2.3. For the case of a perfectly plastic material under plane stress,  $d_n = 1$  and Eq.(8-2) gives results which are identical to those of the Dugdale-Barenblatt model [8.9, 8.10].

The primary limitation of the HRR field and Eq. (8-2), with respect to fatigue crack growth, is the fact that they are based on deformation theory of plasticity which assumes that the plastic strain is only dependent on the current state of stress and thus is independent of the path followed on arriving at this stress state. This condition is generally thought to be inapplicable at the tip of a growing fatigue cracks where unloading occurs behind the advancing crack and plastic deformation occurs at the crack-tip. Nevertheless, in spite of these analytical limitations, Dowling [8.11, 8.12]

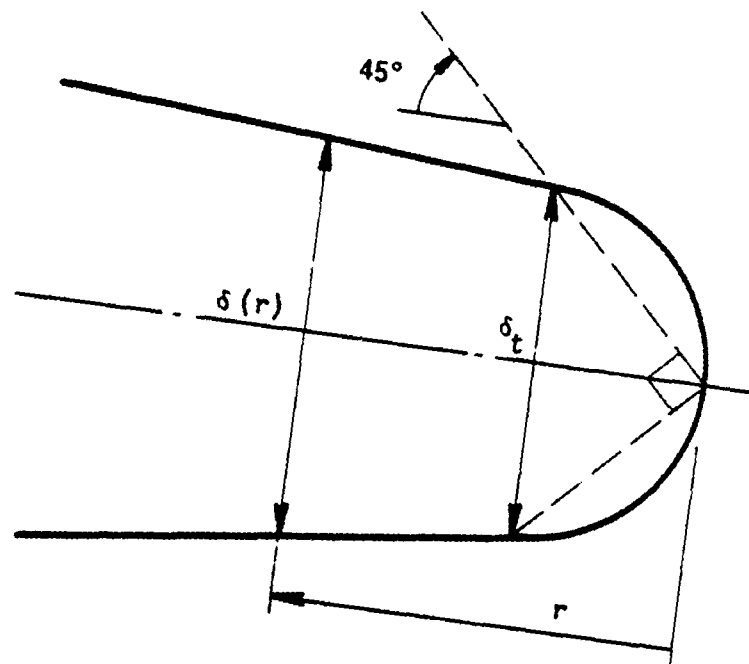


FIGURE 8-1. Operation definition used to determine the crack-tip opening displacement ( $\delta_t$ ) from numerical analyses [8.7].



has demonstrated the utility of the cyclic J-integral,  $\Delta J$ , for correlating the growth rates of large cracks for a variety of specimen geometries and loading conditions ranging from small scale yielding to fully plastic.

Lamda [8.13] has proposed that the  $\Delta J$ -integral can be formally defined by replacing the stress tensor, strain tensor, and displacement vector in Rice's J-integral [8.2] by their respective ranges. Furthermore, he has shown that the resulting  $\Delta J$ -integral is a path-independent, crack-tip field parameter for elastic-plastic materials, provided the constitutive behavior can be described in terms of the cyclic strain energy density as follows:

$$\sigma_{ij} = dW_{ij}/d\epsilon_{ij} \quad (8-3)$$

where  $\sigma_{ij}$  and  $\epsilon_{ij}$  are the stress range and strain range, respectively, and  $W$  is the cyclic strain energy density. Eq. (8-3) requires that the stress range only be a function of the current strain range and not the deformation history. As discussed in Ref. [8.14], these conditions are met by the cyclic stress-strain curve which is based on the stress and strain ranges associated with stable stress-strain hysteresis loops. Consequently, materials exhibiting stable cyclic plasticity appear to be treatable as a nonlinear elastic material through deformation theory of plasticity.

To evaluate the applicability of the above concept, Chan [8.15, 8.16] has used measured stress-strain fields from both large and small fatigue cracks to compute values of Lamda's  $\Delta J$ -integral for different line-contour integration paths around the crack tip. These results showed that  $\Delta J$  was relatively independent of the contour path, for distances greater than several CTOD values from the crack-tip. Moreover, the average contour-generated  $\Delta J$  values were found to be in good agreement with those computed directly from CTOD using:

$$\Delta J = \Delta \sigma \delta \quad (8-4)$$

where  $\Delta \sigma$  is the crack-tip stress range and  $\delta$  is the cyclic CTOD. Eq.(8-4) is significant in that it provides a means of relating the measured  $\delta$  values to  $\Delta J$  while avoiding much of the uncertainty associated with applying the

analytical solutions -- Eqs. (8-1) and (8-2) -- for monotonically loaded, stationary cracks to growing fatigue cracks.

## 8.2 Phenomenological Model for the Growth of Small and Large Fatigue Cracks

Local CTOD values for small cracks in CG and FG Astroloy at several temperatures were determined from the measured displacement fields of Section 7. These values were then used to compute  $\Delta J$  using Eq. (8-4). To facilitate comparison of the resulting small crack growth kinetics with those of large cracks,  $\Delta J$  was converted to an equivalent  $\Delta K$  using the following relationship [8.13]:

$$\Delta K_{eq} = (E\Delta J)^{1/2} = (E \Delta \sigma \delta_r)^{1/2} \quad (8-5)$$

where the crack tip stress range ( $\Delta \sigma$ ) was determined from the measured crack-tip strain range using the appropriate cyclic stress-strain relation from Section 3, and  $\delta_r$  is the vector-resolved value of the cyclic CTOD from Mode I and II. The latter were defined as the respective COD values at 0.5  $\mu m$  from the crack-tip. A summary of the crack-tip deformation parameters, along with the resulting  $\Delta K_{eq}$  values, is provided in Table 8-1.

Eq. (8-5) was also used to analyze available small crack data in a 7075 aluminum alloy at room temperature [8.17]. Resulting  $\Delta K_{eq}$  values for both 7075 aluminum and for Astroloy are given as a function of  $\Delta K_{eq}$  in Figures 8-2 and 8-3, respectively. Results in both materials indicate that  $\Delta K_{eq}$  is related to the applied  $\Delta K$  as follows:

$$\Delta K_{eq} = K_p + B\Delta K \quad (8-6)$$

The first and second terms in Eq. 8-6 are viewed as the plastic and elastic contributions, respectively, to the crack driving force. It is important to note that since  $\Delta K_{eq}$  was determined from measured cyclic crack-tip displacements, it contains the influence of crack closure, as well as plasticity and mixed mode-ness. Consequently, the second (elastic) term in Eq. (8-6) is merely  $\Delta K_{eff}$ . Thus, for the case of Astroloy, the value of  $B$  in Eq. (8-6) should coincide with the independent crack closure measurements of

**THE**

[illegible]

12-454-010y, 23-1

[illegible]

CG Astroloy. 500°C

[illegible]

3374

TABLE 8-1 (CONTINUED)

SUMMARY OF MEASURED CRACK-TIP STRESS, STRAIN AND DISPLACEMENT RANGES  
AND RESULTING  $\Delta K_{eq}$  VALUES FOR SMALL CRACKS IN ASTROLOY

| Crack<br>Length (2a), $\mu\text{m}$ | Inclined Crack<br>Angle, Deg. | Crack-Tip Measurements |                      |                          | $\Delta K_{\text{eq}}$<br>MPa $\sqrt{\text{m}}$ | $\Delta K$<br>MPa $\sqrt{\text{m}}$ |
|-------------------------------------|-------------------------------|------------------------|----------------------|--------------------------|---|-------------------------------------|
|                                     |                               | $\Delta\sigma$ (0)     | $\Delta\sigma$ , MPa | $\delta$ , $\mu\text{m}$ |   |                                     |
| FG Astroloy, 600°C                  |                               |                        |                      |                          |   |                                     |
| 106                                 | 90                            | 0.046                  | 2152                 | 0.104                    | 6.66  | 7.7                                 |
|                                     |                               | 0.057                  | 2234                 | 0.095                    | 6.48  |                                     |
| 133                                 | 90                            | 0.093                  | 2419                 | 0.102                    | 7.02  | 8.8                                 |
|                                     |                               | 0.043                  | 2126                 | 0.132                    | 7.49  |                                     |
| 230                                 | 90                            | 0.036                  | 2056                 | 0.165                    | 8.20  | 11.9                                |
|                                     |                               | 0.071                  | 2317                 | 0.160                    | 8.56  |                                     |

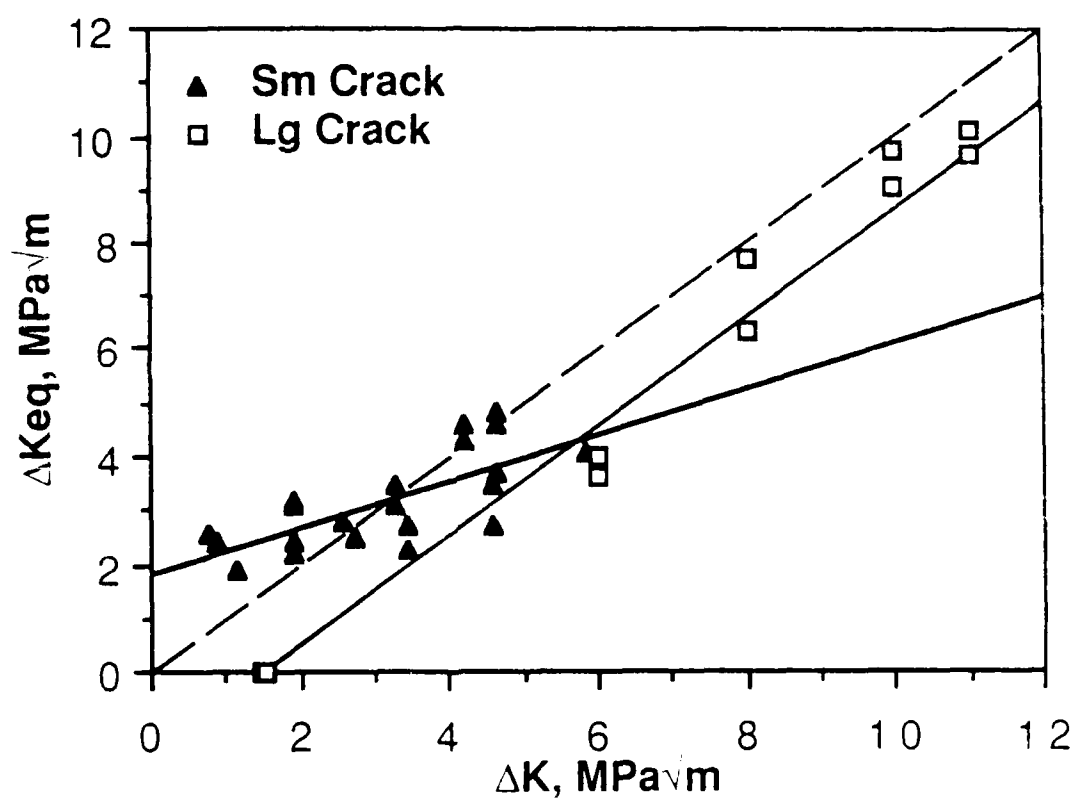


FIGURE 8-2. Equivalent stress versus applied  $\Delta K$  for small and large cracks in a 7075 aluminum alloy.

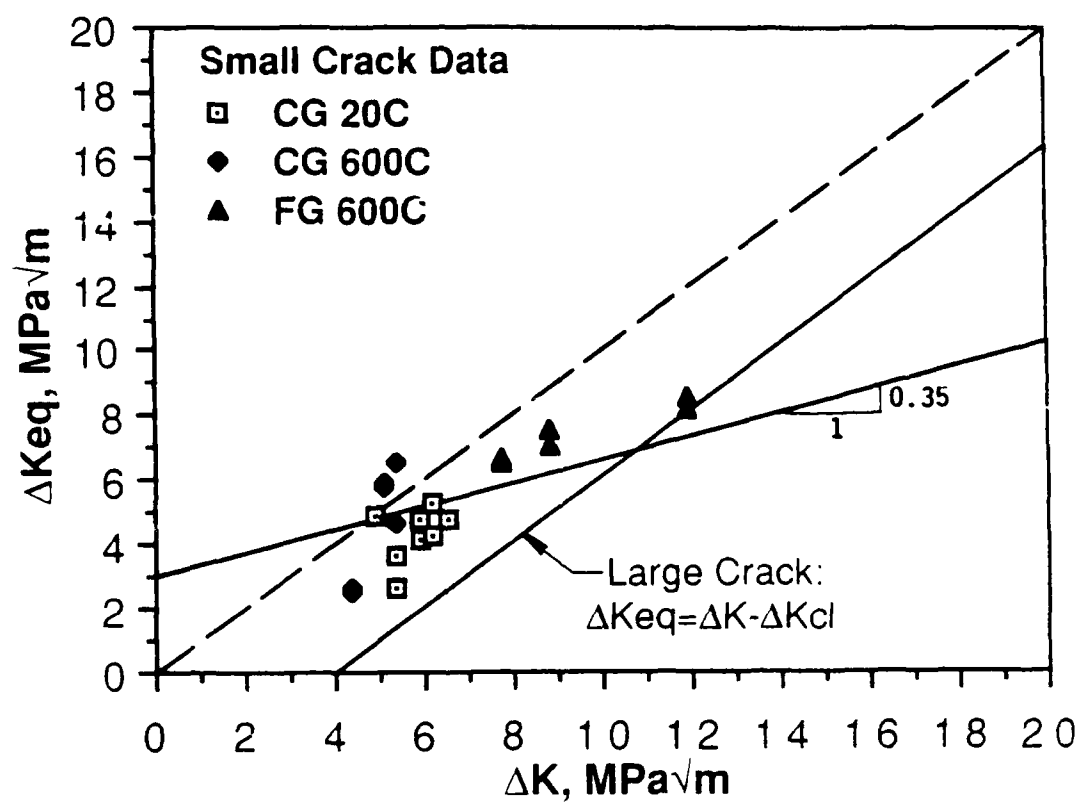


FIGURE 8-3. Equivalent versus applied  $\Delta K$  for small and large cracks in Astroloy at various temperatures.

Section 7 which showed:  $\Delta K_{eff}/\Delta K = 0.35 = \beta$ . This is verified by the fact that the straight line through the Astroloy small crack data in Figure 8-3, constructed using  $\beta = 0.35$ , is shown to provide a reasonable fit to the data.

For comparison, Figures 8-2 and 8-3 also contain the appropriate  $\Delta K_{eq}$  values for large cracks. Since large crack data are obtained under Mode I loading and small scale yielding conditions,  $\Delta K_{eq}$  for large cracks is simply given by:

$$\Delta K_{eq} = \Delta K_{eff} = \Delta K - \Delta K_{C1} \quad (8-7)$$

where  $\Delta K_{C1}$  is the portion of the applied  $\Delta K$  range over which the crack remains closed. For the case of the Astroloy data in Figure 8-3, a value of  $\Delta K_{C1} = 4.0 \text{ MPa}\sqrt{\text{m}}$  has been used based on the large crack results of Soniak and Remy [8.18] given in Section 4.2.

Eqs. (8-6) and (8-7) define a phenomenological model of the mechanical driving force for the growth of small and large cracks, respectively. This model is schematically summarized in Figure 8-4, together with the corresponding crack closure behavior, to emphasize the relationship among the various parameters of the model. In its present form, the model contains three fundamental parameters:  $K_0$  (or  $\Delta K_{C1}$ ), which characterizes crack closure in large cracks;  $\beta$ , which characterizes crack closure in small cracks; and  $\Delta K_p$ , which characterizes the plastic contribution to the crack driving force for small cracks. As indicated in Figure 8-4, the transition between so-called "small" and "large" crack behavior occurs in the model at a specific value of  $\Delta K$ , termed  $\Delta K_{tr}$ , which is defined by the above three parameters as follows:

$$\Delta K_{tr} = (\Delta K_p + \Delta K_{C1})/(1 - \beta) \quad (8-8)$$

The above concept would appear to be contrary to the commonly held notion that the transition from "small" to "large" crack behavior should occur at a given crack size. This issue is further discussed in Section 10.

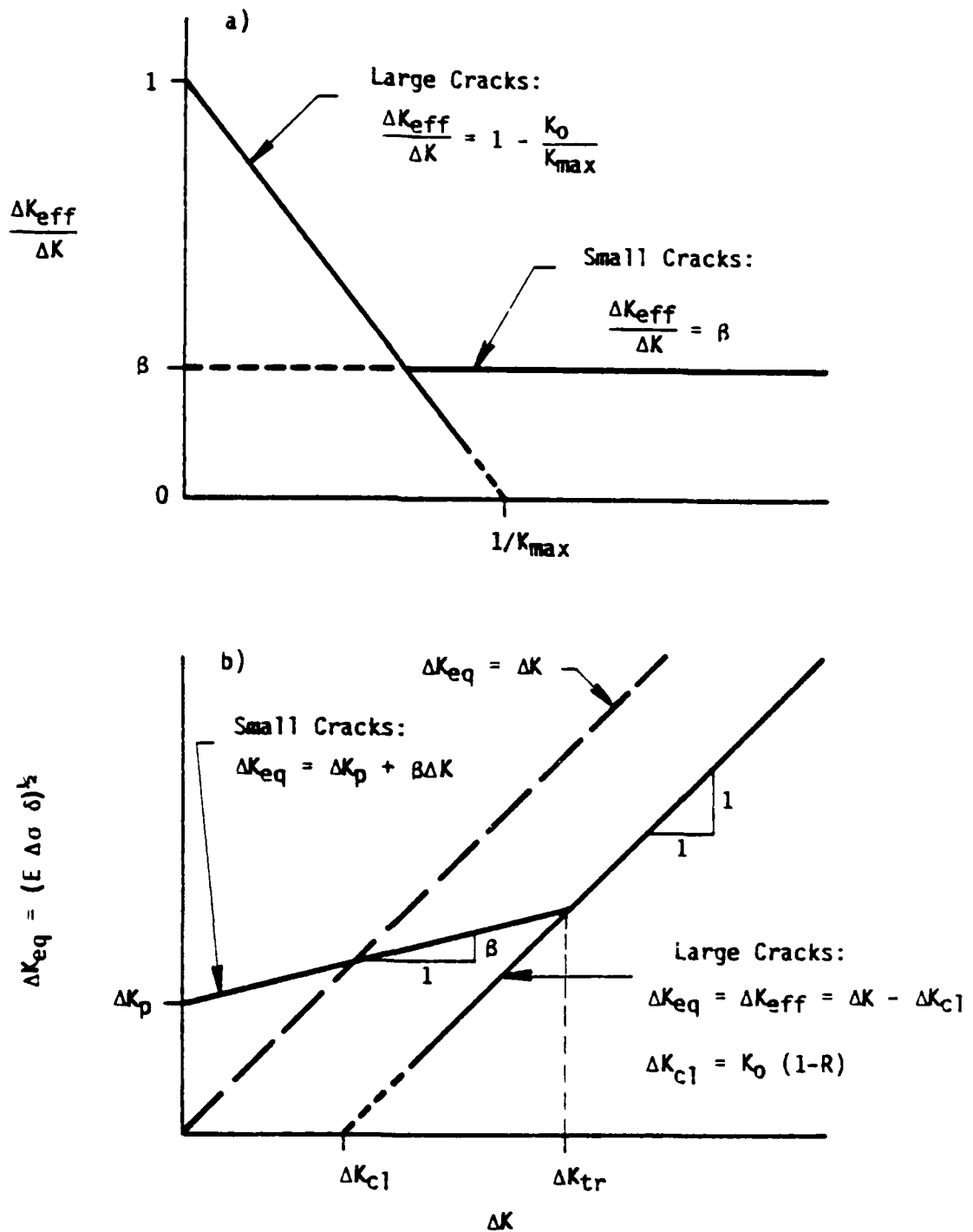


FIGURE 8-4. Phenomenological model for the growth of small and large fatigue cracks: a) is the crack closure behavior and b) is the local mechanical driving force versus applied  $\Delta K$ .



### 8.3 Small and Large Crack Growth Rates as a Function of $\Delta K_{eq}$ Versus $\Delta K_{eff}$

The growth rate data on small cracks obtained using the three-point bend specimens (Section 5) and the single-edge-notched tension specimens (Section 7) were analyzed using the above phenomenological model. In so doing, it is implicitly assumed that the model for the crack driving force is independent of specimen geometry. This is believed to be a good assumption since the model is based on direct measurement of local crack-tip deformation and crack closure, rather than on quantities inferred from remote measurements.

Because of the popularly held belief that crack closure alone is responsible for crack size effects, crack growth rate data were also examined in terms of  $\Delta K_{eff}$ . Within the context of the current measurements, this is equivalent to setting  $\Delta K_p = 0$  in Eq. (8-6) of the above phenomenological model.

Figure 8-5 shows the room temperature data on CG Astroloy as functions of both  $\Delta K_{eq}$  and  $\Delta K_{eff}$ . The large crack data in each case are given parametrically for a range of  $\Delta K_{CI}$  values intended to reflect the uncertainty in the determination of these values. Best estimates of  $\Delta K_{CI}$  based on the room temperature large crack closure measurements of Soniak and Remy [8.16] for necklace Astroloy are 3-5 MPa $\sqrt{m}$ . Based on these results,  $\Delta K_{eq}$  appears to provide a better consolidation of large and small crack growth kinetics than does  $\Delta K_{eff}$ .

Using the same format as that above, Figure 8-6 presents results on CG Astroloy at 600°C. In this case, the best estimate of  $\Delta K_{CI}$ , based on the 650°C large crack data of Soniak and Remy [8.16], is 2-4 MPa $\sqrt{m}$ . Once again  $\Delta K_{eq}$  appears to provide a better consolidation of small and large crack data. However, in this case there appears to be an downturn in the growth rate kinetics at about 3 MPa $\sqrt{m}$ . Such behavior is indicative of an intrinsic threshold for fatigue crack growth,  $\Delta K_{eq/th}$ . Similar results on Waspaloy at 600°C are shown in Figure 8-7. In presenting these results, it is implicitly assumed that the above empirical model parameters, developed for small cracks in Astroloy, are also applicable to Waspaloy. This assumption seems reasonable based on the fact that the growth rate behavior of small cracks is

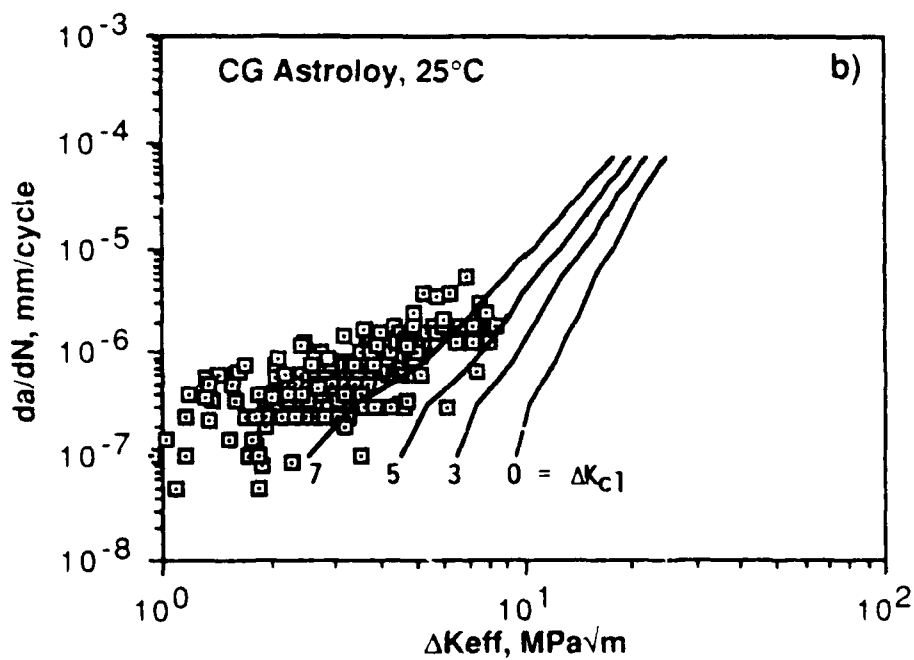
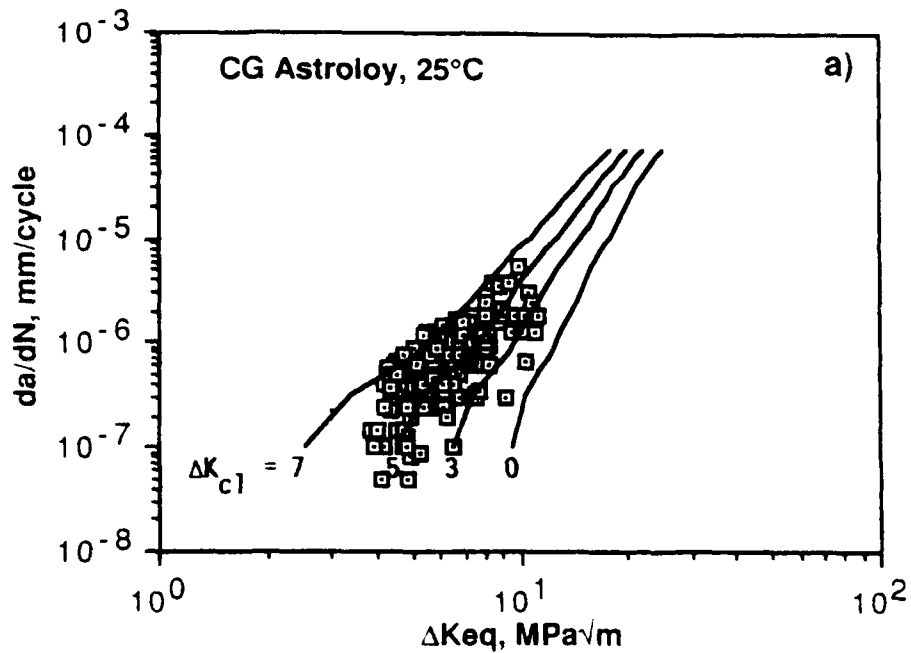


FIGURE 8-5. Comparison of crack growth kinetics of small ( $\square$ ) and large (—) cracks in CG Astroloy at 25°C in terms of a) equivalent and b) effective stress intensity factors.

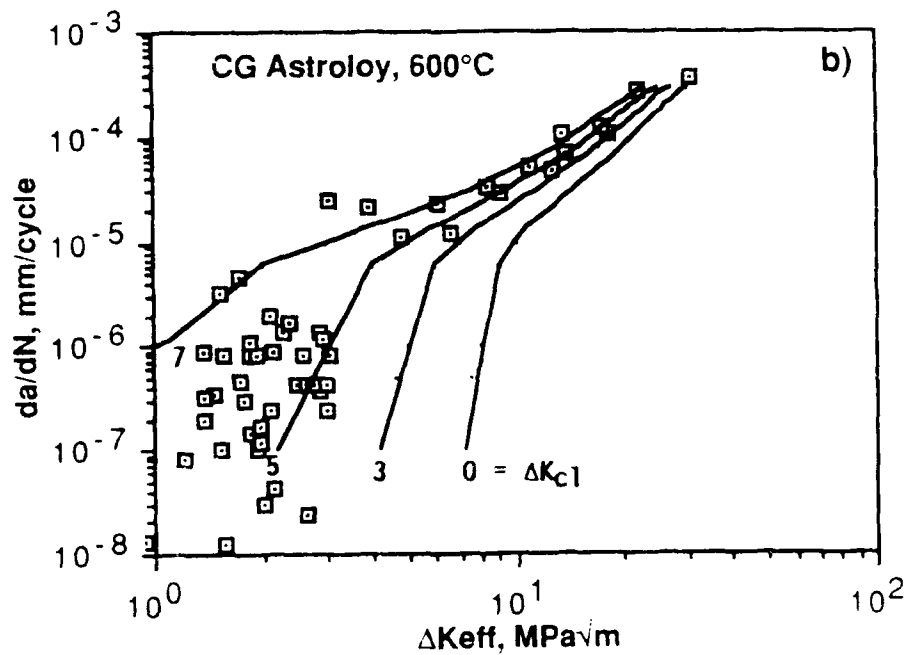
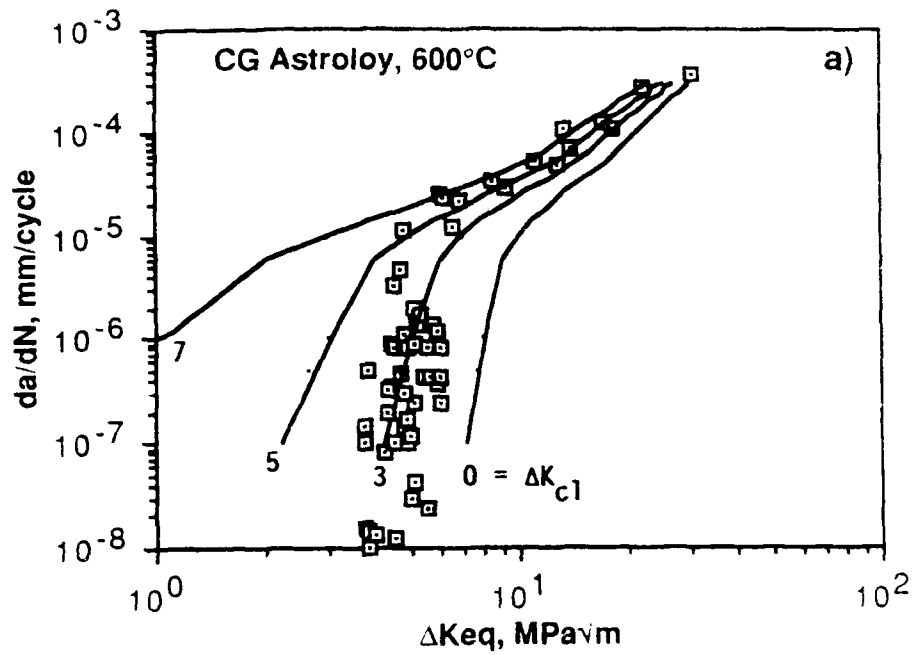


FIGURE 8-6. Comparison of crack growth kinetics of small ( $\square$ ) and large (—) cracks in CG Astroloy at 600°C in terms of a) equivalent and b) effective stress intensity factors.

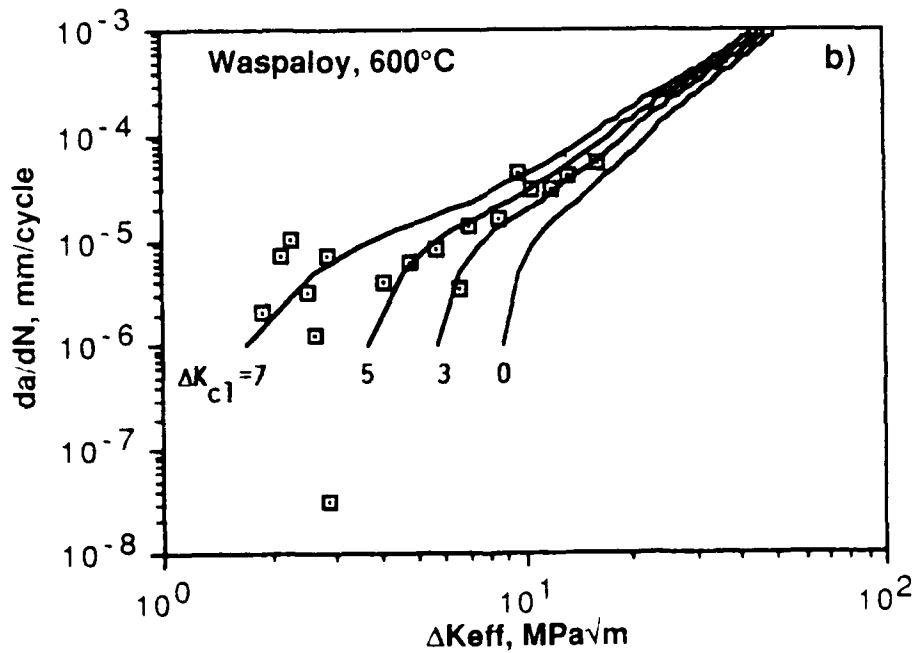
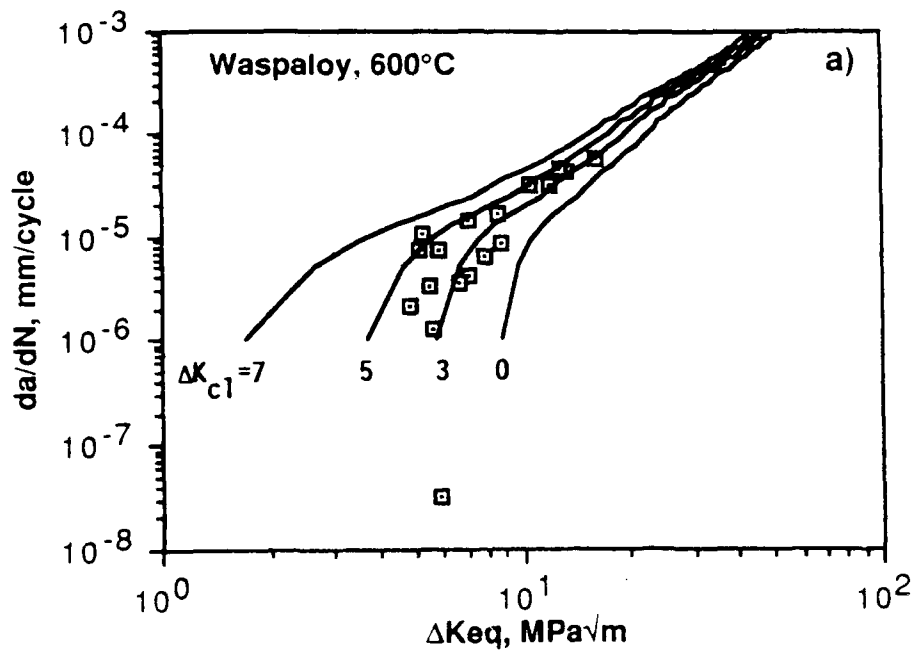


FIGURE 8-7. Comparison of crack growth kinetics in small ( $\square$ ) and large (—) cracks in Waspaloy at 600°C in terms of a) equivalent and b) effective stress intensity factors.

TABLE 8-2

MATERIAL CONSTANTS FOR THE PHENOMENOLOGICAL MODEL FOR THE GROWTH OF SMALL AND LARGE CRACKS

| Alloy       | Temp., °C | $C(1)$                 | $n$  | $\Delta K_{eq}/th$<br>MPa/m | $\Delta K_{cl}$<br>MPa/m | $\beta$ | $\Delta K_p$<br>MPa/m |
|-------------|-----------|------------------------|------|-----------------------------|--------------------------|---------|-----------------------|
| CG Astroloy | 25        | $2.01 \times 10^{-13}$ | 4.29 | 0                           | 5.0                      | 0.35    | 3.0                   |
| CG Astroloy | 200       | $2.39 \times 10^{-11}$ | 2.54 | 0                           | 5.0                      | 0.35    | 3.0                   |
| CG Astroloy | 600       | $1.59 \times 10^{-10}$ | 2.31 | 3.0                         | 4.0                      | 0.35    | 3.0                   |
| Waspaloy    | 600       | $8.75 \times 10^{-11}$ | 2.41 | 3.0                         | 4.0                      | 0.35    | 3.0                   |

(1) Derived for  $da/dN$  in m/cycle and  $\Delta K$  in MPa/m.

relatively insensitive to alloy composition and microstructure, as discussed in Section 5.5.3.

Based on all of the above results it appears that a reasonable representation of the crack growth kinetics for both large and small cracks can be obtained from the following equation:

$$da/dN = C(\Delta K_{eq} - \Delta K_{eq/th})^n \quad (8-9)$$

where C and n are empirical constants, and  $K_{eq/th}$  is the intrinsic threshold stress intensity factor. Values of C, n,  $K_{eq/th}$  and  $\Delta K_{cl}$ ,  $\beta$  and  $\Delta K_p$  [from Eqs. (8-6) and (8-7)] for the materials of interest here are given in Table 8-2.

#### 8.4 References

- 8.1 J.A.H. Hult and F. A. McClintock, "Elastic-Plastic Stress and Strain Distributions Around Sharp Notches Under Repeated Shear," Proc. of the 9th International Congress for Applied Mechanics, Vol. 8, Univ. of Brussels, 1957, pp. 51-58.
- 8.2 J. R. Rice, "A Path Independent Integral and the Approximate Analysis of Strain Concentration by Notches and Cracks," ASME Journal of Applied Mechanics, Vol. 35, 1968, pp. 379-386.
- 8.3 B. A. Bilby, A. H. Cottrell and K. H. Swinden, "The Spread of Plastic Yield from a Notch," Proc. of the Royal Society, Series A, Vol. 272, 1963, pp. 304-314.
- 8.4 Advanced Fracture Mechanics by M. F. Kanninen and C. H. Popelar, Oxford, New York, 1985, p. 295.
- 8.5 J. W. Hutchinson, "Plastic Stress and Strain Fields at a Crack Tip," Journal of Mechanics and Physics of Solids, Vol. 16, 1968, pp. 337-347.
- 8.6 J. R. Rice and G. F. Rosengren, "Plane Strain Deformation Near a Crack Tip in a Power-Law Hardening Material," Ibid, pp. 1-12.
- 8.7 D. M. Tracy, "Finite Element Solutions for Crack-Tip Behavior in Small-Scale Yielding," ASME Journal of Eng. Matls. and Tech., Vol. 98, 1976, pp. 146-151.
- 8.8 C. F. Shih, "Relationship Between the J-Integral and the Crack Opening Displacement for Stationary and Extending Cracks," Journal of Mechanics and Physics of Solids, Vol. 29, 1981, pp. 305-326.

- 8.9 D. S. Dugdale, "Yielding of Steel Sheets Containing Slits," Journal of Mechanics and Physics of Solids, Vol. 8, 1960, pp. 100-104.
- 8.10 G. I. Barenblatt, "The Mathematical Theory of Equilibrium of Cracks in Brittle Fracture," Advances in Applied Mechanics, Vol. 7, 1962, pp. 55-129.
- 8.11 N. E. Dowling and J. A. Begley, "Fatigue Crack Growth During Gross Plasticity and the J-Integral," in Mechanics of Crack Growth, ASTM STP 590, 1976, pp. 82-103.
- 8.12 N. E. Dowling, "Geometry Effects and the J-Integral Approach to Elastic-Plastic Fatigue Crack Growth," in Cracks and Fracture, ASTM STP 601, 1976, pp. 19-32.
- 8.13 H. S. Lamba, "The J-Integral Applied to Cyclic Loading," Engr. Fract. Mech., 1975, pp. 693-703.
- 8.14 S. J. Hudak, Jr., and K. S. Chan, "In Search of a Driving Force to Characterize the Kinetics of Small Crack Growth," in Small Fatigue Cracks, Eds. R. O. Ritchie and J. Lankford, TMS/AIME, 1986, pp. 379-405.
- 8.15 K. S. Chan, "Load Crack-Tip Field Parameters for Large and Small Cracks: Theory and Experiment," ibid, pp. 407-425.
- 8.16 K. S. Chan, J. Lankford and D. L. Davidson, "A Comparison of Crack-Tip Field Parameters for Large and Small Fatigue Cracks," ASME Journal of Engr. Matls. and Tech., Vol. 108, July 1986, pp. 206-213.
- 8.17 D. L. Davidson, "Small and Large Cracks in Aluminum Alloys," Acta Met., to be published.
- 8.18 F. Soniak and L. Remy, "Behavior of Long and Short Fatigue Cracks in a Powder Metallurgy Superalloy at Room and High Temperature," in Fatigue '87, Eds. R. O. Ritchie and E. A. Starke, Jr., EMAS, 1987, pp. 351-360.

## 9. EFFECT OF SMALL CRACK BEHAVIOR ON COMPONENT FATIGUE LIFE

The fatigue lives of actual rig-tested turbine discs have been computed using the phenomenological model for small crack growth presented in Section 8. Predicted versus measured lives are compared in order to assess the utility of the proposed model. The predicted lives based on the small crack model are also compared with those obtained using the conventional linear elastic fracture mechanics and large crack data. The influence of the large crack threshold stress intensity,  $\Delta K_{th}$ , on the latter predictions is also examined.

### 9.1 Analysis of Rig-Tested Discs

Engine disc test data were taken from two sets of rig tests: one for Waspaloy, and a second for Astroloy. The Waspaloy discs were manufactured identically to the Waspaloy material used in the current program. The Astroloy discs were manufactured via a 1160°C hip-plus-forge route resulting in a necklace microstructure having both 5  $\mu m$  and 40  $\mu m$  grain sizes. This microstructure was originally chosen to provide optimum crack growth rate behavior in both the small and large crack regimes [9.1]. In contrast, work in the current program has focused on fine and coarse grained variants of Astroloy in order to obtain a more fundamental understanding of the mechanism of small crack growth. Nevertheless, due to the observed insensitivity of small crack growth to microstructural variations, the coarse grained results from Section 7 are assumed to apply to the analysis of the necklace Astroloy rig tests. However, since large crack growth rates have been shown, both in Section 4 and elsewhere [9.1-9.3], to be sensitive to microstructure, the data from Section 4 were used in making the large crack predictions. Specifically, the large crack data of Figure 4-14 and Figure 4-21 were used for the large crack predictions in necklace Astroloy and in Waspaloy, respectively.

Discs in the rig tests were typically cycled at zero-maximum-zero speed over a period of 12 seconds, thus the applied load ratio was near zero and the nominal cyclic frequency was 5 cpm.

The calculation of applied  $\Delta K$  for use in Eqs. (8-6) and (8-7) were based on Pickard's [9.4] stress intensity factor solutions for corner cracks and surface cracks, and incorporated disc stress distributions which accounted for



residual stresses imparted during manufacturing, particularly those generated by heat treatment. The analysis techniques used have been previously validated against rig tests which contained preintroduced (large) cracks of known initial size [9.5]. Several disc features were analyzed -- that is bores, diaphragms and bolt holes -- depending on the location in the disc where the particular failure originated.

Since none of the discs analyzed were precracked, the initial crack size was assumed to be either a semicircular corner or surface crack having the radius or the average grain size of the material -- that is, 40  $\mu\text{m}$  for both Waspaloy and Astroloy. This is considered a physically realistic lower limit of the integration since crack growth across the initial grain was rarely observed in the small crack experiments. In one instance, failure in an Astroloy disc clearly originated from a 60  $\mu\text{m}$  ceramic inclusion, located near a free surface. This particular defect was idealized as a 90  $\mu\text{m}$  surface crack based on its near-surface location and the fact that little or no initiation life was expected.

With regard to the implementation of the phenomenological model for the growth of small cracks, the transition between small and large crack behavior was made at a transition  $\Delta K_{tr}$  defined by Eq. (8-8)

## **9.2 Comparison of Predicted Versus Measured Disc Lives**

The ratios of predicted to measured lives for all of the discs analyzed are summarized in Figure 9-1. The life ratios labeled "Small Crack" were obtained using small crack kinetics below  $\Delta K_{tr}$  and large crack kinetics above  $\Delta K_{tr}$ , whereas those labeled "Large Crack" were obtained using the large crack kinetics throughout the computation. As one might expect, the small crack predictions give consistently smaller life ratios than do the large crack predictions, although the relative difference between the two sets of predictions varies greatly, depending on the particular case analyzed.

On average, the life ratio for the small crack predictions was 0.77. This value is consistent with the fact that crack initiation undoubtedly contributed to the measured cyclic lives, but was not included in the predictions. For example, for actual discs the initiation life has been estimated to be between 5 percent and 10 percent of the total fatigue life [9.5]. An average life ratio in the case of the large crack predictions is

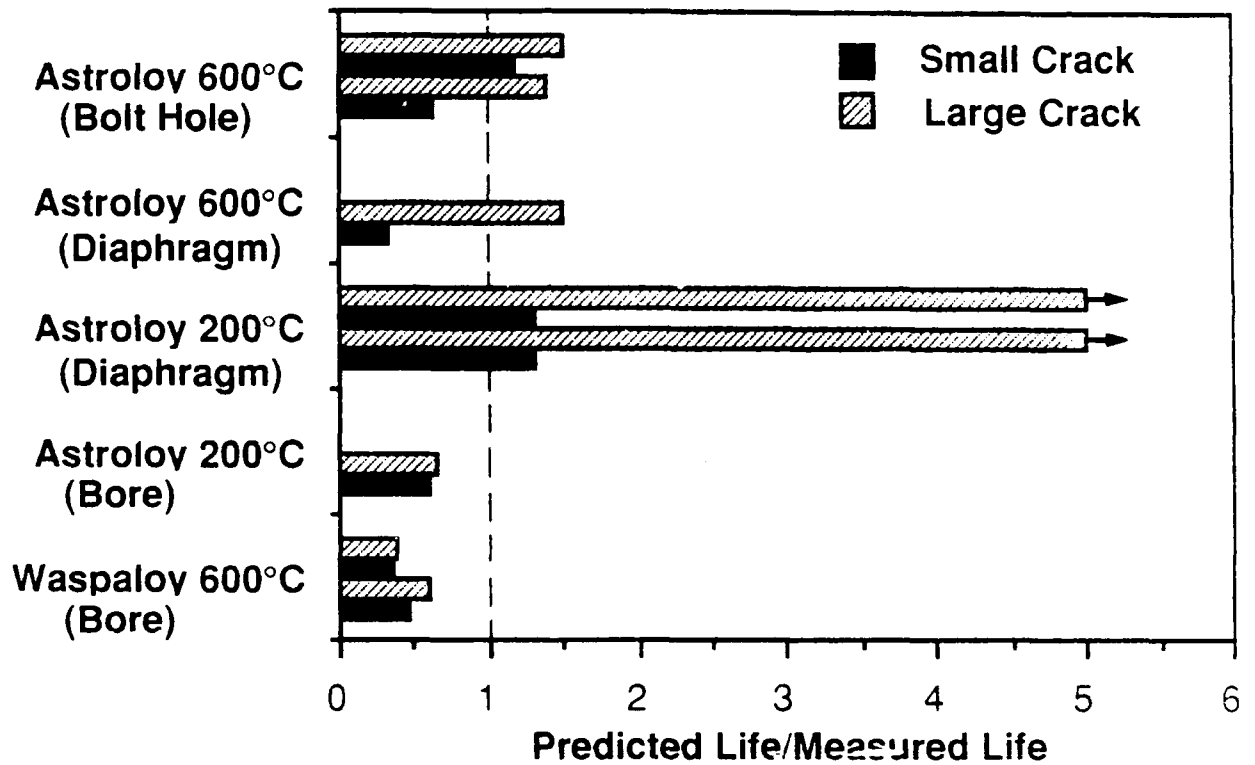


FIGURE 9-1. Influence of the small crack effect on the cyclic life ratio for various disc temperatures and failure locations.

somewhat more difficult to interpret due to the large overprediction which occurred for the case of the Astroloy diaphragm cracks at 200°C. Excluding these overpredictions gives a life ratio for the large crack predictions of 1.0, however, including the overpredictions gives a life ratio of between 26 and infinity. The uncertainty in the latter value arises from the fact that the long crack predictions in the case of the Astroloy diaphragm crack at 200°C predicted a life which was several orders of magnitude larger than the measured life since the initial  $\Delta K$  in the computation was less than the measured  $\Delta K_{th}$  value for necklace Astroloy. Overall, the small crack predictions appear to provide a more realistic view of the behavior of the rig-tested discs.

The actual predicted versus measured lives are compared in Figure 9-2. As indicated, most of the predictions are within a factor of  $\pm 2$  of the measured lives. The shortest life was for the case of bolt hole cracking in Astroloy at 600°C and was due to the presence of a near-surface 60  $\mu m$  ceramic inclusion. The longest life was for one of the diaphragm cracks in an Astroloy disc at 200°C. In general, these results show that the deviation between the small and large crack predictions increases as the life increases. This is not surprising since the lower stresses, and associated stress intensity factors, for these cases cause more crack growth to occur below  $\Delta K_{tr}$  in the small crack model. The major deviations are therefore associated with the marked reduction in the growth rates of the large cracks as the long crack threshold is approached.

In order to further examine the influence of the large crack threshold on the predicted lives, selected discs were analyzed using the measured long crack growth rates above about  $10^{-6}$  mm/cycle to obtain a power law relation which was extrapolated below  $\Delta K_{th}$ . In other words, the near-threshold behavior was ignored and a simple Paris law was used to describe the growth rates. These results, labeled "Large/no  $\Delta K_{th}$ ", are given in Figure 9-3 where they are compared with the previous small and large crack predictions. Although the Large/no  $\Delta K_{th}$  predictions still overpredict the measured lives, the deviation is now only about a factor of two. Thus, it appears that a first order engineering approximation for small crack effects can be obtained by simply ignoring the long crack threshold and using a simple Paris Law to describe the fatigue crack growth kinetics. The utility of this approach as

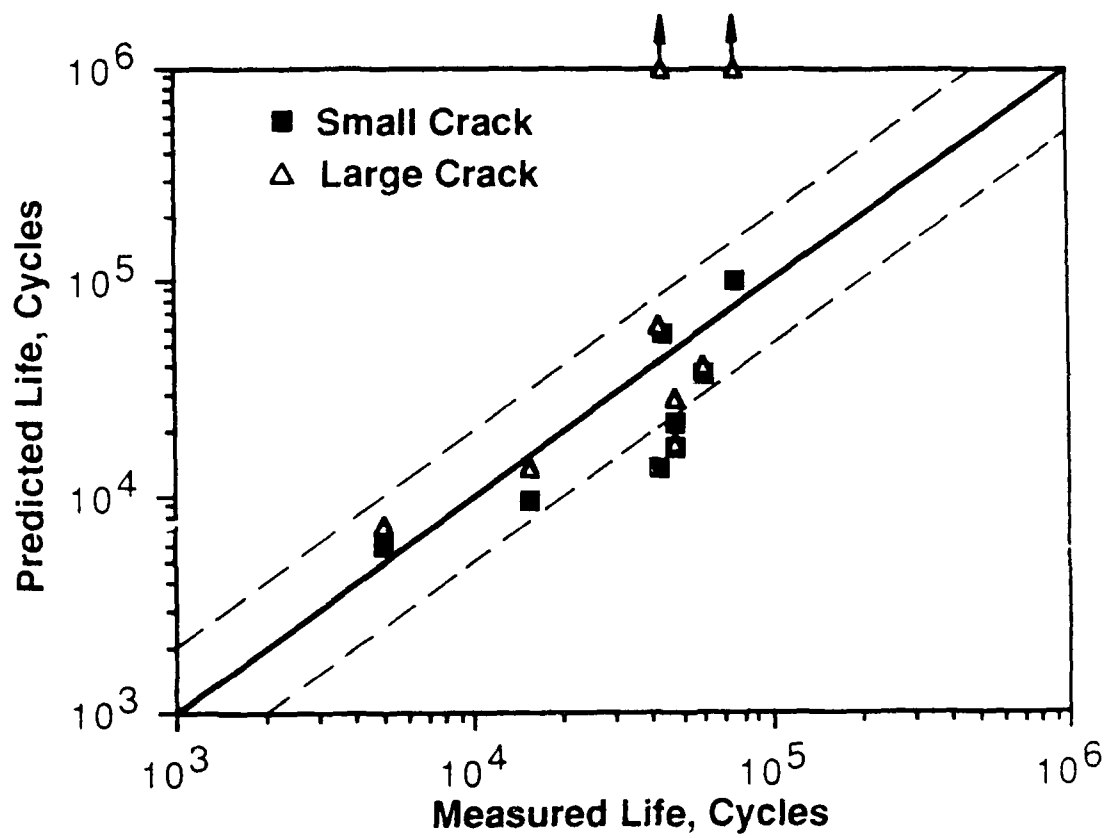


FIGURE 9-2. Comparison of measured disc lives with those predicted using small versus large crack growth kinetics.

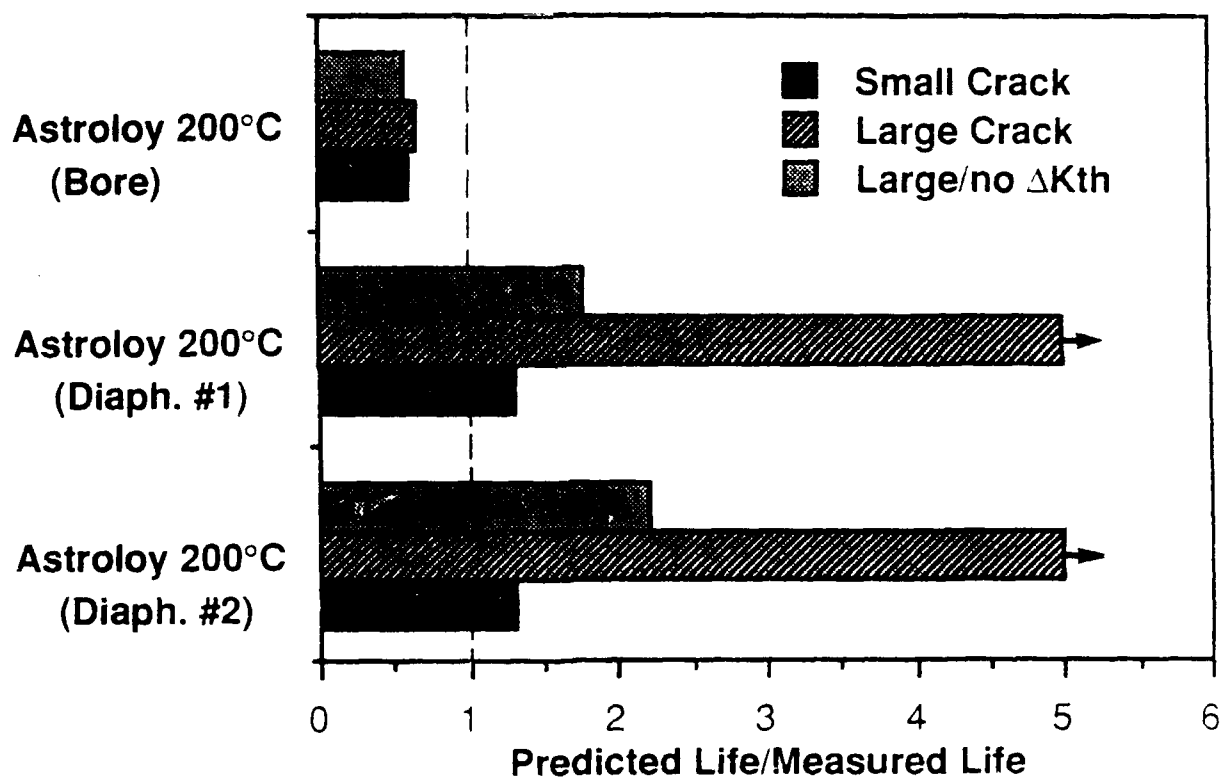


FIGURE 9-3. Influence of various crack growth rate "laws" on the cyclic life ratio.

well as the viability of the phenomenological small crack model is further discusses further in Section 10.

### 9.3 References

- 9.1 C. W. Brown, J. E. King and M. A. Hicks, "Effect of Microstructure on Long and Short Crack Growth in Nickel Base Superalloys," Metals Science, Vol. 18, 1984, pp. 374-380.
- 9.2 M. A. Hicks and J. E. King, "Temperature Effects on Fatigue Thresholds and Structure Sensitive Crack Growth in a Nickel-Base Superalloy," Int. J. of Fatigue, Vol. 5, April 1983, pp. 67-74.
- 9.3 J. E. King, "Fatigue Crack Propagation in Nickel-Base Superalloys-- Effects of Microstructure, Load Ratio, and Temperature," Materials Science and Technology, Vol. 3, September 1987, pp. 750-764.
- 9.4 A. C. Pickard, "The Application of Three-Dimensional Finite Element Methods to Fracture Mechanics and Fatigue Life Prediction," EMAS, 1986.
- 9.5 A. C. Pickard, M. A. Hicks and R. H. Jeal, "Applications of Fatigue Analyses: Aircraft Engines," Fatigue '87, Vol. IV, Eds. R. O. Ritchie and E. A. Starke, Jr., 1987.

## 10. DISCUSSION

Based on the metallography, selected area electron channeling, and fractography of Section 6, it appears that small and large cracks in Ni-base superalloys grow by a similar mechanism. The electron channeling patterns from within individual grains of Astroloy containing small cracks showed that the preferred crack plane was  $\{111\}$ . These results are in agreement with those of Beevers [10.1] on small cracks in Astroloy obtained using the same technique. Moreover, this preferred cracking orientation is consistent with that which has been determined for large cracks using a variety of techniques [10.2-10.6]. These results are also consistent with the slip character of Ni-base alloys, as well as the crystallographic facetting observed on the fracture surfaces of both small and large cracks. Furthermore, the fracture morphologies for small and large cracks also exhibit the same temperature and applied stress dependence. Thus, it appears that the mechanism of crack extension in small and large cracks is fundamentally the same and that apparent differences in their kinetics, when expressed in terms of  $\Delta K$ , are due to differences in mechanical driving force and not to actual differences in their mechanism of extension.

The local crack-tip deformation and crack closure measurements of Section 7 provide a direct means of assessing those processes which influence the crack driving force for small cracks. Based on the ratio of crack size to plastic zone size (typically,  $a/r_p = 1$  to 5), it is clear that the linear elastic fracture mechanics (LEFM) concept of small scale yielding (SSY:  $a/r_p > 50$ ) [10.7] does not hold for small cracks. As evidenced by the data obtained on CG Astroloy at room temperature, SSY can even be violated when the applied stress is less than the materials yield strength. Violation of the SSY condition is consistent with enhanced crack-tip strains and altered strain distribution exhibited by small cracks, relative to those which exist at large cracks at the same  $\Delta K$ . In view of this situation, it is not surprising that the crack closure behavior of small and large cracks differs so significantly, as shown in Section 7.4. In addition to these effects, small cracks in coarse grained Ni-base superalloys also exhibit significant mixed-Mode displacements due to their preferred cracking planes within the crystallite. This effect also needs to be included in the crack driving force for small cracks.

As demonstrated in Sections 7 and 8, local cyclic CTOD measurements appear to capture all of the above effects. Thus, converting these local CTOD measurements to  $\Delta J$ , or equivalently to  $\Delta K_{eq}$ , provides a measure of the crack driving force which results in crack growth kinetics which are independent of crack size, within experimental scatter (Section 8.3). These results also provide insight into why previous attempts to explain small crack effects solely on the basis of crack closure have met with limited success [10.8-10.11]. In these instances, it was generally assumed that the growth of small cracks was a closure-free process. This view probably developed due to the fact that remote compliance measurements were of insufficient precision to detect crack closure in small cracks. Consequently, the primary difference between small and large cracks was attributed to the closure which occurred in large cracks, and was measurable by remote techniques. In view of the current results, it is clear that the erroneously neglecting crack closure in small cracks is approximately offset by erroneously neglecting the plasticity contribution to the crack driving force. When crack closure is more precisely measured -- as in the present study, or in a parallel study [10.12] -- it is found that  $\Delta K_{eff}$  only partially accounts for the observed crack size effects.

As indicated in Section 8.2, the current version of the phenomenological model for the growth of small cracks suggests that the transition from "small" to "large" crack behavior occurs at a specific value of  $\Delta K$ , termed  $\Delta K_{tr}$ . This concept is inconsistent with the popular view that this transition should occur at a given crack length,  $a_{tr}$ . However, in spite of numerous attempts to precisely define  $a_{tr}$ , this quantity remains elusive -- for example, see Refs. [10.13-10.15]. This situation suggests that the transition from "small" to "large" crack behavior may depend on additional factors. For example, in light of the current results, it is conceivable that  $a_{tr}$  could also depend on the extent of the plasticity contribution to the crack driving force ( $\Delta K_p$ ), as well as the relative closure characteristics of small and large cracks ( $\beta$  and  $\Delta K_{cl}$ , respectively) -- all of which can differ significantly with material and applied stress level.

With regard to the influence of applied stress level, it should also be pointed out that one limitation of the current version of the proposed phenomenological model is that  $\Delta K_p$  is taken to be constant at about 3 MPa $\sqrt{m}$ . Intuitively, it seems that  $\Delta K_p$  should be a function of the applied stress



range ( $\Delta S$ ), and perhaps the load ratio ( $R$ ). Unfortunately, we currently have insufficient data to define this functional relationship. Assuming  $\Delta K_p = K_p(\Delta S, R)$  then it is also likely that  $\Delta K_{tr} = \Delta K_{tr}(\Delta S, R)$ . In order to verify this additional experiments, conducted at higher stresses and under strain controlled conditions, would be required.

In spite of the above limitations, the proposed phenomenological model is capable of providing more realistic predictions of component life than the classical LEFM approach in which crack growth kinetics are defined in terms of  $da/dN(\Delta K)$  and  $\Delta K_{th}$ . These results raise important questions regarding the usefulness of large crack threshold data for fatigue life assessment in situations where cracks initiate and grow from a free surface.

The utility of  $\Delta K_{th}$  can also be questioned based on the fact that it can be extremely irreproducible under certain conditions. This is particularly true for Ni-base superalloys at room temperature where  $\Delta K_{th}$  values can range from about 7 to 20  $\text{MPa}\sqrt{\text{m}}$  with significant differences also occurring in crack growth rates to  $\Delta K$  values appreciably above  $\Delta K_{th}$  [10.16-10.18]. Although the data generated in the current study suggest that this variation in  $\Delta K_{th}$  is sensitive to grain size, other studies have reported fatigue crack growth rates in Astroloy to be insensitive to grain size [10.16]. Interestingly, the current study found that this irreproducibility disappears at elevated temperature (Section 4), thereby suggesting that it may be related to the extremely rough fracture surfaces and associated roughness-induced crack closure which develop at room temperature. This view is consistent with reported difficulties in the use of the compliance technique to monitor fatigue crack growth in Al-Li alloys which also develop extensive roughness-induced crack closure [10.19-10.20]. Such difficulties may contribute to the recently reported geometry dependence of near-threshold fatigue crack growth rates in Ni-base superalloys [10.21], since remote crack closure measurement are known to be geometry dependent [10.22].

Roughness-induced crack closure is also largely responsible for microstructural effects in the near-threshold fatigue crack growth rates of large cracks [10.23-10.25]. In the case of small cracks where crack closure is reduced due to the larger crack openings, the fatigue crack growth rates become relatively insensitive to microstructure, as discussed in Section 5.6.3. Thus, over-emphasis of the near-threshold large crack data can

result in improper alloy selection. For example, this appears to have been the case in Astroloy where the necklace microstructure, having duplex grain sizes of 5  $\mu\text{m}$  and 40  $\mu\text{m}$ , is commonly selected over a finer grained variant based on a comparison of their large crack growth rates in the near-threshold regime. In retrospect, the fine grained alloy would appear to have been the better selection based on the insensitivity of small crack growth rates to microstructure, combined with the superior strength and crack initiation resistance of fine grained alloys.

The results of the current study serve to establish the utility of  $\Delta K_{eq}$  as a driving force for the growth of both small and large fatigue cracks. Ideally, one would like to compute the local value of  $\Delta K_{eq}$  using the applied  $\Delta K$  as prescribed boundary conditions. In theory, it is possible to model the mixed-mode, elastic-plastic crack growth process under cyclic loading using numerical analysis. In fact, such techniques have been used to model aspects of the problem. For example, the finite element technique has been applied to the analysis of anisotropic effects in surface cracks (see the Appendix) and crack closure in large fatigue cracks [10.26-10.29], while the boundary integral equation technique has been applied to the analysis of cracks in a previously existing plastic field [10.30]. However, due to the complexity and corresponding cost of such analyses only selected cases can be analyzed. Consequently, these results are essentially numerical "experiments" and thus are difficult to generalize.

Simpler analyses, such as those based on the Dugdale-Barenblatt idealization, provide a viable alternative to numerical analysis. These have served to enhance our understanding of fatigue crack closure in large versus small cracks [10.31,10.32], and interactions of small crack with the material microstructure [10.33,10.34]. One of the latter cases [10.34] is particularly relevant to the current results in that it elucidates the contributions to  $\Delta K_p$  from variations in the yield strength of individual grains due to their crystallographic orientation. However, one of the practical limitations of Dugdale-Barenblatt type models is the fact that the solutions become unbounded when the applied stress equals the materials yield strength. Unfortunately, this is the region of greatest practical interest -- both for analysis of elevated temperature specimens and for application of results to life prediction in turbine discs.

## 10.1 References

- 10.1 P. Newman and C. J. Beevers, "Growth of Short Fatigue Cracks in High Strength Ni-Base Superalloys," in Small Fatigue Cracks, Eds. R. O. Ritchie and J. Lankford, TMS/AIME, 1986, pp. 97-116.
- 10.2 M. Gell and G. R. Leverant, Acta Met., Vol. 16, 1968, p. 553.
- 10.3 D. J. Duquette and M. Gell, Met. Trans., Vol. 2, 1971, p. 1325
- 10.4 K. Sadananda and P. Shahinian, "Analysis of Crystallographic High Temperature Fatigue Crack Growth in a Nickel Base Alloy," Met. Trans., Vol. 12A, 1981, pp. 343-351.
- 10.5 J. N. Vincent and L. Remy, "Temperature Dependence of the Pseudo-Cleavage Mechanism in the Threshold Regime of a Superalloy," in Fatigue Thresholds, Vol. 1, Eds. J. Backlund, A. F. Blom and C. J. Beevers, EMAS, 1982, pp. 441-454.
- 10.6 M. Gell and G. R. Leverant, in STP 520, ASTM, 1973, pp. 37-67.
- 10.7 W. F. Brown, Jr. and J. E. Scrawley, "Plane Strain Crack Toughness Testing of High Strength Metallic Materials," ASTM STP 410, 1969.
- 10.8 J. F. McCarver and R. O. Ritchie, Mater. Sci. and Eng., Vol. 55, 1982, p. 63.
- 10.9 J. L. Breat, F. Mudry and A. Pineau, Fat. Eng. Mat. Struct., Vol. 6, 1983, p. 349.
- 10.10 K. Minakawa, J. C. Newman, Jr. and A. J. McEvily, Fat. Eng. Mat. Struct., Vol. 6, 1983, p. 359.
- 10.11 E. Zaiken and R. O. Ritchie, Mat. Trans., Vol. 16A, 1985, p. 1467.
- 10.12 J. M. Larsen, "The Effects of Slip Character and Crack Closure on the Growth of Small Fatigue Cracks in Titanium-Aluminum Alloys," Ph.D. Dissertation, Carnegie Mellon University, Pittsburgh, PA, December 1987.
- 10.13 D. Taylor and J. F. Knott, Fat. Eng. Mat. Struct., Vol. 4, 1981, p. 147.
- 10.14 J. Lankford, Fat. Fract. Eng. Mats. Struct., Vol. 8, 1985, p. 161.
- 10.15 S. J. Hudak, Jr. and K. S. Chan, in Small Fatigue Cracks, Eds. R. O. Ritchie and K. S. Chan, TMS/AIME, 1986.
- 10.16 R. S. Vecchio, J. S. Crompton and R. W. Hertzberg, Fat. Fract. Engng. Mater. Struct., Vol. 10, No. 4, 1987, pp. 333-342.
- 10.17 F. Soniak and L. Remy, Fatigue '87, Eds. R. O. Ritchie and F. A. Starke, Jr., EMAS, 1987, pp. 351-360.

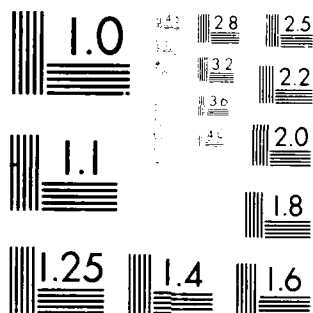
- 10.18 J. Lankford and D. L. Davidson, *ibid*, pp. 51-71.
- 10.19 J. H. FitzGerald, Private Communication.
- 10.20 J. K. Donald, Private Communication.
- 10.21 R. W. Hertzberg, "A Study of Fatigue Crack Propagation in Powder Metallurgy Hot Isotatically Pressed Nickel-Base Alloy," AFOSR-83-0029, Final Report, August 1986.
- 10.22 J. L. Horng and M. E. Fine, Materials Sci. and Eng., Vol. 67, 1984, pp. 185-195.
- 10.23 N. Walker and C. J. Beevers, Fat. Eng. Mat. Struct., Vol. 1, 1979, p. 135.
- 10.24 K. Minakawa and A. J. McEvily, Scripta Met., Vol. 6, 1981, p. 633
- 10.25 S. Suresh and R. O. Ritchie, Met. Trans., Vol. 13A, 1982, p. 1627.
- 10.26 H. D. Dill and C. R. Saff, ASTM STP, 1976, pp. 306-319.
- 10.27 B. Budiansky and J. W. Hutchinson, J. Applied Mech., Vol. 45, 1978, pp. 267-276.
- 10.28 H. Fuhring and T. Seeger, Eng. Fract. Mech., Vol. 11, 1979, pp. 99-122.
- 10.29 J. C. Newman, Jr., ASTM STP 748, 1981, pp. 53-84.
- 10.30 T. A. Cruse and S. T. Raveendra, "A Comparison of Long and Short Crack Elastoplastic Response Using the Boundary Element Method," submitted to Engr. Fract. Mech..
- 10.31 J. C. Newman, Jr., AGARD Conf. Proceedings No. 328, 1982, pp. 6.1-6.26.
- 10.32 J. C. Newman, Jr., M. H. Swain and E. P. Phillips, in Small Fatigue Cracks, Eds. R. O. Ritchie and J. Lankford, TMS/AIME, 1986, p. 427.
- 10.33 K. Tanaka, *ibid*, p. 343.
- 10.34 K. S. Chan and J. Lankford, Acta Metall., Vol. 36, 1988, pp. 193-226.

AD-A199 842 GROWTH OF SMALL CRACKS IN AEROENGINE DISC MATERIALS(U) 3/3  
SOUTHWEST RESEARCH INST SAN ANTONIO TX  
J V HUDAK ET AL; JUN 88 AFML-TR-88-4090  
UNCLASSIFIED F33615-85-C-5051 F/G 11/6.1 NL

END

DATE

12 88



MICROCOPY RESOLUTION TEST CHART  
NATIONAL BUREAU OF STANDARDS-1963-A

## 11. CONCLUSIONS

1. Small cracks in all three alloys were found to initiate within slip bands, however these were sometimes found to emanate from pores, particularly in FG Astroloy. Selected area electron channeling patterns on grains containing room temperature cracks in CG Astroloy showed that the formation of small cracks occur preferentially on {111} planes, as might be expected based on the slip character of this material.
2. The classical small crack problem occurs at elevated temperature (200°C to 600°C), as well as room temperature, in Ni-base superalloys, thus the phenomenon can be of practical significance.
3. Based on the similarity in the fracture surface morphology of small and long cracks as a function of temperature and applied stress, it is concluded that the mechanism of crack propagation is similar in both cases, thus crack size effects are attributed to differences in mechanical driving force.
4. The crystallographic nature of crack growth in small cracks in Ni-base superalloys leads to mixed-mode displacement of the crack faces. The degree of mixed-modeness depends on the specific orientation of the crack relative to the loading axis and on the magnitude of  $\Delta K$ .
5. The kinetics of small crack growth at both room temperature and 600°C are not measurably different in Astroloy and Waspaloy having similar grain sizes (30  $\mu\text{m}$  versus 42  $\mu\text{m}$ , respectively) indicating an insensitivity to alloy composition and microstructural details. In contrast, limited data at 600°C in FG Astroloy did not exhibit the classical small crack effect and were found to grow significantly slower than small cracks in CG Astroloy.
6. Strain fields at the tips of small cracks in all three alloys and over a range of temperatures was surprising homogeneous, relative to the slip character of these alloys, indicating that multiple slip occurs in the highly strained crack-tip region. Consequently, the measured strain fields provide no clue as to why crack growth occurs on a particular crystallographic plane.
7. The ratio of crack size to measured crack-tip plastic zone size ( $a/r_p$ ) was found to range from 1 to 5, consequently the linear elastic fracture mechanics concept of small scale yielding ( $a/r_p > 50$ ) did not hold for most of the small cracks examined.

8. Although the crack opening displacements of both small and large fatigue cracks exhibit the same  $\sqrt{r}$ -dependence as predicted from elastic theory, meaningful  $\Delta K$  values cannot be determined by combining these measurements with the elastic displacement equations for a static crack. This dichotomy is believed to be caused by cyclic plasticity at the tip of a fatigue crack which generates a local stress field which differs fundamentally from that found by either elastic or plastic analysis of monotonically-loaded stationary cracks.
9. Significant crack closure occurs in both small and large cracks, although its magnitude and dependence on fatigue loading variables differs in each case: In long cracks  $\Delta K_{C1} = K_0(1 - R)$ , whereas in small cracks  $\Delta K_{C1} = \alpha \Delta K$ , where  $K_0$  and  $\alpha$  are material constants.
10. Formulating the driving force for the growth of fatigue cracks in terms of  $\Delta K_{eq}$  which accounts for crack closure, plasticity and mixed-modeness in small cracks, and crack closure in long cracks, results in crack growth kinetics which are independent of crack size.
11. Using a phenomenological model for the growth of small cracks based on the above results gave better predictions of disc lives compared to conventional linear elastic fracture mechanics and long crack data. The latter approach can significantly overpredict disc life due to the misleadingly high  $\Delta K_{th}$  values exhibited by large cracks, compared to those in small cracks.
12. The near threshold crack growth rates exhibited by large cracks are in general not applicable to life prediction of actual components and furthermore can lead to improper material selection.



## APPENDIX

### FINITE ELEMENT ANALYSES IN NON-ISOTROPIC MATERIALS

Linear elastic fracture mechanics has been found to be applicable to the prediction of fatigue crack propagation behavior in most gas turbine disc materials where the crack in question is long compared to material microstructural dimensions. An investigation has been undertaken to identify whether linear elastic fracture mechanics can be used to correlate short crack growth behavior when account is taken in the fracture mechanics solutions of material anisotropy and inhomogeneity. This has been achieved by constructing 2D and 3D finite element models of cracks in anisotropic bodies and of cracks in local regions of anisotropy within an otherwise isotropic body. The latter case represents a crack growing within an individual microstructural unit.

This appendix describes the method developed for the calculation of crack tip stress intensity factors for anisotropic materials. The first part of this appendix covers work on 2-dimensional models while the remainder covers the subsequent work which developed the method for 3-dimensional models with local anisotropy.

#### A.1 Two-Dimensional Finite Element Models

A two-dimensional model was constructed using 8 node isoparametric quadrilateral plane strain elements, Figure A-1. The principal model consisted of a 2 inch (50.8 mm) perpendicular, edge crack contained within a 4 inch (101.6 mm) square region of anisotropic material. The remainder of the 52 inch (1320.8 mm) x 20 inch (508 mm) specimen was assumed to be isotropic. Since the analyses were linear elastic, the scale of the model was unimportant. Additional results were obtained for the cases where the whole

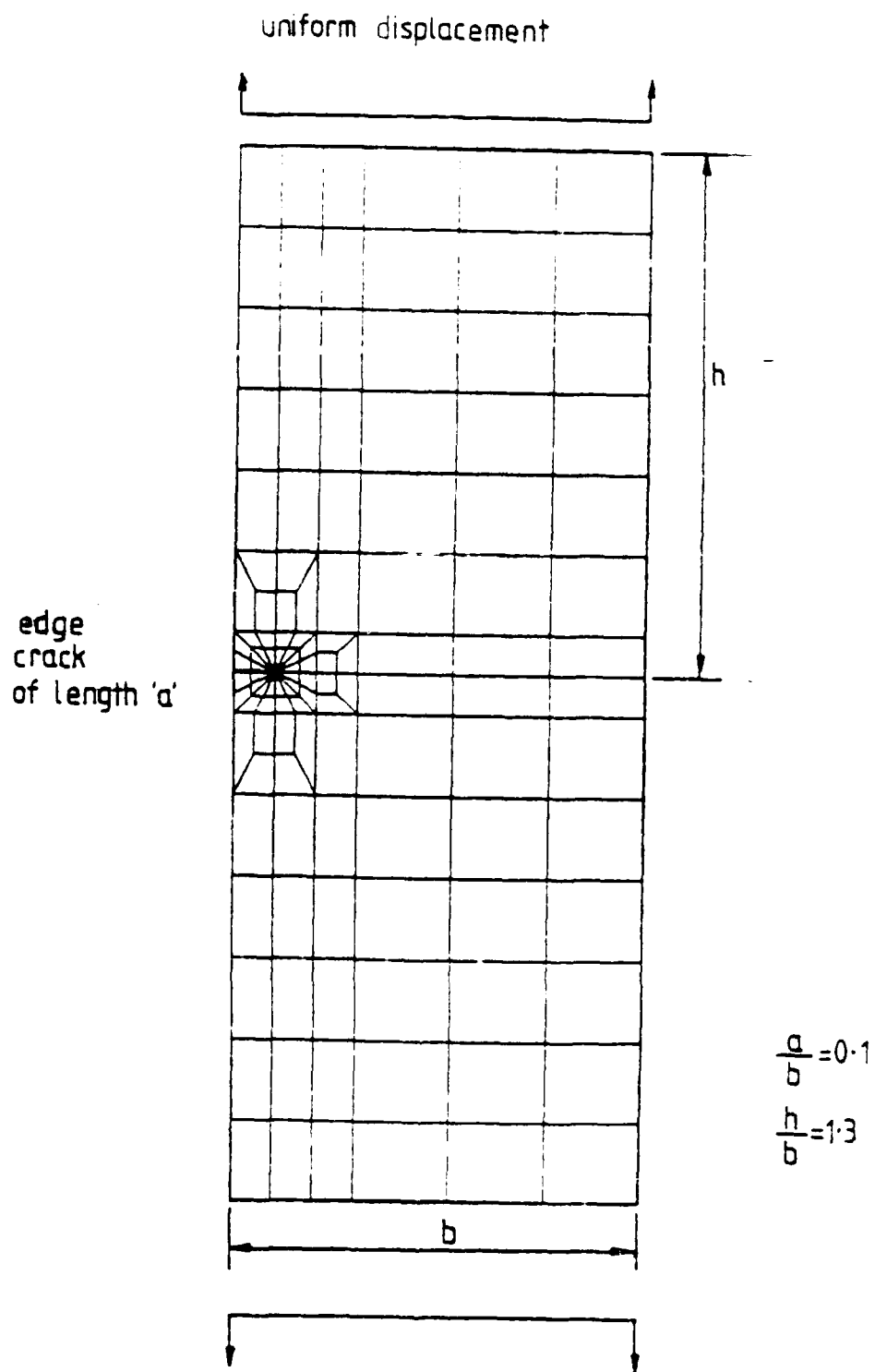


FIGURE A-1. 2-D Finite Element Model

of the model was anisotropic or isotropic. The relative dimensions of the model were chosen to allow comparison of the calculated stress intensities with published results for the isotropic case [A.1]. The crack tip elements were isoparametric quadrilaterals degenerated to 3 sides and 6 nodes with the mid-side nodes closest to the crack tip moved to the quarter point position to model the elastic singularity. The detail close to the crack is shown in Figure A-2. The model was elastically loaded by a fixed displacement of the top and bottom edges thereby preventing rotation.

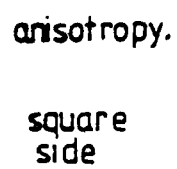
The anisotropic region was modelled with the elastic properties of SRR99, a single crystal nickel base turbine blade material. The isotropic material was represented by MAR-M-002, an equiaxed nickel base turbine blade alloy of a similar composition to SRR99. These materials were chosen because of the availability of elastic property data. It is expected that the ratio of anisotropic to isotropic elastic properties for a disc alloy such as Waspaloy will be similar to those considered for SRR99 and MAR-M-002. The elastic properties at 20°C used in the models are given in Table A-1.

The finite element models were run using the MARC program, level K1.3.

#### A.1.1 Elastic Properties of Rotated Anisotropic Material

SRR99 is a face centered cubic nickel base material. Considering Hooke's Law in a generalized form.

$$\sigma_i = \sum_{j=1}^6 C_{ij} E_j \quad (A-1)$$



A-4

TABLE A-1  
ELASTIC MATERIAL PROPERTIES

ANISOTROPIC MATERIAL  
(SR99 at 20°C)

ELASTIC STIFFNESS GPa

$C_{11}=250$   
 $C_{12}=156$   
 $C_{66}=115$

ISOTROPIC MATERIAL  
(MAR-M-002 AT 20°C)

|                 |               |
|-----------------|---------------|
| YOUNG'S MODULUS | $E=227.5$ GPa |
| POISSON'S RATIO | $\nu=0.3$     |

Provided the axes of elastic and global material symmetry are coincident, the elastic stiffness matrix can be represented by three independent values,

$$C_{11} = C_{22} = C_{33}$$

$$C_{12} = C_{13} = C_{23}$$

$$C_{44} = C_{55} = C_{66}$$

$$C_{ij} = C_{ji}$$

$$\text{All other } C_{ij} = 0$$

Typical values of  $C_{ij}$  for SRR99 at 20°C are given in Table A-1.

In the case where the global and elastic material axes are not coincident, the form of Hooke's Law for a material such as SRR99 which exhibits axes of symmetry of order 4 reduces to a stiffness matrix with 7 independent constants.

$$\begin{vmatrix} \sigma_x \\ \sigma_y \\ \sigma_z \\ \tau_{yz} \\ \tau_{zx} \\ \tau_{xy} \end{vmatrix} = \begin{vmatrix} C_{11} & C_{12} & C_{13} & 0 & 0 & C_{16} \\ & C_{11} & C_{13} & 0 & 0 & -C_{16} \\ & & C_{33} & 0 & 0 & 0 \\ & \text{sym} & & C_{44} & 0 & 0 \\ & & & & C_{44} & 0 \\ & & & & & C_{66} \end{vmatrix} \begin{vmatrix} \epsilon_x \\ \epsilon_y \\ \epsilon_z \\ \gamma_{yz} \\ \gamma_{zx} \\ \gamma_{xy} \end{vmatrix} \quad (\text{A-2})$$

The full 6x6 3-dimensional form of the stress-strain relationship has been considered to allow the computer code written for rotation to be used for 3-dimensional models.

To obtain the global elastic properties of a region of anisotropic material with known local-properties, the following transformation was performed. The conventions observed are given in Figure A-3.

Within the local system.

$$\epsilon = [S]\sigma$$

Within the global system

$$\epsilon' = [S']\sigma'$$

and the elastic compliance matrices  $[S]$  and  $[S']$  are related as follows

$$[S'] = N[S]N^T$$

Where  $[N]$  is given by

$$\begin{bmatrix} \alpha_1^2 & \beta_1^2 & \gamma_1^2 & \beta_1\gamma_1 & \gamma_1\alpha_1 & \alpha_1\beta_1 \\ \alpha_2^2 & \beta_2^2 & \gamma_2^2 & \beta_2\gamma_2 & \gamma_2\alpha_2 & \alpha_2\beta_2 \\ \alpha_3^2 & \beta_3^2 & \gamma_3^2 & \beta_3\gamma_3 & \gamma_3\alpha_3 & \alpha_3\beta_3 \\ 2\alpha_2\alpha_3 & 2\beta_2\beta_3 & 2\gamma_2\gamma_3 & \beta_2\gamma_3+\beta_3\gamma_2 & \gamma_2\alpha_3+\gamma_3\alpha_2 & \alpha_2\beta_3+\alpha_3\beta_2 \\ 2\alpha_3\alpha_1 & 2\beta_3\beta_1 & 2\gamma_3\gamma_1 & \beta_1\gamma_3+\beta_3\gamma_1 & \gamma_1\alpha_3+\gamma_3\alpha_1 & \alpha_1\beta_3+\alpha_3\beta_1 \\ 2\alpha_1\alpha_2 & 2\beta_1\beta_2 & 2\gamma_1\gamma_2 & \beta_1\gamma_2+\beta_2\gamma_1 & \gamma_1\alpha_2+\gamma_2\alpha_1 & \alpha_1\beta_2+\alpha_2\beta_1 \end{bmatrix}$$

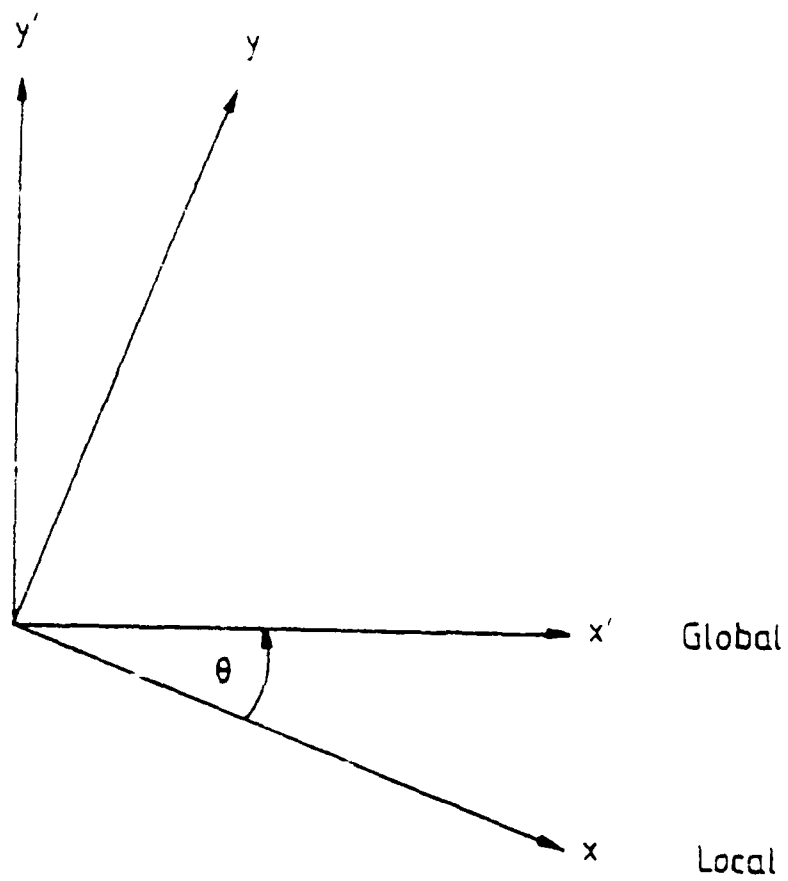


FIGURE A-3. Rotation of Elastic Constants



where  $\alpha_i$ ,  $\beta_i$  and  $\gamma_i$  are the direction cosines of the angles relating the global system to the local system as follows

$$\begin{bmatrix} x' \\ y' \\ z' \end{bmatrix} = \begin{bmatrix} \alpha_1 & \beta_1 & \gamma_1 \\ \alpha_2 & \beta_2 & \gamma_2 \\ \alpha_3 & \beta_3 & \gamma_3 \end{bmatrix} \begin{bmatrix} x \\ y \\ z \end{bmatrix}$$

For the 2-dimensional model considered, the matrix of direction cosines is given as follows.

$$\begin{bmatrix} C & S & 0 \\ -S & C & 0 \\ 0 & 0 & 1 \end{bmatrix} \quad ; \quad \begin{array}{l} C = \cos\theta \\ S = \sin\theta \end{array}$$

where  $[N]$  is given by

$$\begin{bmatrix} C^2 & S^2 & 0 & 0 & 0 & SC \\ S^2 & C^2 & 0 & 0 & 0 & -SC \\ 0 & 0 & 1 & 0 & 0 & 0 \\ 0 & 0 & 0 & C & -S & 0 \\ 0 & 0 & 0 & S & C & 0 \\ -2SC & 2SC & 0 & 0 & 0 & 1 \end{bmatrix}$$

The variation of the elastic stiffness for SRR99 versus rotation of the property axes about the common z axis is shown in Figure A-4.

#### A.1.2 Calculation of Elastic Strain Energy Release Rate 'G' using MARC

The elastic singularity at the crack tip was modelled using singular isoparametric elements with quarter point mid-side nodes [A.2]. MARC has the facility to determine the strain energy difference by means of a differential

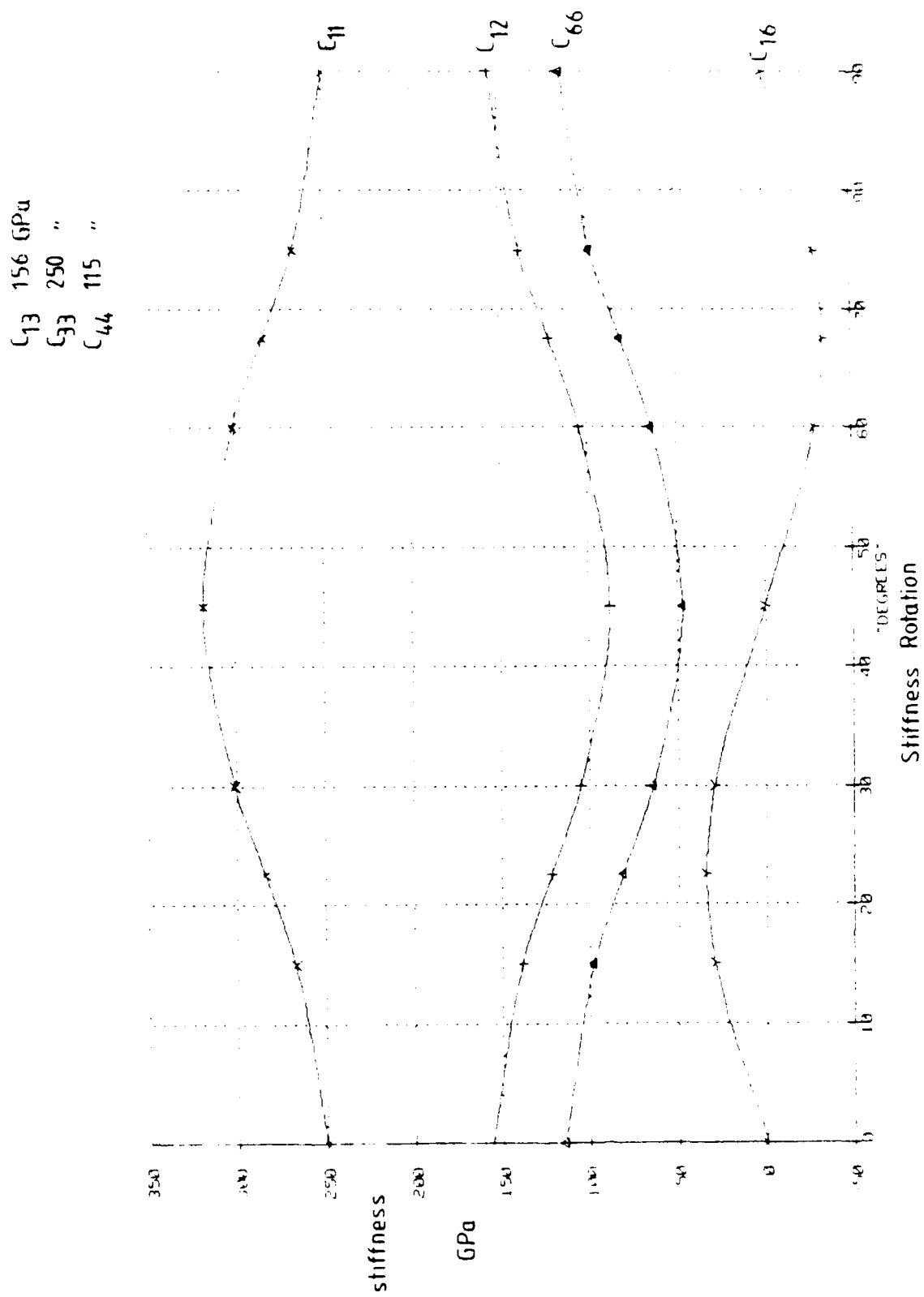


FIGURE A-4. Stiffness of SRR99 at 20°C

stiffness calculation for a pre-defined crack advance [A.3]. The finite element model with the perpendicular edge crack was run with rotated local anisotropy, rotated whole model anisotropy and complete isotropy. The values of 'G' for the colinear differential crack advance and the remote stress derived from the MARC program output are given in Table A-2.

### A.1.3 Plane Elastic Anisotropy

Plane problems in terms of Hooke's Law are reduced to a form involving a maximum of six independent elastic constants.

$$\begin{bmatrix} \epsilon_x \\ \epsilon_y \\ \gamma_{xy} \end{bmatrix} = \begin{bmatrix} S_{11} & S_{12} & S_{16} \\ S_{21} & S_{22} & S_{26} \\ S_{61} & S_{62} & S_{66} \end{bmatrix} \begin{bmatrix} \sigma_x \\ \sigma_y \\ \tau_{xy} \end{bmatrix}$$

where  $S_{ij}$  refers to either the plane stress compliance  $a_{ij}$  or the plane strain compliance  $b_{ij}$ . The relationship between  $a_{ij}$  and  $b_{ij}$  is given in Table A-3.

The method employed for the consideration of anisotropic elasticity was outlined by Sih et al [A.4]. The analytic functions required for the expressions describing stresses and displacements require parameters which are the conjugate pairs of roots of the following characteristic equation.

$$S_{11}u^4 - 2S_{16}u^3 + (2S_{12} + S_{66})u^2 - 2S_{26}u + S_{22} = 0 \quad (A-3)$$

The general expressions for stress and displacements in a small region around the crack tip for the symmetric and skew symmetric loadings are as follows, where  $r$  is a radial distance from the crack tip rotated at an angle  $\theta$  anticlockwise from the colinear crack direction.

TABLE A-2

ELASTIC STRAIN ENERGY RELEASE RATE 'G' AND REMOTE STRESS  
FOR A STRAIN OF 0.3846E-3

|                     | ROTATION OF<br>ANISOTROPIC<br>PROPERTIES | AVERAGE REMOTE<br>STRESS $\sigma$<br>(MPa) | G<br>(1E-3 MPa $\sqrt{m}$ ) | G/ $\sigma$<br>(1E6/ $\sqrt{m}$ ) |
|---------------------|--|--|-----------------------------|-----------------------------------|
| LOCAL ANISOTROPY    | 0°                                       | 94.1                                       | 6.98                        | 74.17                             |
|                     | 15°                                      | 94.2                                       | 7.25                        | 76.98                             |
|                     | 30°                                      | 94.6                                       | 7.81                        | 82.60                             |
|                     | 45°                                      | 94.7                                       | 8.15                        | 86.01                             |
| COMPLETE ANISOTROPY | 0°                                       | 58.0                                       | 3.67                        | 63.22                             |
|                     | 15°                                      | 65.8                                       | 4.57                        | 69.36                             |
|                     | 30°                                      | 90.2                                       | 7.85                        | 87.00                             |
|                     | 45°                                      | 110.7                                      | 11.24                       | 101.51                            |
| COMPLETE ISOTROPY   |  | 94.7                                       | 7.51                        | 79.31                             |

TABLE A-3

RELATIONSHIP BETWEEN PLANE STRAIN ( $b_{ij}$ ) AND  
PLANE STRESS ( $a_{ij}$ ) ELASTIC COMPLIANCE

Plane strain:  $b_{ij}$

Plane stress:  $a_{ij}$

$$b_{11} = \frac{a_{11}a_{33} - a_{13}^2}{a_{33}}$$

$$b_{12} = b_{21} = \frac{a_{12}a_{33} - a_{13}a_{23}}{a_{33}}$$

$$b_{22} = \frac{a_{22}a_{33} - a_{23}^2}{a_{33}}$$

$$b_{16} = b_{61} = \frac{a_{16}a_{33} - a_{13}a_{36}}{a_{33}}$$

$$b_{66} = \frac{a_{66}a_{33} - a_{36}^2}{a_{33}}$$

$$b_{26} = b_{62} = \frac{a_{26}a_{33} - a_{23}a_{36}}{a_{33}}$$

### Symmetric Loading

$$\sigma_x = \frac{K_1}{\sqrt{(2\pi r)}} \operatorname{Re} \left[ \frac{\mu_1 \mu_2}{\mu_1 - \mu_2} \left( \frac{\mu_2}{\sqrt{(\cos\theta + \mu_2 \sin\theta)}} - \frac{\mu_1}{\sqrt{(\cos\theta + \mu_1 \sin\theta)}} \right) \right]$$

$$\sigma_y = \frac{K_1}{\sqrt{(2\pi r)}} \operatorname{Re} \left[ \frac{1}{\mu_1 - \mu_2} \left( \frac{\mu_1}{\sqrt{(\cos\theta + \mu_2 \sin\theta)}} - \frac{\mu_2}{\sqrt{(\cos\theta + \mu_1 \sin\theta)}} \right) \right]$$

$$\tau_{xy} = \frac{K_1}{\sqrt{(2\pi r)}} \operatorname{Re} \left[ \frac{\mu_1 \mu_2}{\mu_1 - \mu_2} \left( \frac{1}{\sqrt{(\cos\theta + \mu_1 \sin\theta)}} - \frac{1}{\sqrt{(\cos\theta + \mu_2 \sin\theta)}} \right) \right]$$

Displacements parallel and perpendicular to crack face.

$$u = \frac{K_1 \sqrt{(2r)}}{\sqrt{(\pi)}} \operatorname{Re} \left[ \frac{1}{\mu_1 - \mu_2} (\mu_1 p_2 \sqrt{[\cos\theta + \mu_2 \sin\theta]} - \mu_2 p_1 \sqrt{[\cos\theta + \mu_1 \sin\theta]}) \right] \quad (A-4)$$

$$v = \frac{K_1 \sqrt{(2r)}}{\sqrt{(\pi)}} \operatorname{Re} \left[ \frac{1}{\mu_1 - \mu_2} (\mu_1 q_2 \sqrt{[\cos\theta + \mu_2 \sin\theta]} - \mu_2 q_1 \sqrt{[\cos\theta + \mu_1 \sin\theta]}) \right]$$

### Skew-Symmetric Loading

$$\sigma_x = \frac{K_2}{\sqrt{(2\pi r)}} \operatorname{Re} \left[ \frac{\mu_1 \mu_2}{\mu_1 - \mu_2} \left( \frac{\mu_2^2}{\sqrt{(\cos\theta + \mu_2 \sin\theta)}} - \frac{\mu_1^2}{\sqrt{(\cos\theta + \mu_1 \sin\theta)}} \right) \right]$$

$$\sigma_y = \frac{K_2}{\sqrt{(2\pi r)}} \operatorname{Re} \left[ \frac{1}{\mu_1 - \mu_2} \left( \frac{1}{\sqrt{(\cos\theta + \mu_2 \sin\theta)}} - \frac{1}{\sqrt{(\cos\theta + \mu_1 \sin\theta)}} \right) \right]$$

$$\tau_{xy} = \frac{K_2}{\sqrt{(2\pi r)}} \operatorname{Re} \left[ \frac{1}{\mu_1 - \mu_2} \left( \frac{\mu_1}{\sqrt{(\cos\theta + \mu_1 \sin\theta)}} - \frac{\mu_2}{\sqrt{(\cos\theta + \mu_2 \sin\theta)}} \right) \right]$$

Displacements parallel and perpendicular to crack face.

$$\begin{aligned}
 u &= \frac{K_2 \sqrt{(2r)}}{\sqrt{(\pi)}} \operatorname{Re} \left[ \frac{1}{\mu_1 - \mu_2} (p_2 \sqrt{[\cos \theta + \mu_2 \sin \theta]} - p_1 \sqrt{[\cos \theta + \mu_1 \sin \theta]}) \right] \\
 v &= \frac{K_2 \sqrt{(2r)}}{\sqrt{(\pi)}} \operatorname{Re} \left[ \frac{1}{\mu_1 - \mu_2} (q_2 \sqrt{[\cos \theta + \mu_2 \sin \theta]} - q_1 \sqrt{[\cos \theta + \mu_1 \sin \theta]}) \right] \\
 p_j &= S_{11} \mu_j^2 + S_{12} - S_{16} \mu_j \\
 q_j &= S_{12} \mu_j + (S_{22}/\mu_j) - S_{26}
 \end{aligned} \tag{A-5}$$

For mixed mode conditions, the strains energy release rate for colinear crack extension is given by

$$\begin{aligned}
 G &= \frac{S_{22} K_I^2}{2} \operatorname{Re} \left[ i \frac{\mu_1 + \mu_2}{\mu_1 \mu_2} \right] + \frac{S_{11} K_{II}^2}{2} \operatorname{Im} [\mu_1 + \mu_2] \\
 &+ \frac{1}{2} K_I K_{II} \left[ S_{22} \operatorname{Re} [i/(\mu_1 \mu_2)] + S_{11} \operatorname{Im} (\mu_1 \mu_2) \right]
 \end{aligned} \tag{A-6}$$

For the orthotropic case when the crack lies in a plane of symmetry, both  $\operatorname{Re}(i/\mu_1 \mu_2)$  and  $\operatorname{Im}(\mu_1 \mu_2)$  equal zero and the modes of cracking are independent and can be written as follows.

$$\begin{aligned}
 G &= K_I^2 \left[ \frac{S_{11} S_{22}}{2} \right]^{\frac{1}{2}} \left[ (S_{22}/S_{11})^{\frac{1}{2}} + \frac{2S_{12} + S_{66}}{2S_{11}} \right]^{\frac{1}{2}} \\
 &+ K_{II}^2 \frac{S_{11}}{\sqrt{2}} \left[ (S_{22} S_{11})^{\frac{1}{2}} + \frac{2S_{12} + S_{66}}{2S_{11}} \right]^{\frac{1}{2}}
 \end{aligned}$$

The values of  $\mu_1$ ,  $\mu_2$  and the relevant functions of  $\mu_1$  and  $\mu_2$  for the elastic conditions considered are given in Table A-4.

Because of difficulties encountered in solving simultaneously for  $K_I$  and  $K_{II}$  by the method of differential crack advance, although this has been done for isotropic materials [A.5], attention was given to the method of displacement extrapolation.

#### A.1.4 Displacement Extrapolation for Calculation of $K_I$ and $K_{II}$

For a small region surrounding the crack tip, the expressions for displacements parallel and perpendicular to the crack face have been given, Eqns. (A-4, A-5). Putting  $\theta = 180$  degrees such that 'r' lies along the crack face modifies those expressions as follows.

##### Symmetric Loading

$$u = K_I / (2r/\pi) \operatorname{Re} \left[ \frac{i}{\mu_1 - \mu_2} (\mu_1 p_2 - \mu_2 p_1) \right] \quad (A-7)$$

$$v = K_I / (2r/\pi) \operatorname{Re} \left[ \frac{i}{\mu_1 - \mu_2} (\mu_1 q_2 - \mu_2 q_1) \right]$$

##### Skew Symmetric Loading

$$u = K_{II} / (2r/\pi) \operatorname{Re} \left[ \frac{i}{\mu_1 - \mu_2} (p_2 - p_1) \right] \quad (A-8)$$

$$v = K_{II} / (2r/\pi) \operatorname{Re} \left[ \frac{i}{\mu_1 - \mu_2} (q_2 - q_1) \right]$$

$$p_j = S_{11} \mu_j^2 + S_{12} - S_{16} \mu_j$$

$$q_j = S_{12} \mu_j + \frac{S_{22}}{\mu_j} - S_{26}$$



TABLE A-4

## SOLUTIONS TO CHARACTERISTIC EQUATION

|  | <u>ROTATION OF ANISOTROPIC MATERIAL</u> |          |          |         | <u>ISOTROPIC</u> |     |
|--|---|----------|----------|---------|------------------|-----|
|  | 0°                                      | 15°      | 30°      | 45°     | 60°              |     |
| Re(μ <sub>1</sub> )                          | 0.69294                                 | -0.91824 | -0.86637 | 0.0     | 0.86637          | 0.0 |
| Im(μ <sub>1</sub> )                          | 0.72100                                 | 1.10320  | 1.80300  | 2.34800 | 1.80300          | 1.0 |
| Re(μ <sub>2</sub> )                          | -0.69294                                | 0.44570  | 0.21652  | 0.0     | -0.21652         | 0.0 |
| Im(μ <sub>2</sub> )                          | 0.72100                                 | 0.53548  | 0.45059  | 0.42589 | 0.45059          | 1.0 |
| Re [ i $\frac{\mu_1 + \mu_2}{\mu_1 \mu_2}$ ] | 1.42200                                 | 1.63870  | 2.25360  | 2.77390 | 2.25360          | 2.0 |
| Im(μ <sub>1</sub> +μ <sub>2</sub> )          | 1.44200                                 | 1.63870  | 2.25360  | 2.77390 | 2.25360          | 2.0 |
| Re(1/μ <sub>1</sub> μ <sub>2</sub> )         | 0.0                                     | 0.0      | 0.0      | 0.0     | 0.0              | 0.0 |
| Im(μ <sub>1</sub> μ <sub>2</sub> )           | 0.0                                     | 0.0      | 0.0      | 0.0     | 0.0              | 0.0 |

Summing the corresponding displacement above for the symmetric and skew symmetric cases gives the displacements for the mixed mode condition. Substitution of the isotropic properties into those expressions leads to the following.

$$u = K_{II} \sqrt{(2r/\pi)} (2S_{11}) ; S_{11} = \frac{1 - \nu^2}{E} \text{ for plane strain}$$

$$v = K_I \sqrt{(2r/\pi)} (2S_{22}) ; S_{22} = \frac{1 - \nu^2}{E} \text{ for plane strain}$$

Calculation of the relative movement of opposite pairs of crack face nodes along and normal to the crack plane and their substitution into the displacement Equations (A-7,A-8) will lead to values of  $K_I$  and  $K_{II}$  at distances 'r' from the crack tip. Extrapolation of these values to  $r = 0$  gives the crack tip  $K_I$  and  $K_{II}$ .

To allow a comparison between the calculated K values for isotropic bodies and those published [A.1], K has been normalized with respect to  $K_0 = \sigma \sqrt{\pi a}$

$\sigma$  = remote stress

a = crack length

The values calculated for K and  $K/K_0$  are given in Table A-5. The result for the isotropic case is within the bounds expressed by Rooke and Cartwright [A.1], i.e., ,  $1.180 \pm 0.047$  max.

#### **A.1.5 Crack Extension and Branching**

The extension of a crack within a single crystal material cannot be assumed to lie perpendicular to the remote stress direction or colinear with the original defect. Putting aside the crystallographic nature of mixed mode

single crystal cracking, consideration has been given to the hypothesis that crack propagation will occur in a radial direction in which the elastic strain energy release rate is a maximum. The value of 'G' for a radial crack advance has been calculated by two methods: (a) differential crack advance within the finite element program, and (b) use of nodal displacements from the finite element program output to supply stress intensity factors and hence 'G' for crack branching.

The differential crack advance technique was used for the models with local anisotropy rotated by 30° and 0°. The nodal advance used in this technique is shown in Figure A-5.

The method using nodal displacements involved angular stress intensity factors  $k$ . The convention used is given in Figure A-6. It was suggested [A.6] that at crack branching initiation, the angular stress intensity factors are given by

$$\begin{aligned} k_I &= \frac{1}{2} \cos(\theta/2) \left[ K_I(1 + \cos\theta) - 3K_{II} \sin\theta \right] \\ k_{II} &= \frac{1}{2} \cos(\theta/2) K_I \sin\theta + K_{II} (3 \cos\theta - 1) \end{aligned} \quad (A-9)$$

Using the values for  $K_I$  and  $K_{II}$  obtained from the displacement extrapolation method,  $k_I$  and  $k_{II}$  can be calculated from Eqn (A-9). Replacement of  $K$  by  $k$  in Eqn. (A-6) gives 'G' for values of crack branching angle, [A.7]. This method has the advantage that only a single run of the finite element model is required.

In order to justify the use of the displacement extrapolation/angular stress intensity method, the results of a comparison between that method and

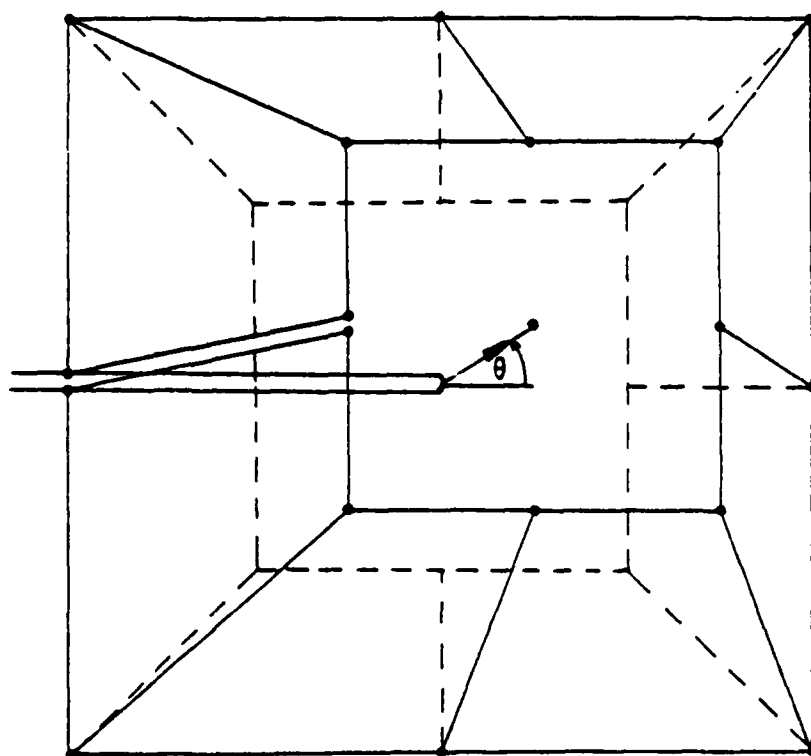


FIGURE A-5. Extension by Node Advance

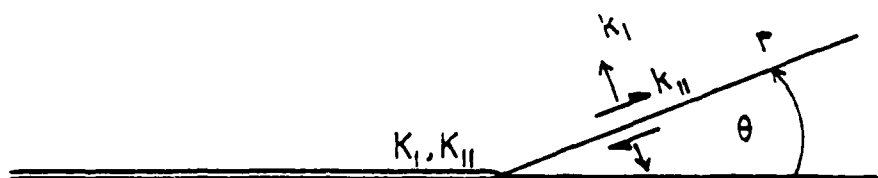


FIGURE A-6. Definition of Angular Stress Intensity Factors

the differential crack advance method, for local anisotropy rotated by  $30^\circ$  and  $0^\circ$ , is shown in Table A-5. The results are plotted in Figure A-7. The sets of curves for 'G' versus branching angle for the models considered are given in Figures A-8 and A-9.

#### **A.1.6 Angled Edge Crack Models**

As an introduction to the modelling of angled edge cracks, results previously calculated by the method of displacement extrapolation for an isotropic material were used to determine the strain energy release rate for a range of crack branching angles. For cracks angled at  $30^\circ$  and  $45^\circ$  to the direction perpendicular to that of loading, the maximum values of 'G' were obtained for crack branching angles of  $-30^\circ$  and  $-40^\circ$ . Using the values of  $K_I$  and  $K_{II}$  obtained by the method of Hellen and Blackburn [A.5] intensity factor method gave a crack branching angle of  $-44^\circ$  for the  $45^\circ$  edge crack model.

#### **A.1.7 Discussion on 2-Dimensional Analyses**

As shown in Figure A-7, the angular stress intensity factor method gave results very similar to those obtained by the method of differential crack advance. The former was favored because of the advantage of requiring only a single program run for each model.

Rotation of local anisotropy and complete model anisotropy gave maximum strain energy release rates at, or within 4 degrees of the colinear crack direction using LEFM. On the basis that for homogeneous isotropic materials crack propagation is suggested to occur in the direction of maximum 'G', the present work indicates that crystallographic mixed mode fracture in anisotropic regions cannot be predicted by energy considerations. However, the method developed is capable of determining the crack tip stress intensity factors  $K_I$ ,  $K_{II}$  and, for 3D cases  $K_{III}$  and the strain energy release rate for

TABLE A-5

$K_I$  AND  $K_{II}$  FOR CO-LINEAR EXTENSION DETERMINED BY DISPLACEMENT  
EXTRAPOLATION METHOD

|                              | ROTATION OF<br>ANISOTROPY | $K_I$<br>(MPa/m) | $K_I/K_0$ | $K_{II}$<br>(MPa/m) | $K_{II}/K_0$ |
|------------------------------|---------------------------|------------------|-----------|---------------------|--------------|
| LOCAL ANISOTROPY             | 0°                        | 17.24            | 1.026     | 0.00                | 0.00         |
|                              | 15°                       | 17.56            | 1.044     | 0.64                | 0.04         |
|                              | 30°                       | 18.18            | 1.077     | 0.61                | 0.04         |
|                              | 45°                       | 18.56            | 1.097     | 0.00                | 0.00         |
| WHOLE SPECIMEN<br>ANISOTROPY | 0°                        | 12.56            | 1.214     | 0.00                | 0.00         |
|                              | 15°                       | 13.92            | 1.184     | 0.01                | 0.01         |
|                              | 30°                       | 18.25            | 1.133     | 0.01                | 0.00         |
|                              | 45°                       | 21.80            | 1.103     | 0.00                | 0.00         |
| ISOTROPIC                    |                           | 19.40            | 1.148     | 0.00                | 0.00         |
| ROOKE and<br>CARTWRIGHT      |                           |                  | 1.180     |                     | 0.00         |

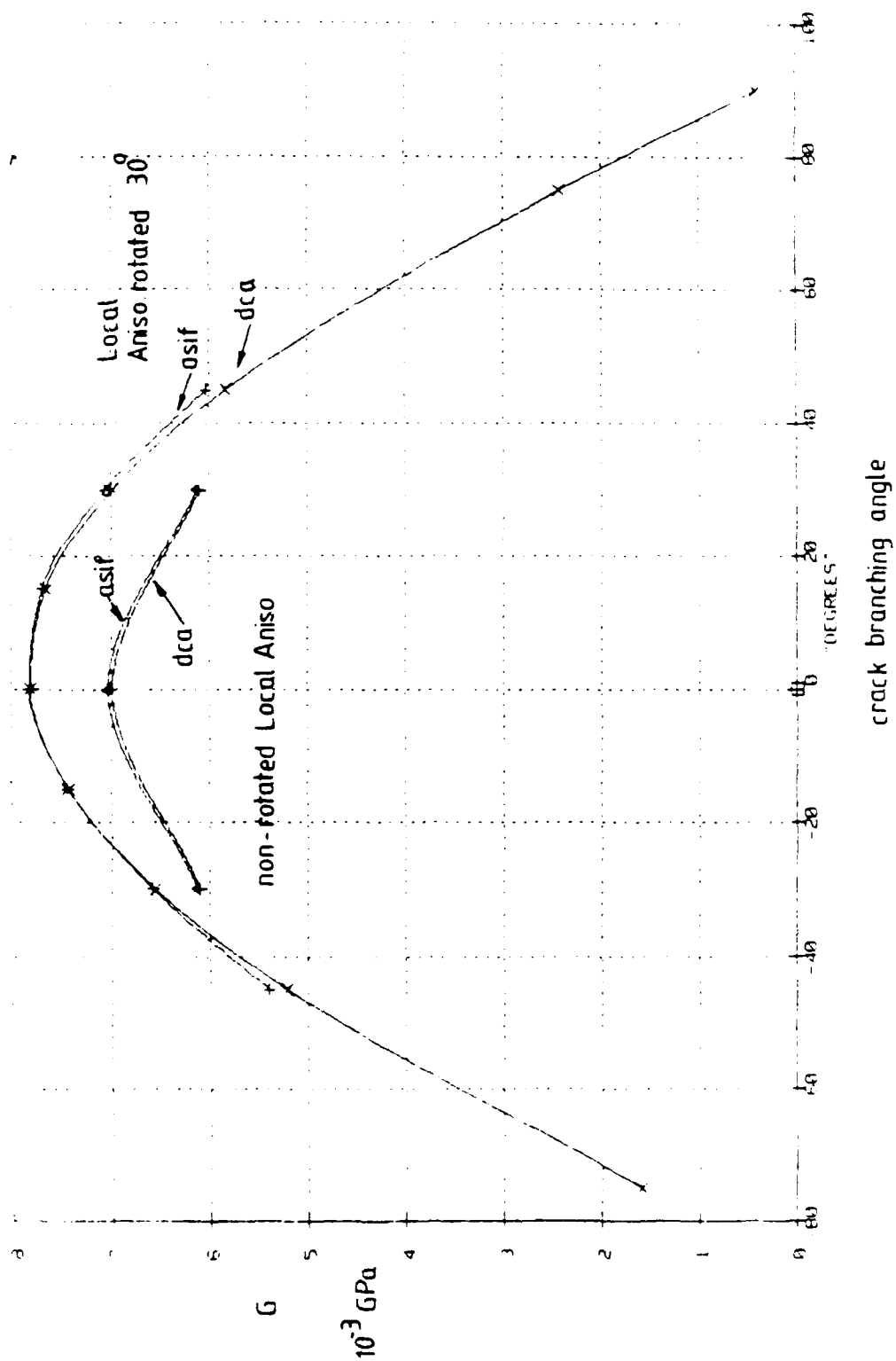


FIGURE A-7. Strain energy release rate from a) differential crack advance [dca] b) angular SIF [asif].



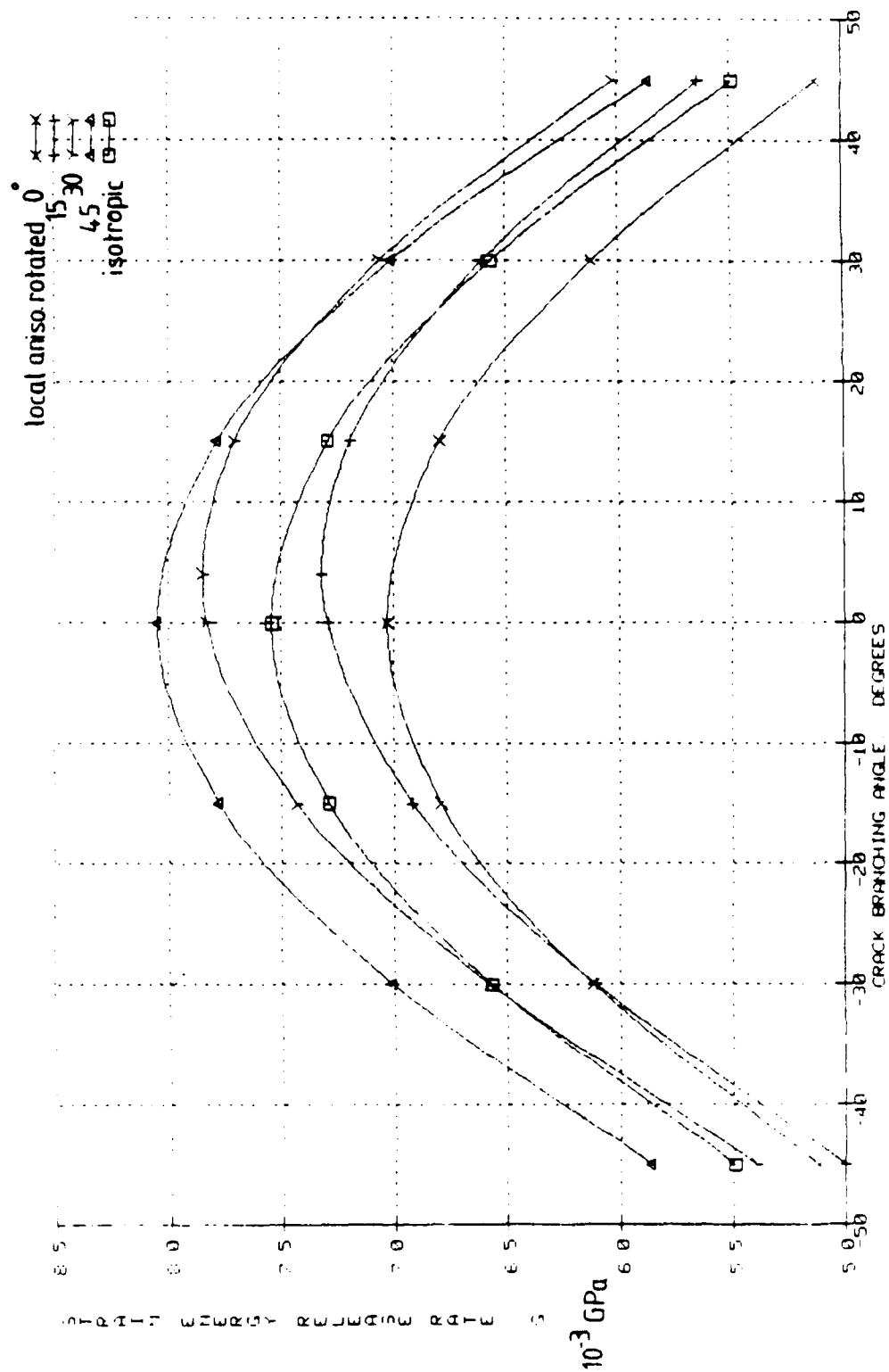


FIGURE A-8. Strain Energy Release Rate by Angular S.I.F. Method

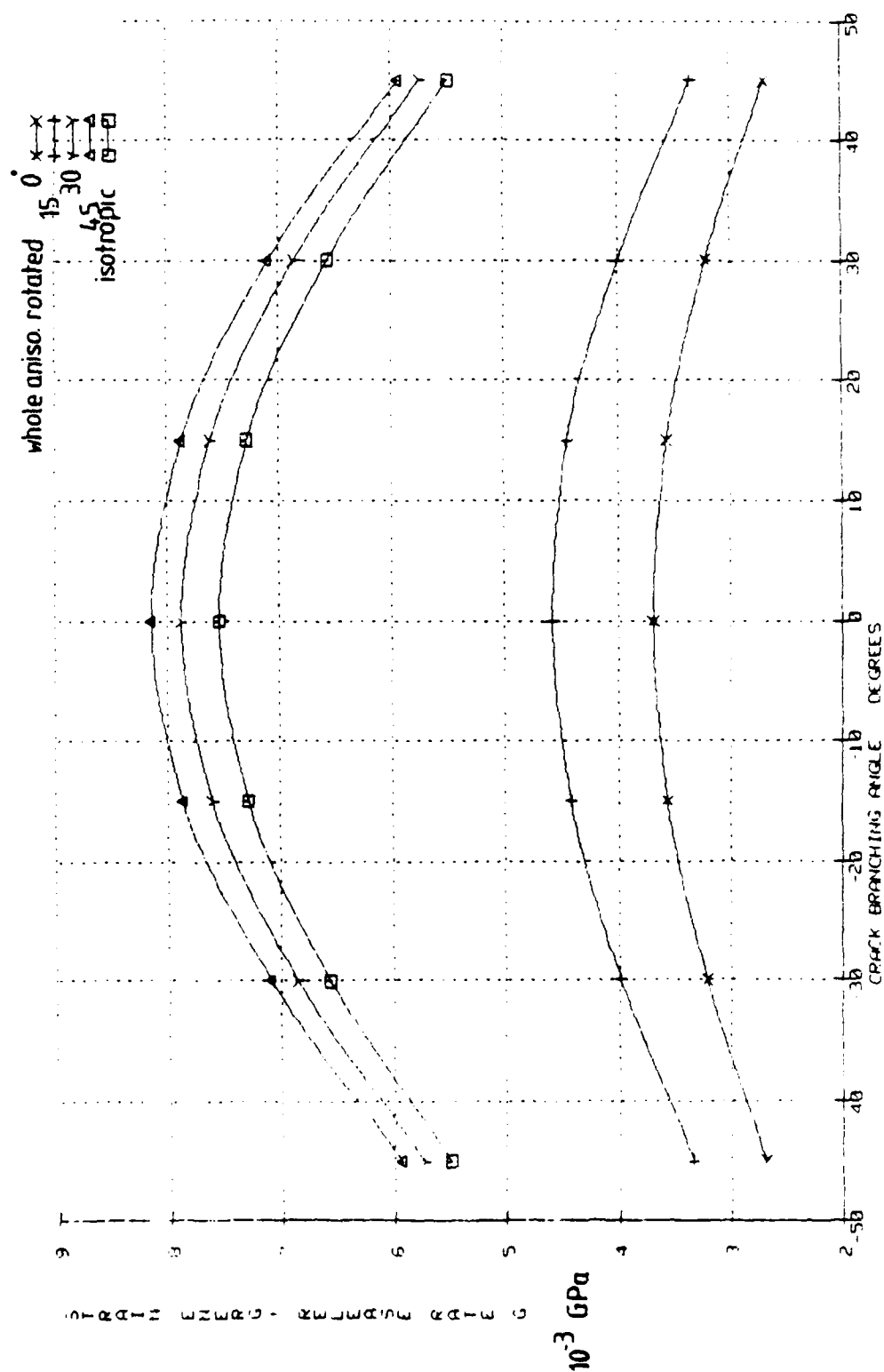


FIGURE A-9. Strain Energy Release Rate by Angular S.I.F. Method

a crack extension on a particular crystallographic plane. Although  $K$  is preferred for the correlation of fatigue crack propagation, questions arise as to its suitability and consideration should be given to local crack tip sensitivity during mixed mode fracture, the involvement of local shear strain and whether the possible significant crack tip stress system affects the assumed material homogeneity. Use of  $K_{II}$  or  $K_{III}$  as a correlating parameter for shear type fracture may, however, be possible.

## **A.2 Three-Dimensional Stress Intensity Factors for Cracks in Locally Anisotropic Material**

This section describes the method used for the calculation of crack front Stress Intensity Factors in 3-dimensional locally anisotropic materials. Two finite element models have been developed, an angled edge through-crack and a semicircular surface crack in uniaxially loaded rectangular prismatic blocks. The models were considered isotropic for comparison with published results and then modified so that the crack was contained within a region of local anisotropy to simulate the structure sensitivity experienced by small cracks. The method of calculation described can be applied to the edge and semicircular surface cracks for any orientation of crack and material anisotropy.

### **A.2.1 Three-Dimensional Finite Element Models**

Two finite element models were constructed using 20 node isoparametric brick elements. The crack fronts were represented by 20 node isoparametric brick elements with one face degenerated to create 15 node wedges. The elastic singularity at the crack front was represented by movement of the midside nodes closest to the crack front to the quarter point position, Figure A-10. The quarter point node coordinates were computer generated using FORTRAN Code written specifically for this work. Both models were developed using PATRAN, a finite element pre/post processing package.

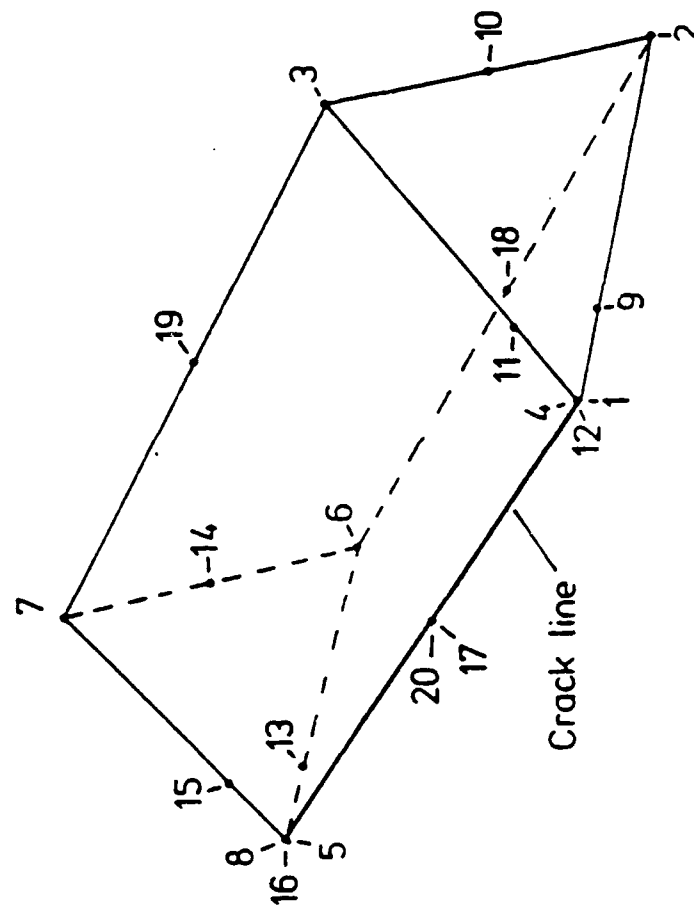


FIGURE A-10. 3D Brick Quarter Point Crack Tip Element Configuration

The linear elastic models were uniaxially loaded by a fixed uniform vertical displacement of the top face nodes, zero vertical displacement of the bottom face nodes and a limited number of horizontal nodal zero displacements.

#### **A.2.2 30 Degree Angled Edge Through-Crack Model**

Figure A-11 shows the 48 finite element mesh of the model and an enlarged view of the region of local anisotropy. The crack was angled at 30 degrees to the horizontal X' axis. The relative dimensions were chosen to allow comparison between the calculated and published stress intensity results for the completely isotropic case.

#### **A.2.3 Perpendicular Semicircular Surface Crack**

Figure A-12 shows the 404 finite element mesh of the model and an enlarged view of the crack in relation to the bottom half of the region of local anisotropy. The angle of the crack and the relative dimensions of the model were chosen to allow comparison between the calculated and published stress intensity results for the completely isotropic case.

#### **A.2.4 Elastic Properties Of Models**

As with the 2-dimensional models, the anisotropic regions of the 3-dimensional models were represented by SRR99, a single crystal nickel base turbine blade material. The isotropic material was represented by MAR-M-002, an equiaxed nickel base turbine blade alloy of a similar composition to SRR99. The elastic properties at 20°C of the two materials used in the models are given in Table A-1.

The finite element models were run using the MARC program, level K1.3.

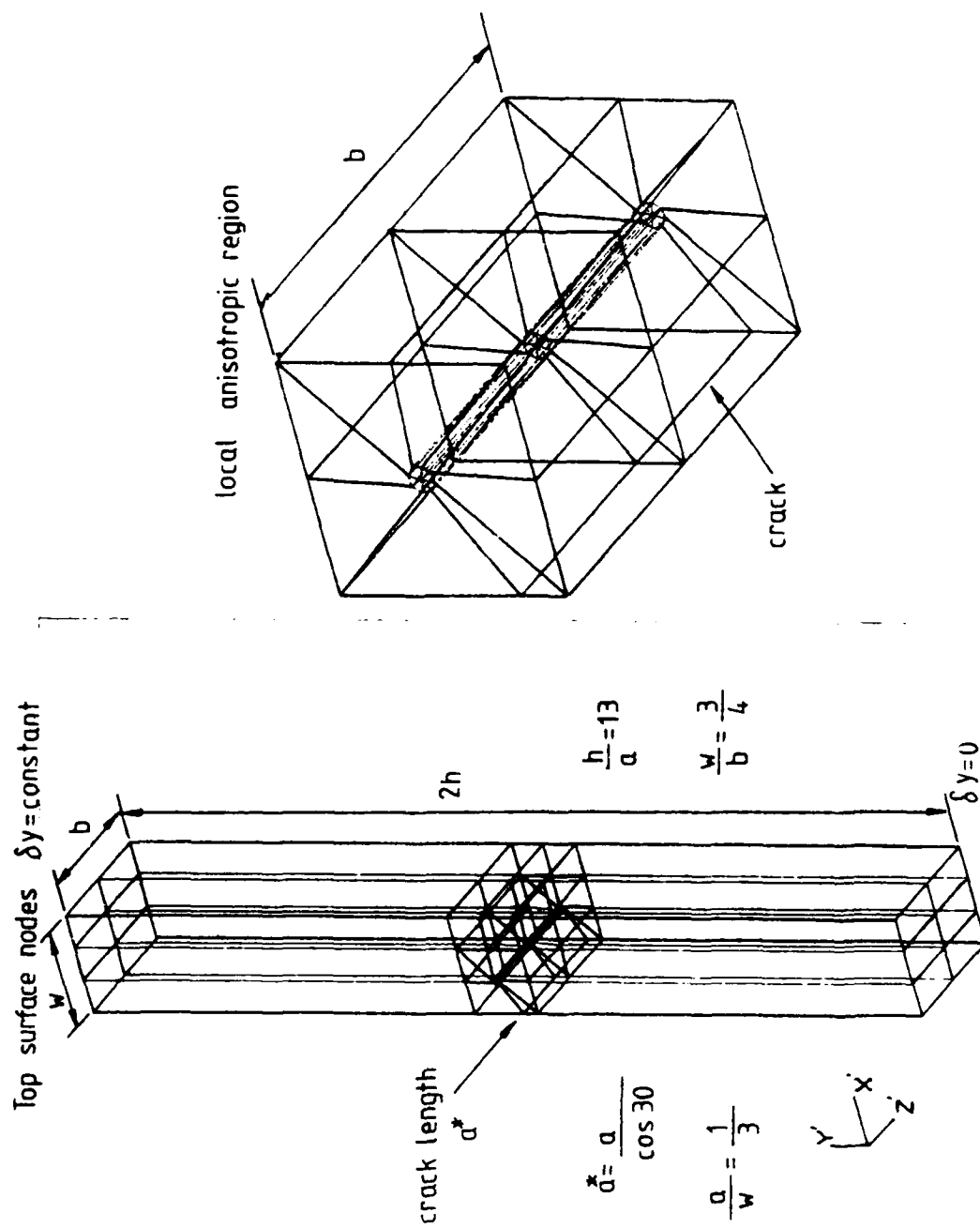


FIGURE A-11. Edge Crack Mesh

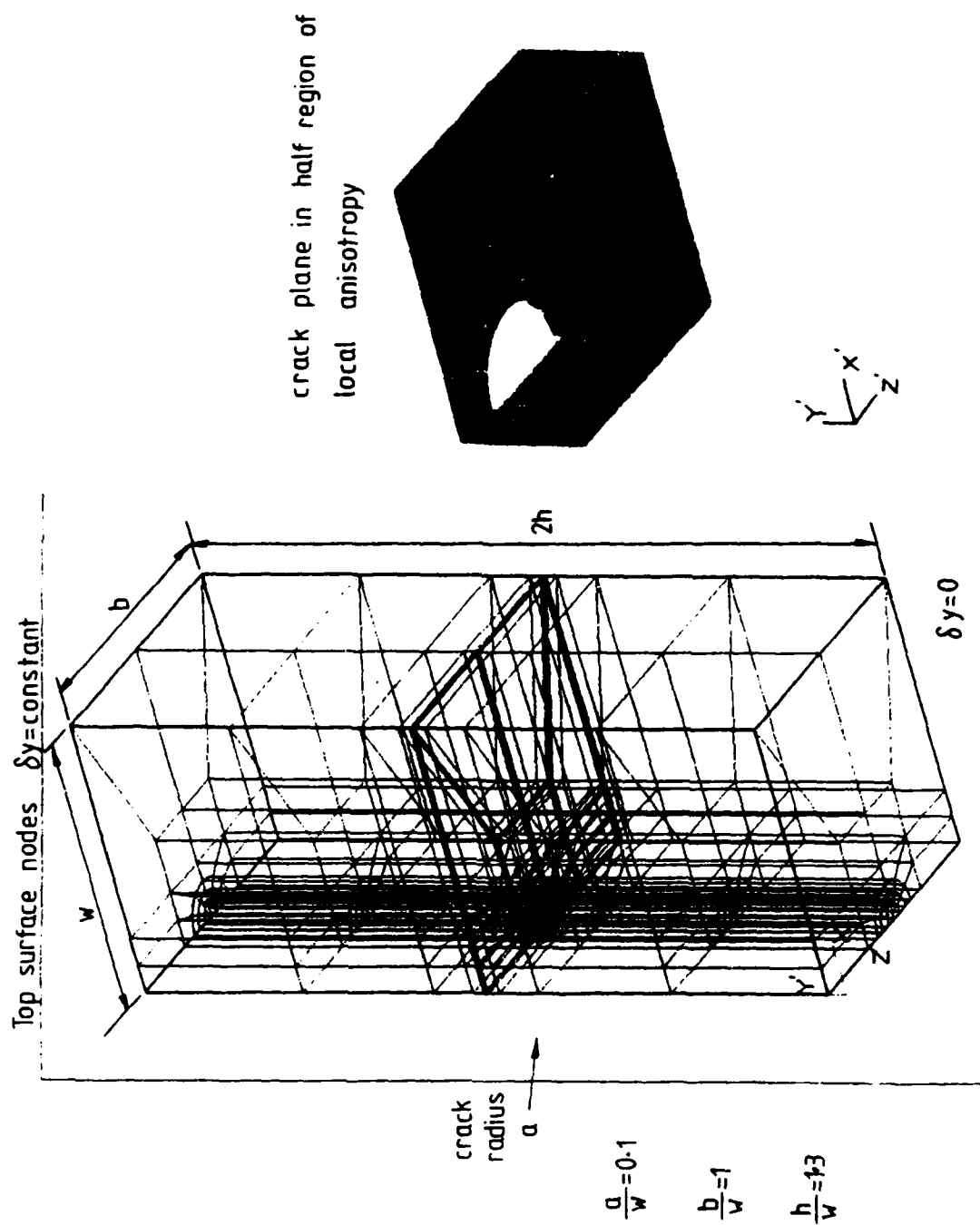


FIGURE A-12. Surface Crack Mesh

#### **A.2.5 Crack Orientation Within Anisotropic Region**

The models with local anisotropy were designed to consider a crack along a locally oriented (111) crystallographic plane. The direction of crack advance perpendicular to the global Y'Z' plane was taken to be the locally oriented ( $\bar{1}\bar{1}0$ ). Figures A-13a and A-13b show a general and plan view respectively of the semicircular crack in relation to the low index axes of local anisotropy. An identical relationship was assumed for the angled edge through-crack model where the crack front was parallel to the global Y'Z' plane and perpendicular to the local ( $\bar{1}\bar{1}0$ ) direction.

Figure A-14 shows how the orientation of a semicircular surface crack was defined in terms of the global coordinate axes of the model. The orientation defined in Figure A-14 can be applied to the edge through-crack with the angle  $\delta = 90^\circ$  across the crack front.

#### **A.2.6 Elastic Properties Of Rotated Anisotropic Material**

MARC, the finite element package used for the analysis, has the facility to orient the elastic stiffness matrix. However, because the calculations of the stress intensity factors required a knowledge of the local elastic compliance along the crack front, the rotation of anisotropy was performed by computer programs written for this work.

To obtain the global elastic properties of a region of anisotropic material with known local properties, the transformation described in Section A.1.1 was performed. The conventions observed for the rotating coordinate systems are given in Figure A-15.



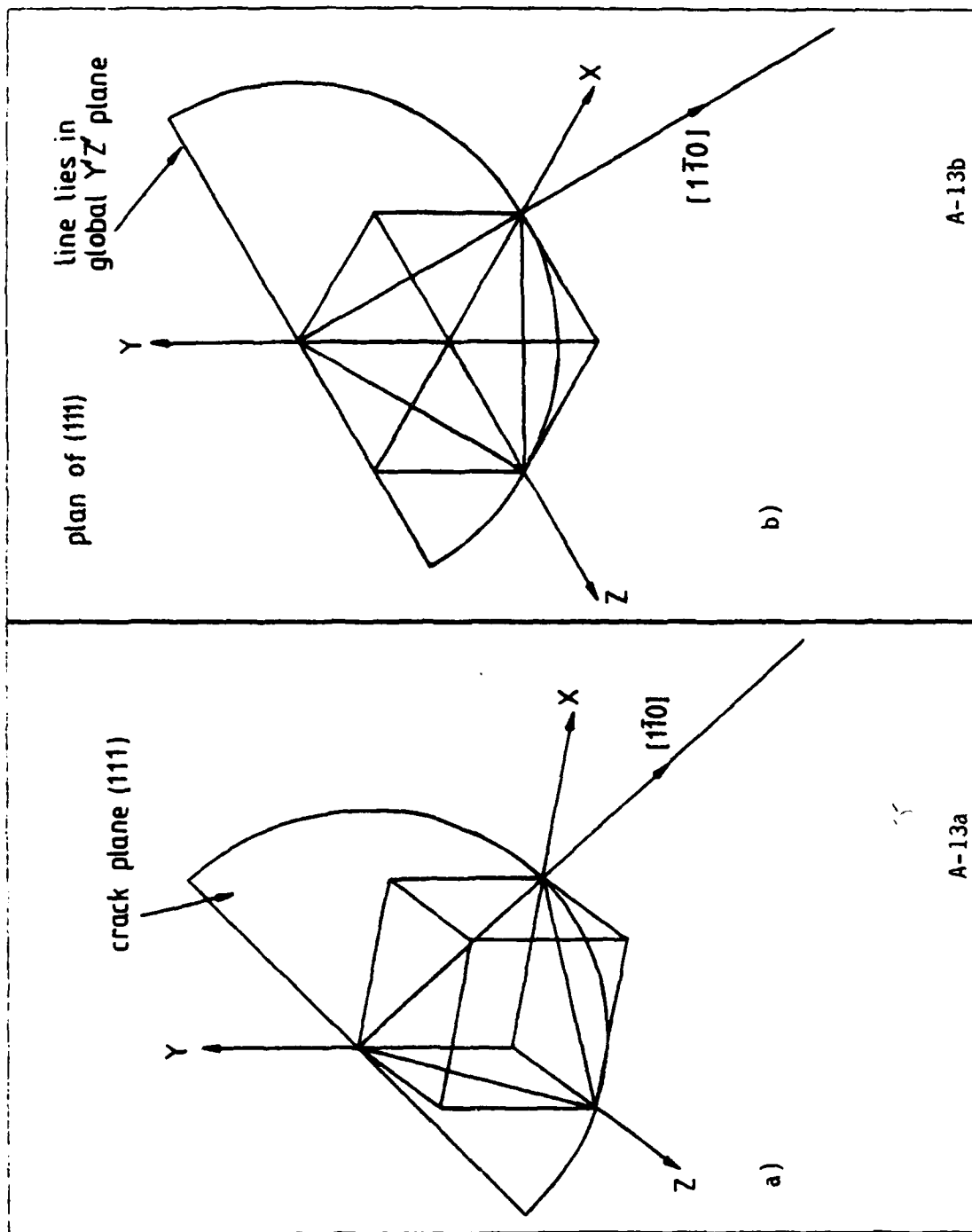


FIGURE A-13. Low Index Axes in Relation to Crack Plane

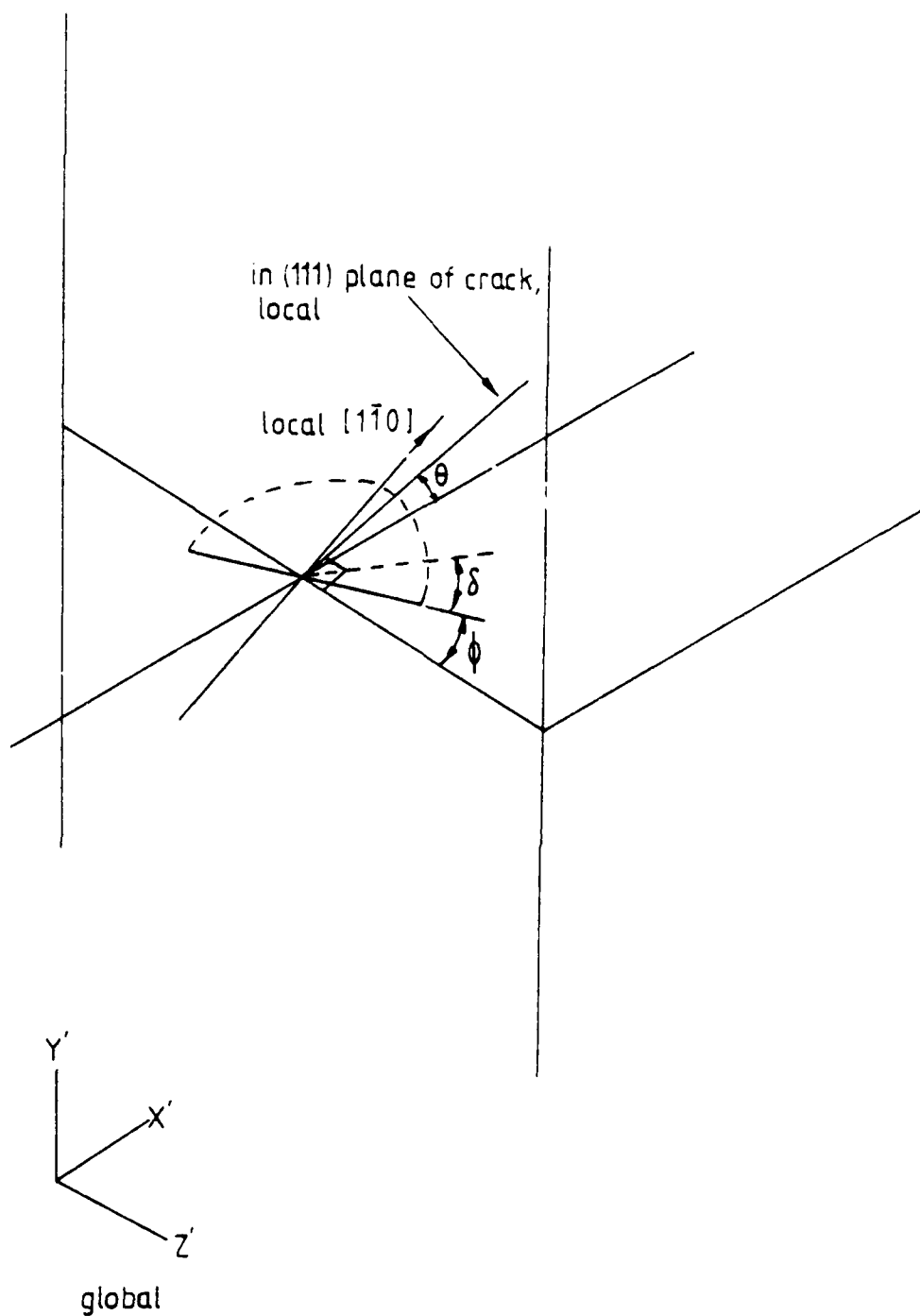


FIGURE A-14. Crack Orientation

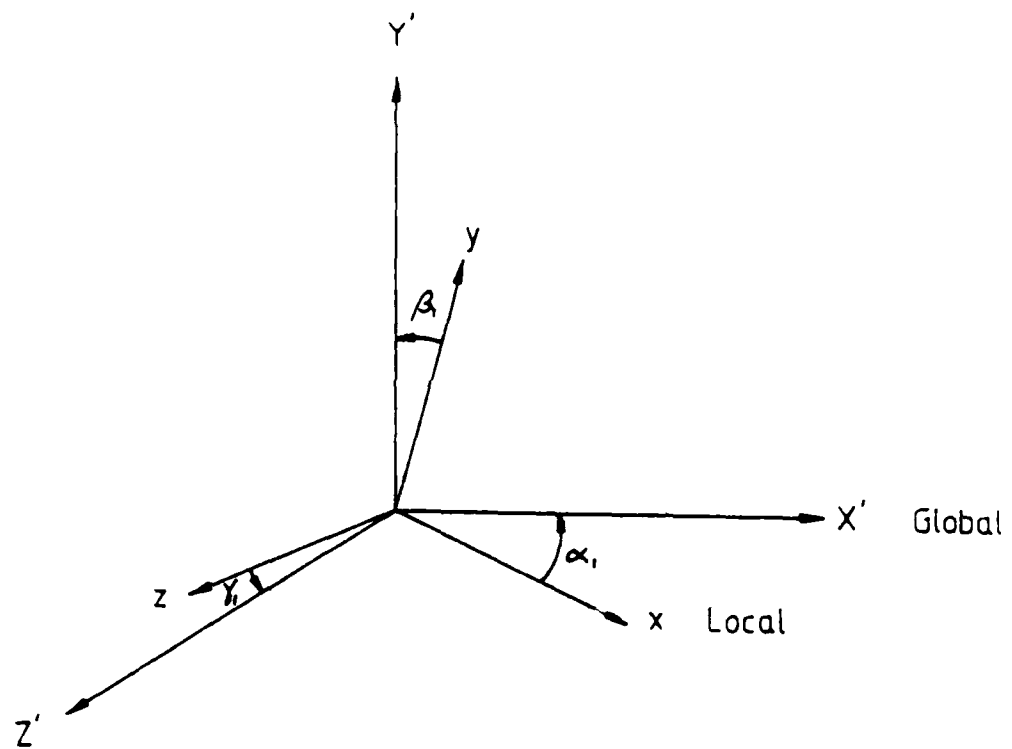


FIGURE A-15. Rotation of Elastic Constants

### A.2.7 Three-Dimensional Elastic Anisotropy

Provided attention is restricted to a sufficiently small region around the crack front, problems involving elastic anisotropy can be reduced to a sum of the plane and antiplane solutions. The method used for 3-dimensional elastic anisotropy was derived from the solution to plane problems described by Sih et al [A.4]. Referring to the notation given in Figure A-16, the analysis of the plane problem assumed the  $r$  axis to be parallel to the leading edge of the crack and the  $p$  and  $q$  axes to be parallel and normal to the crack surface with the  $pq$  plane being a plane of elastic symmetry. For the semicircular crack, the axis  $p$  was an extension of the radius of the semicircle and  $q$  was the  $(111)$  direction.

#### Plane Elastic Anisotropy

The stresses and displacements close to the crack front for plane symmetric and skew-symmetric loadings are given in Section A.1.3. Figure A-17 shows the notation used for plane extension.

#### Antiplane Elastic Anisotropy

The analytic functions required for the expressions describing stresses and displacements require parameters which are conjugate pairs of roots of the following characteristic equation.

$$a_{55}u^2 - 2a_{45}u + a_{44} = 0$$

The expressions for stress and displacement in a small region around the crack tip for the shear loading are as follows, where  $r$  is a radial distance from the crack front rotated at an angle  $\theta$  anticlockwise from the coplanar crack direction.

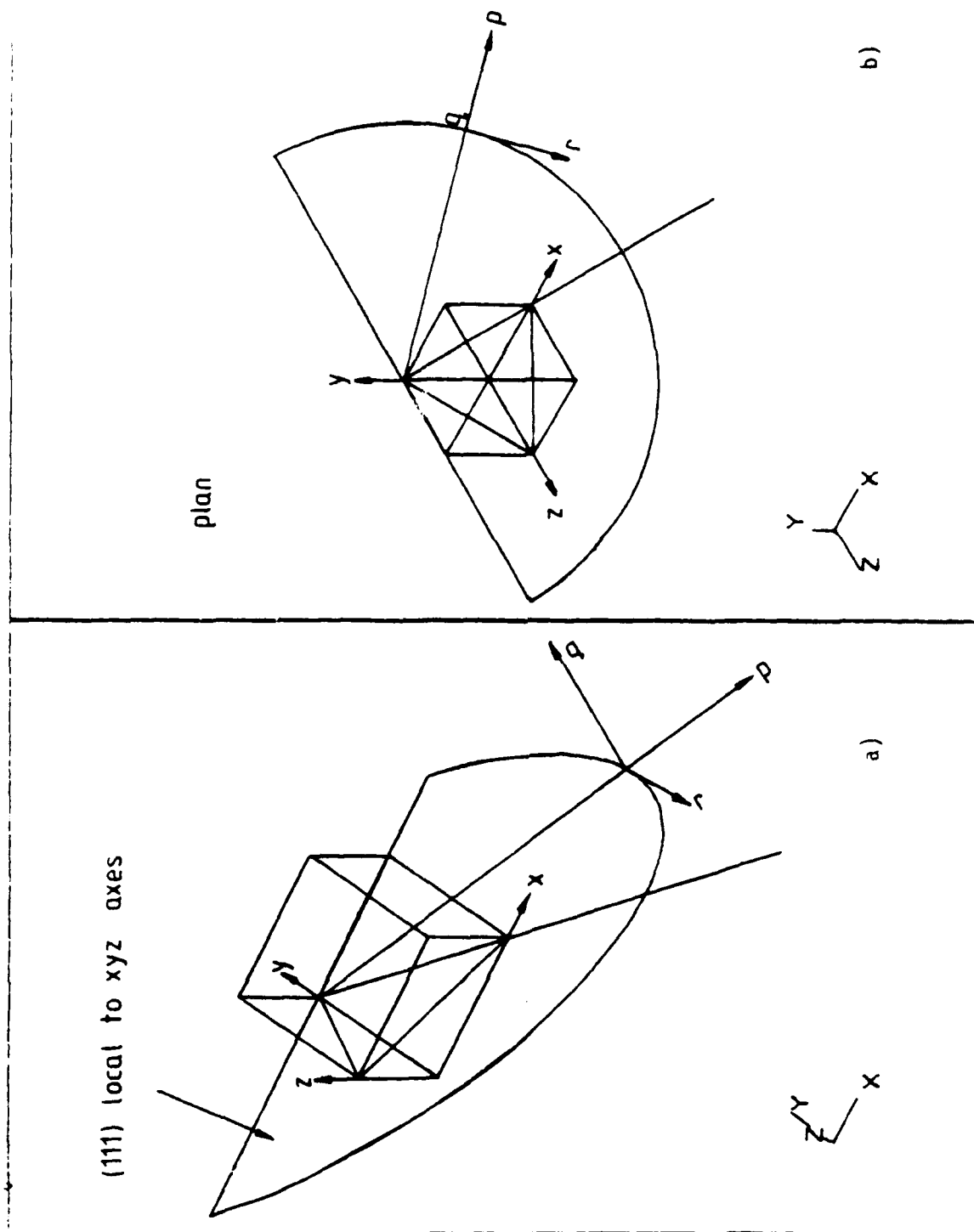


FIGURE A-16. Crack Front Coordinate Axes

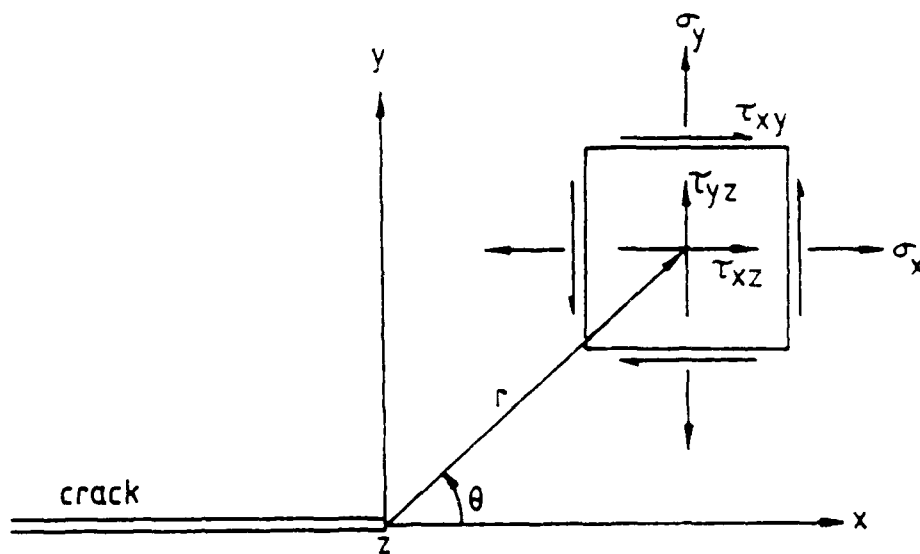


FIGURE A-17. Notation for Plane Extension

### Antiplane Shear Loading

$$\tau_{xz} = - \frac{K_{111}}{\sqrt{(2\pi r)}} \operatorname{Re} \left[ \frac{\mu_3}{\sqrt{(\cos\theta + \mu_3 \sin\theta)}} \right]$$

$$\tau_{yz} = \frac{K_{111}}{\sqrt{(2\pi r)}} \operatorname{Re} \left[ \frac{1}{\sqrt{(\cos\theta + \mu_3 \sin\theta)}} \right]$$

Displacement parallel to the crack front is given by

$$w = K_{111} \sqrt{(2r/\pi)} \sqrt{(a_{44}a_{55} - a_{45}^2)} \operatorname{IM}[\sqrt{(\cos\theta + \mu_3 \sin\theta)}] \quad (\text{A-10})$$

### A.2.8 Displacement Extrapolation For Calculation of KI, KII and KIII

For a small region surrounding the crack tip, the expressions for displacements parallel and perpendicular to the crack face and parallel to the crack front have been given, Eqns. (A-4,A-5,A-10). Putting  $\theta = 180$  degrees such that 'r' lies along the crack face modifies those expressions as follows

### Plane Symmetric Loading

$$u = K_1 \sqrt{(2r/\pi)} \operatorname{Re} \left[ \frac{i}{\mu_1 - \mu_2} (\mu_1 p_2 - \mu_2 p_1) \right] \quad (\text{A-11})$$

$$v = K_1 \sqrt{(2r/\pi)} \operatorname{Re} \left[ \frac{i}{\mu_1 - \mu_2} (\mu_1 q_2 - \mu_2 q_1) \right]$$

### Plane Skew Symmetric Loading

$$u = K_{11} \sqrt{(2r/\pi)} \operatorname{Re} \left[ \frac{1}{\mu_1 - \mu_2} (p_2 - p_1) \right] \quad (\text{A-12})$$

$$v = K_{11} \sqrt{(2r/\pi)} \operatorname{Re} \left[ \frac{1}{\mu_1 - \mu_2} (q_2 - q_1) \right]$$

$$p_j = s_{11}\mu_j^2 + s_{12} - s_{16}\mu_j$$

$$q_j = s_{12}\mu_j + (s_{22}/\mu_j) - s_{26}$$

### Antiplane Shear Loading

$$w = K_{III} \sqrt{2r/\pi} \sqrt{(a_{44}a_{55} - a_{45}^2)}$$

Summing the corresponding displacements above for the symmetric and skew symmetric cases gives the displacements for the mixed mode plane condition. Equations (A-11) to (A-13) can be reduced to the isotropic case by substitution of the following values.

$$\mu_1 = \mu_2 = i$$

$$S_{16} = S_{26} = a_{45} = 0$$

$$S_{11} = S_{22} = (1-\nu)/E \quad ; \text{ Plane strain}$$

$$S_{12} = -\nu(1+\nu)/E \quad ; \text{ Plane strain}$$

$$a_{44} = a_{55} = 2(1+\nu)/E$$

$$u = 2S_{11} K_{III} \sqrt{(2r/\pi)} \quad (14)$$

$$v = 2S_{22} K_{III} \sqrt{(2r/\pi)} \quad (15)$$

$$w = a_{44} K_{III} \sqrt{(2r/\pi)} \quad (16)$$

Calculation of the relative movement of opposite pairs of crack face nodes parallel to the normal, the binormal and the tangent to the crack front (pqr in Figure A-16) and their substitution into the displacement Equations (A-11) to (A-13) will give values of  $K_I$ ,  $K_{II}$  and  $K_{III}$  at a distance 'r' from the crack tip. Extrapolation of these values to  $r = 0$  will give the crack tip stress intensity factors K.

### A.2.9 Elastic Strain Energy Method

The elastic strain energy difference was calculated in MARC by a differential stiffness method [A.3] and the Strain Energy Release Rate 'G' was calculated by dividing the strain energy difference by the area of crack advance. The mesh distortion associated with the calculation of G is shown in



Figure A-18. All the values of G obtained by the Strain Energy Method assumed advance of the crack in its existing plane. The results were used to verify the  $K_I$ ,  $K_{II}$  and  $K_{III}$  values calculated by the Displacement Extrapolation (Section A.2.8) as follows:

#### Verification Of Calculated K Values

The method of differential stiffness for the calculation of G leads to problems in the simultaneous solution for  $K_I$ ,  $K_{II}$  and  $K_{III}$ . However, the values of G associated with each of the three modes of opening can be calculated as follows [A.4]

$$G_I = - \frac{K_I}{2} S_{22} \operatorname{Im} \left[ \frac{K_I(\mu_1 + \mu_2) + K_{II}}{\mu_1 \mu_2} \right] \quad (A-17)$$

$$G_{II} = \frac{K_{II}}{2} S_{11} \operatorname{Im} [ K_{II}(\mu_1 + \mu_2) + K_I \mu_1 \mu_2 ] \quad (A-18)$$

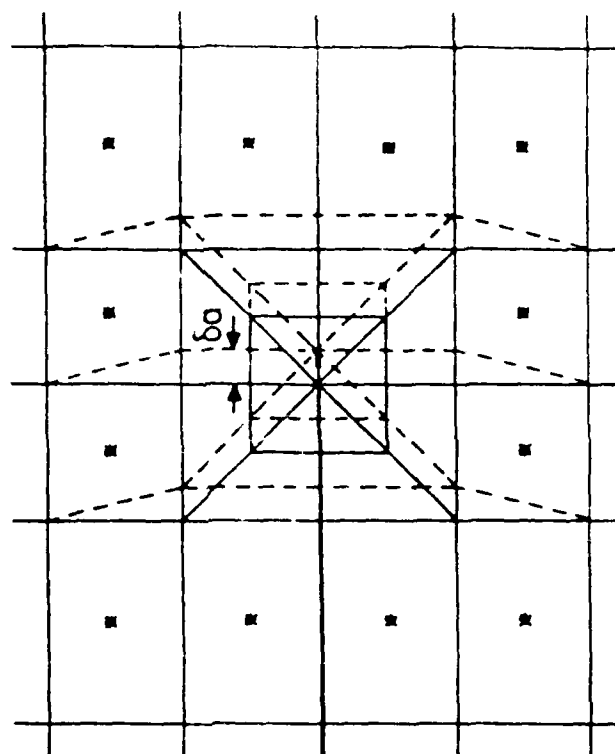
$$G_{III} = \frac{K_{III}^2}{2} \frac{a_{44} a_{55}}{\sqrt{(a_{44} a_{55} - a_{45}^2)}} \quad (A-19)$$

For coplanar crack advance and general anisotropic conditions the value of G is given as

$$G = G_I + G_{II} + G_{III} \quad (A-20)$$

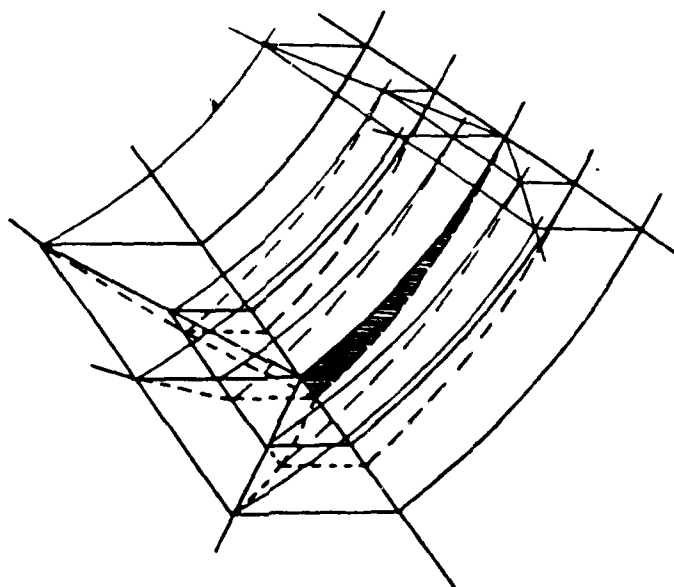
Substitution of the values of  $K_I$ ,  $K_{II}$  and  $K_{III}$  from displacement extrapolation into the above equations allows comparison between a directly calculated and a derived value for G and hence a means of verifying the values of K.

In addition, for cracking on the (111) plane, a plane of elastic symmetry as specified in the derivation of the characteristic Equation (A-4)



Element thickness =  $B$   
 Change in crack area =  $\Delta A = B \cdot \delta a$   
 Only the starred elements show a stiffness  
 change on crack extension.

FIGURE A-18(a). Differential stiffness energy release calculation - mesh distortion.



Shaded region = change in crack area

FIGURE A-18(b). Energy release rate calculation, 3D crack front.

only exists at two points around the semicircular crack front. The comparison between the calculated and derived values of G allows assessment of the extent to which the plane assumption must be rigidly applied.

#### A.2.10 Results of 3-Dimensional Analyses

The computer coding developed for the generation of elastic properties, the calculation of the roots of the characteristic equations and the calculation of stress intensity factors from the displacement extrapolation method was used for both the isotropic and locally anisotropic models.

##### 30 Degree Angled Edge Through-Crack

The 48 element FE model used for this analysis was set up as a preliminary trial to investigate the use of MARC with 3-dimensional locally anisotropic crack models. As a consequence of the coarseness of the mesh and the resulting scatter of the rear-tip nodal displacements, the stress intensity results for the isotropic case were lower than the published results for angled edge cracks [A.1, A.8] by at least 7 percent. Having developed the techniques for handling such problems, efforts to refine and rerun the job were diverted in preference of the semicircular surface crack model.

The stress intensity factors for the angled edge crack were normalized with respect to

$$K_0 = \sigma \sqrt{\pi a^*}$$

where  $\sigma$  = remote uniaxial stress

$a^*$  = crack length

Figure A-19 shows the normalized Mode I stress intensity factors, for the isotropic and locally anisotropic models and the isotropic plain strain results given by the Rooke and Cartwright [A.1] and Preston and Pickard [A.8].

Figure A-20 shows the normalized Mode II and Mode III stress intensity factors for the isotropic and locally anisotropic models. The plane strain Mode II results according to Rooke and Cartwright [A.1] and Preston and Pickard [A.8] are also shown.

Figure A-21 shows  $G_{de}/G_e$ , the ratio of strain energy release rates derived by displacement extrapolation and calculated by the energy method. The lack of symmetry of  $G_{de}/G_e$  along the crack front of the anisotropic model indicated that the displacement extrapolation method and the strain energy method were unable to give equivalent results with the coarse mesh provided.

#### Semicircular Surface Crack

The stress intensity factors were normalized with respect to

$$K_0 = 2 \sigma \sqrt{a/\pi}$$

where  $\sigma$  = remote uniaxial stress

$a$  = crack radius

Although the method of analysis was applicable to angled surface cracks, it was decided to validate the model for the isotropic case by comparison with published results [A.1, A.9, A.10] and so a perpendicular surface crack model was developed.

Figure A-22 shows the normalized Mode I stress intensity factors for the isotropic model around the crack front for  $\delta = 0$  to  $90^\circ$  compared with the full curve by Rooke and Cartwright [A.1] and surface and full crack depth results by Hellen and Blackburn [A.9] and Pickard [A.10]. According to Hellen and Blackburn [A.9], the results at a free surface should be treated as under

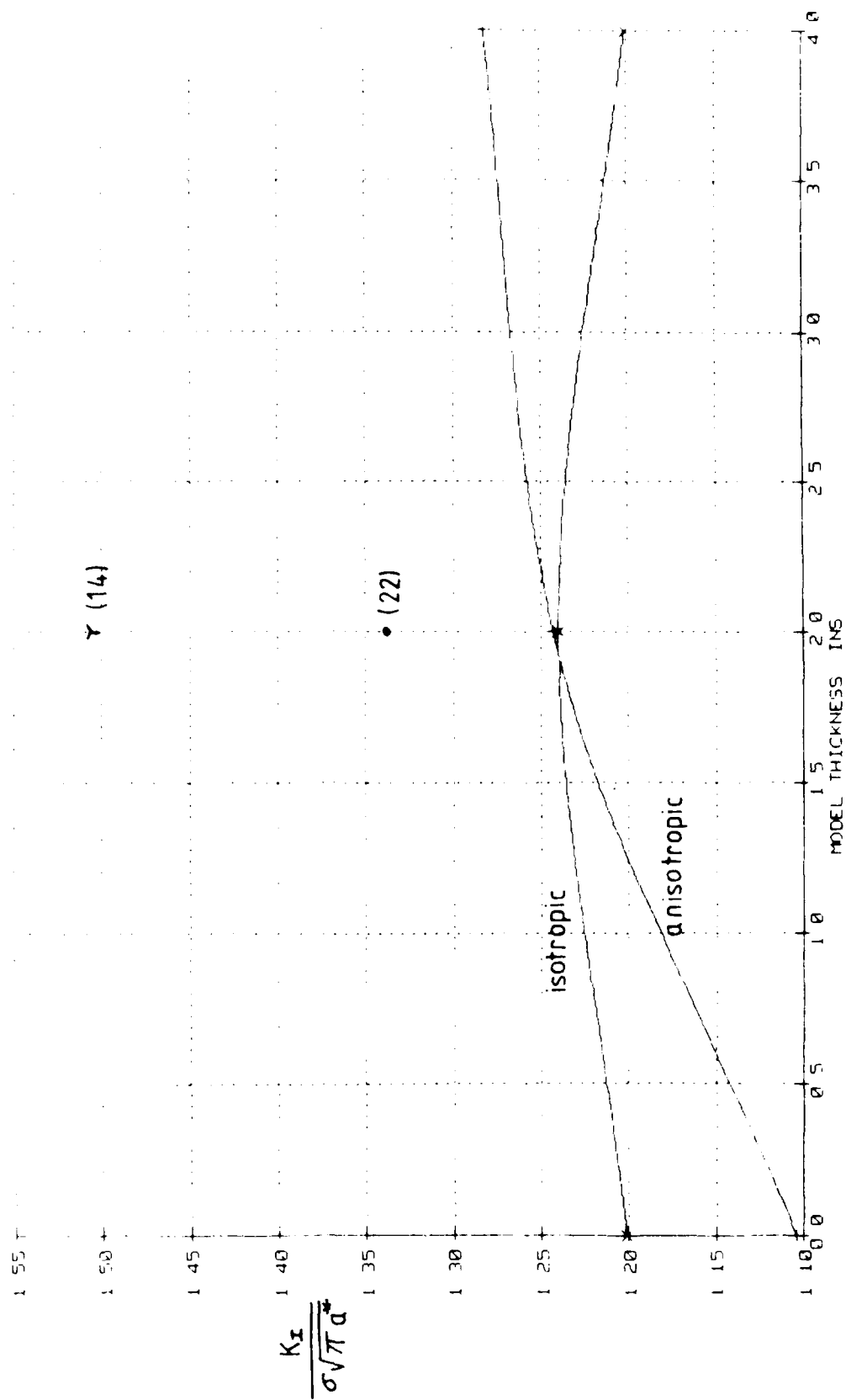


FIGURE A-19. 30 Degree Angled Edge Through-Crack

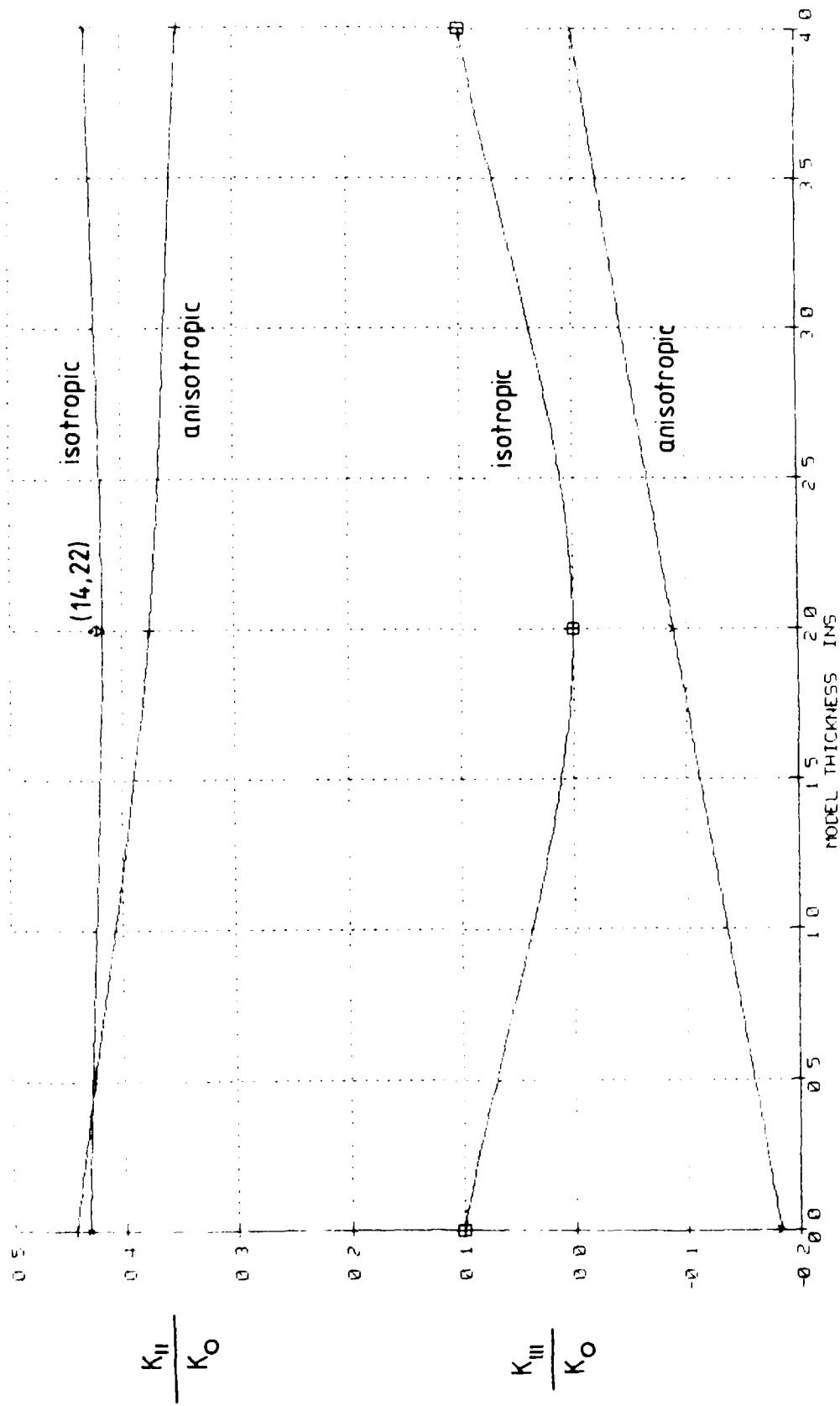


FIGURE A-20. 30 Degree Angled Edge Through-Crack

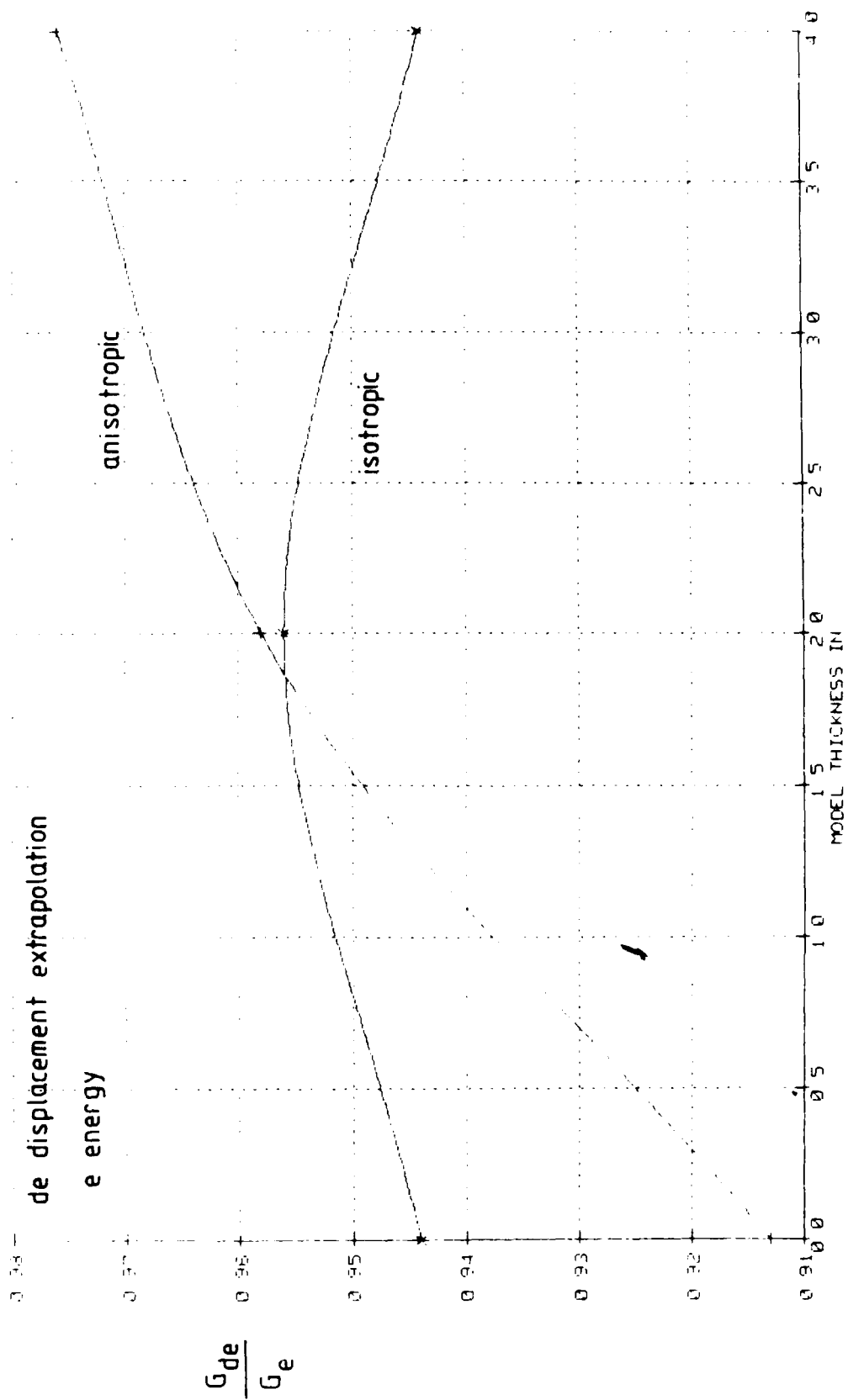


FIGURE A-21. 30 Degree Angled Edge Through-Crack

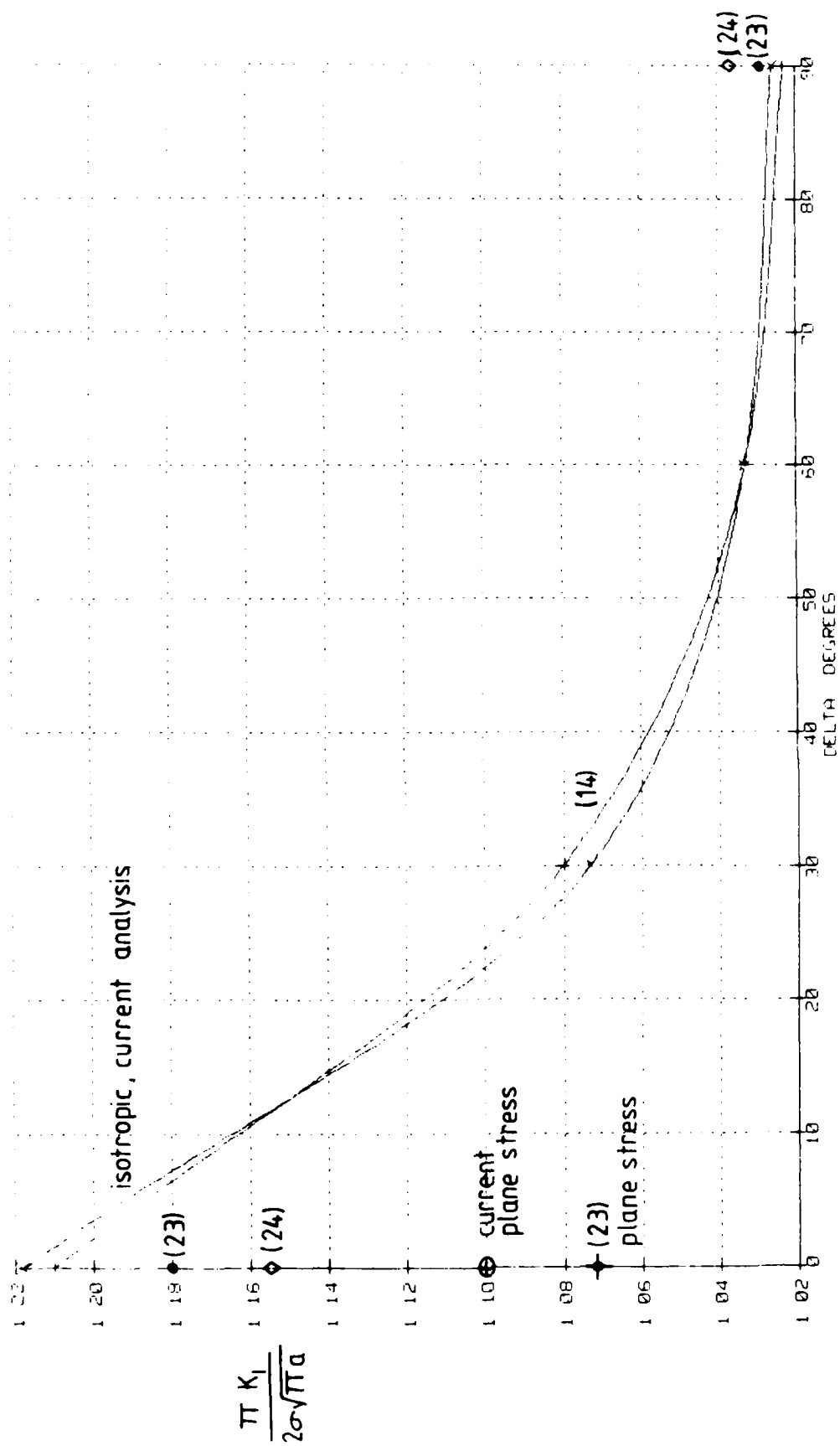


FIGURE A-22. Semicircular Surface Crack



plane stress and their result and that given by the current analysis are shown in Figure A-22.

Figure A-23 shows the isotropic and locally anisotropic normalized Mode I stress-intensity factors given by the current analysis for  $\delta = 0$  to  $180^\circ$ .

The normalized  $K_{II}$  and  $K_{III}$  values for the locally anisotropic case are given in Figure A-24. For the isotropic case the  $K_{II}$  and  $K_{III}$  values were zero. The Mode II anisotropic plane stress solution at the free surface is also given in Figure A-24.

Figure A-25 shows  $G_{de}/G_e$ , the ratio of strain energy release rates derived by displacement extrapolation and calculated by the energy method. Although it is recognized that the energy method provides a weighted average value for the strain energy release rate close to the free surface, whereas that derived from the displacement extrapolation K values is specific to the surface, the two values of G were much closer when plane stress conditions were assumed for the Modes I and II solutions, both for the isotropic and the locally anisotropic cases.

#### A.2.11 Conclusions

The displacement extrapolation technique was used to determine 3-dimensional stress intensity factors in locally anisotropic materials. This technique has the advantage of being able to separate the values of K for each of the three modes of opening and when used with quarter point elements at the crack front, is expected to yield accurate results. However, because of the material anisotropy the 3-dimensional solutions should strictly only be valid at points where a plane of elastic symmetry exists simultaneously perpendicular to the crack plane and crack front. In order to check the

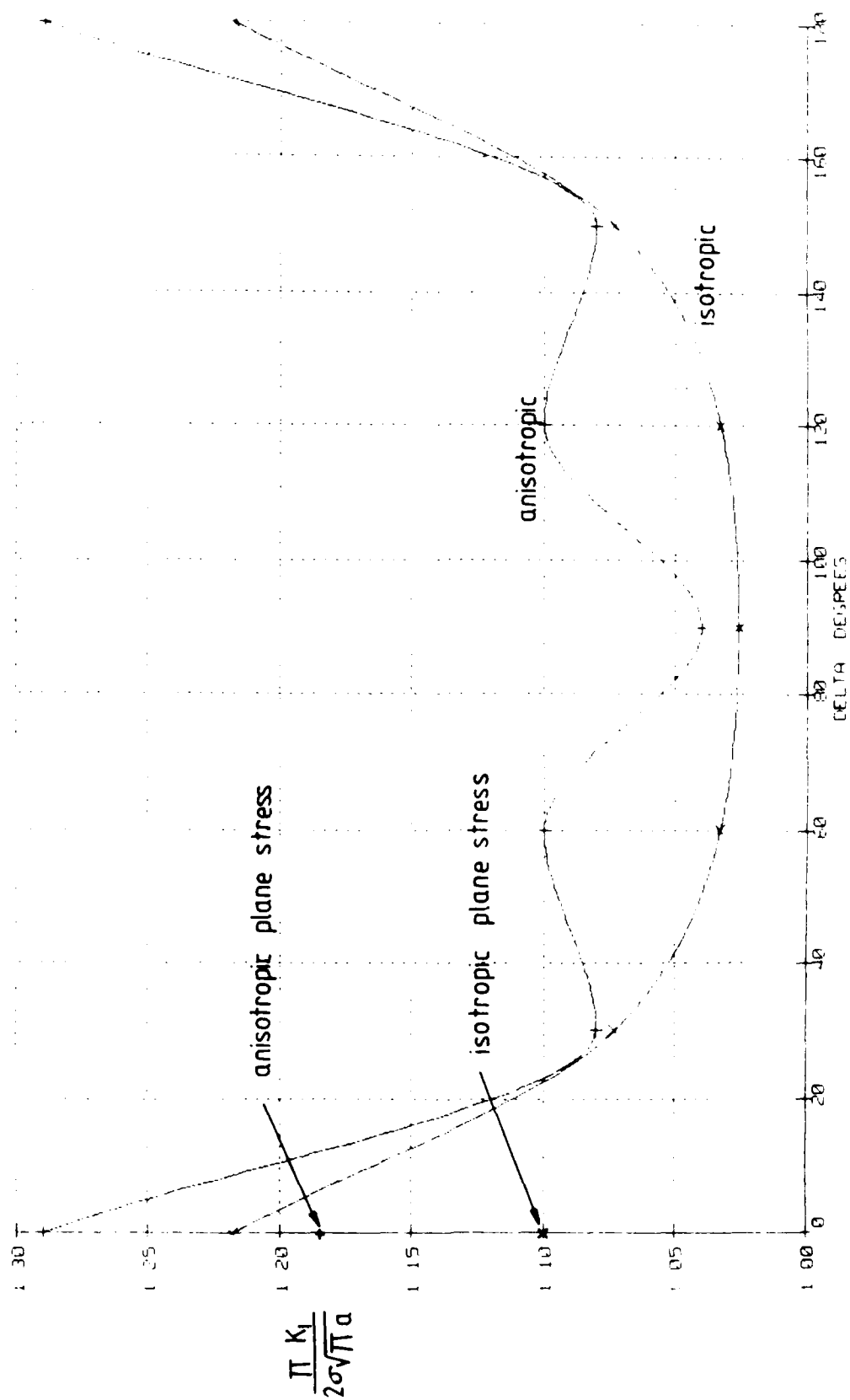


FIGURE A-23. Semicircular Surface Crack

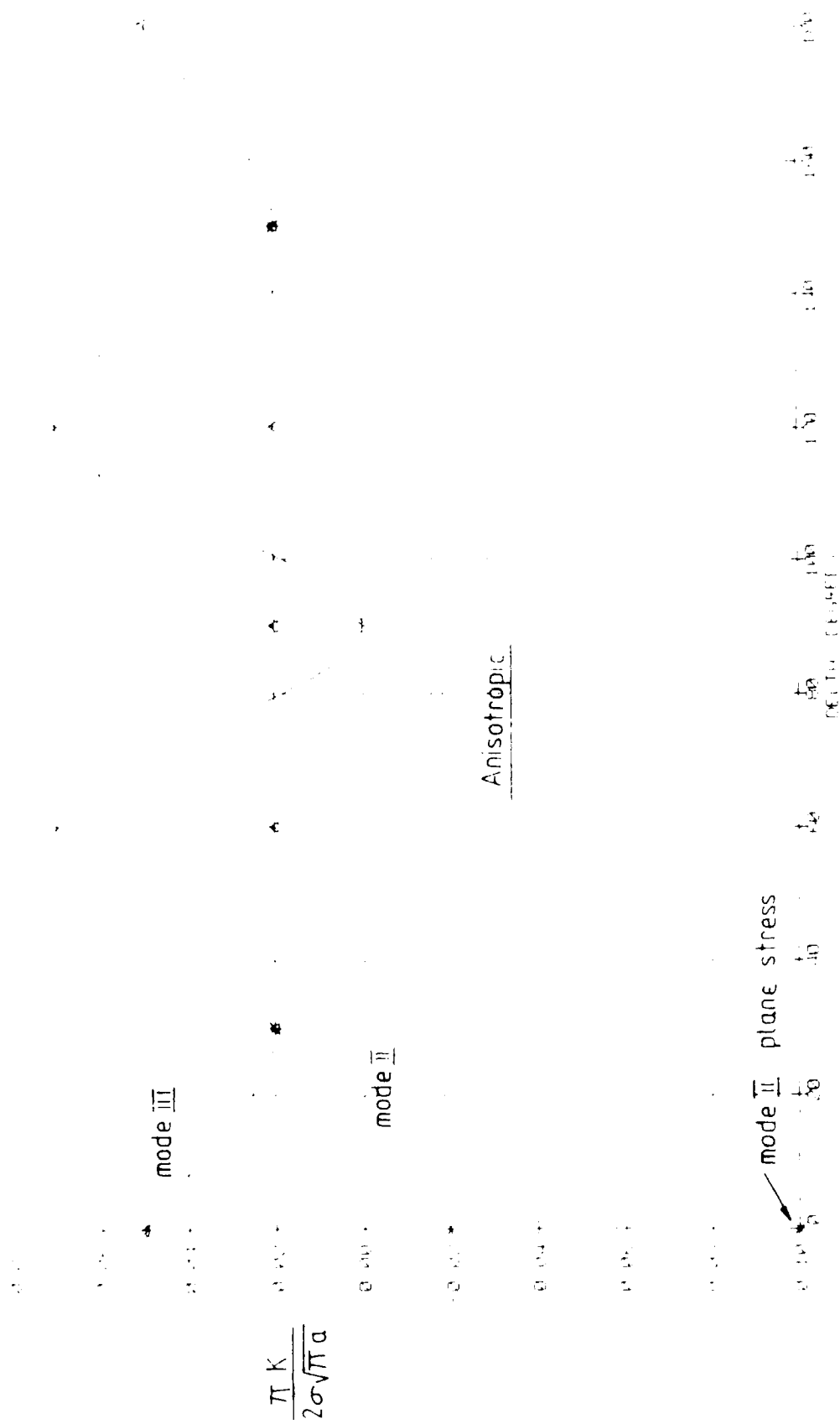


FIGURE A-24. Semicircular Surface Crack

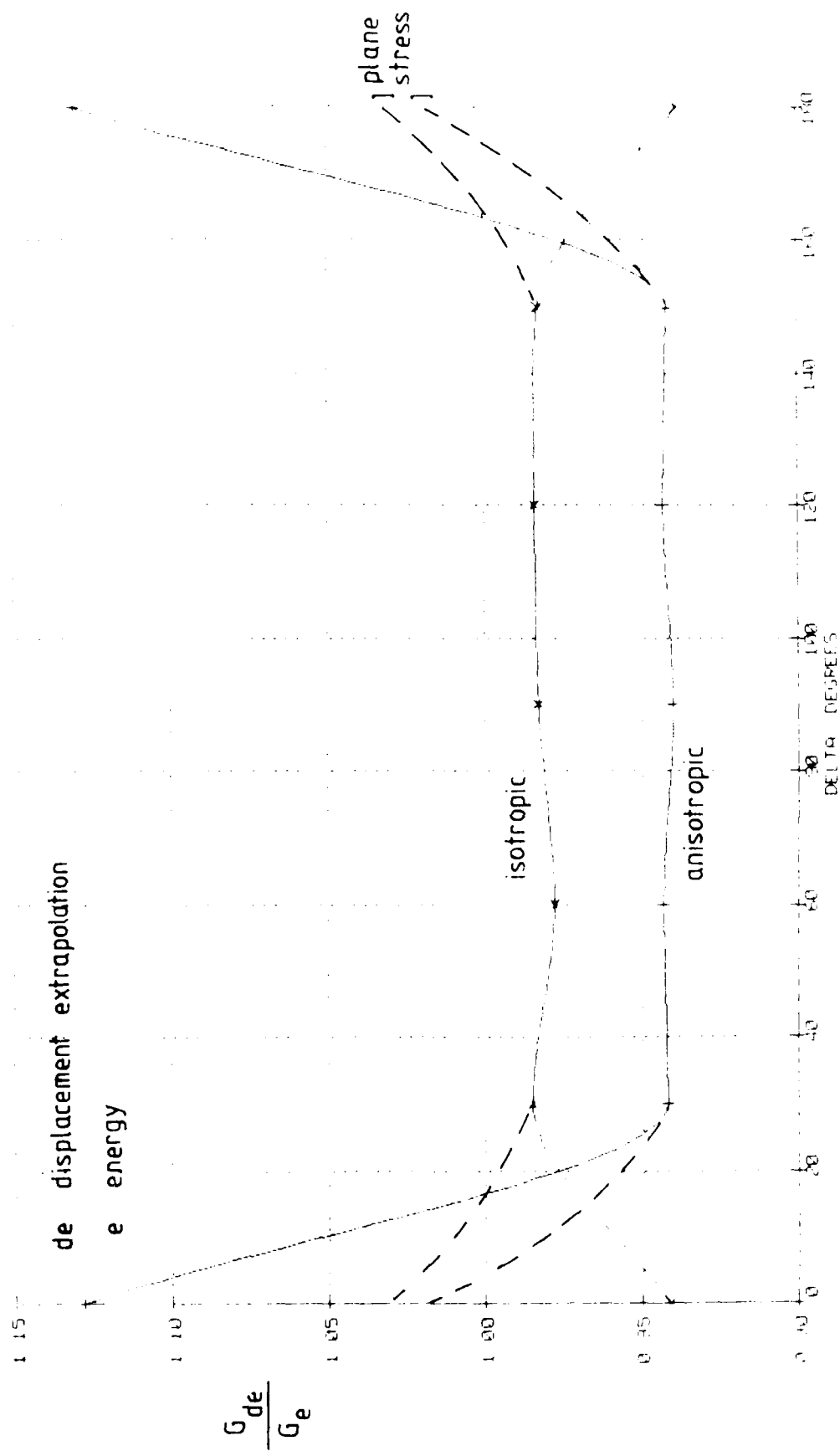


FIGURE A-25. Semicircular Surface Crack

rigidity of this symmetry restriction, the elastic strain energy release rate  $G$ , derived from the  $K$  values, was compared with the  $G$  calculated by the differential stiffness (energy) method. The values of  $G_{de}/G_e$  given for the perpendicular semicircular surface crack model show that the symmetry requirement does not need to be enforced rigidly. Confidence in the locally anisotropic  $K$  values being consistently higher than the corresponding isotropic values leads to interesting consequences for the presentation of 'small' crack growth data in relation to those for 'long' cracks.

Although the effect of plane stress conditions at the free surface would be very localized, the disparity between the displacement extrapolation and the differential stiffness (energy) methods was reduced by such an assumption. Together with metallurgical features which hinder crack advance along the free surface, the plane stress condition could be a contributory factor in the successful modelling of crack shapes. Accurate component life prediction depends very much on knowledge of the crack shape and accurate stress intensity solutions. The results given here indicate that the stress intensity solutions used to present small crack data may require revision.

### A.3 Summary

This report considers the calculation of stress intensity factors in a material containing a small crack in a region considered to be locally anisotropic. The finite element analysis work was developed in two stages, a) 2D plane solutions and b) 3D solutions. Both stages involved the calculation of isotropic solutions to check the models and methods against published results before the introduction of local anisotropy. All the analyses assumed linear elasticity.

### 2D Finite Element Analysis

A perpendicular edge crack model was constructed using 8 node isoparametric quadrilateral plane strain elements. The crack tip was constructed using degenerate crack tip elements to represent the elastic singularity. Stress intensity factors were calculated by both the strain energy method and the displacement extrapolation method.

The modelling of crystallographic crack branching was investigated for a range of orientations of local anisotropy. The strain energy release rate peaked at or very close to the direction of colinear crack advance and it was concluded that this parameter could not be relied upon to predict the direction of crystallographic crack growth.

### 3D Finite Element Analysis

Two models, an angled edge through crack and a perpendicular semicircular surface crack, were constructed using 20 node isoparametric brick elements. The crack tip region was constructed using degenerate quarter point elements to represent the elastic singularity. Strain energy calculations for the locally anisotropic model were used to verify the displacement extrapolation results. The anisotropic region around the crack was orientated such that the crack ran along a close packed plane.

The results of the analyses, for a limited number of anisotropic orientation and geometric configurations, have revealed that increased stress intensities (on average, 5 percent greater than the isotropic case, Figure A-23) may be observed for particular configurations compared to those derived using isotropic, homogeneous models.

#### A.4 References

- A.1 D. P. Rooke and D. J. Cartwright, Compendium of Stress Intensity Factors, HMSO.
- A.2 R. S. Barsoum, "On the Use of Isoparametric Finite Elements in Linear Fracture Mechanics," Int. J Numer. Meth. Engng. 10, pp. 25-37 (1976).
- A.3 T. M. Parks, "A Stiffness Derivative Finite Element Technique for Determination of Crack Tip Stress Intensity Factors", Int. J Fracture, 10, pp. 487-502 (1974).
- A.4 G. C. Sih, P. C. Paris and G. R. Irwin, "On Cracks in Rectilinearly Anisotropic Bodies," Int. J Fracture Mech. 1, pp. 189-203 (1965).
- A.5 T. K. Hellen and W. S. Blackburn, "The Calculation of Stress Intensity Factors for Combined Tensile and Shear Loading," Int. J Fracture, 11, pp. 605-617 (1975).
- A.6 R. J. Nuismer, "An Energy Release Rate Criterion for Mixed Mode Fracture," Int. J. Fracture 11, pp. 245-250 (1975).
- A.7 F. Lemant and A. Pineau, "Mixed Mode Fracture of a Brittle Orthotropic Material - Example of Strongly Textured Zinc Sheets," Eng. Fract. Mech. 14, pp. 91-105 (1981).
- A.8 T. J. Preston and A. C. Pickard, "Stress Intensity Factor and Potential Drop Calibrations for Angled Edge Cracks in Tensile Specimens," Internal Rolls Royce Report ASR99191, 1983.
- A.9 W. S. Blackburn and T. K. Hellen, "Calculation of Stress Intensity Factors in Three Dimensions by Finite Element Methods," Int. J Num. Meth. Engng. 11, pp. 211-229, 1977.
- A.10 A. C. Pickard, "The Application of 3-Dimensional Finite Element Methods to Fracture Mechanics and Fatigue Life Prediction," EMAS, 1986.

FILMED  
2-8